Characterizing DNA Origami Linear Assemblies

Dissertation
zur
Erlangung des Doktorgrades
Dr. rer. nat.

der Fakultät für Biologie
an der
Universität Duisburg-Essen

vorgelegt von
Lena Johanna Stenke, geb. Winat

aus Mettmann
April 2023

"If we knew what it was, we were doing, it would not be called research, would it?"

– Albert Einstein

In the context of this doctoral work, the following articles were published:

Growth Rate and Thermal Properties of DNA Origami Filaments, Stenke, LJ. and Saccà, B., Nano Letters 22, (2022)[1]

Design, Mechanical Properties, and Dynamics of Synthetic DNA Filaments, Stenke, LJ. and Saccà, B., Bioconjugate Chemistry 34, (2023)[2]

The primordial life of DNA dynamic networks, Winat, LJ. and Saccà, B., Nature Catalysis 3, (2020)[3]

The following article was accepted for publication:

Sequence-dependent folding of monolayered DNA origami domains, Gambietz, S., Stenke, LJ. and Saccà, B.

The following article is in preparation for publication:

DNA Origami Polymerization with a DNA Reaction Network, Stenke, LJ., Weiß, M., Saccà, B.

Die der vorliegenden Arbeit zugrunde liegenden Experimente wurden am Zentrum für Medizinische Biotechnologie der Universität Duisburg-Essen in der Arbeitsgruppe Bionanotechnologie unter der Leitung von Prof. Dr. Barbara Saccà durchgeführt.

1. Gutachterin: Prof. Dr. Barbara Saccà
2. Gutachter: Prof. Dr. Stefan Westermann
3. Gutachter: Prof. Dr. Francesco Ricci

Vorsitzender des Prüfungsausschusses: Prof. Dr. Michael Ehrmann

Tag der mündlichen Prüfung: 14.07.2023

DOI: 10.17185/duepublico/78769
URN: urn:nbn:de:hbz:465-20250108-124037-8

Zusammenfassung

Im Zuge dieser Dissertation wurden die linearen Verbünde des 24-Helix DNA Origamis mit je einem A- und einem B-Ende, welche perfekt formkomplementär und partiell homokomplementär zueinander sind, untersucht. Ziel war der Vergleich der Polymerisationsmechanismen Hybridisierung und Basenstapelung, sowie die Charakterisierung des Einflusses von Grenzflächensymmetrien auf die kinetischen und thermodynamischen Eigenschaften. Außerdem wurden die Auswirkungen von Basenpaarlücken auf die auf Basenstapelkräften basierende isologe Dimerisierung betrachtet[1]. Um ein dynamischeres Polymerisationsverhalten zu erreichen, wurde der Output eines autokatalytischen DNA-Reaktionsnetzwerks als Treibstoff verwendet. Darüber hinaus wurde eine Feinabstimmung und Reversibilität realisiert.

Die Dimere wiesen je acht oder 16 Helices mit einer Lücke von einem BP auf. Eine höhere Anzahl an Lücken wirkte sich zwar nachteilig auf die thermische Assemblierung aus, trug jedoch erheblich zur thermischen Stabilität bei. Es wurde ein Stacking-Schwellenwert von mindestens acht (33 %) aktivierten Helices für die Monomereinheiten ermittelt, welcher einer Energie von -7,35 kcal/Mol entsprach. Die Stapelungsstärke wurde erfolgreich mit den sequenzspezifischen Stapelenergien korreliert. 67 % (BB) anstelle von 33 % (AA) unvollkommenen Helices erhöhten die anfängliche Dimerisierungsrate um den Faktor zwei ($k_a^{in} = 0.14\ \text{min}^{-1}$ für AA und $0.3\ \text{min}^{-1}$ für BB) und halbierten die effektive Assoziationszeit.

Der Grad der Komplementarität aller Assoziationstypen AB, AA und BB bestimmte die Gleichgewichtsverteilung der zufälligen Basenstapelung. Während die kinetische Assoziation der BB-Stapelung bevorzugt wurde, konnte nach Kurzem ein Schrumpfen des Filaments beobachtet werden. Die kritischen Konzentrationen der Hybridisierung und Stapelung lagen im pikomolaren Bereich, wobei die Hybridisierung temperaturabhängig und die Stapelung temperaturunabhängig war. Polymere auf Stapelbasis wuchsen zu Anfang zehnmal schneller als Hybridisierungspolymere, insbesondere in der ersten Stunde. Die Hybridisierung zeigte anfangs flexiblere Verbindungen, wohl durch notwendige Strangablösungen, während beide Mechanismen Polymere aus Monomeren und auch Oligomeren bilden konnten. Allerdings konnte nur die Stapelung neue Monomere durch Spaltung oder Eingliederung in bestehende Filamente integrieren. Insgesamt war die thermische Stabilität der Hybridisierungspolymerverbindungen um zwei °C höher als die der durch Stapeln entstandenen Polymere. Die gezielte Aktivierung der zu hybridisierenden Helices ermöglichte eine Feinabstimmung der Polymerisation, wobei die alleinige Aktivierung der äußeren Helices kinetisch die der vollständigen Aktivierung übertraf.

Schließlich wurde das dynamische Verhalten eines adaptierten autokatalytischen DNA-Reaktionsnetzwerks erfolgreich in die DNA-Origami-Hybridisierungs-Polymerisation integriert, indem eine Bindestelle für identische fuel-Stränge an den Monomer-Enden eingeführt und optimiert wurde. Die Kopplung des allmählich freigesetzten fuel-Strangs an die Polymerisation hatte hauptsächlich Auswirkungen durch die verringerte Gesamtstrangfreisetzung, aber nicht wesentlich auf die Reaktionskinetik. Die Erweiterung des fuel-Strangs um eine Toehold-Domäne, ermöglichte eine Feinabstimmung der Polymerisationskinetik sowie die vollständige Reaktionsumkehr.

Abstract

This thesis describes the linear assembly of a 24-helix bundle DNA origami structure displaying two interfaces, A and B, that are perfectly shape-complementary and partially self-complementary. The aim was to explore the effects of two distinct association mechanisms, hybridization and stacking, on the polymerization of the structure, as well as the influence of interface symmetries on the kinetic and thermal properties of the assemblies. The base stacking-driven isologous dimerization process and the impact of one base pair gapped helices on interface associations were also investigated[1]. To achieve a more dynamic polymerization behavior, the output of an autocatalytic DNA reaction network was used to fuel the polymerization process, with finetuning and reversibility also being achieved.

The dimers presented 8 or 16 helices with a one base pair gap. Higher numbers of gapped helices adversely affected thermal assemblies while contributing significantly to thermal stability upon heating. A threshold of at least 8 (or 33 %) activated helices was found to be necessary for the successful stacking of the monomer subunits, with a resulting stacking energy threshold of -7.35 kcal/mol. Stacking forces were successfully correlated to sequence-specific stacking energies. Increasing the extent of gapped helices to 67 % (instead of 33 %) led to a two-fold increase in the initial dimerization rate (k_a^{in} = 0.14 min^{-1} for AA- and 0.3 min^{-1} for BB-stacking, respectively), and effectively halved the stacking time.

The equilibrium distribution followed the degree of shape-complementarity for all types of random stacking associations: namely AB, AA, and BB. While kinetic assemblies were favored for BB-stacking, filament depletion could also be observed shortly after assembly. Critical concentrations of hybridization vs. stacking were in the picomolar range, with hybridization c_{crit} temperature-dependent and stacking temperature independent. Stacking-based polymers initially elongated ten-fold faster than hybridization-based species, especially in the first hour. Hybridization initially had a more flexible connection with necessary strand displacements, while both mechanisms grew from monomers and oligomers. However, only stacking could integrate new components into equilibrium filaments through scission. Overall, the thermal stability of hybridization polymer connections was two °C higher than for stacking obtained polymers. Arranging the placements of hybridized helices could finetune polymerization with only outer helices outperforming complete activation.

Lastly, the dynamic behavior of an adapted autocatalytic DNA reaction network was successfully integrated into the DNA origami hybridization polymerization by introducing and optimizing an integrated interface binding identical fuel strands. Coupling the DRN's gradual release of the fuel strand to the polymerization was limiting mainly by the decreased total strand release but surprisingly not notably in the reaction kinetics. Introducing a five-base toehold domain in the fuel strand allowed for finely tuning the polymerization kinetics to reverse the reaction altogether.

Table of Contents

Introduction

DNA as a Construction Material

DNA in a Historical View

Deoxyribonucleic acid (DNA) or nuclein, as it was named originally, was discovered in 1869 by Friedrich Miescher when he tried to isolate protein from leukocyte nuclei but instead discovered a new substance with resistance to proteolysis, which contained significantly more phosphorus[4,5]. His student Richard Altmann discovered the acidic properties of the nucleus content, which led to the naming of nucleic acid[6]. Four years later, in 1893, Albrecht Kossel and Albert Neumann revealed the presence of four distinct bases in nucleic acid[7]. Years later, in 1919, Phoebus Levene postulated the structure of nucleic acids comprised of a phosphate group, a sugar molecule, and one of the four nitrogen-containing bases[8]. In 1944, Oswald Avery and his colleagues finally demonstrated that desoxyribonucleic acid carries hereditary information[9]. Based on these findings, Erwin Chargaff was inspired to investigate the chemistry of nucleic acids further and found that the number of purine and pyrimidine bases of a sample were identical, clearing the path for the known base pairing rule[10].

In the end, it was James Watson and Francis Crick in a laboratory in Cambridge, England, who combined their research and the pre-established information with some questionably involuntary contribution of Rosalind Franklin to proclaim:

"We have discovered the secret of life."

-Francis Crick, February 28, 1953[11]

In a two-page publication, they introduced the double helical structure of DNA and the hydrogen bonding of adenine with thymine and cytosine with guanine[12]. This study was followed by a more extensive description of genetic replication a few months later[13]. Rosalind Franklin's and Raymond Gosling's remarkably detailed X-ray crystal structure of sodium deoxyribose nucleate (B-DNA) was published in Nature on April 25, 1953, alongside the first paper by Watson and Crick[14]. Maurice Wilkins working in the same laboratory at Kings College, who had obtained X-ray crystal structures of DNA in 1951, also published his findings in the same issue[15]. Watson, Crick, and Wilkins received the Nobel prize in physiology or medicine in 1962 after Franklin's untimely death from cancer in 1958[11]. The base complementary hydrogen bonding of a purine with a pyrimidine base is taught today as Watson-Crick base pairing, although it has come to be referred to as Watson-Crick-Franklin base pairing lately.

In the years following the discovery of the structure of DNA, much progress heavily driven by Francis Crick[16–18] was made in understanding one of the most important, if not **the** most important, molecule of life and its cellular functions. As of today, all five nucleobases present in DNA and RNA were detected on extraterrestrial meteoroids[19], and science has come a long way to find new and creative ways to utilize DNA's intrinsic properties.

DNA and its Properties

Under physiological conditions, replicable in *in-vitro* assays, DNA is present in the most common right-handed B-form (Figure 1a)[20]. In this configuration, the double-stranded antiparallel helix has a diameter of 2 nm and is vertically divided into a major groove with a width of 22 Å and a minor groove with a width of 12 Å. One helical turn comprises 10.5 base pairs and spans a helical pitch of 3.4 nm[21,22]. The nucleobases can be divided into purine (adenine A, guanine G) and pyrimidine (thymine T, cytosine C) bases depending on the presence of two or one carbon-nitrogen rings, respectively (Figure 1e). Hydrogen bonding non-covalently binds one purine base to one pyrimidine base. The Watson-Crick-Franklin complementary base pairing of A=T and G≡C comes from the specific formation of two hydrogen bonds between adenine and thymine, while guanine and cytosine form three hydrogen bonds.

Consequently, the G-C content of dsDNA predominantly affects the double-strand's melting temperature[23]. While the nucleobases are directly bound to the pentose sugar deoxyribose via a glycosidic bond, the DNA backbone constantly alternates a deoxyribose molecule with a phosphate group (Figure 1d). The orientation of the antiparallel helices is defined by the chemical group present at the strand ends. At the 3' end, the deoxyribose presents a hydroxyl group, while at the 5' end, a phosphate group is exposed. Within the nucleotide, ribose and phosphate are linked via an ester bond towards the 5' orientation. Individual nucleotides are linked via phosphodiester bonds at the 3' end of the growing ssDNA chain. Overall the DNA molecule carries negative charges along the phosphate backbone, which favors the binding of cations[24].

Next to the well-hydrated B-form of the DNA double helix, more configurations are known, of which the A- and Z-forms are relatively well characterized (Figure 1b,c). The A-form (Figure 1b) results from low humidity conditions in dried DNA or DNA crystals[25]. The jolted right-handed helix presents 11 bases per turn and spans over 2.8 nm per helical pitch with a diameter of 2.3 nm[26]. Contrary to A- and B-DNA, transient Z-DNA is left-handed and shows no significant difference between major and minor grooves (Figure 1c). Its 4.46 nm helical pitch encompasses a 12 base pair turn with a diameter of 1.8 nm[27].

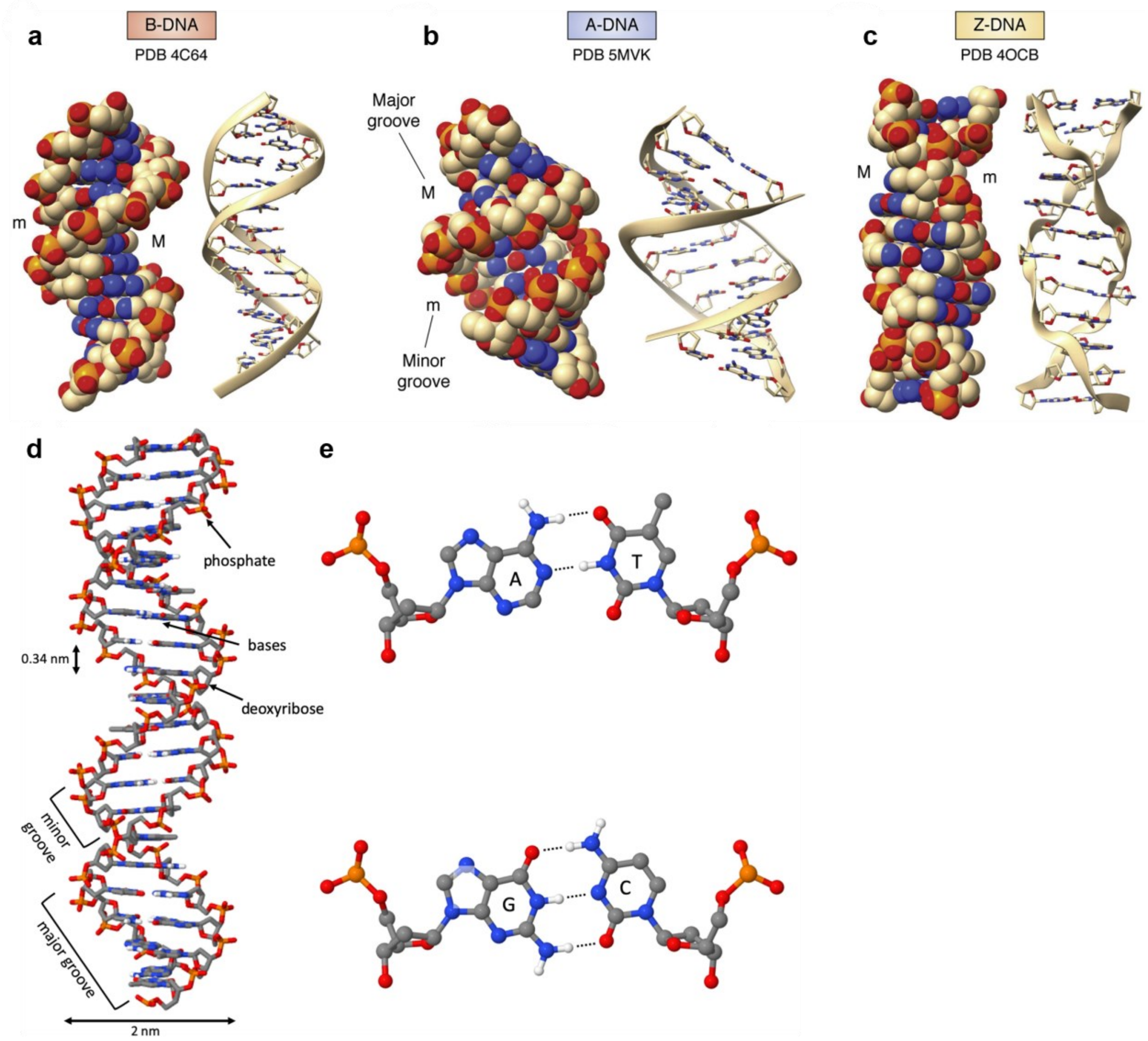

Figure 1 ***The structure of DNA***

a-c) Three types of DNA with different helical configurations. Depicted are a) the most common right-handed B-form, b) the right-handed jolted A-form, and c) the left-handed Z-form. d) The B-form deoxyribonucleic acid molecule has an antiparallel orientation of strands comprised of repetitions of deoxyribose and phosphate as the backbone and a nitrogen-containing nucleobase coding for amino acids in base triplets. One turn of dsDNA comprises 10.5 bases, which span over 3.4 nm with a helix diameter of 2 nm in B-DNA. e) The complementary pairing of adenine with thymine and guanine with cytosine is realized via two or three hydrogen bonds.

(a-c) reprinted from Neidle (2021)[20] under CC BY license, d) and e) adapted from Minchin and Lodge (2019)[21] under CC BY 4.0 license)

DNA Stabilizing Factors

Horizontal and vertical forces act to stabilize the DNA double helix. These are base-specific hybridization, also referred to as base pairing, as described by Watson and Crick[12,13], and base stacking. Base hybridization relies on the formation of two or three electrostatic hydrogen bonds formed by A=T or G≡C pairs, respectively (Figure 1e)[28]. The physical-chemical driving forces underlying base hybridization stem from the dipole-dipole interaction between a partial positive (δ+) hydrogen atom sharing electrons with a covalently bound partial negative (δ-) nitrogen. The δ+ hydrogen of one nucleobase can then non-covalently bind to either δ- nitrogen or oxygen of an oppositely facing base[29]. Base stacking is based on π π-electron interactions of orbital overlaps between the aromatic bases of the DNA strands. Although there are only two types of stabilizing mechanisms, there are three types of intrinsic interactions: intra-strand base stacking, inter-strand base stacking (Figure 2), and the already mentioned inter-strand base hybridization[30,31]. The essential contributors to helix stacking stabilization are surface electron clouds induced by London dispersion effects, also called induced dipole-dipole attractions, and electrostatic interactions[30]. Intramolecular stacking interactions shape the geometry of the helix[32].

The nearest neighbor model[33–35] integrates the energy contributions from hybridization and stacking forces to help estimate the overall thermal stability contributed by each dinucleotide association. The resulting melting temperature of dsDNA polymers linearly depends on the GC-content of the respective structure[23,36–39] and buffer salt concentrations[35,39–41]. An obvious explanation for this behavior lies within the different numbers of hydrogen bonds forming a base pair (Figure 1e), with A=T forming two and G≡C forming three H-bonds. Accordingly, AFM mechanical rupture measurements demonstrated a GC pair being stronger than an AT pair, with the former separating at 20 pN and the latter at 14 pN[38]. Stacking forces measured by AFM merely ranged close to 2 pN. However, alternative AFM-based force experiments on immobilized 10 bp-long DNA revealed global rupture forces ranging from 10 pN to 20 pN[42].

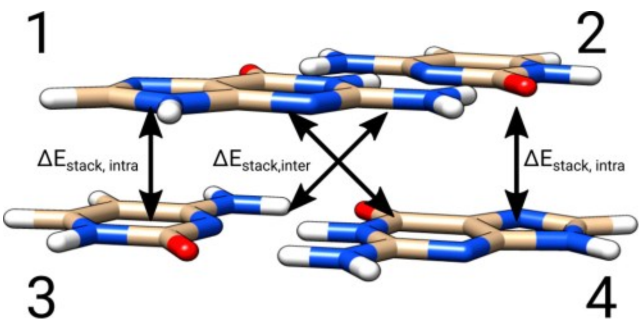

Figure 2 ***Base stacking interactions***
Illustration of stacking interactions between four adjacent bases of two dinucleotide pairs with intramolecular and intermolecular base stacking.

(Reprinted with permission from Kruse et al.[31] Copyright 2019 American Chemical Society)

PAGE-derived data aligns well with the linear dependence of GC content and melting temperature and indicates that stacking plays the major role in stabilizing the DNA helix[39,43]. Much research has been done to separate base hybridization and stacking contributions to helical stabilization. Protozanova et al.[44], for example, evaluated the stacking free energy based on PAGE assays[39] of nicked DNA fragments and provided a reference table for all possible base stack combinations. In their work, GC stacking had the highest free energy with -2.17 kcal/mol, and GC-containing regions were generally more stable due to base stacking interactions. Additionally, they concluded that base hybridization forces had little to even slightly adverse effects (AT: 0.57 kcal/mol, GC: -0.11 kcal/mol) on molecular stabilization, which could be in line with the geometrical constraints imposed by the sugar-phosphate backbone[45] and the binding of water molecules into the minor groove of AT associations[46]. Kilchherr et al.[47], in another approach, investigated stacking forces in DNA origami blunt ends including four instead of two nicked nucleotides and also provided an energetic table where ${}^{G}_{C}|{}^{C}_{G}$ was determined to have the highest stacking energy of -3.42 kcal/mol.

Estimates from 2020 indicate that one hydrogen bond between nucleobases of a DNA molecule contributes −0.72 kcal/mol to the stability of the helix[48]. This would need to be multiplied by a factor of two or three to account for the total number of hydrogen bonds in base pairing. This puts DNA H-bonds on the weaker side of the H-bond scale, with typical hydrogen bonds ranging from -2 to -15 kcal/mol, and the weakest found around -0.5 kcal/mol[49]. In this context, claims from Mo[50], in which an AT and a CG pair had a binding energy of -12.4 kcal/mol and -25.4 kcal/mol, respectively, seem overestimated.

Quantum mechanic evaluations attributed the majority of intrinsic stabilization of the DNA molecule to Watson-Crick-Franklin base pairing but stressed the additional importance of stacking[30]. However, criticism of these claims is founded in the simulation conditions, which did not consider the solvent or possible aqueous surroundings. Alternative quantum chemical analysis stresses the importance of diagonal intermolecular stacking forces between δ+ amino groups and δ- carbonyl groups and their crucial role in double helix stability, which considers the overall GC content and the sequence-specific base order[51]. Hydrogen bonds were also considered stabilizing factors. Consequently, CGG DNA triplets had the overall highest formation energy of -44.8 kcal/mol with combined intra- and intermolecular forces.

Nanotechnology

The physicist and Nobel laureate Richard Feynman was the first to broadly address the potential implications of the emerging field of Nanotechnology in his 1959 talk “There is plenty of room at the bottom”[52]. He addressed the limits of the, at that time, widely practiced miniaturization when “manipulating and controlling things on a small scale” and anticipated the marvels of building constructs from the bottom by rearranging atoms. It took 25 more years for Norio Taniguchi to finally coin the term “Nanotechnology” at a conference talk[53]. However, K. Eric Drexler communicated the coming implications of this vital field in his book “Engines of Creation: The Coming Era of Nanotechnology”[54], published in 1987. One of the breakthrough nanotechnology experiments was performed by IBM scientists Don Eigler and Erhard Schweizer, who placed 35 xenon atoms on a nickel surface with a scanning tunnel microscope (STM) to depict the IBM logo[55,56] (Figure 3).

There are two principal ways of obtaining nanosized objects. The top-down approach breaks down larger materials to create desired nanosized objects[57], similar to a sculptor carving a statue from a marble block. For the bottom-up approach, a fitting macroscale analogy would be a mason assembling a house brick by brick. On the nano level, this is equivalent to atoms or molecules being arranged into larger higher-ordered structures, frequently achieved by self-assembly[58].

Per definition, nanotechnology deals with structures from 1 to 100 nm in size whose physical properties are fundamentally different from those of macromolecular objects[59,60]. Plenty of nanoparticles have been introduced so far, originating from many different materials like lipids[61], metals[62–64], or carbon[65], to name a few. One widely known application of nanoparticles with a size similar to that of receptors on eukaryotic cells is the active targeting and delivery of drugs like cytostatic cancer agents to reduce

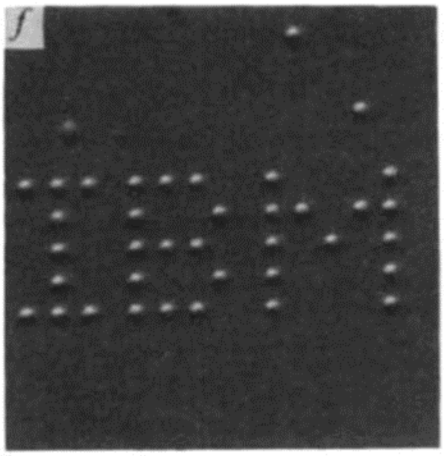

Figure 3 ***Arranging xenon atoms with Angstrom precision with STM***
35 xenon atoms precisely placed with a scanning tunnel microscope on a nickel surface to depict the IBM logo. (Reproduced with permission from Springer Nature from Eigler and Schweizer, 1990[56])

required drug amounts and undesired side-effects[57,59,60,66]. *In vitro* and *in vivo* diagnostic nano-biosensors enable the identification of a broad range of targets like cancer[67], viruses[68], antibodies[69], and many more analytes[70–73]. Other nanotechnology applications include carbon nanotubes which, depending on the fabrication, can exhibit extreme mechanical strength[74] or superconductive properties[75], among others. The potential of this field is as infinite as the human imagination.

Bionanotechnology and DNA Tiles

Combining nanotechnology with biotechnological research yields the exciting and emerging field of bionanotechnology, where biomaterials are engineered to display pre-planned desired behaviors[76,77]. One may distinguish two approaches to this field: one approach relies on the re-engineering of biologically inspired, often cellular processes, like kinesin walking on a microtubule; a second approach instead uses biological materials to engineer entirely new structures and functions. DNA nanotechnology, invented by Ned Seeman in 1982[78], belongs to this category and uses the DNA holliday junction (HJ), or four-way junction, as the building motif of all DNA nanostructures. The HJ results from two double helices exchanging one of their strands at a common point (crossover) and plays a vital role in the homologous recombination of chromosomes and genetic repairs in the cell[79,80].

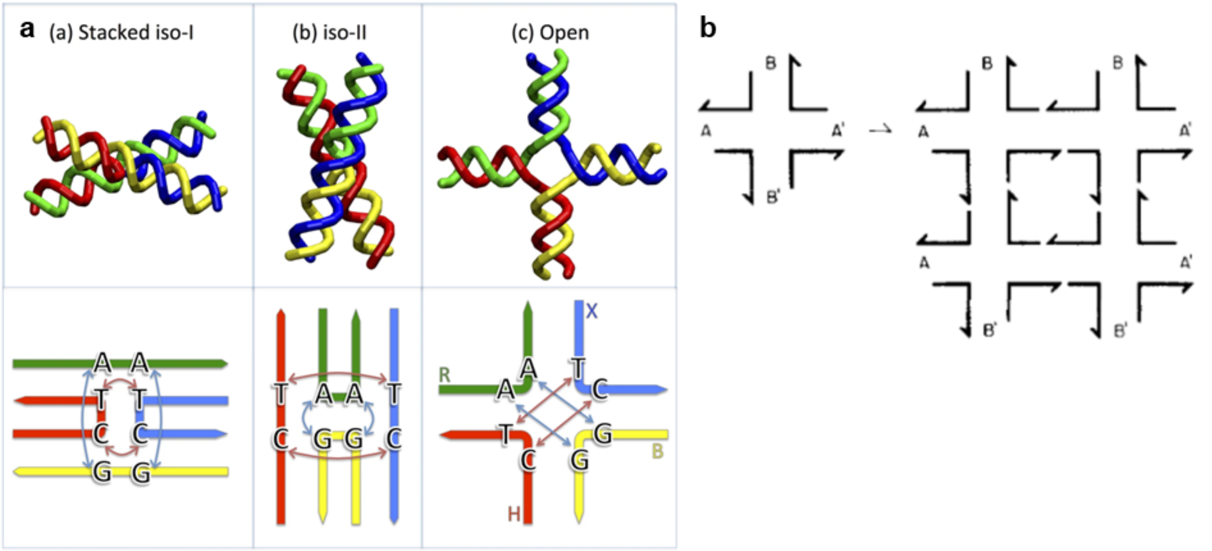

Figure 4 ***Conjugations and associations of the four-way holliday junction***
a) Examples of junction conformation with four complementary single DNA strands. Iso-I and iso-II forms are stabilized via stacking. b) Four-way junctions can be assembled into 2D lattices by complementary sticky ends.
(a) reprinted under CC BY 4.0 license from Wang et al. (2016)[86], b) reprinted from Seeman (1982)[78] with permission from Elsevier)

Figure 4a illustrates the open and closed form of a HJ, with the latter occurring in two distinct conformations according to the pairs of bases that stack at the crossover. DNA nanotechnology originated from Seeman's idea to create artificial and rationally designed crystals. His first approach was therefore to generate immobile open DNA junctions as the building units of larger frameworks[78,81], where macromolecules could be positioned with high precision[78,82,83]. For this purpose, he proposed connecting complementary sticky ends of a four-way junction tile into 2D lattices (Figure 4b), resulting in large and stable crystal-like arrays[78]. From here, a new field of DNA nanoscience emerged. Four-arm junctions were expanded to five- and six-arm junctions[84], and more stable double-crossover (DX) tiles[85] were developed, which were widely adopted and used for more advanced applications[86–89]. Periodic assembly into higher-ordered structures ultimately resulted in 3D polyhedral shapes and crystals, with some of them even able to reconfigure their structure upon the addition of external triggers[90,91]. A major drawback to this so-called tile-based approach, however, is the sensitivity to stochiometric disbalances in the strands that are needed to assemble the target object[92], besides the fact that the design of such structures is extremely challenging and experimental assembly procedures are often laborious and time-consuming.

DNA Origami

A significantly more robust bottom-up concept for DNA assemblies is DNA origami. The term origami translates to "folding paper" in Japanese and describes intricately folded three-dimensional (3D) structures from a single sheet of paper. Paul Rothemund revolutionized the field of DNA nanotechnology in 2006 by introducing a straightforward approach to building scaffold-based structures from the single-stranded 7429 bases long genome of the M13 phage[93]. He successfully simplified previous approaches of incorporating shorter scaffold strands into tile lattices[94] or wire-frame octahedrons[95]. In short, the long single-stranded scaffold is folded by a multitude of oligonucleotides referred to as staples, which are typically partially complementary to at least two scaffold regions (color-coded in Figure 5a)[96]. This way, almost any imaginable 2D and 3D[97,98] shape can be created with a new set of staples. Software tools have been developed to facilitate the construction process[97,99]. Although there have been some advances in the isothermal self-assembly of DNA origami structures[100,101], the most widely used and reliable self-assembly method relies on the thermal annealing of the mixture of strands over a certain temperature gradient and in

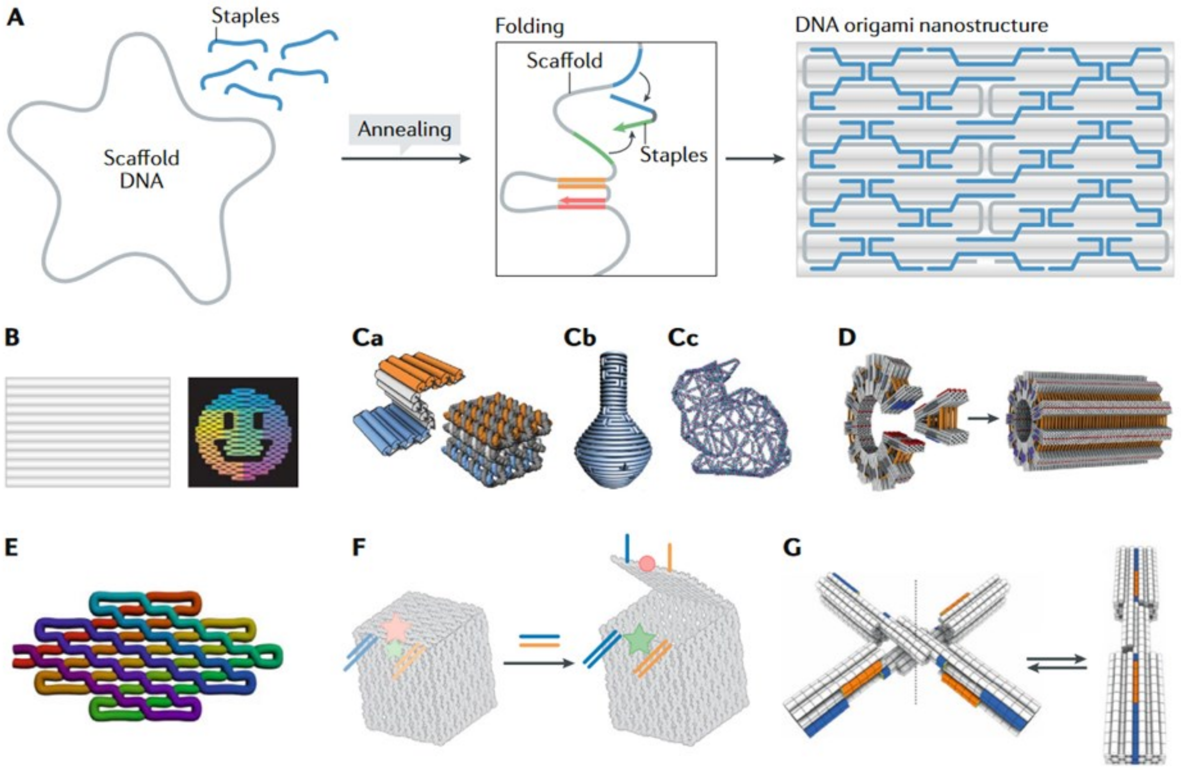

Figure 5 ***DNA origami***
a) Annealing of DNA origami from one long single-stranded scaffold and a multitude of staples complementary to different scaffold regions, which enable the desired folding. b-g) examples of 2D and 3D DNA origami structures, hierarchical self-assembly, and functionalization.
(Reproduced with permission from Springer Nature from Dey et al. (2021)[96])

suitable cation buffer conditions[96,102–104]. Using excess staple strands in relation to the scaffold minimizes the formation of misfolded structures due to truncated or deleted sequences being replaced by the correct ones that can fully hybridize and consequently exhibit better binding energies. Large excess of staples should however be avoided to reduce the formation of kinetically trapped intermediates[105]. The process of DNA origami formation is believed to start from an initial scaffold bending followed by a cooperative binding cascade of staple strands over the thermal annealing process, which favors the formation of structures at their thermodynamic optimum[102,103].

A range of structures and applications has gradually emerged from planar 2D sheets[93] (Figure 5b), over asymmetric[106] and curved structures[107] (Figure 5c) to supramolecular hierarchical assemblies of multiple DNA origami architectures[108,109] (Figure 5d). Lately, dynamic behaviors[110–112] (Figure 5f) and reconfigurable structures[113] (Figure 5g) have extended the range of functionalities[114]. One of the major advantages of DNA origami is the nanometer-scale precision with which objects can be placed on the structures by attachment to the component helices[115,116]. Some prominent examples can be found in nanofabrication, in which a DNA origami scaffold is used to assemble or precisely place artificial building materials like metal wires[117,118], nanoparticles[119], and carbon nanotubes[120]. The same principle can be applied to organic materials like fluorophores placed onto a DNA origami platform at defined inter-molecular distances, thus allowing for precise distance measurements[121], manipulation of the activity of individual enzymes[122], or spatial arrangement of complete enzyme cascades[123]. A fascinating possibility is engineering molecular DNA machines that react to environmental stimuli. A prominent example is a molecular cage releasing cargo upon simultaneous recognition of two target molecules[124] or a robotic arm made of DNA helices that rotates on top of a DNA origami platform due to an applied electric field[125]. The DNA origami structure investigated in this thesis is described in detail in a following chapter (pp. 18).

Biological and Synthetic Linear Polymers

With structures and functions that have developed over millions of years, nature is an excellent inspiration for material science and for adapting natural strategies to engineer new man-made materials[126]. An emerging field in this area is synthetic biology. This can be divided into two sub-fields, with each of them employing both the top-down as well as the bottom-up fabrication approach[127]. One sub-field takes naturally derived components to produce unnatural or unprecedented behavior while the other strives to mimic natural behavior with unnatural components[128]. This work, for example, aims to re-engineer and characterize naturally derived structures in the form of polymers by repurposing natural components to exhibit new functions. Thus, a general understanding of the natural inspiration and naturally derived polymers will support the assessment of the research outcome.

Nature usually employs a bottom-up approach when assembling macromolecular or polymer structures like DNA from nucleotides, proteins from amino acids, or actin filaments from G-actin monomers[129–131]. Other examples are microtubules[132] or bacterial flagella[133,134] originating from the commutative non-covalent binding of repeating monomer subunits. All of these associations share an interesting point: the end-product's properties, that is the filament or polymer, differ significantly from those of the original building unit. Length and stiffness (in the form of persistence length) are only two examples[135,136].

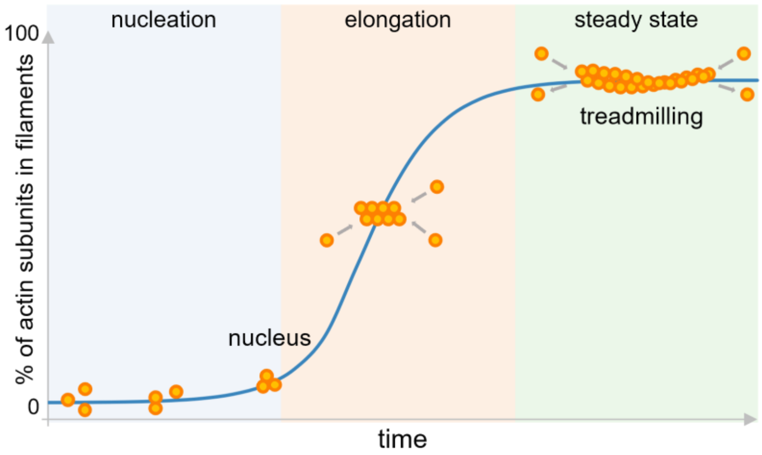

Figure 6 ***Three phases of actin polymerization***
Monomers associate into a trimeric nucleus in the initial nucleation phase, from which binding to the plus- and minus-end occurs rapidly during elongation. The steady-state is maintained through treadmilling in which the majority of monomers bind to the plus-end (barbed end) and dissociate at the minus-end (pointed end) after hydrolysis to regulate the structure length. The concentration of not-integrated subunits gives the critical concentrations.

Actin filaments are biological polymers abundant in eukaryotic cells crucial for muscle motility and the mechanical properties of the cytoskeleton[137]. The actin monomer consists of 375 amino acids, has a molecular weight of 43 kDa[130], and is expressed in six different isoforms with only minor variations[138]. G-actin monomers display tight binding sites that mediate the head-to tail polymerization with other monomers, forming filamentous actin (F-actin). Both G-actin monomers and the polymerized F-actin are ATPases, though F-actin is a more effective ATPase and is crucial for regulating filament length[137]. Actin polymerization can be divided into three phases (Figure 6). First, three 5 nm-sized G-actin molecules[139] with bound adenosine triphosphate (ATP) form a nucleus after the activation of the monomers upon replacement of Ca^{2+} ions with Mg^{2+} ions[140]. Once the nucleus is formed, the growth or elongation of the filamentous F-actin starts, with G-actin monomers binding to the fast-growing barbed end (plus end) as well as to the slow-growing pointed end (minus end). This is caused by the rapid association of ATP-bound monomer at the plus end, followed by ATP hydrolysis with the subsequent release of the inorganic phosphate and rapid dissociation of ADP-bound monomer at the minus end[130]. The difference in the association/dissociation rates of the monomers at the two ends of the growing filament results in a different critical concentration of monomers needed for polymerization at the two ends, leading to a phenomenon called “treadmilling”. Accordingly, at monomer concentrations intermediate between the critical concentrations for the plus and minus ends, a net ATP-actin monomer association at the barbed end is balanced by a net

ADP-actin dissociation at the pointed end. This maintains the steady state of the polymer and ensures its net polarized growth at the plus end. The resulting F-actin filament has a diameter of 8 nm with two strands coiling around each other[130,139]. Under physiological conditions, the critical concentration for elongation is around 0.1 µM with a sizeable forward rate constant of 8.8 $\mu M^{-1}s^{-1}$ at the barbed end opposed to 2.2 $\mu M^{-1}s^{-1}$ at the pointed end with similar dissociation constants of 2.0 s^{-1} and 1.4 s^{-1} respectively[140–142]. Measured activation energies depend significantly on experimental factors and evaluation methods but could reach a maximum of 69.1 kcal/mol[143].

Another biological polymer that has been extensively introduced in this work is the DNA molecule. This can be used to build macromolecular structures exemplary in the form of DNA origami (pp. 1, pp. 8). In turn, those DNA origami structures can associate into supramolecular polymers via hierarchical self-assembly[144–146]. In contrast to most other natural filaments, supramolecular linear polymers have repeating building units connected by non-covalent bonds, with these being either hydrogen bonds and/or stacking bonds[147]. Shape-complementarity of the monomer edges will support their association by either mechanism[113,144,148].

DNA origami filaments derived from shape-complementarity and edge stacking of the component monomers were shown to incorporate more than 100 building blocks and were highly sensitive to buffer ion conditions so that low $MgCl_2$ concentrations could even reverse the polymerization state into a mixture of dissociated monomers[113]. Finetuning of the polymerization vs. monomer state is also possible when monomers are connected through hybridization. Protruding strands bound to a DNA origami cube scaffold present binding sites for two types of base complementary connectors, leading to the formation of hierarchical structures. Careful planning of these binding sites allows for reversible thermal disruption of the connector bonds by elevating the temperature by only 5 °C. Additionally, altering the stoichiometry of the connector strands has a similar effect[149]. Replacing mutually complementary connector strands with an oligonucleotide “fuel” that is partially complementary to protruding single strands on each side of a 3D DNA origami building block also allows for reversible polymerization. Since the fuel strand presents an unpaired toehold domain, its addition to a mixture of monomers drives the polymerization process, while the fully complementary anti-fuel can reverse it. The number of connecting sites and binding length of the fuel strand, as well as the concentration of Mg^{2+} ions, allow sophisticated control of the reaction[150].

There are many more examples of successfully implemented DNA origami building units for supramolecular polymerization[151–153] and even more for tile-based approaches[154–156]. One notable concept regulates the formation of tile-based DNA tubes by activator strands released through the output of base excision repair enzymes[157]. Another remarkable combination of the tile-based approach with DNA origami yields complete control over the entire polymerization process, including nucleation, growth, and termination. In short, DNA nanotubes formed from two types of tiles can be seeded and capped with different types of DNA origami structures[89].

Out-of-Equilibrium Systems

The opposite of death is life. But how is life maintained exactly? The answer to that is energy. Molecular processes of the living cell are driven by different types of fuel, a predominant one being ATP. Energy is obtained by the hydrolysis of ATP into ADP and one inorganic phosphate, or AMP and one pyrophosphate unit[158]. This drives the entire molecular machinery, integrating sensory input data to generate sensitive output via signaling reaction networks. The previously described and tightly regulated actin polymerization (Figure 6) is an excellent example of an energy-consuming thermodynamic uphill reaction in which self-organization is crucial. Many biomimetic approaches, including self-assembling DNA structures, drive towards equilibrium states of energy minimization and could also be described as thermodynamically dead[159].

Chemical Reaction Networks

New concepts of reaction networks integrating external stimuli have emerged over the last few years. One promising concept that employs a bottom-up approach for responding to biochemical stimuli via self-organizing behaviors is based on chemical reaction networks (CRN)[160]. CRN are defined as a set of reactions whereby chemical species convert into one another, with each reaction described by a defined kinetic equation and all kinetic equations related to one another in a complex network. CRN often lead to the emergence of novel properties in the system to which they are applied, one of these being the appearance of spatio-temporal oscillations. One of the first studied chemical oscillators is the out-of-equilibrium Belousov-Zhabotinsky reaction, in which periodic redox reactions result in the spontaneous generation of oscillating patterns due to changes in the concentration of some intermediate species[161]. Without external influences, the system lasts for about 10 minutes at 20°C and will ultimately converge toward thermodynamic equilibrium. Researchers have since then endeavored to understand the emergence of complex natural patterns. A promising strategy relies on the use of biological macromolecules for the bottom-up building of artificial systems that mimic, although in a less complex way, several non-equilibrium aspects of their natural counterparts, providing prototypes that are easier to understand and manipulate. In nature, enzymes are widely used to keep the system in a non-equilibrium state, and the same principle is applied in synthetic biology research[160]. For example, an in vitro approach to an enzyme-driven oscillating (bio)chemical reaction network employs the autoactivation of the trypsin precursor trypsinogen in microfluidic flow reactors. This drives the autocatalysis of more trypsin and a time-delayed two-step activation of the irreversible inhibitor molecule by first cleaving a lysine residue from the pro-inhibitor, which is then ultimately activated by the aminopeptidase[162].

Nucleic Acid Logic Operations

DNA and RNA components can also be integrated into chemical reaction networks. There are two types of nucleic acid logic operations in CRNs; one is catalyzed by enzymatic reactions, and one relies solely on strand displacements. So far, more research has gone into enzyme-catalyzed energy transfer for chemical reaction networks. A prominent example is the genelet toolbox that uses RNA, its polymerization by RNA polymerase, and its degradation by RNase H, as a dynamic regulator of bistable synthetic switches that function as stimulators or inhibitors on other genelets[163]. The concept was later successfully evolved to mimic natural behavior in synthetically derived transcriptional networks[164,165]. Another way to combine the unique DNA self-recognition properties with several enzymes catalyzing data integration is the PEN toolbox, where DNA **P**olymerase, **E**xonuclease, and **N**ickase regulate the interactions of up to eight toggle switches or gene analogues[166]. The genelet and PEN toolbox concepts were further used to construct cell-like oscillating behavior[167–170].

Mimicking the dynamic steady states of cellular filament polymerization with a DNA analog can be achieved by introducing a BamHI cleavage site leaving a four-nucleotide overlap at the ends of short double-stranded DNA fragments. Adding ATP to the system will subsequently favor the ligation between two fragments by T4 DNA ligase until a steady state is reached, whereby cleavage and ligation occur concurrently. After ATP depletion, cleavage of the polymers into fragments will dominate[171]. Other highly promising DNA logic operations in the form of nanoswitches rely on the conformational changes of DNA triplexes reacting to external stimuli like the binding of antigens[172] or the change in pH[173,174].

Enzyme-free DNA Reaction Network

Many enzyme-free DNA-fueled reaction circuits are based on the principle of toehold-mediated strand displacement[111,175,176] (Figure 7). In this process, an invader strand will displace a shorter, partially complementary strand of a double-stranded DNA duplex displaying a single-stranded overhang called toehold. The invader strand is complementary to the entirety of the longer part of the duplex and initially binds to the toehold domain forming a three-way branch while migrating and displacing the incumbent strand[175]. This particular process is driven by the change in free energy obtained by hybridizing and stacking complementary sequences. One DNA duplex can contain more than two initial DNA strands to enable a cascade of strand displacement reactions, opening up a new toehold domain every iteration[177]. That way, entire catalytic cycles solely based on DNA can be programmed, which optionally integrate several inputs[177–179]. Apart from toehold-mediated strand displacement, it is possible to perform logic operations via algorithmic self-assembly similar to computer logic gates based on a seed structure that encodes the initial information of the cascade[180].

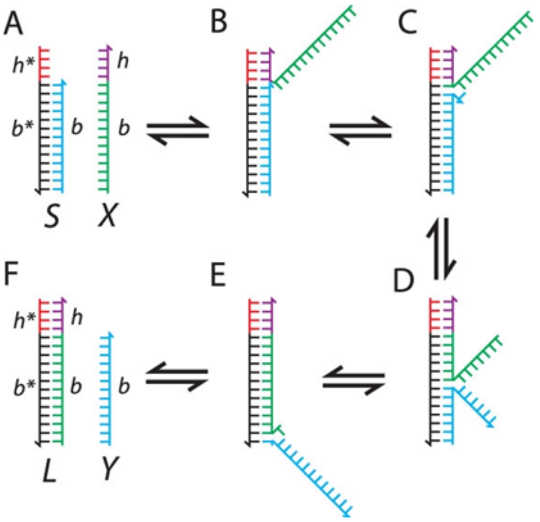

Figure 7 ***Toehold-mediated strand displacement***
Branch migration induced by the binding of the perfectly complementary invader strand X to the toehold h of the duplex S to displace the b strand and form duplex L.*
(Reprinted with permission from Simmel et al.[175] Copyright 2019 American Chemical Society)

One brilliant example of an autocatalytic chemical reaction network driven entirely by DNA logic operations and thus referred to as a DNA reaction network (DRN) is displayed in Figure 8[181]. This DRN plays a crucial role in this thesis. A carefully planned cascade of toehold-mediated strand displacements enables the exponential production of the reaction-driving oligonucleotides called *U* (nomenclature changed from original reference). There are two sets of *U strands*, *U1* and *U2*, which differ in a part of their sequence involved in the formation of the *U complex* (Figure 8 *U1|2* black domain). The remaining part of their sequences is identical, so they can bind to the *fuel complex* interchangeably. After initial binding of *U1* or *U2* to a complementary single-stranded region of the *fuel complex*, with consequent displacement of the *fuel strand*, the *V strand* can bind to the intermediate complex’s single-stranded region. This, in turn, displaces the *connector strand*, yielding a “dead” (i.e., unable to react further) *fuel complex* species. The *connector strand* displaces the *U1 strand* from the initial *U complex* and frees a toehold domain for the *helper strand*, the binding of which eventually displaces the *U2 strand*. Overall, one *U*, *V*, and *helper strand* are consumed to release two *U strands* and one *fuel strand*, leading to a net (autocatalytic production) of *U strand*. *V* and *helper strands* are used in excess to sustain the production of *U* for a sufficiently long time and thus place the focus of the reaction on the *U strands*. From this principle, Srinivas and coworkers developed three sets of intricately intercommunicating DNA reaction networks to create a DNA oscillator successfully.

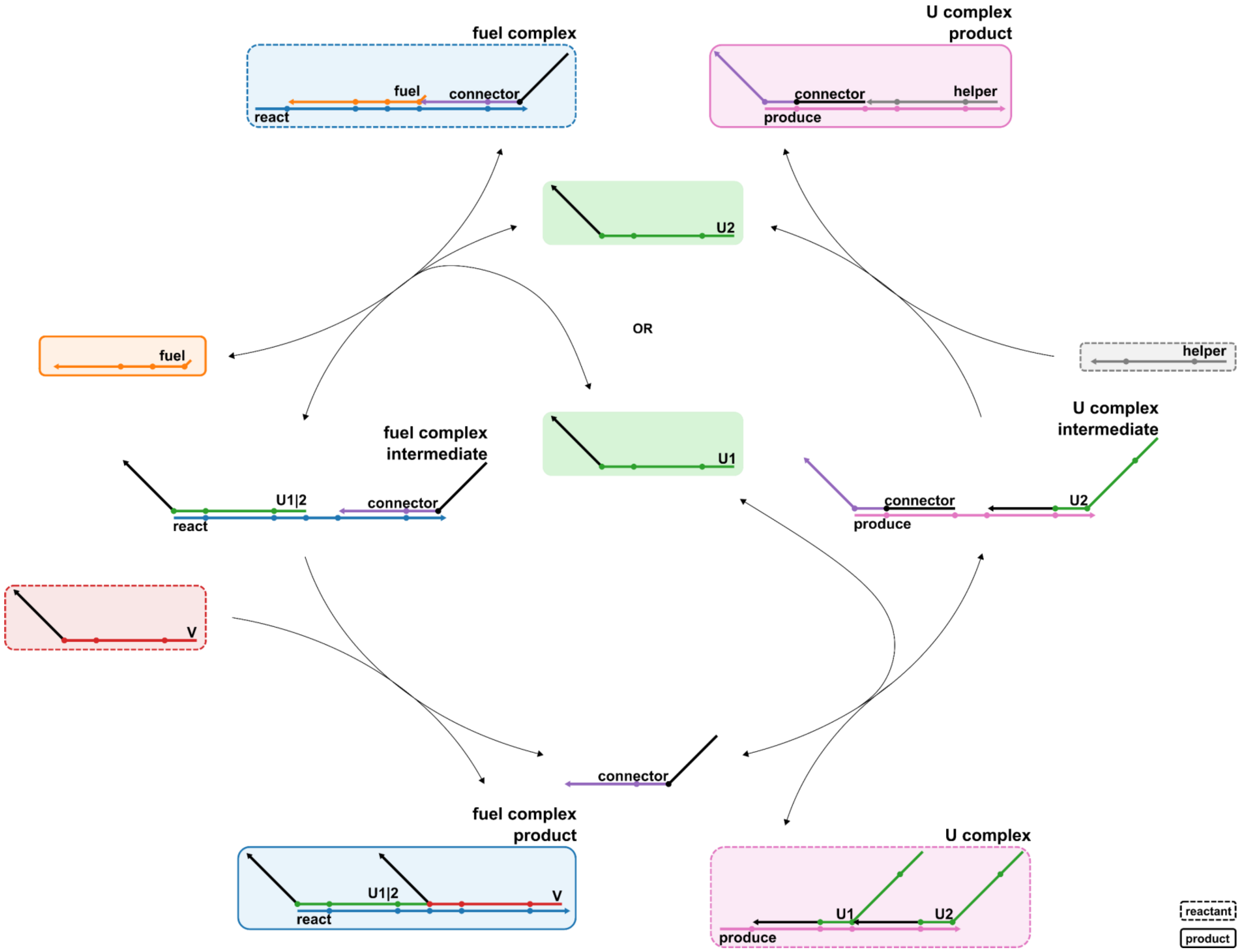

Figure 8 ***Autocatalytic DNA Chemical Reaction Network - schematic representation***
The U1 and U2 strand differ in sequence in the black region but can both bind to the fuel complex's single-stranded region to displace the fuel strand. Subsequently, the V strand binds to the intermediate complex's single-stranded region and displaces the connector strand, yielding the fuel complex unreactable. The connector strand displaces the U1 strand from the initial U complex and frees the binding site for the helper strand, which displaces the U2 strand. Overall, one U, V, and helper strand are consumed to release two U strands and one fuel strand. V and helper strands are used in excess to place the focus of the reaction on the U strands.

The 24-Helix Bundle as a versatile Building Unit

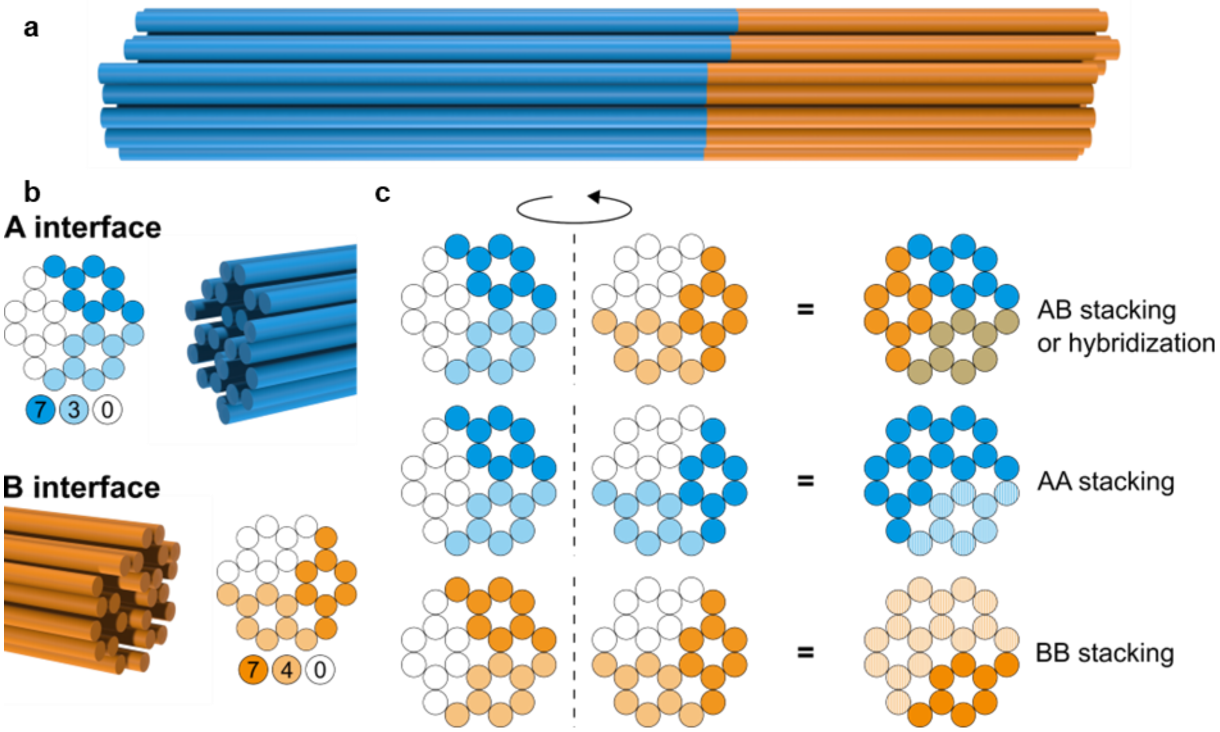

Figure 9 ***Interface association possibilities of the 24-Helix Bundle***
a, b) The 24-helix bundle DNA origami has two distinct interfaces characterized by their protrusion levels. The A-interface has three sections à eight helices that are elevated 7, 3, and 0 bases from their plane of reference (shown by increasing opacity), while the B-interface protrudes 7, 4, and 0 bases per patch. c) All three protruding sections align perfectly when pairing the A- and B-interfaces (upper panel). Each interface is also partially self-complementary upon 60° rotation. For the A-interface, sections protruding 7 and 0 bases can stack perfectly, while the three-base protruding patch is left with a one base pair gap marked by the shaded helices (middle panel). The B-interface can perfectly stack with the four-bases protruding patch, leaving the other 16 helices with a one base pair gap (lower panel).

Previous studies in the Saccà lab resulted in the design of a versatile DNA origami structure made of 24 helices ordered into a bundle according to a honeycomb lattice layout. The bundle consists of three patches of eight helices, with each patch displaying a distinct height profile at the A- and B-interfaces[136] (Figure 9a and b). Fully formed, the bundle has a diameter of 18 nm and a length of 102 nm, which causes a rod-like appearance (Supplementary Figure 4). The origami is assembled from the M13mp18 scaffold, with 128 staples forming the structure's core. In the inactive state, part of the scaffold at the interfaces is left unpaired to prevent undesired interactions. To activate monomer association, two types of staples can be added. In a first type, staples are designed to form blunt ends at the edges of the monomer, enabling ππ-electron stacking at selected monomer interfaces. In a second type, staples are designed to connect two distinct monomer interfaces by base hybridization. In the active form, the A-interface is perfectly shape-complementary to the patches of the

B-interface, and the AB association can be either formed by base stacking or hybridization. Additionally, the isologous interfaces (AA and BB) are partially shape-complementary by blunt end stacking. For the A-interface, 16 out of 24 helices stack perfectly, leaving a small one base pair gap (1 bp gap) at the remaining eight helices (also written as (16/8)). The B-interface only has eight helices stacking perfectly, with the remaining helices exhibiting a 1 bp gap (8/16).

Based on these association possibilities, various higher-ordered structures can be assembled (Figure 11). When activating solely one of the two possible interfaces for stacking, the self-complementarity of the monomer will enable its dimerization at the AA- or BB-interface. Additional activation of the outer facing edges of these dimers leads to long and ordered filaments with the same internal structure, consisting of AA-stacking followed by BB-stacking, independently of the originating dimer. Depending on the type of dimer used as starting building block, these filaments are called $(ABBA)_n$ or $(BAAB)_n$. When activating both stacking interfaces simultaneously, concurrent association of AA, BB, and AB will occur, leading to randomly ordered $(AB)_{rand}$ filaments. An ordered AB head-to-tail association can be achieved by applying base hybridization-driven polymerization. In this case, the activated monomer will first bind two sets of hybridization staples to its A- and B-interface, subsequently displacing one set for successful interface association into the $(AB)_n$ polymer. The fluorophore labeling strategy to monitor tip associations is shown in Figure 10.

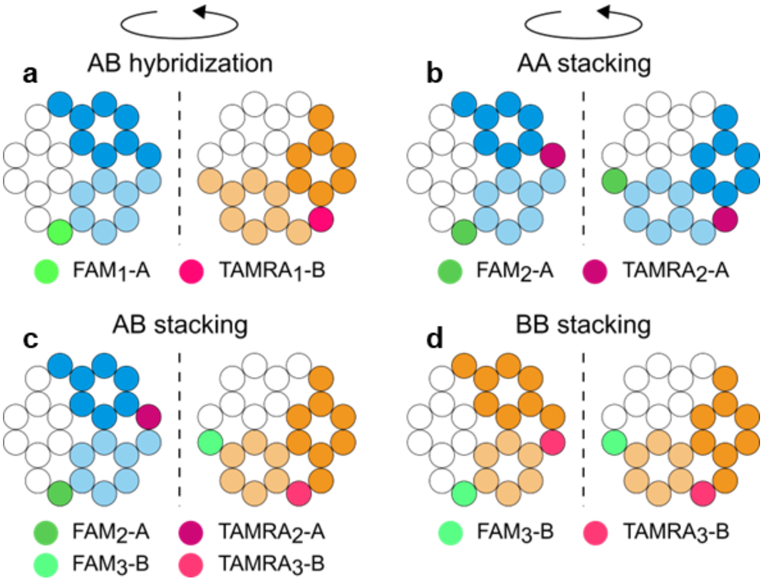

Figure 10 ***Fluorophore labeling for interface association monitoring***
The spectrally overlapping 6-carboxyfluorescein (FAM) and carboxytetramethylrhodamine (TAMRA) were used as donor and acceptor fluorophores to monitor tip associations and were integrated at the blunt ends of the helices. Placements were chosen based on staple configurations, the position of gapped helices, and isologous symmetries. a) FAM at helix 19 and TAMRA at helix 20 were used to monitor hybridization associations, b) FAM at helix 20 and TAMRA at helix 13 for AA-stacking, c) FAM at helices 14 and 20 and TAMRA at helices 13 and 19 for all associations in random stacking, and d) FAM at helix 14 and TAMRA at helix 19 for BB-stacking.

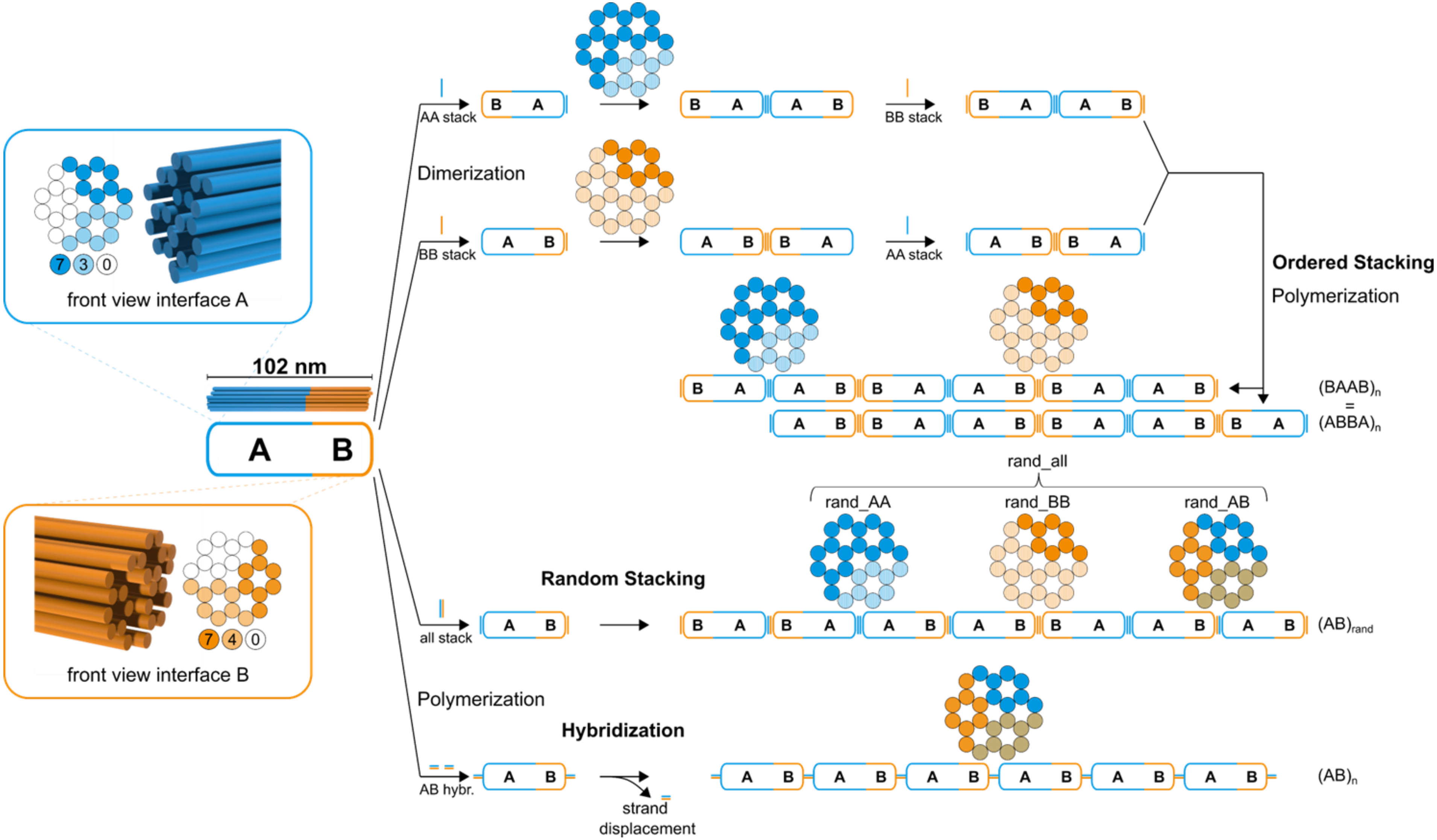

Figure 11 ***Dimerization and polymerization flow chart of the 24-helix bundle***
When activating only one interface for stacking, isologous BAAB or ABBA dimer self-association will occur based on the inherent partial self-complementarity. Activating the remaining dimer interface will lead to ordered, structurally identical (BAAB)$_n$ or (ABBA)$_n$ polymers. Simultaneous activation of the A- and B-interface for stacking will cause random association at the AA, BB, and AB interfaces leading to the (AB)$_{rand}$ polymer. The ordered head-to-tail association of the A with the B tip can be achieved by base-hybridization into the (AB)$_n$ polymer. This also requires displacing one set of staples bound to the activated monomer.

Aims and Scope

This study investigates the kinetics and thermodynamic properties of DNA origami linear assemblies and can be divided into two research sub-areas. One considers how DNA origami subunits associate into dimers and polymers and the effects of different association types and mechanisms on the kinetic and thermal features of the reaction. The second part integrates a DNA origami-based polymerization with the out-of-equilibrium properties of a DNA-based CRN.

Characterizing linear DNA Origami Associations

Much work has been done in the design of polymeric DNA origami assemblies as described in the section *Biological and Synthetic Linear Polymers (pp. 10)*. However, characterization of these structures has usually been performed at equilibrium conditions or at the endpoints of metastable kinetic traps. The energetic paths traveled during the assembly of these structures are difficult to unravel due to the complexity and multitude of interactions taking place simultaneously. Although several experimental and simulation studies contributed to the elucidation of fundamental concepts of DNA origami assembly[102,182–186], many aspects of DNA origami assembly, particularly concerning the hierarchical association of pre-formed origami, are mostly obscure up to this point. This work aims to characterize the kinetics and thermal paths that DNA origami linear assemblies travel to reach equilibrium. Therefore, the two types of association mechanisms, that is, the geometrically assisted blunt end stacking and the hybridization-mediated association, will be investigated and compared in terms of kinetic behavior and thermal stability. This will be achieved, among other approaches, by detailed monitoring of each interface association type by Förster resonance energy transfer (FRET), using fluorophores at suitably placed positions of the interacting interfaces (Figure 10). Thorough screening of initial monomer concentrations and reaction temperatures will yield detailed insights into the energetic profile of the process, especially the initial reaction velocity. Studying dimer stacking as a finite model system also will disclose detailed information on dimerization's thermal and kinetic properties, as will single-molecule studies of stacking forces. The capability to tune monomer association by modifying the number of gapped helices will be explored as well. For the randomly stacking polymers, the equilibrium distribution of AB, AA, and BB stacks will be determined and correlated to interface symmetries and stacking energies. Hybridization and stacking reactions will be tested for their temperature-dependent critical concentrations.

Additionally, the kinetics of the initial polymerization phase and its impact on polymer length distribution will be explored by various methods. In particular, the results obtained by direct observation of the binding events over the course of surface-assisted polymerization will aid in learning more about the mechanisms of DNA origami polymerization. Thermal stability and kinetic studies will be examined, also considering dimers as building units. Lastly, the polymer-to-monomer interconversion shown by hybridized vs. stacked systems, and the effects of differently placed hybridization sites for finetuning the assembly process, will be examined. Overall, a global picture of association kinetics, thermal stability, mechanisms, and dynamics of DNA origami linear assemblies will be achieved.

Coupling a DRN with DNA Origami Polymerization

DNA origami supra-molecular assemblies are usually built by adding oligonucleotides that induce either hybridization or stacking associations at the interfaces, after which the desired equilibrium state is reached and characterized. Synthetic biology, however, strives to go further and develop dynamic systems that react to external signals and literally move “out” of their equilibrium condition. This may lead to non-dissipative metastable systems that escape from kinetic traps reaching another thermodynamic minimum, or to dissipative out-of-equilibrium systems with a transient or even sustained dynamic behavior. In this thesis, a first step along this path will be done by coupling the DNA origami polymerization to an external fuel source that drives and controls the reaction. The growth and shrinkage of natural polymers is a tightly regulated process that is hard to replicate with its intricate responsive processes. This work will employ an autocatalytic DNA reaction network to fuel polymer growth and a toehold-mediated strand displacement reaction to control monomer association dynamics and induce polymer shrinkage if required. Experimental conditions will be optimized to integrate DRN and DNA origami, and both systems will be adapted for a viable interplay. To understand the impact of various parameters on the kinetic behavior of the system, reference polymerizations will be driven in controlled conditions. In this way, the contributions given by external addition of fuel strands will be isolated and compared to those derived by fuel released from the reaction network.

Materials and Methods

Materials and Chemicals

Table 1 **Equipment**

Equipment	Supplier
AFM Bioscope with a Nanoscope V controller	Bruker Corporation
AFM MultiMode8 with a Nanoscope V controller	Bruker Corporation
Centrifuge 5424R, 5430R, 5810R	Eppendorf SE
CFX96 Touch Real-Time PCR Detection System	Bio-Rad Laboratories Inc.
C-Trap® Optical Tweezers	Lumicks
DS-11 Spectrophotometer	DeNovix
Electrophoretic systems (AGE, PAGE)	Bio-Rad Laboratories Inc.
Spark 10M Multi Mode Microplate Reader	Tecan Group Ltd.
Thermocycler: Mastercycler nexus eco; nexus gradient; nexus x2e	Eppendorf SE
ThermoMixer	Eppendorf SE
Transmission electron microscope JEOL JEM 1400 Plus	JEOL GmbH
Transmission electron microscope Zeiss EM 910	Carl Zeiss AG
Typhoon FLA 9000 Gel Imaging Scanner	GE Healthcare

Table 2 ***Consumables and chemicals***

Consumables and chemicals	Supplier
1 kb DNA ladder	Carl Roth GmbH + Co. KG
100 kDa MW cutoff filtration devices, Amicon Ultra 0.5 mL	Merck Millipore
3 kDa MW cutoff filtration devices, Amicon Ultra 0.5 mL	Merck Millipore
96-well microplates black clear-bottom	Greiner Bio-One GmbH
96-well PCR plates	Bio-Rad Laboratories Inc.
AFM probes: ScanAsyst-Air, FASTSCAN_D_SS	Bruker Corporation
Agarose	Lonza
Ammonium acetate	TCI Chemicals
Ammonium persulfate (APS)	Carl Roth GmbH + Co. KG
Boric acid	Carl Roth GmbH + Co. KG
Bromophenol blue	Merck
E.coli XL1-Blue competent cells	Agilent technologies
Ethanol	VWR
Ethidium bromide	Sigma-Aldrich
Ethylenediaminetetraacetic acid disodium salt dihydrate (EDTA)	Merck
Freeze 'N Squeeze™ DNA Gel Extraction Spin Columns	Bio-Rad Laboratories Inc.
GelStar Nucleic Acid Gel Stain	Lonza
Glycerin	Merck
M13mp18 scaffold (7249 bases)	Affymetrix
Magnesium chloride hexahydrate	Merck
Mica	Plano GmbH
NAP DNA Purification Columns	Cytiva

NucleoSpin Gel and PCR Clean-up Kit	Macherey-Nagel
Oligonucleotides	Sigma-Aldrich, Integrated DNA Technologies
pET 28a (+) plasmid	Sigma-Aldrich
Phusion polymerase	Thermo Fisher Scientific Inc.
Polyethylene glycol 8000	Merck
Sodium chloride	Carl Roth GmbH + Co. KG
TEM copper grids 6 nm continuous carbon film	Quantifoil
Tetramethyl ethylenediamine (TEMED)	Carl Roth GmbH + Co. KG
Tris base	Merck
Tris(2 carboxyethyl)phosphine (TCEP)	Sigma-Aldrich
Uranyl formate	Polysciences Europe GmbH

Software

Blender

3D renders of the 24-helix bundle were created with the open-source Blender software v.3.1 licensed under the GNU General Public License, and DNA origami design files were imported with the *caDNAno2Blender* plug-in created by Björn Högberg (https://github.com/bhogberg/caDNAno2Blender).

caDNAno

2D or 3D DNA origami based on honeycomb or square lattices were designed and modified with the caDNAno v.2.2.0 software[97] and obtained staple sequences exported as .csv files.

Fiji

AGE and PAGE, and AFM polymerization images were processed with the ImageJ distribution Fiji v.1.53 developed by the National Institutes of health[187]. The AnalyzeSkeleton ImageJ Plugin[188] was used to determine the initial polymer length distribution.

Inkscape

Illustrations of the 24-helix bundle interfaces, reaction schematics, and DRN overview were created with the open-source vector graphics software Inkscape v.1.1, licensed under the General Public License.

NanoScope Analysis

Unprocessed AFM images obtained from the Bruker BioScope or MultiMode microscope in .spm format were flattened and optimized for publication with NanoScope Analysis v.2.0.

OriginPro

Data graphs were prepared for publication with OriginPro2023.

Python

Data analysis of Förster resonance energy transfer polymerization curves was performed with Python v.3.7 and the matplotlib, numpy, openpyxl, pandas, and scipy libraries.

Buffers

Table 3 **Buffer recipes**

	TEMg12.5	**TEMg16**	**TEMg20**	**TBEMg**	**TBE**
Tris Base	5 mM	5 mM	5 mM	40 mM	45 mM
EDTA	1 mM	1 mM	1 mM	2 mM	1 mM
$MgCl_2$	12.5 mM	16 mM	20 mM	12.5 mM	-
Boric Acid	-	-	-	40 mM	40 mM
pH	8	8	8	8	8

PEG buffer		**DNA running buffer (5x)**	
PEG8000	15 %w/v	TBEMg buffer (10x)	10 % v/v
Tris Base	5 mM	Glycerin	40 % v/v
EDTA	1 mM	Bromophenol blue	0.1 % w/v
NaCl	505 mM		

Methods

DNA Origami Design and Assembly

DNA origami design and alterations were done with the caDNAno software tool (v2.2.0) developed by Nick Conway and Shawn Douglas[97]. The 24-helix bundle structure was initially designed, and its equilibrium states were characterized by Dr. Wolfgang Pfeifer[136]. 3D renders for better visualization were created with the 3D graphics software *Blender* by importing caDNAno .json files with the plugin *caDNAno2Blender* created by Björn Högberg. The monomer core (sequences pp. 147) was assembled in TEMg16 with a ten-fold excess of staple strands with respect to the scaffold concentration ranging from 10 nM to 50 nM over the following temperature ramp:

65 °C for 5 min,
65−55 °C (with a temperature decrease of 1 °C every 5 min),
55−30 °C (with a temperature decrease of 1 °C every 15 min),
30−20 °C (with a temperature decrease of 1 °C every minute),
hold at 20 °C.

Interface staples for DNA origami association were added in a ten-fold excess if not stated otherwise, and fluorescently labeled staple strands were also introduced during assembly.

Agarose Gel Electrophoresis

Separation by size and electrophoretic mobility can be performed with an agarose gel electrophoresis (AGE) and applied to large kDa and small MDa DNA structures. The migration capacities can be adjusted accordingly by varying the concentration of the agarose matrix. Assembled DNA structures can be separated not only from excess staple strands but also from misfolded structures. For the here examined 5 MDa DNA origami monomers, a 1 % (w/v) agarose solution in TBEMg buffer (see Buffers) was generally used. 200 fmol of DNA origami sample was mixed accordingly with the 5x DNA loading dye (see Buffers), and the pre-cooled agarose gels were run at 80 V and 4 °C for 3 h covered in TBEMg buffer. Afterward, the gel was stained either in ethidium bromide or Gelstar stain for 5 min, and DNA bands were recorded by dye excitation at 532 nm, and emission was detected with a LPG filter set on a Typhoon FLA 9000.

Freeze´n´Squeeze DNA Gel Extraction

To extract correctly folded and associated DNA origami bands from agarose gels, the respective bands were visualized with a DNA stain or incorporated fluorophores and subsequently cut from the gels. The resulting gel pieces were then placed in Freeze 'N Squeeze™ DNA Gel Extraction Spin Columns, frozen at -20 °C for 5 min, and the DNA constructs were eluted via centrifugation at 13,000 rcf for 7 min.

Ultrafiltration Purification

An alternative for removing excess staples without preceding gel electrophoresis is the size-exclusion ultrafiltration on cellulose filters[104]. Up to 500 µl of a sample solution could be separated with a weight cutoff filter of 100 kDa by equilibrating the membrane with 500 µl of TEMg5 at 5,000 rcf for 5 min and subsequent addition of the sample solution, which was filtered at 5,000 rcf for 2 min and washed thrice with 400 µl TEMg5. Finally, the concentrated origami sample was eluted with 2,000 rcf for 2 min, and the buffer magnesium concentration was adjusted to desired values.

Polyethylene Glycol Purification

Assembled monomers could also be purified by Polyethylene Glycol (PEG) precipitation to remove unbound staple strands and especially fluorescently labeled excessive oligonucleotides. Up to 300 µl of a 50 nM DNA origami sample were adjusted to a final $MgCl_2$ concentration of at least 20 mM in TEM buffer and a volume of 1 ml. Afterward, equimolar amounts of sample and PEG buffer (see Buffers) were mixed by gently inverting the reaction vessels, and subsequent centrifugation at 20,000 rcf at room temperature for 25 min precipitated the large structures in a pellet. Subsequently, the supernatant was discarded, and the structures were resuspended in according volumes of TEMg16 buffer. To facilitate the resuspension, gentle heating to 35 °C and shaking at 400 rpm in a ThermoMixer could be applied overnight.

Polyacrylamide Gel electrophoresis

Polyacrylamide gel electrophoresis (PAGE) is more suitable for matrix-based size and mobility separation for smaller DNA complex structures and individual oligonucleotides. To analyze native complexes of hybridized oligonucleotides, a 15 % acrylamide gel was prepared, as shown in Table 4.

Table 4 ***Native PAGE 15 %***

	Final concentration	**Volume**
Acrylamide 40 % (19:1)	15 %	4.5 ml
TBE 5x	1x	2.4 ml
ddH2O		5.1 ml
TEMED		10 µl
APS		100 µl

2 µl of a 1 µM sample were mixed with 2 µl TE buffer and 2 µl DNA loading dye (see Buffers), of which 2 µl were loaded into the wells. As a size reference, 0.8 µl of a DNA low-range marker were loaded, and the remaining wells were filled with diluted loading dye. The gel was equilibrated for 15 min before and after carefully washing the wells and running at 4 °C at 60 V for 3.5 h in TBE buffer. Subsequently, gels were stained in a 1:10000 GelStar TBE bath to visualize ssDNA and dsDNA equally and were scanned using the same protocol as AGE.

Atomic Force Microscopy

Structures with a size ranging from a few nanometers to several micrometers can be visualized via atomic force microscopy (AFM). This technique relies on the deflection of a laser beam reflected from the surface of a cantilever, which is attached to a thin sharp tip moving over the sample surface. In general, 10 µl of a 1 nM DNA origami solution containing monomers, dimers, or polymers were adsorbed to a freshly cleaved mica surface at room temperature for 3 min before being carefully washed with ddH_2O and thoroughly dried. Samples were subsequently scanned in ScanAsyst air mode with a MultiMode microscope or BioScope Resolve (Bruker), both equipped with a Nanoscope V controller and ScanAsyst-Air probes with a 0.4 N/m spring constant and a tip radius of 2 nm. A scan rate of around 1 Hz and close to 500 samples/line for an area of 5 x5 µm to 10 x10 µm were commonly chosen as scanning parameters. Images were finally analyzed using the NanoScope Analysis v2.0 software.

Live-View AFM

The BioScope Resolve AFM equipped with a Nanoscope V controller (Bruker) offers a fast and straightforward approach for Fast Tapping in fluid. With this technique, the 24-helix bundle polymerization was recorded for hybridization and random stacking from 3 nM monomers or isologous stacking from 2 nM dimers in TEMg20 buffer containing 50 mM NaCl. As described previously, monovalent sodium ions were used to weaken the surface adhesion slightly[189–192]. 500 µl of the building block solution was absorbed on a freshly cleaved mica surface at room temperature for 3 min before imaging a 4 µm x 4 µm area with 400 samples/line at 6.25 Hz in Fast Tapping Mode. Super sharp FASTSCAN-D-SS probes with a 1 nm tip and 0.25 N/m spring constant were used for scanning with a drive amplitude at 200 mV and an amplitude setpoint ranging from 600 mV to 900 mV. One frame per 32 sec could be recorded by additionally disabling line retracing. Polymerization was initialized after successfully imaging the individual building units by adding 500 µl TEMg20Na50 buffer containing 100 nM polymerization staples. Up to 500 individual images were recorded for several hours with manual adjustments of the amplitude setpoint when required.

Transmission Electron Microscopy

DNA origami polymer samples were prepared as previously described[136,193] for transmission electron microscopy (TEM), where a beam of electrons passes through a material sample fixed on a grid matrix to project the sample onto a detector. Briefly, DNA filaments diluted to 1 nM in the respective TEMg buffer were absorbed onto freshly glow-discharged copper grids covered by a 6 nm continuous carbon film. After blotting off the remaining sample, the TEM grids were negatively stained twice with 1 % uranyl formate (the first stain coat was removed immediately, and the second coat was incubated for one minute). The grids were dried, and imaging was done on a Zeiss EM 910 transmission electron microscope with 120 kV accelerating voltage and a LaB6 cathode for most AuNP-labeled polymers. Alternatively, a JEOL JEM 1400 Plus with a LaB6 Filament and a TVIPS TemCam-F416 camera was used for TEM imaging at the Imaging Center Essen (IMCES).

Temperature-dependent FRET Spectroscopy

To characterize thermal profiles of association and dissociation of dimer and polymer interfaces, temperature-dependent Förster resonance energy transfer (FRET) was used to monitor two exemplary adjacent helices of interest. FRET relies on a direct, radiation-free energy transfer between two proximate fluorophores with a spectral overlap of the donor emission and acceptor excitation wavelengths[194]. For dimer formation, two scaffold equivalents and one set of stacking staples were used to monitor the cooling and melting profiles, which reasonably approximate the folding and unfolding of the entire structure. Therefore, 50 nM of the unfolded scaffold was premixed with a ten-fold excess of core and A- or B-stacking staples and a two-fold excess of fluorescently labeled oligonucleotides in TEMg16. FAM (6-carboxyfluorescein) was used as a donor and TAMRA (carboxytetramethylrhodamine) as an acceptor dye. Changes in FAM emission (ex. 450-490 nm, em. 510-530 nm recorded with the CFX96 Touch Real-Time PCR System) for dimer association with quadruplicates à 20 µl for a donor-only reference and donor-acceptor sample were recorded by cooling down from 75 °C to 25 °C with a rate of -0.1 °C/min. Inversely, the thermal stability was examined by heating from 25 °C to 75 °C with +0.1 °C/min. The FRET efficiency was determined based on Eq. 1 from the quotient of donor-acceptor fluorescence intensity (I_{DA}) and donor-only fluorescence intensity (I_D).

$$E_{FRET} = 1 - \frac{I_{DA}}{I_D} \qquad \text{Eq. 1}$$

The melting temperature (T_m) was determined as the maximum of the first derivative of the normalized thermal curve ($d^2\theta / dT^2 = 0$), whereas the temperature equal to $\theta = 0.5$ was indicated as $T_{0.5}$ or the reaction half-point. For polymer interface associations into equilibrium structures, the polymerization was performed for several hours under isothermal conditions. For this reason, initial cooling curves were not feasible to approximate the realistic thermal association profiles and were omitted. Instead, polymerization association was performed in the PCR plates at 40 °C for 20 h first, and cooling was performed after the melting.

Isothermal FRET Spectroscopy

Isothermal FRET spectroscopy was used to monitor the interface association of DNA origami dimers and different types of polymers, as well as for DRN reaction progress monitoring (see p. 35). Monomers were pre-assembled with a ten-fold excess of core staples and a two-fold excess of fluorescently labeled interface oligonucleotides when no primary purification was feasible. 6-FAM was used as the donor fluorophore, whereas TAMRA was the acceptor dye. Redundant interface staples were omitted from the interface staple mix accordingly. Different initial monomer and dimer concentrations ranging from 5 to 40 nM were screened at 30 °C, 35 °C, and 40 °C for kinetic characterization of the different association types and interface combinations. Triplicates of 100 µl for the donor-only and donor-acceptor preparations were adjusted to a magnesium concentration of 20 mM with $MgCl_2$, placed in clear-bottom 96 well microplates with black walls, and covered with transparent adhesive foil to prevent evaporation. The samples were placed in the Tecan Spark 10M plate reader to be thermally equilibrated for at least 15 min, and afterward, monomer baseline measurements were recorded. The FAM fluorophore was excited with a 485 nm filter with an excitation bandwidth of 20 nm, and emission was recorded with a 535 nm filter and 25 nm emission bandwidth. Using a multichannel pipette, a ten-fold excess of polymerization staples was introduced to the monomers, and changes in FAM emission were recorded over time until an equilibrium was reached. The reading gain was set manually to accommodate the varying intensities of the differently concentrated samples. FAM-emission was recorded from the bottom of the wells after three seconds of shaking and one second of settling time with 15 flashes. A later chapter describes data analysis in detail (p. 36).

For isothermal FRET spectroscopy of DNA origami polymers induced by the binding of a fuel strand released from a DRN, the inactive interface with one set of fluorescently labeled strands was already introduced during monomer thermal annealing. The excess staples, including the fluorophores, were removed via Polyethylene Glycol Purification (p. 29) and optical density measurements with the calculated extinction coefficient determined the monomer concentration. 15 nM of initial monomers were used for DRN assays with $MgCl_2$ concentration varying in TEMg buffer to suit the experimental requirements. Otherwise, the experimental setup was similar to the above, and details about data analysis can be found in a later chapter (p. 37).

Optical Tweezers

Single-molecule force measurements for molecules of interest can be performed by trapping polystyrene beads in a focused IR laser beam and tethering the structure between long DNA handles non-covalently attached to the beads[195]. DNA handles for attaching DNA origami constructs to polystyrene beads were synthesized from a circular pET 28a (+) plasmid with two sets of primers (pp. 147) for binding the A- and B-interface, respectively. The origami binding primers with single-stranded hangovers were complementary to two or three central scaffold sections opposite to the DNA origami's interface of interest. A PEG-spacer separated the origami-binding part from the primer region integrated into the plasmid. At the other end of the handle, a digoxigenin- or a biotin-modified primer was used for PCR amplification, yielding a total of four double-stranded DNA-handles with a length of 3051 base pairs and a 32-nucleotide-long single-stranded extension for origami integration. Specifically, two handles were used for trapping a BAAB dimer at the B-interfaces, and two handles were used for trapping an ABBA dimer at the A-interfaces. Phusion Polymerase was used for construct enrichment, and the desired tether was first purified via ammonium acetate and then ethanol precipitation. Handle bands were cut from a 1 % AGE and stained with ethidium bromide. A NucleoSpin extraction kit was used to isolate the handles, which were then eluted and stored in Tris buffer. The DNA origami dimers were assembled from 2 nM scaffold with a ten-fold excess of core and stacking staples and a two-fold excess of handles in TEMg16. A random binding of DNA handles could be assumed.

Nonetheless, the resulting constructs were not further purified to prevent material loss, as only constructs with digoxigenin and biotin attached to a stacked dimer could bind to both beads and be trapped. 5 µl of undiluted α-digoxigenin beads were incubated with 5 µl dimer complexes at room temperature for 10 min and diluted in a 1:100 ratio in TEMg16, and streptavidin beads were used in a 1:1000 dilution. All force measurements were performed on a dual beam C-Trap (Lumicks) in TEMg16 at room temperature. The origami-handle construct was preincubated with the α-digoxigenin beads to facilitate the weaker digoxigenin bond and then optically trapped in the stationary IR-Laser. A streptavidin-coated bead was then trapped in the discretionary trap and moved close to the second handle, where it could attach to the DNA origami dimer construct. Force-distance curves of the stacking bond rupturing were recorded by pulling the streptavidin-coated bead steadily away.

AuNP-Labeling of DNA Origami

Gold nanoparticles (AuNP) with a diameter of 20 nm were synthesized by Dr. Michael Erkelenz applying previously established protocols[62,63,196,197]. Briefly, the thiol-group of a thiol-conjugated oligonucleotide ([ThiC6]-TAATAATAATAATAAT) was deprotected with a 50-fold excess of tris(2-carboxyethyl)phosphine (TCEP) for 20 min at room temperature. Subsequently, the oligonucleotide was desalted by size exclusion chromatography in ddH_2O and concentrated with a 3 kDa molecular weight cutoff filtration device by centrifugation at 16,000 rcf for 20 min. Meanwhile, the AuNPs were washed with 1 % Tween 20 at 10,000 rcf for 15 min and resuspended to 0.05 % Tween 20. Eventually, the AuNPs and 1000-fold excess oligonucleotide were conjugated after thorough mixing by stepwise addition of NaCl from 50 mM to 200 mM and incubation overnight at room temperature. The final oligonucleotide-coated gold nanoparticles were washed three times with ddH_2O and added in a 1:1 ratio to 2 nM origami monomers, previously purified by ultrafiltration (p. 29) and randomly stacked in filaments at 40 °C for 20 h. Eight protruding arms extending from the DNA origami A-subunit surface presented the complementary sequence to the AuNP-conjugated oligomers, and hybridization was performed by incubation at room temperature for 48 h. Finally, characterization by negative stain Transmission Electron Microscopy (p. 31) was performed.

DNA Reaction Network Complex Annealing

DRN *fuel* and *U complexes* were assembled in equimolar ratio using the calculated extinction coefficients and absorbance at 260 nm in TEMg12.5 adapted from Srinivas et al.[181]. Annealing was performed by cooling the solution from 95 °C to 20 °C at -1 °C/min. *Fuel complexes* were mixed with a five-fold excess of *V* and *helper strands* in TEMg12.5 or alternative $MgCl_2$ buffer concentrations and heated to the desired temperature. Adding the *U complex* to the remaining components instantly initiated the DRN reaction. A small fraction of unbound *U1|2 strands* could start the DRN reaction by displacing the *fuel strand* from the *fuel complex* (Figure 8). For isothermal FRET spectroscopy of the *fuel* release, the *fuel* oligonucleotides were exchanged equally for fluorescently labeled strands with a fluorescein (FAM) and a rhodamine (TAMRA) dye. Otherwise, proceedings for standard DRN initialization were followed, and fluorophore energy transfer was recorded as described for isothermal FRET spectroscopy (p. 33). Data analysis is described in detail in a later chapter (p. 37).

Data Analysis

Equilibrium Filaments - FRET Data Analysis

FRET kinetic data were obtained from triplicates of the donor-reference and donor-acceptor assay. Custom python scripts were developed to automate and standardize data analysis and to process the individually obtained .xlsx files. The time point of polymerization staple addition was determined based on deviations from the set measurement time intervals, and an extra 30 seconds were added to account for manual handling. The mean intensities of the donor and donor-acceptor triplicates ($\bar{x}_D$ and $\bar{x}_{DA}$) and corresponding standard deviations (σ_D and σ_{DA}) were determined. The FRET efficiency (E_{FRET}) was calculated based on Eq. 2.

$$E_{FRET} = 1 - \frac{\bar{x}_{DA}}{\bar{x}_D} \qquad \text{Eq. 2}$$

Afterward, the standard deviation of the E_{FRET} curve was calculated from the individual means and standard deviations according to Eq. 3.

$$\sigma_{FRET} = \sqrt{\left(\frac{1}{\bar{x}_D}\right)^2 \times \sigma_{DA}^2 + \left(\frac{\bar{x}_{DA}}{\bar{x}_D}\right)^2 \times \sigma_D^2} \qquad \text{Eq. 3}$$

If the baseline measurements were slightly above zero due to technical deviations, the initial values and corresponding curve were adjusted accordingly. The equilibrium E_{FRET} was adjusted to correspond to the initially present monomer concentration to compare the individual FRET curves better. Estimations of the critical monomer concentration (c_{crit}) at equilibrium revealed negligible values, with $c_{crit} << c_0$ (Figure 21).

To a first approximation, the growth of a linear polymer at its tips over time *t* can be described as the difference of polymer growth and shrinkage[198] as described by Eq. 4.

$$\frac{dF}{dt} = k_f c n - \delta F \qquad \text{Eq. 4}$$

With *F* being the number of monomers bound in filaments, k_f being the rate of binding of monomers into polymers (on-rate), *c* the number of free monomers in solution, *n* the number of actively growing filament tips, and *δ* the rate of polymer disassembly or turnover (off-rate).

The number of monomers bound into filaments is the difference between the total amount of monomers A and the number of free monomers (Eq. 5).

$$F = A - c \qquad \text{Eq. 5}$$

At timepoints close to t = 0, the concentration of free monomers in solution approximates the total initial monomer concentration $c \approx A$. Combining this with Eq. 4 and Eq. 5 removes the polymer disassembly part of the equation (Eq. 6).

$$\frac{dF}{dt} = k_f cn - \delta(A - c), \qquad \frac{dF}{dt} = k_f An \ (at\ t = 0) \qquad \text{Eq. 6}$$

Accordingly, assuming a constant number of filament tips and applying a linear fit to the initial reaction curves gives the initial reaction rate of the polymerization. This was achieved by applying a variable fit that included at least five data points of the experimentally determined and normalized FRET curves, spanning a time interval of up to one hour. The best linear fit and corresponding slope were used to determine the initial reaction rate.

Filaments fueled by DRN - FRET Data Analysis

FRET profiles obtained from the DRN-fueled 24-helix bundle filaments varied significantly in equilibrium FRET efficiency. In contrast to the previously examined polymers with a different FRET strategy for each type of interface association (Figure 10), the same FRET strategy with identical FRET staples and position in the head-to-tail association (Figure 37a and b) was used to monitor all fuel strand driven reactions. Therefore, comparing the absolute equilibrium E_{FRET} values for the fuel-specific labeling strategy allowed conclusions to rank polymer lengths in relative terms when comparing one isolated factor like salt or temperature conditions or excess of fuel strands. Since the normalization of the FRET efficiency would conceal valuable information on these filament properties, FRET profiles were only set to zero at t = 0 and are otherwise given as untreated E_{FRET} variations over time. Apart from that, the data analysis protocol was identical to the equilibrium filaments described above.

Random Stacking statistical Distribution Analysis

Random stacking association at each individual interface gives rise to three possible outcomes and three relative populations: AB, AA, and BB. Collecting single-molecule TEM images allowed the identification of the interface configurations and yielded 49 % AB, 28 % AA, and 23 % BB (Figure 20). Assuming that the relative populations are exclusively driven by the respective interface stacking energies (E_i), the equation for the Boltzmann distribution can be applied to relate the observed binding probabilities (P_i) to the individual binding energies. Eq. 7 shows the Boltzmann equation for an arbitrary interface binding event, which is determined by the binding energy E_i, Boltzmann constant k_B, temperature T, and the sum of all binding probabilities Z.

$$P_i = \frac{e^{\frac{-E_i}{k_B T}}}{Z} = \frac{e^{\frac{-E_i}{k_B T}}}{\sum_i e^{\frac{-E_i}{k_B T}}} \qquad \text{Eq. 7}$$

Solving Eq. 7 for the three individual states yields Eq. 8.

$$\begin{cases} P_{AB} = \dfrac{e^{\frac{-E_{AB}}{k_B T}}}{Z} \\ P_{AA} = \dfrac{e^{\frac{-E_{AA}}{k_B T}}}{Z} \\ P_{BB} = \dfrac{e^{\frac{-E_{BB}}{k_B T}}}{Z} \end{cases} \qquad \text{Eq. 8}$$

Introducing the experimentally determined values $P_{AB} = 0.49$, $P_{AA} = 0.28$, and $P_{BB} = 0.23$ and with $Z = 1$ yields the following interface association energies E_i at temperature T (Eq. 9).

$$\begin{aligned} E_{AB} &= -k_B T ln(P_{AB}) = 0.71 k_B T \\ E_{AA} &= -k_B T ln(P_{AA}) = 1.27 k_B T \\ E_{BB} &= -k_B T ln(P_{BB}) = 1.47 k_B T \end{aligned} \qquad \text{Eq. 9}$$

Results and Discussion

The following chapter contains results from the article *Growth Rate and Thermal Properties of DNA Origami Filaments* by Stenke, LJ. and Saccà, B., published in ACS Nano Letters in 2022[1].

Dimerization

Dimeric structures offer a valuable system to examine isolated interface associations of the 24-helix structure and investigate the mechanisms and kinetics behind the stacking association in more detail. The BAAB or the ABBA dimer can be formed by the isologous self-association either at the A- or B-interface, which is induced by the formation of blunt end helices between the unpaired scaffold and complementary staple strands. Two modes of association can achieve the relatively simple and finite dimer equilibrium state (Figure 12b). In a one-step dimerization, the scaffold strand is mixed with an excess of core staples and oligonucleotides, activating one of the interfaces for stacking. The resulting dimer is assembled over the same thermal gradient described for the monomers. In a two-step dimerization, monomers are first fully assembled over a thermal gradient before the respective interface stacking strands are introduced in excess at isothermal conditions (30 °C to 40 °C).

The successful formation of dimers from both described assembly approaches was shown by agarose gel electrophoresis of 50 nM samples in TEMg16 compared to a monomer reference band (Figure 12a). The one-step samples were assembled with ten-fold staple excess over the same thermal annealing profile described for the monomers (p. 28). At the same time, the two-step dimers were self-assembled with the identical staple excess at 40 °C for 20 h. The electrophoretic migration profiles of self-assembled BAAB and ABBA dimers were similar for both approaches and types of dimers, and they were clearly distinguishable from the monomer band. Hence, finite dimeric structures successfully assemble, regardless of the traveled pathway towards equilibrium.

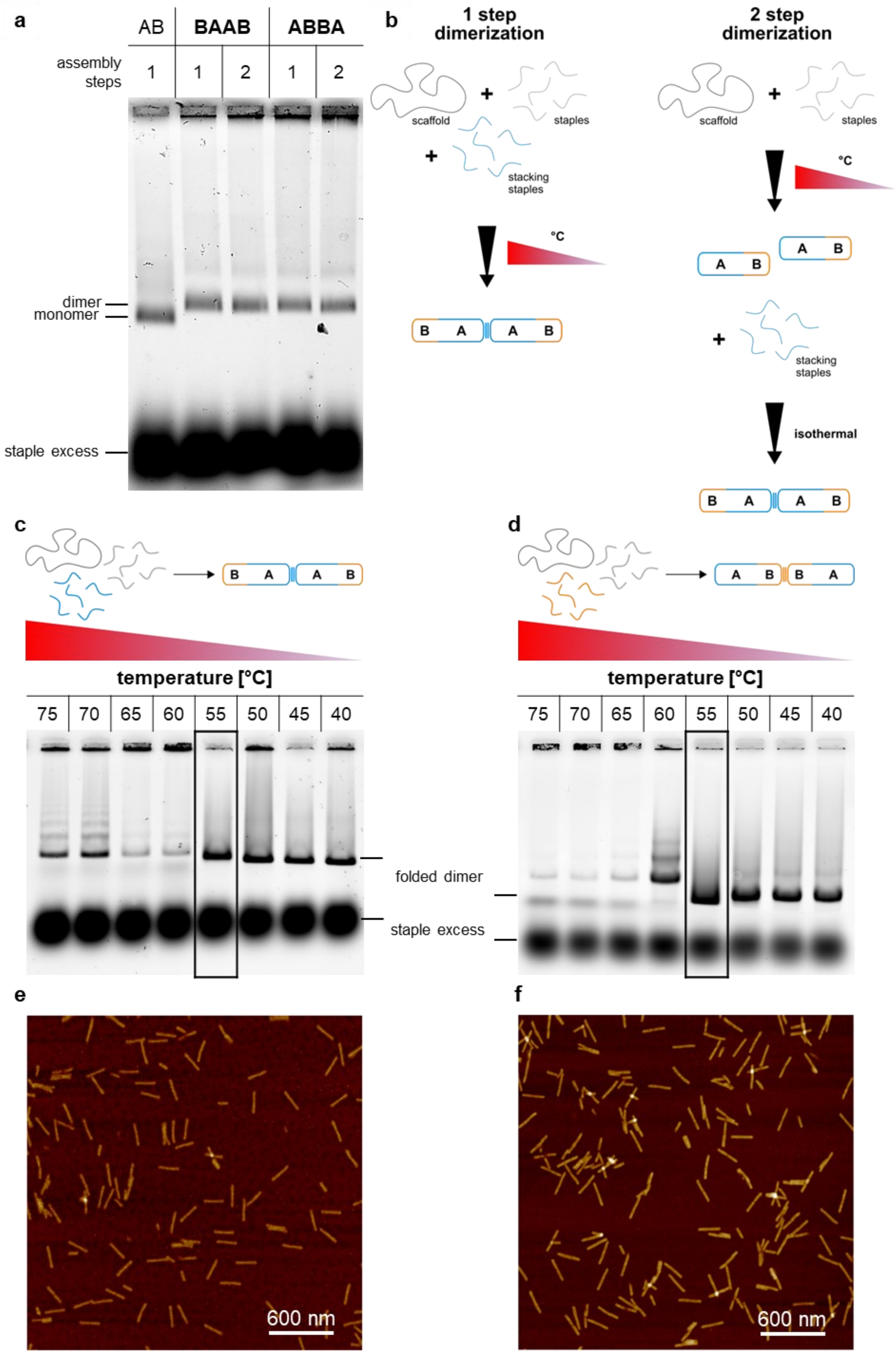

Figure 12 ***Dimerization characterization***

a) AGE comparison of the equilibrium constructs of 1-step or 2-step dimerization of 50 nM scaffold and ten-fold excess of staple strands in TEMg16 with a difference in folding mechanisms depicted in b). Migration profiles of thermal gradient dimer assemblies of 50 nM monomer in TEMg16 from 75 °C to 40°C at -0.1°C/min for c) AA and d) BB association with association temperatures marked and samples imaged at 55 °C (e): BAAB and f): ABBA).

To further investigate the one-step dimerization process in more detail, 50 nM of scaffold with a ten-fold excess of core and stacking staples were annealed over a temperature gradient from 75 °C to 40 °C with -0.1 °C/min, and samples were collected every 5 °C. The dimerization reaction was subsequently stopped by insertion into liquid nitrogen. Figure 12c and d depict the electrophoretic migration profiles of the AA and BB association, respectively. For both types, temperature values higher than 60 °C resulted in unfolded or partially folded monomeric structures with slower migrating bands. Below 55 °C, the migration bands depicted dimer characteristics for both interface types. Interestingly, at 55 °C, the band corresponding to the ABBA dimer migrated slightly faster when compared to samples at lower temperatures, indicating that the dimer is in its most compact form. AFM images of 55 °C samples demonstrated successful dimerization for the BAAB and ABBA dimers.

Thermal Analysis of Dimerization

In order to monitor the isologous stacking association and dissociation of the AA and BB-interface throughout a thermal gradient, the FRET interface labeling strategy described in Figure 10 was applied. Dimers from 50 nM scaffold, a ten-fold excess of staples, and a two-fold excess of fluorescently labeled oligonucleotides were first assembled at a rate of -0.1 °C/min from 75 °C to 25 °C and subsequently melted. Figure 13a and b show the cooling and melting profiles for the AA and BB association and their theoretical equilibrium curves, respectively. A hysteresis, or a deviation between the cooling and melting curves, could be observed for both association types, with the ABBA dimer exhibiting about a two-fold larger hysteresis extent than the BAAB dimer. Two main analysis methods for melting point comparison were applied to the cooling and heating curves (p. 32), summarized in Table 5. One temperature point, referred to as $T_{0.5}$, indicates the temperature half-point where 50 % of the sample has transitioned from the unfolded to folded state θ or vice versa. A more commonly used characterization of melting temperature, referred to as T_m, pinpoints the temperature at which $d^2\theta/dT^2 = 0$, describing the turning point of either the cooling or melting curve at which folding or unfolding events most rapidly occur. Figure 13c illustrates the resulting plots of a first-order derivative of the corresponding cooling and melting curves with the temperature values at the curve maxima (and minima) indicating the melting temperature T_m. A more global approach for quantifying association (cooling) and dissociation (melting) hysteresis, is the comparison of the area between the respective curves[199], also referenced in Table 5.

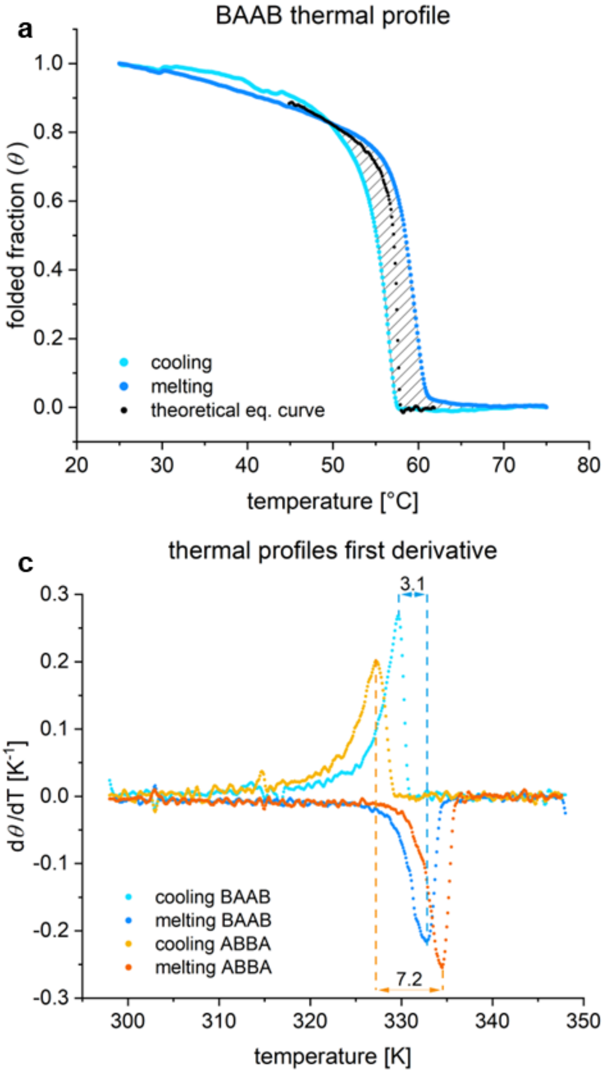

Figure 13 ***Thermal profiles of the dimerization process***
50 nM of fluorescently labeled dimer precursor were assembled and subsequently disassembled from 75 °C to 25 °C with a cooling/heating rate of +/- 0.1 °C for the a) AA- and b) BB-interface association. c) Melting temperatures of the curves can be deducted from the first-order derivative.

Table 5 ***Dimer melting temperatures***

dimer	**temp. scan**	**$T_{0.5}$ [°C]**	**T_m [°C]**	**A [θ °C]**
BAAB	heat.	58.5	59.8	7.08
	cool.	55.1	56.7	4.18
	Δ	3.4	3.1	2.90
ABBA	heat.	60.1	61.4	12.4
	cool.	52.5	54.2	6.38
	Δ	7.6	7.2	6.03

Regardless of the analysis method, the BB association exhibited more than a two-fold extent in hysteresis compared to the AA association. When the unfolded ABBA sample was cooled down for dimer association, 50 % of bonds were formed at $T_{0.5}$ = 52.5 °C with the fastest formation rate at T_m = 54.2 °C. In comparison, 50 % of BAAB associations were completed at $T_{0.5}$ = 55.1 °C and T_m = 56.7 °C. Therefore, the AA dimer associates at temperature values around 2.5 °C higher than the BB dimer. After forming the structures, the subsequent melting cycle measures the dimer stacking stability. Interestingly, the AA-stacking dissociated first, with 50 % of bonds broken at $T_{0.5}$ = 58.5 °C, followed by the fastest disintegration at T_m = 59.8 °C. Set side by side, the BB-stacking was about 1.6 °C more stable when heated, with $T_{0.5}$ = 60.1 °C and T_m = 61.4 °C.

Taking the lower association and higher dissociation temperatures into account resulted in the enlarged hysteresis of the BB-interface when compared to the BAAB dimer, with a difference in cooling and melting temperatures of up to 7.6 °C and 3.4 °C and an area under the curve of 6.03 θ °C and 2.9 θ °C, respectively. While the presence of hysteresis between the assembly and disassembly of origami structures is well-known[199], the energetic barrier for interface formation and dissociation must simultaneously be higher for the BB-interface. The most prominent difference between the BAAB dimer and its ABBA counterpart is the number of perfectly stacking helices which are 16 out of 24 for the AA-interface and 8/24 for the BB-interface (Figure 9). The remaining helices exhibit a design-induced one base pair gap (1 bp gap) between blunt ends facing each other. For the formation process, less perfectly stacking helices could lead to a more straight forward formation process and higher association temperature. Once the stacking connection has formed, heating up the constructs might promote the inherently flexible DNA helices to partially bridge the 1 bp gaps, contributing to the observed (higher) interface stability.

The Effect of the One Base Pair Gap on Stacking

Further insight into the significance of the 1 bp gap described above, which is present to varying degrees at the A- and B-stacking interfaces, and spans only 0.34 nm[22], could be achieved by systematically altering the number of gapped helices. Therefore, the number and position of helices separated by a 1 bp gap were gradually increased, starting from only the perfectly stacking helices and single-stranded scaffold loops. Blunt ends at the gapped helices were introduced iteratively to ultimately form the well-established dimer design. Two pairs of matching fluorophores were placed within the constantly stacking regions to enable FRET spectroscopy monitoring of the association and dissociation of the different design variants (Figure 10, Figure 14a and d).

The starting reference structure for both interfaces contained only perfectly stacking helices and unpaired scaffold at the remaining helices. The number of perfectly vs. imperfectly (i.e. 1 bp gap) stacking helices for the starting construct was (16/0) for the A- and (8/0) for the B-interface. Figure 14a and d display schematic views of each interface's activated helices. Due to the underlying interface design, which incorporated several blunt ends formed by the same staple, this could result in blunt end formation at one helix but not at its respective shape-complementary counterpart (this is indicated as “partially activated”). As the matching helix consisted of unpaired scaffold domains, no stacking interaction could occur, with no observable effect on the thermal curves (Figure 14e and f: compare B(8/8) vs. B(8/8+), Figure 15b: compare B(8/8) vs. B(8/8+)). Due to shape-complementarity reasons, each design variant generally resulted in the formation of two additional helices encompassing a 1 bp gap.

The experimental setup for the temperature-dependent FRET assays was identical to that described for the dimers in the previous section (p. 41). Figure 14 displays the individual cooling and melting curves for each construct with increasing numbers of blunt ends, as wells as an overview of active helices for each construct. For A-stacking, the base structure included 16 perfectly stacking helices and eight inactive helices A(16/0), which were gradually activated to include eight imperfectly stacking helices A(16/8) with a 1 bp gap. Similarly, B-stacking was characterized by starting with eight perfectly stacking blunt ends B(8/0) and gradually increasing the number of imperfectly stacking helices to include 16 with a 1 bp gap B(8/16).

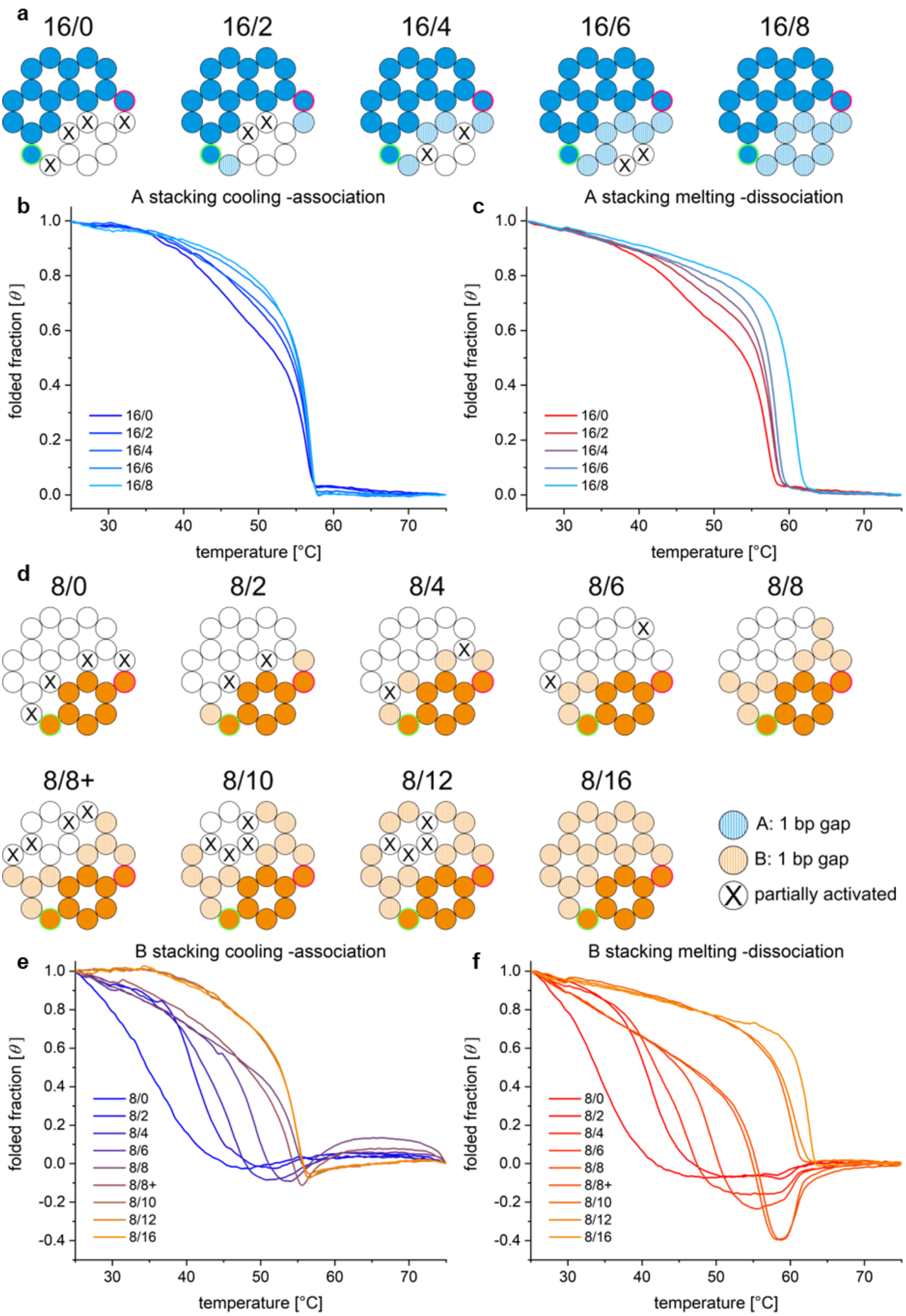

Figure 14 ***Interface activation series for one base pair gap and resulting thermal profiles***
a) AA- and b) BB-stacking was stepwise activated from perfectly stacking helices (16/0 or 8/0) to further incorporate imperfect connections. 25 nM dimers were associated (b and e for AA and BB, respectively) and subsequently dissociated (c and f) over a thermal gradient from 75 °C to 25 °C with +/- 0.1 °C/min.

Generally, an increase in blunt ends caused the thermal cooling and melting curves to shift towards higher temperatures. This effect could be observed to a greater extent in the melting curves, regardless of A- or B-stacking (Figure 14c and f). After a defined threshold number of activated helices, the cooling (or association) profiles revealed a nearly identical curve profile. For the A-interface cooling curves, the behavior of the association curves was similar for structures A(16/6) and A(16/8) (Figure 14b). The same could be observed for B(8/10), B(8/12), and B(8/16) of the B-interface cooling (Figure 14e). Additionally, the association temperatures (T_m) for A(16/2) and above were all between 56.6°C and 56.8°C (Figure 15a). For B-association, temperatures were similar for structures B(8/8) and higher, with T_m ranging from 54.7°C to 55.1°C (Figure 15b).

Regarding the dissociation temperatures (melting curves) of the individual interfaces, no such threshold value could be observed, and the temperature shift effect for each additional imperfect blunt end helix was more significant than observed in the cooling curves. In contrast to the partially overlapping cooling curves, the curves for the completely activated interfaces A(16/8) and B(8/16) were shifted by more than 2 °C compared to their next closest structure. The absolute difference in the T_m values from the weakest to the most robust structure was merely 0.3 °C, with 56.5 °C for A(16/0) to 56.8 °C for A(16/8). For B-interface cooling, the difference was 16.9 °C, from B(8/0) forming at 38.1 °C to B(8/16) forming at 55 °C. For the dissociation (or melting) of the structures, A(16/0) melted at 57.2 °C, while A(16/8) melted 3.7 °C higher at 60.9 °C due to the presence of eight imperfectly stacking helices. Sixteen of such gapped helices in the ABBA dimer increased the melting temperatures by a total of 28.3 °C from B(8/0) melting at 34 °C to B(8/16) melting at 62.3 °C (Figure 15a and b).

Based on findings from Kilchherr et al.[47], the theoretical stacking energies can be calculated by taking the sum of the sequence-dependent stacking energies of each helix pair (Figure 15a and b, right axis). This approach disregards the impact of the 1 bp gap but can aid in better understanding sequence-specific differences between the two dimer species. The eight perfectly stacking helices B(8/0) of the B-interface release a theoretical stacking energy of -9.78 kcal/mol. Interestingly, this B(8/0) construct was the only interface variation with association temperatures higher than dissociation temperatures and a resulting negative hysteresis value of -4.1 °C (Figure 15c and d).

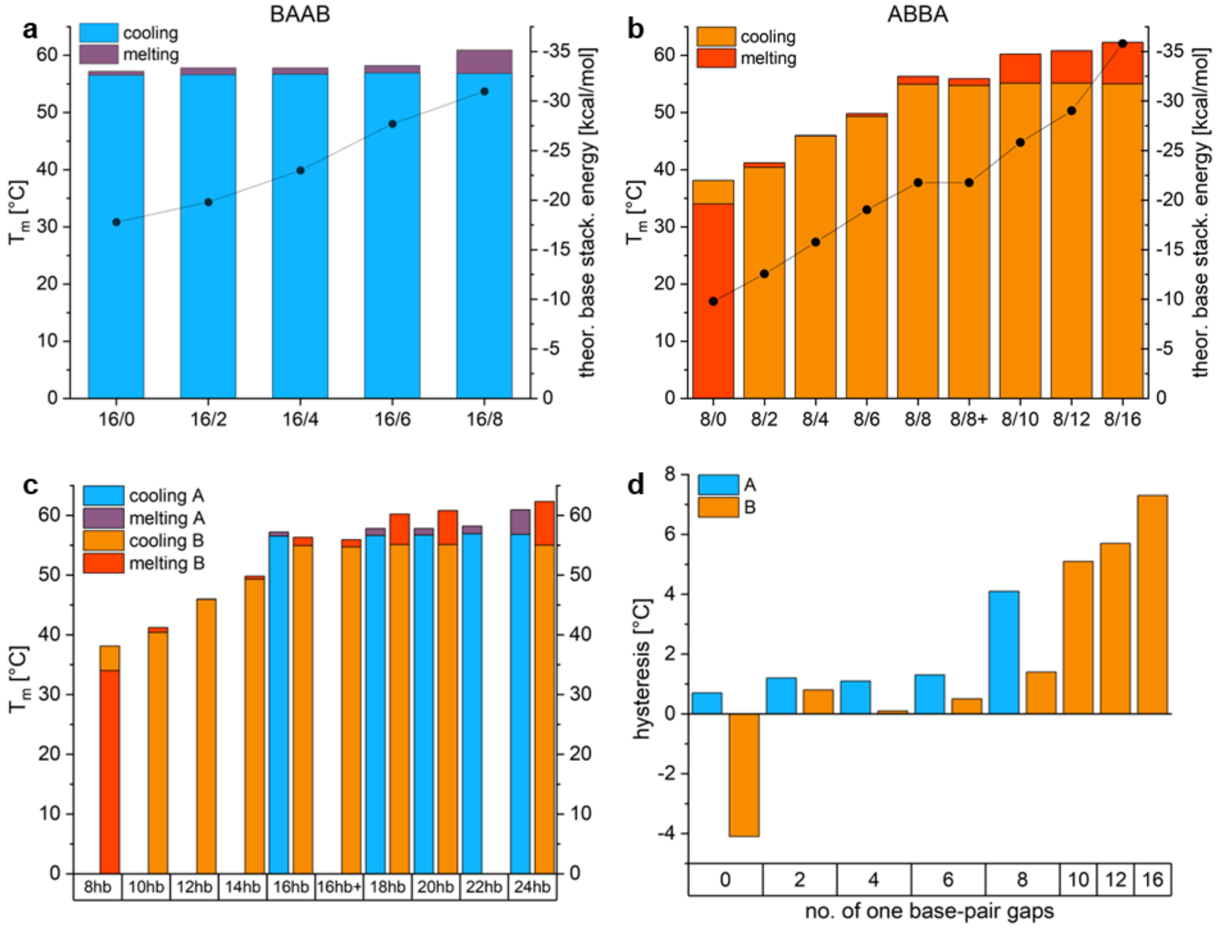

Figure 15 ***Thermal features of dimer interface titrations***
Cooling and melting temperatures of $T_m = d^2\theta /dT^2 = 0$ of a) BAAB and b) ABBA dimer interface titrations with increasing numbers of imperfect 1 bp gaps and theoretical stacking energies (right axis of a and b). c) The total number of stacked helices and respective cooling and melting temperatures are compared and d) hysteresis extends for the addition of imperfectly stacking helices shown.

Combined with the overall low T_m values of 38.1 °C and 34 °C for association and dissociation, this result points to an inherently instable interface association close to not even taking place. It is plausible that a noticeable energy barrier must be overcome for two 5 MDa structures to stack to each other, and for the here characterized DNA origami bundle, this barrier is most likely close to -9 kcal/mol. When comparing the A(16/0) and B(8/8) dimers, both with 16 helices involved in interface stacking, the A-interface has a theoretical stacking energy of -17.78 kcal/mol, whereas for the B-interface, those energies would be around -21.76 kcal/mol. Nevertheless, the association temperature for A was 56.5 °C, which is 1.6 °C higher than in B, and its dissociation temperature was still 0.9 °C higher (57.2 °C) (Figure 15c). From a global view, theoretical stacking energies do not fully represent the stacking behavior observed from a partially gapped interface but can be employed to forecast behavioral trends when taking the less effective binding into account.

Interface stacking association, as monitored by the cooling curves, might be enhanced by adding imperfect or gapped stacking bonds but only up to a certain threshold. For the dimeric structures examined here, this threshold might be located at stacking energies near -20 kcal/mol for interface association (Figure 15a and b). The cooling and melting temperatures of the B-interface appeared to scale with the theoretical stacking energy up to the B(8/8) construct. From 16 stacking helices onward, both interface association types seemed to have reached a threshold temperature for the interface association. However, their dissociation stability still increased with the addition of gapped helices. This indicates that imperfect stacks play a minor, yet to some extent noticeable, role in interface association but a significant part in interface thermal stability once the structures are assembled. The hysteresis-extent was observed to scale with the total number of additional gapped helices (Figure 15d).

A noticeable feature of the B(8/4), B(8/6), B(8/8), and B(8/8+) melting curves (Figure 14f) was a brief but noticeable drop of the FRET efficiency below zero at temperatures between 50°C and 60°C. An explanation for this phenomenon could be found in the individual donor-only and donor/acceptor FAM intensity curves. The specific species exhibited a peak in the intensity of the FAM signal of the donor/acceptor samples in the given temperature range (Supplementary Figure 1), which revealed the underlying cause for the negative E_{FRET} values. A plausible explanation for this phenomenon is that at the given temperature range, the TAMRA fluorophore attached to the oligonucleotide could sterically destabilize the interface leading to a reduced quenching effect. This disruptive effect could be circumvented by increasing the thermal stability of the interface upon further addition of blunt ends.

Overall, the observed effects might be explained as follows. For the cooling curves, the temperature gradually decreased from 75 °C to 25 °C with -0.1 °C/min, going from a state of higher thermal energy and free monomers to a state of lower thermal energy and bound dimers. Higher temperatures are generally accompanied by increased Brownian motion, which is supposed to increase the likelihood of two interfaces to meet and stack. On the other hand, enhanced molecular motion may also favor the disruption of the just formed bond. Stronger stacking bonds generated by a higher number of stacking helices will therefore stabilize the interfaces at higher temperatures up to a specific threshold value. Once the stacking bonds have formed, heating of the system may induce more molecular motion and possibly favor the stretching of the DNA double helix over the distance of a 1 bp gap (0.34 nm) that comprises only 0.17 %

of the total length of a DNA origami dimer (200 nm). This would explain why the gradual introduction of gapped helices has a progressively significant effect on the thermal stability of the stacked dimer.

Characterizing partial Dimer Stacking Forces

Single-molecule stacking forces were measured for modified partially stacking dimers to correlate the theoretical stacking energies to experimental observations and better understand sequence-dependent behavior. In order to record the rupture of the actual stacking bonds and not that of the double-stranded DNA-handles connecting the dimers to the beads, only partially stacking and, therefore, weaker structures were examined and forces below 30 - 50 pN were applied[200]. Several variations of activated helices were tested for the A- and B-interface to identify such a transiently stacking interface (Figure 16a). Six to 16 helices were activated by adding a ten-fold excess of the respective stacking strands to 10 nM of the pre-assembled monomer, which was subsequently dimerized in TEMg16 at 40 °C for 20 h. The resulting structures were compared against a monomer reference lane on a 1 % agarose gel stained with EtBr (Figure 16b; lanes containing a mixture of mono- and dimers are indicated with a “*” symbol).

For the BAAB and the ABBA dimer, the structures with six activated helices (and a theoretical stacking energy of -6.44 kcal/mol and -7.06 kcal/mol, respectively) did not form dimeric structures under the given conditions. With eight activated helices and sequence-dependent stacking energies of -13.2 kcal/mol and -9.78 kcal/mol for the A- and B-interfaces, a mixture of monomers and dimers could be identified after a two-step assembly process. Sixteen activated helices with respective stacking energies of -17.78 kcal/mol and -26.02 kcal/mol resulted in defined dimer bands without monomer traces. Subsequently, interfaces with eight stacking helices for A- and B-interfaces were chosen for future experiments to represent the weakest possible stacking structures. Interpretation of the AGE data with theoretical stacking energies supported the postulated energetic stacking threshold (p. 48). For the B-interface with six blunt end helices and a stacking energy of -7.06 kcal/mol, no dimer association could be observed, while successful stacking was shown for eight helices with -9.78 kcal/mol. Hence, the postulated threshold value would be above -7.06 kcal/mol and below -9.78 kcal/mol for the two-step assembly of the 24-helix bundle.

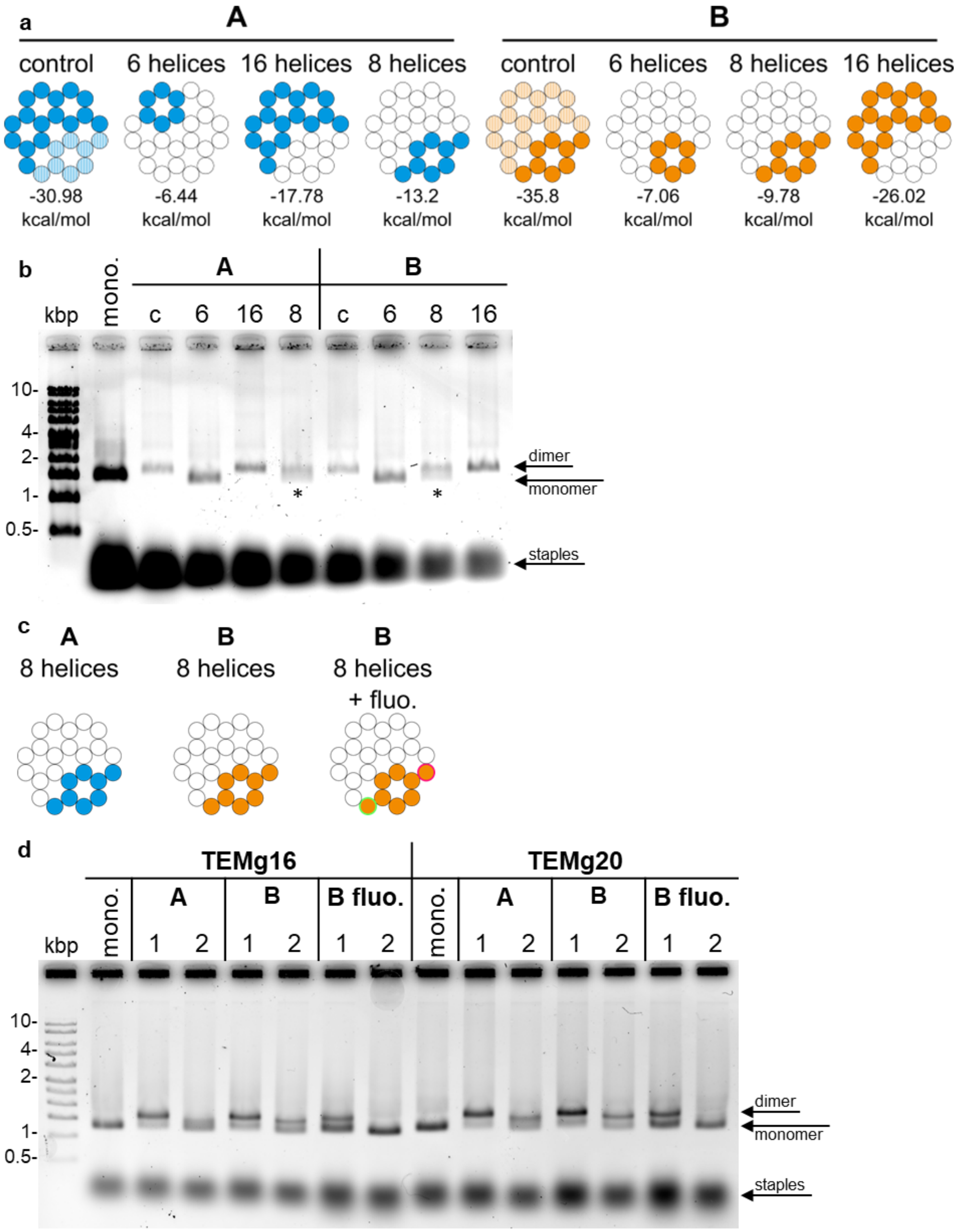

Figure 16 ***AGE profiles of varying helix activations for dimer stacking***

*a) Varying combinations of actively stacking helices and their respective theoretical stacking energies from six to 16 helices as compared to the fully active interfaces of A- and B-stacking as control. b) Dimers were formed from 10 nM previously assembled monomers in TEMg16 at 40 °C for 20 h, and a 1 % AGE gel stained with ethidium bromide visualized the extent of dimer formation. Constructs with marginal dimerization properties are marked with *, and the effects of differences in the assembly process were further characterized by d) 1 % AGE stained with EtBr. For the B dimer, the impacts of conjugating stacking oligonucleotides with fluorophore dyes FAM and TAMRA were examined (c), while for both A and B dimer variants, the effects of $MgCl_2$ concentration and the number of assembly steps were tested.*

Further investigations into the assembly process of the eight helix stacked structures were conducted to characterize the effects of magnesium chloride concentration on dimer formation. The potential difference between TEMg16, used for monomer formation, and TEMg20, used for polymerization, was investigated regarding the dimer formation. Furthermore, the impacts of the presence of fluorophores conjugated to the stacking-inducing staples (Figure 16c) and the overall number of assembly steps were analyzed by AGE (Figure 16d). Comparing the bands for TEMg16 and TEMg20 assemblies yielded no observable difference in the population distributions between mono- and dimers, rather just an overall slightly shorter migration rate for TEMg20 structures. B-stacking in the presence or absence of fluorescein dyes at two of the eight stacking helices (otherwise wholly sequence-identical) revealed a population shift towards the monomeric structures induced by the presence of the fluorophores. For the one-step assembly, the distribution shifted from mostly dimers in absence of fluorophores to an equal distribution of mono- and dimers in presence of fluorophores. For the two-step assembly, the addition of fluorophores caused a shift from an equal distribution of mono- and dimers to monomers only. Generally, fluorophores appeared to introduce a steric hindrance for weakly stacking interfaces that further weakened the bond and most likely enhanced the threshold for interface association.

All tested structures demonstrated a significantly lower dimer yield for the two-step dimerization process in which the monomers were first assembled over a thermal gradient and, subsequently, dimerized upon addition of a ten-fold excess of stacking staples and incubated at 40 °C for 20 h. Adding stacking staples to the unassembled monomer core and running the same thermal gradient as for monomer assembly resulted in a higher yield of dimers. Temperatures higher than 40 °C were preferred for successful dimerization of the structures. No difference between the one- or two-step assembly could be identified for dimer structures with higher interface stability, such as the ones with fully activated helices (Figure 12a).

For the weakly stacking dimers to be characterized by optical tweezers (C-Trap), a one-step assembly in TEMg16 and in absence of fluorophores was chosen accordingly. The dsDNA-handles connecting the origami to the trapped polystyrene beads via non-covalent bonds (biotin/streptavidin or digoxigenin/αDig) was integrated into the outward-facing tips of the DNA origami bundle during assembly. The integrity of the so-formed structures was confirmed via AFM in air (Figure 17a and b). As previously observed via gel electrophoresis (Figure 16b and d), a good fraction of

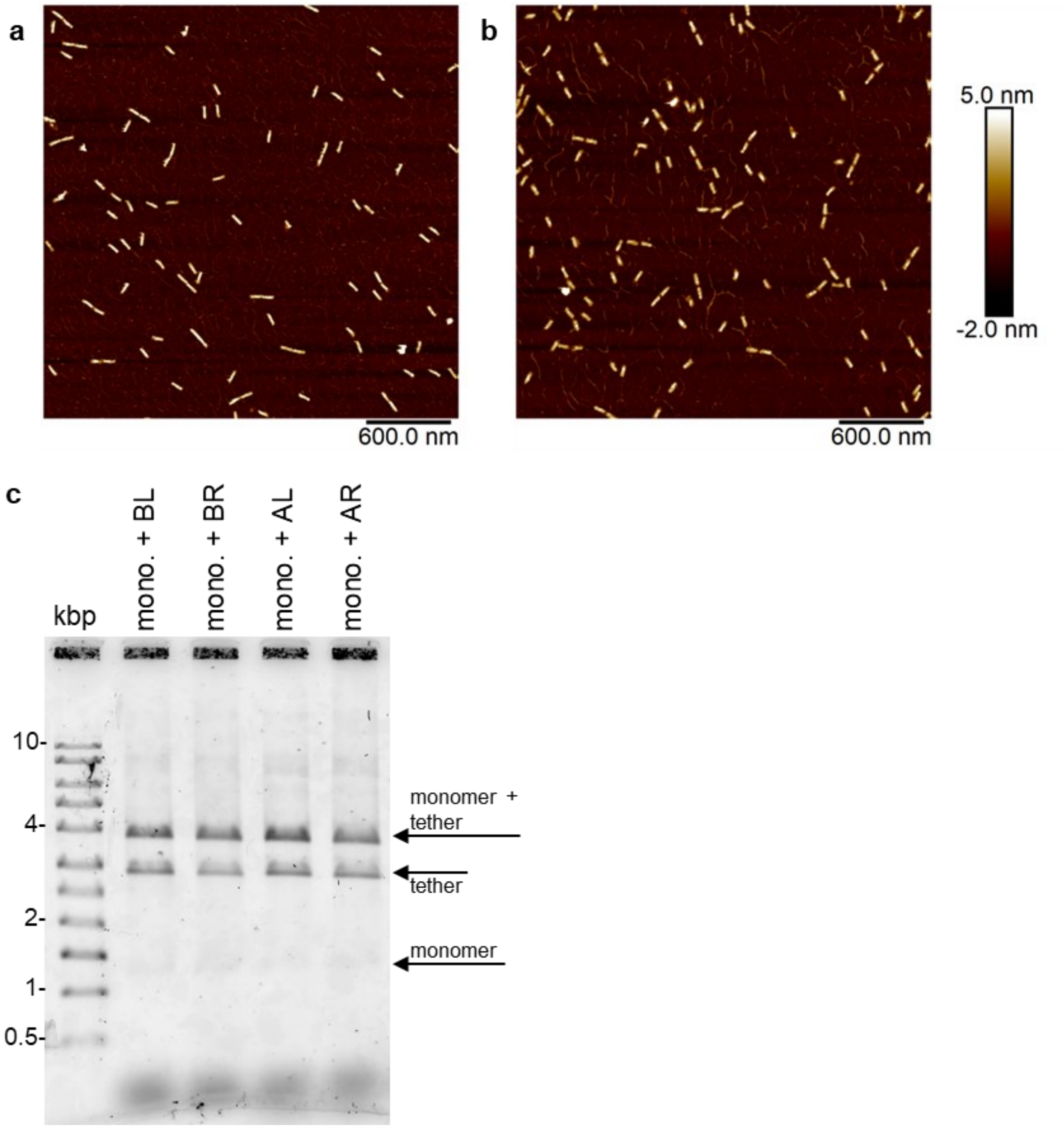

Figure 17 ***Tether-DNA attachment to dimers with eight helices stacking and individual monomers*** *AFM in air images of 1 nM dimer assembled over a thermal gradient with two-fold excess of biotin- and digoxigenin-conjugated DNA-tethers of 3051 bp length incorporated into the non-stacking interfaces via base-hybridization of 33 bases. a) BAAB dimers and b) ABBA dimers stack via eight helices interacting respectively with different sequences. c) Integration of the four different tethers into DNA origami was controlled via 1 % AGE of 4 nM monomers and a two-fold excess of tether. BL tether is conjugated to digoxigenin at the 5' end and integrates into the inactive B-interface. BR is conjugated to biotin, and AL and AR present the same modifications while binding to the inactive A-interface.*

monomers did not dimerize, but the overall yield distribution was comparable to the gel bands. For the ABBA dimers with a theoretical stacking energy of -9.78 kcal/mol as compared to the BAAB dimers with -13.2 kcal/mol, all observed B-stacking interactions broke upon mica-surface contact (Figure 17b), while not all A-stacking bonds did (Figure 17a). The monomers' linear orientation and pairwise proximity indicated the given dimer formation in solution. Complete integration of tethers could not be precisely visualized by AFM but was demonstrated for the monomers via agarose gel electrophoresis (Figure 17c). Additionally, only complete constructs with two tethers connecting a dimer could eventually be caught by both polystyrene beads allowing for the recording of force-distance (FD) curves.

Single-molecule measurements performed with a dual trap optical tweezer were used to investigate individual dimer stacking forces and sequence-dependent effects of two otherwise identical interfaces (Figure 18d). Although both constructs had exactly eight blunt ends activated, sequence-specific theoretical stacking energies differed by more than 30 %, as A-stacking energy was -13.2 kcal/mol and B-stacking energy was -9.78 kcal/mol. The forces required to break the dimer bond were recorded by non-covalent attachment of one extremity of each DNA-handle to the corresponding polystyrene bead trapped by an infrared laser beam. Since the other extremity of each handle integrates at opposite sides of the same origami structure, the final object is tethered between two distinct optical traps and ready to be subjected to gradual stretching forces (Figure 18f). One IR-trap was moved outwards at a constant speed (0.05 µm/s), applying forces to the stacking interface. By pulling on the dimer structure, forces were applied to the full tethers. Assuming that the central origami object behaves like a non-extendable rigid body, the FD profiles obtained can be interpreted as the spring-like mechanical response of the DNA-handles, according to the extended worm-like chain model[200]. Resulting exemplary force-distance curves are displayed in Figure 18a for A-stacking and Figure 18b for B-stacking. The force at which the stacking bonds broke was determined to be the difference between the peak force value and the baseline plateau (marked by vertical grey arrows). At short bead-to-bead distances, as required for construct attachment and tethering, an increase in forces could be observed caused by the bead’s mutual repulsion (areas marked with grey boxes).

For BAAB dimers, eight FD-curves were analyzed. Bond breakage forces ranged from 19.45 pN to 30.14 pN, with a median value of 29.01 pN representing the central cluster of forces (Figure 18c, blue boxplot). B-stacking forces were significantly lower, ranging from 7.03 pN to 12.58 pN, with a median force of 12.05 pN (Figure 18c, orange boxplot). This observation correlated well with the trend in theoretical stacking energies. Previously conducted AGE experiments (Figure 16b and d) already suggested a possible energetic threshold for interface stacking of the here characterized DNA origami bundle. According to the observed AGE data (Figure 16), the dimerization threshold value lies between -7.06 kcal/mol and -9.78 kcal/mol (Figure 18e, red bar). When assuming a linear dependence of observed stacking forces and energies as postulated by Kilchherr et al.[47], the y-intercept of a linear fit of the experimental forces versus energies is near -7.35 kcal/mol (Figure 18e, y-intercept), which lies well inside of the energy interval suggested for the stacking threshold by AGE. Based on the described fit, increasing the calculated stacking energy by 1 kcal/mol leads to an additional 5 pN interface stability. Of course, these observations will vary for different shapes of DNA origami and would need more experiments to be confirmed, but they can give a guide-idea for future designs.

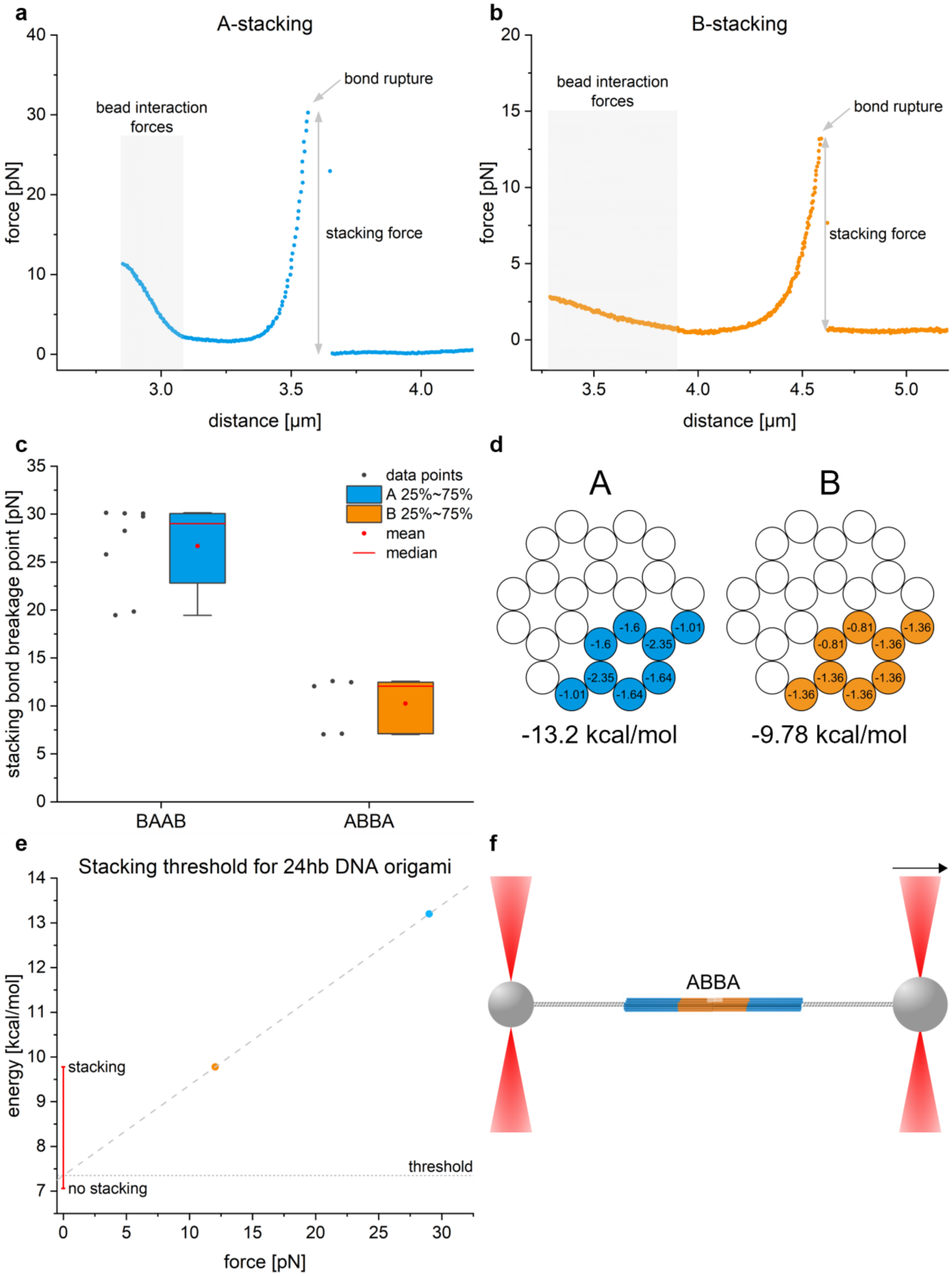

Figure 18 ***Force-distance curves of dimers with eight stacking helices and different interface sequences***

Exemplary FD-curves of partial a) A-stacking and b) B-stacking with bond rupture forces representing the force fraction between peak force and baseline. d) Actively stacking helices and the sequence-dependent stacking energies are marked. c) Correlating to the higher stacking energies of -13.2 kcal/mol of the A-interface, stacking bond rupturing forces were correspondingly higher for A with a median value of 29 pN and 12.05 pN for B. e) Correlating the observed bond breakage forces and their respective stacking energies and additionally considering the postulated stacking threshold yields a theoretical stacking threshold near -7.35 kcal/mol for the 24-hb DNA origami. f) A dual optical trap setup with the dimer tethered between two polystyrene beads was used. Exemplarily shown for the ABBA dimer.

The Kinetics of Dimerization

Kinetic characterization of the fully activated interfaces at isothermal conditions was performed via Förster resonance energy transfer spectroscopy (p. 33). Pre-assembled monomers were marked with a fluorescein (FAM) and rhodamine (TAMRA) dye placed at a maximum distance inside perfectly stacking patches at the interface of interest (Figure 10). Two functional FRET-pairs were formed upon dimerization, and a decrease in donor emission was recorded. Initial monomer concentrations from ca. 10 to 38 nM were tested for AA- and BB-stacking at 30 °C, respectively, by adding a ten-fold excess of stacking staples (Figure 19a and b). The resulting FRET-curves revealed the kinetic course of the dimerization process for both interfaces and data evaluation was performed as described on page 36. In short, the initial linear slope of the curves indicates the association rates for each initial monomer concentration[198]. The initial association rate coefficient (k_a^{in}) can be derived as a metric of the interface association velocity at the examined temperature (30 °C) by plotting these rates versus the corresponding monomer concentrations.

Table 6 ***Initial dimerization rates***

init. monomer conc. [nM]	**9.86**	**19.46**	**28.79**	**37.88**
initial rate AA [nM min^{-1}]	0.65 ± 0.04	2.1 ± 0.1	3.36 ± 0.14	4.76 ± 0.26
initial rate BB [nM min^{-1}]	1.55 ± 0.06	3.73 ± 0.13	6.14 ± 0.16	11.02 ± 0.19

Surprisingly, the AA dimerization was slower than the BB dimerization by a factor of more than two (Table 6, Figure 19b and c), and the extracted apparent association rate coefficients (k_a^{in}) were 0.14 min^{-1} and 0.3 min^{-1} respectively (Figure 19c and d). Dimerization half-times (or the timepoint at which 50 % of the monomers were successfully stacked into dimers) (Figure 19e) decreased with rising initial monomer concentrations, and association rates increased. However, in contrast to the association rates, dimerization half-times did not follow a linear trend but reached a plateau at initial monomer concentrations of 20 nM. Half-times for AA-stacking were around 8 min, while BB-stacking took less than 4 min. Overall, the dimerization of two 5 MDa structures proceeded relatively fast at 30 °C. The standard-procedure for obtaining two-step dimers was performed at 40 °C and can therefore be expected to yield significantly higher association rates.

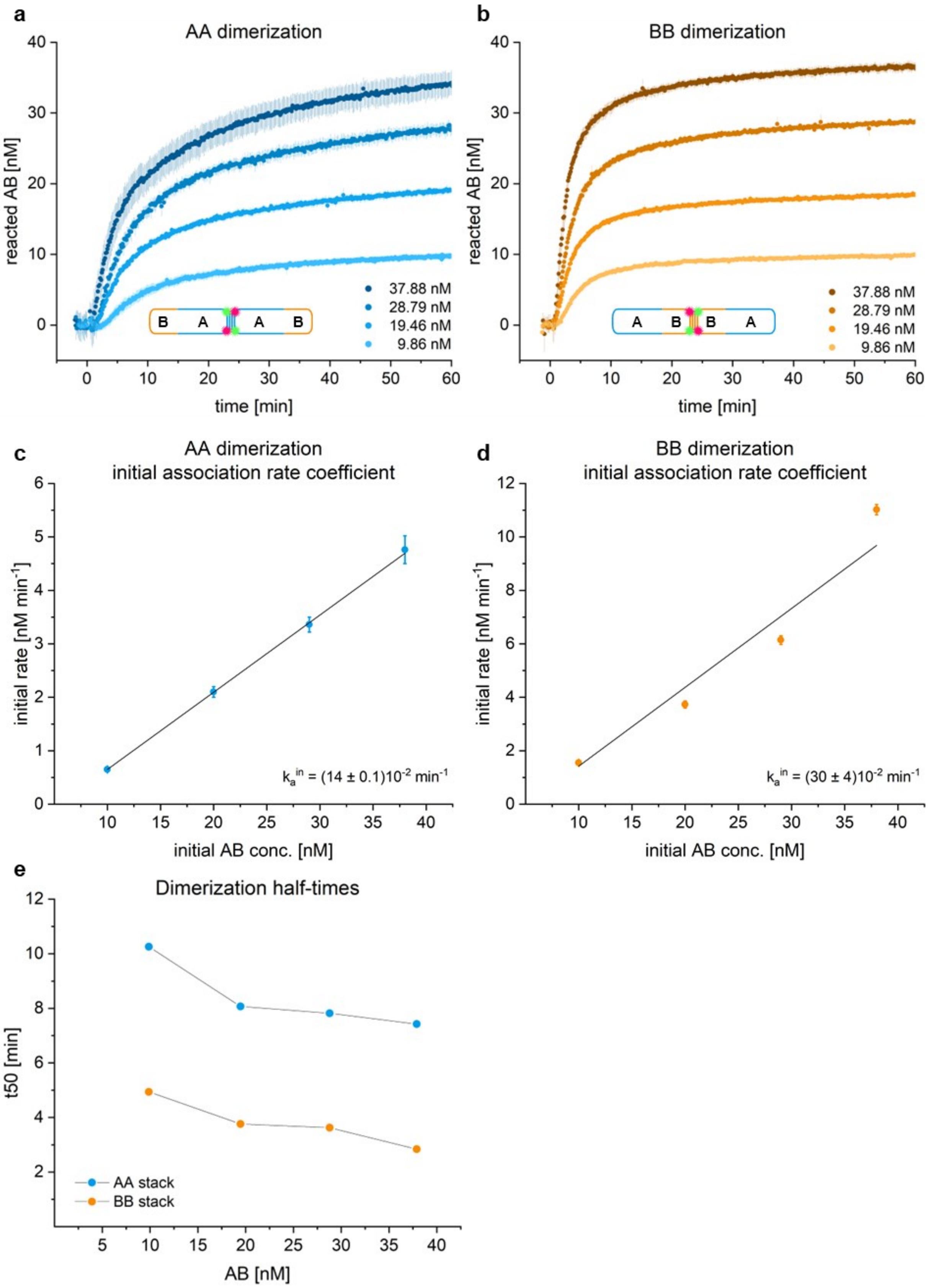

Figure 19 ***Monitoring dimer association by isothermal FRET analysis and DLS***
Concentration-dependent FRET kinetic curves for a) AA and b) BB isothermal association at 30 °C with initial concentration of pre-assembled monomer ranging from 10 to 38 nM. Linear fit of the early reaction revealed initial association rate coefficients (k_a^{in}) for the respective interfaces (c and d). e) Dimerization half-times in respect to the initial monomer concentration.

The interface disparity is essential when considering possible causes for the significantly differing AA and BB dimerization association rates. For the FRET experiments, only fully activated interfaces (A(16/8) and B(8/16)) were examined. One or two of the three eight-helix patches featured the 1 bp gap while being mutually shape-complementary otherwise. As discussed previously (pp. 46), sequence-specific theoretical stacking energies play a more important role in interface stability than in interface association, and the 1 bp gap has different impacts on association compared to dissociation. The sterically less demanding and arguably more flexible B-interface facilitated ABBA dimerization for the here-examined isothermal association.

Conclusion

The association of dimer interfaces is an excellent model to begin to understand the stacking behavior of the 24-helix bundle. Although the presence of eight or even 16 helices with a one base pair gap between the stacking helices complicates the system, significant progress has been made in understanding their implications on dimerization association and interface stability.

For the wholly activated interfaces, the assembly process, regardless of one- or two-step, yields a near 100 % conversion rate, which could be shown by AGE and AFM studies (Figure 12). For the examined 5 MDa structures, a dimerization association threshold for 24 activated helices between 55 °C and 60 °C could be identified by electrophoretic profiles (Figure 12c and d). This could be narrowed down to around 56.7 °C for BAAB dimers and 54.2 °C for ABBA dimers (Figure 13). Interface stability upon melting was increased by the formation of blunt end helices, even if gapped. The impact on interface melting was significantly larger than on interface association, leading to a considerably higher thermal hysteresis in BB constructs. It was previously observed that nucleotide gaps in a double helix could be compensated by directional bending and increased flexibility[39,201–203]. This phenomenon could also cause a distorted helical conformation at the gapped blunt ends.

The effect of additional gapped helices on association temperatures was buffered after a certain threshold with temperature depending on the individual interface and sequence-dependent stacking energies. For both interfaces, more than six activated blunt ends were required to successfully stack two 5 MDa monomers, while eight helices created a weak metastable stacking bond for a fraction of the origami.

The sequence-dependent stacking energy could also be demonstrated with single molecule force spectroscopy when comparing two otherwise identical dimers. In addition to sequence-dependent effects, the presence of the 1 bp gap impacted dimerization kinetics in a somewhat unexpected way. A surplus of gapped helices in the BB dimerization sped up the isothermal dimer association by more than two-fold compared to AA dimerization, although the A-interface displays a more precise isologous self-complementarity.

For future design approaches specifically addressing dimer association and dissociation kinetics, an energetic barrier might be introduced by adding 1 bp gaps to an otherwise shape-complementary interface. This design motif would decrease the association temperature while simultaneously speeding up the reaction velocity. Additionally, thermal stability upon heating would be almost comparable to a complete stack design. These findings could lead to more intricately designed DNA origami interactions.

The following chapter contains results from the article *Growth Rate and Thermal Properties of DNA Origami Filaments* by Stenke, LJ. and Saccà, B., published in ACS Nano Letters in 2022[1].

Polymerization

Interface Distribution of the randomly stacked Polymer

In contrast to the well-defined outcomes of the dimerization process, polymer equilibrium states are more challenging to characterize. For example, polymer length is influenced by a multitude of factors and is not easily measurable, nor are the interface associations apparent, particularly in the case of a randomly stacking polymer. A detailed kinetic characterization, however, requires certain presumptions, including the interface distribution in a randomly stacked polymer, so a statistical analysis of random stacking at equilibrium was conducted. For this purpose, ultrafiltration-purified (p. 29) monomers modified with eight protruding DNA oligonucleotides integrated into the A-side of the bundle were activated for random stacking and polymerized at 40 °C for 20 h. Subsequently, gold-nanoparticles coated with the complementary sequence were introduced and hybridized to the A-subdomain (Figure 20a). This enabled the identification of monomer orientation within the polymers imaged with TEM.

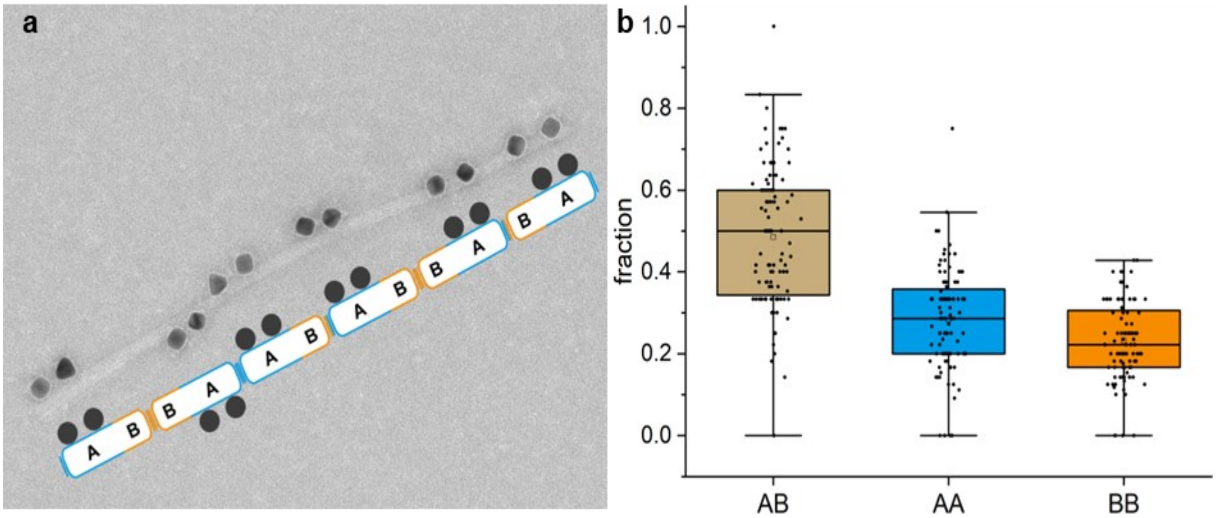

Figure 20 ***Random stacking distribution analysis***
a) The random interface association distribution was identified by labeling the DNA origami A subunit at random stacking polymerization equilibrium with two gold nanoparticles and subsequent TEM imaging. b) Evaluation of more than 80 images with over 900 stacking associations yielded a bond distribution with favored AB interactions, followed by AA interactions and BB interactions.

Table 7 ***Statistical distribution of random stacking populations***

	AB	**AA**	**BB**
fraction	0.49 ± 0.17	0.28 ± 0.12	0.23 ± 0.09
n	429	258	205
theor. stacking energy with 1 bp gap [kcal/mol]	-34.27	-17.78	-9.78
theor. stacking energy w.o. 1 bp gap [kcal/mol]	-34.27	-30.98	-35.8

892 bonds from more than 80 individual TEM images were analyzed (Table 7) and revealed a 49 % prevalence of the AB-interaction, followed by 28 % AA- and 23 % BB-stacking (Figure 20b). This observation also aligned well with the total number of gapped helices at the interface connections (Figure 9). With its perfectly matching complementarity, AB-stacking was the predominant equilibrium state, while BB-stacking and 16 helices presenting the 1 bp gap were the least abundant. Next to the interface shape-complementarity, sequence-dependent stacking energies must be considered to understand the equilibrium polymer configuration.

As discussed for the thermal profiles of the dimerization (pp. 46), the one base pair gap affected the initial assembly and the subsequent stability of the resulting interface stacking bond in distinct ways. A more substantial stabilizing effect on already established bonds was observed for the dimers, while the association was far less impacted. Here, the equilibrium product of the random stacking assembly was examined. Thus, the effect of the presence of the 1 bp gap could be assumed to be secondary compared to a perfectly stacking helix. Comparing the theoretical stacking energies when ignoring any effect of the 1 bp gap versus assuming a perfect stacking interaction (Table 7) confirms the underlying assumption. Ignoring the presence of the 1 bp gap yields a trend in theoretical stacking energy that follows the observed trend of interface association. Including the energetic contribution of all helices, gapped or not, yields inconsistent data, with BB-stacking being the most favorable bond, which was not the case here.

Activating isologous interfaces for dimer stacking enables the transition of one species (unbound monomer) to another species (dimer), while random stacking is open to three possible interface combinations (AB, AA, BB). Applying the Boltzmann distribution, as illustrated in detail in the methodology section on page 38, aids in deriving the stacking energies for the formation of the AB-, AA-, and BB-interfaces at temperature T. E_{AB} was found to be 0.71 k_BT, E_{AA} 1.27 k_BT, and E_{BB} 1.47 k_BT (at 40 °C: E_{AB}: 4.42 kcal/mol, E_{AA}: 7.9 kcal/mol, and E_{BB}: 9.15 kcal/mol). The obtained values were significantly lower than the stacking energies calculated from the sum of all perfectly stacking helices ($E_{AB(sum)} = -82\ k_BT$, $E_{AA(sum)} = -43\ k_BT$, and $E_{BB(sum)} = -26\ k_BT$). The calculated difference is profound and points to a divergence in calculation methods. Secondly, it suggests that some cooperativity effect might be in place when multiple helices stack, including those separated by a 1 bp gap, lowering the energy cost needed to establish the dimer bond. Thirdly, the gapped helices may affect the energy cost to establish the binding unit.

Critical Concentration Determination

A robust measure for the association and dissociation of monomers to a polymeric structure is the critical monomer concentration (c_{crit}). This is the concentration of monomers in equilibrium with the polymer. At $c > c_{crit}$, polymerization is favored; at $c < c_{crit}$, polymer dissociation is favored. Essentially, c_{crit} indicates the monomer concentration above which spontaneous polymerization occurs[204]. Reversing this concept by determining the concentration of free monomers and putting them in relation to the polymer-bound monomers at equilibrium will indicate the critical concentration. Unlike for biopolymers like F-actin[205] and microtubules, the here obtained value will combine the rates of both tips.

To estimate the c_{crit}, 100 µl of a 1 nM monomer solution in TEMg20 was polymerized using either hybridization or random stacking staples and allowed to reach equilibrium at temperatures and durations indicated in Table 8. On average, a monomer solution spread over a mica surface area of 100 µm^2 contained about 2315 ± 85.3 monomers as estimated from ten independently evaluated samples (Supplementary Figure 2). Imaging of the polymer samples was performed under identical conditions, and the critical concentrations were calculated by counting the number of monomers adsorbed on the mica surface and using the values obtained at 1 nM concentration as reference (Table 8, Figure 21).

Table 8 ***Critical concentration absolute numbers and concentration***

		hybridization			**random stacking**		
	ref.	**30 °C**	**35 °C**	**40 °C**	**30 °C**	**35 °C**	**40 °C**
time		16 h	12 h	8 h	3 h	2 h	1.5 h
total	2315 ± 85.3	258.1 ± 15.4	73.2 ± 12.9	24.1 ± 8.9	3.7 ± 1.3	7.5 ± 11.3	6.4 ± 3.6
c_{crit} [nM]	-	0.1115 ± 0.0067	0.0316 ± 0.0056	0.0104 ± 0.0038	0.0016 ± 0.0006	0.0032 ± 0.0049	0.0028 ± 0.0015

In contrast to cellular biopolymers with critical concentrations in the micromolar ranges[205,206], all tested polymers revealed critical concentrations in the picomolar ranges (c_{crit} depicted in nM to put in better relation to the working range of monomer concentration). For the random stacking, obtained critical concentrations were relatively consistent, even with increasing temperatures. c_{crit} ranged between 0.0032 ± 0.0049 nM and 0.0016 ± 0.0006 nM, with just a negligible fraction of monomers being unbound. For hybridization, the observed critical concentration was temperature-dependent with c_{crit} = 0.1115 ± 0.0067 nM at 30 °C and about a ten-fold decrease to 0.0104 ± 0.0038 nM at 40 °C. Interestingly, the critical concentration of actin polymers from 10 °C to 35 °C was nearly constant[207]. Generally, c_{crit} was noticeably higher for hybridization than random stacking, likely due to the different underlying mechanisms and the necessary staple displacement for hybridization.

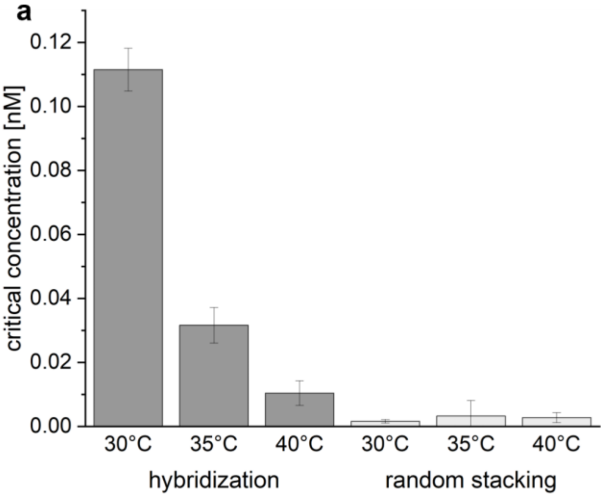

Figure 21 ***Critical concentration of hybridization and random stacking***
Critical concentration as determined from unbound monomers at different equilibrium conditions in relation to a monomer reference. Polymers obtained from hybridization (dark grey) and random stacking (light grey) activation were elongated at 30 °C, 35 °C, and 40 °C and imaged with AFM in air.

A possible reason for the extremely low values of critical monomer concentration measured might be the fact that monomer-to-monomer associations are almost irreversible. Furthermore, surface-dependent effects cannot be excluded, with adsorption and electrostatic interactions acting differently on monomers and polymers.

A general observation for all AFM experiments on polymers was that the surface coverage of µm-long filaments did not correspond to the expected coverage from the same concentration of unpolymerized monomers. Occasionally, massive local clusters of interconnected polymers could be identified (Supplementary Figure 10a). However, free monomers and short oligomeric structures were evenly distributed, enabling the statistical analysis of monomer distributions.

Initial Length Distribution of Hybridization and Random Stacking Polymers

The increase in polymer clustering at longer polymer lengths makes the statistical analysis of the sample at equilibrium difficult and error-prone, firstly by obscuring polymer pathways within the clusters and secondly by decreasing the chances of finding structures by AFM imaging. As the effect gradually worsens during the polymerization process, particularly for longer filaments, only initial polymerization time points were analyzed and taken as indicative of polymer length in the initial phase of the reaction.

The polymer length distribution over time for the different reaction types could be monitored by incubating a 1 nM monomer sample in TEMg20 at 40 °C with a ten-fold excess of polymerization staples for hybridization (Figure 22a - d) or random stacking (Figure 22e - h). The reaction was stopped by immersion into liquid nitrogen at time points ranging from 1 min to 1 h and even up to 20 h (Supplementary Figure 3). After the samples were carefully thawed on ice to inhibit further reaction, eight to ten AFM measurements in air were recorded per sample for statistical analysis with the AnalyzeSkeleton ImageJ Plugin[188]. The so obtained bar graphs and a corresponding representative image for 1 min, 5 min, 30 min, and 1 h are shown in Figure 22. After 1 h reaction, structural clustering prevented reliable analysis of further time points as the amount of sample homogeneously spreading over the mica surface decreased (Supplementary Figure 3 shows exemplary AFM images of hybridization and random stacking equilibrium and corresponding uneven sample distribution).

For polymerization based on the hybridization mechanism, the length distribution exhibited a large majority of monomers within the first five minutes and a slowly but steadily increasing oligomer length of up to 500 nm within the first hour. The random stacking yielded noticeable oligomers of up to 1.5 µm within the first minute of the polymerization reaction, where the hybridization length distribution was more than four times shorter. Within the first hour of the random stacking polymerization, filament lengths reached up to 2.4 µm or 24 monomers. Monomers were rarely observable, corresponding well to the near-negligible critical concentration discussed previously (p. 63).

For hybridization, the initial length distribution slowly but steadily shifted to a mixture of short oligomers, including up to four or five monomers per filament and a large population of monomers and dimers. Comparing 30 min to 1 h time-points revealed that polymer growth mostly occurred at pre-formed short oligomers, with rare elongation events at monomeric sites. A close look at random stacking revealed a first association of monomers into short oligomers, which in turn self-associated into higher-order filaments. From these observations, the polymerization of the origami bundle cannot be explained according to the linear condensation mechanism[146,208,209]. Indeed, this polymerization mechanism states that there is an equal likelihood for interfaces to react with each other regardless of monomer, oligomer, or polymer origin. Therefore, shorter oligomers are most common in the polymer length distribution. With a demonstrated negligible amount of monomers at equilibrium (Figure 21) and an early shift to higher-order structures, this distribution is unlikely for the origami bundle polymerization. The rate of stacking polymerization, as observed from the initial reaction, is significantly higher than for hybridization. Nevertheless, a more detailed understanding of the underlying mechanisms could be achieved by examining the complete polymerization length distribution from the start to the equilibrium, as described in Pfeifer et al.[136]. Unfortunately, dissolving the occurring clusters would consequently manipulate the observed length distribution due to shear forces.

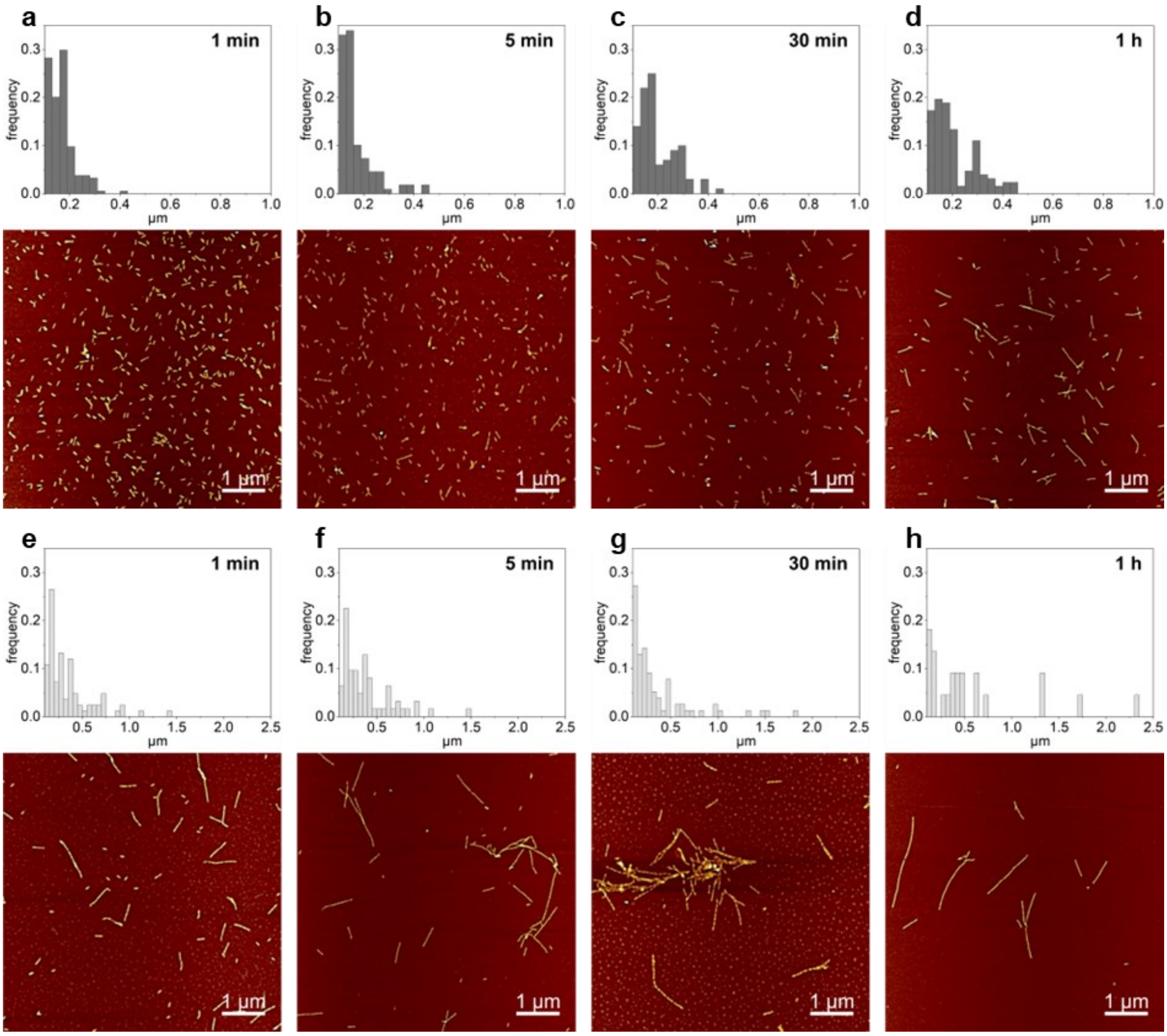

Figure 22 ***Length distribution of hybridization and random stacking over time***
Time course monitoring of different reaction types after inducing a 1 nM monomer sample in TEMg20 at 40 °C with a ten-fold excess of polymerization staples, either for a - d) hybridization or e - h) random stacking and stopping the polymerization at indicated time points (1 min to 1 h) by insertion in liquid nitrogen. Samples were thawed on ice, and AFM imaged in air. Up to ten measurements were statistically evaluated to obtain length distributions shown in bar graphs.

Polymerization Live-View

Cellular protein-based supramolecular assemblies such as F-actin or microtubules rely on non-covalent bonds between connected units, while most chemically derived polymers are connected through covalent bonding[147,210]. Classical synthetic polymerization can be approximated with three models based on the degree of conversion in relation to the molecular weight of the growing polymers. The mechanisms are called step growth (see also linear condensation p. 65), living chain growth, and chain growth[211,212]. However, in chemistry and biology, matters are usually more complex than the models developed to describe them. For the polymerization of globular proteins into quasi-one-dimensional filaments, the idealized polymerization mechanism is described with the nucleation-elongation chain growth[210], and programmable tile-to-tile binding follows a nucleation and growth mechanism[213].

Polymers derived from DNA origami subunits, and a representative of the supramolecular polymer approach, display features that are midway between cellular and chemical filaments. It is crucial to understand more about the underlying mechanisms. So what would be more suitable than observing the reaction directly? Therefore, a protocol for FastScan AFM imaging in fluid was established to balance DNA origami adhesion to the mica surface with a certain degree of structure mobility to enable reliable scanning of the polymerization process. As divalent cations, such as the commonly used magnesium, mediate strong adhesion interactions between the DNA molecules and the mica surface, monovalent cations were added to the buffer to perturb adhesion forces slightly. Sodium chloride has already been reported to increase the surface mobility of 2D DNA origami structures imaged by AFM[189–192]. So far, most studies reported the use of TAE buffers with either 10 mM or 12.5 mM $MgCl_2$, while NaCl concentrations varied broadly from 25 mM up to 700 mM, with experimental setups similarly targeting the alignment of 2D origami mediated either by symmetry or blunt end stacking.

High NaCl concentrations (TEMg12.5 + 500 mM NaCl) increased the surface mobility of the 24-helix bundle monomers to a point where no height profiles could be recorded with PeakForce tapping at 32 s/frame (256 samples/line). In contrast to the flat 2D origami structures typically used in similar experiments, the 24-helix bundle is based on a 3D honeycomb design which generally reduces the volume-to-surface ratio. The shape of the monomer must therefore be considered when searching for the right compromise between stable adhesion and sufficient mobility. Previous characterization of the polymerization equilibrium products revealed higher yields for TEMg buffer with 20 mM $MgCl_2$ (TEMg20)[136]. Hence, different TEMg20 buffers, containing decreasing NaCl concentrations from 500 mM to 25 mM, were screened for ideal imaging conditions, and TEMg20 with an added 50 mM NaCl was found suitable at room temperature.

Polymerization processes of $(AB)_n$ (Figure 23) and $(AB)_{rand}$ (Figure 24) from 3 nM monomer, as well as $(ABBA)_n$ (Supplementary Figure 5) and $(BAAB)_n$ (Supplementary Figure 6) from 2 nM of the respective dimers, were recorded for several hours each. Polymers formed by hybridization initially exhibited a relatively flexible subunit assembly and became more rigid over time. This is most likely due to a small number of helices initially displacing their corresponding isologous staples. Once two subunits are partially bound, further staple displacement and binding of the remaining helices is facilitated by spatial proximity. The white arrows in Figure 23 mark the binding and progression of at least three short oligomers into one polymer. After three hours of polymerization, the observed length distribution was quite heterogenous with few long polymers and a variety of oligomers and monomers.

The white arrows in Figure 24 also point out the formation of a filament from several subunits for random stacking. In contrast to hybridization polymerization, stacked filaments do not demonstrate much flexibility and reveal a more homogenous length distribution after three and five hours. As observed for the initial length distribution (Figure 22), stacked filaments quickly surpassed the hybridization filaments in length, although no structures significantly longer than 1 µm could be observed under surface-assisted assembly conditions. It should be noted that the length or area in contact with the mica surface heavily influences the migration of the structures. The initial salt conditions were optimized to enable monomer migration but only allowed for little movement of larger structures, impeding the growth of long filaments.

In contrast to hybridization assemblies, successful stacking does not require strand displacement, facilitating the initial association. Similar to hybridization, many initial dissociation events were observed, and two explanations for these observations are equally likely. As staples activating stacking were introduced in a ten-fold excess, an approximately simultaneous binding to most of the 24 helices could be assumed. Therefore, dissociation events could be due to interfaces aligning off their favorable symmetry. If only a few helices initially get activated for stacking, though, the weak interaction forces alone would be sufficient to disturb some initial binding events.

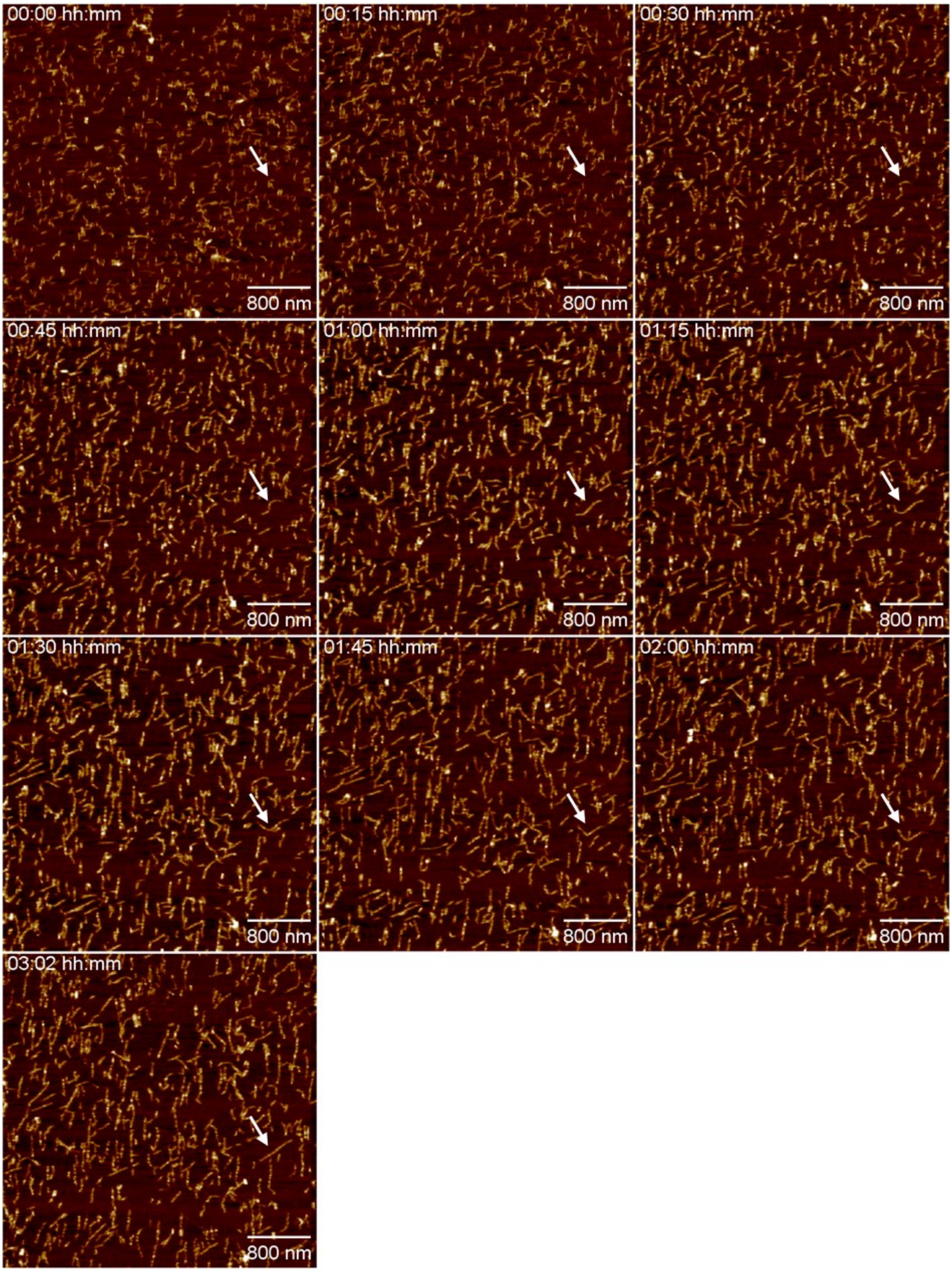

Figure 23 ***Time-lapse of hybridization polymerization over 3 h***
Mica surface-assisted hybridization polymerization of 3 nM monomer in TEMg20 + 50 mM $NaCl_2$ at room temperature captured at a rate of one frame per 32 seconds with 256 samples/line in PeakForce Fast Tapping mode with PEAKFORCE-HIRS-F-A probe at a 200 mV drive amplitude. The white arrow traces exemplary polymer formation from several short oligomers over all frames.

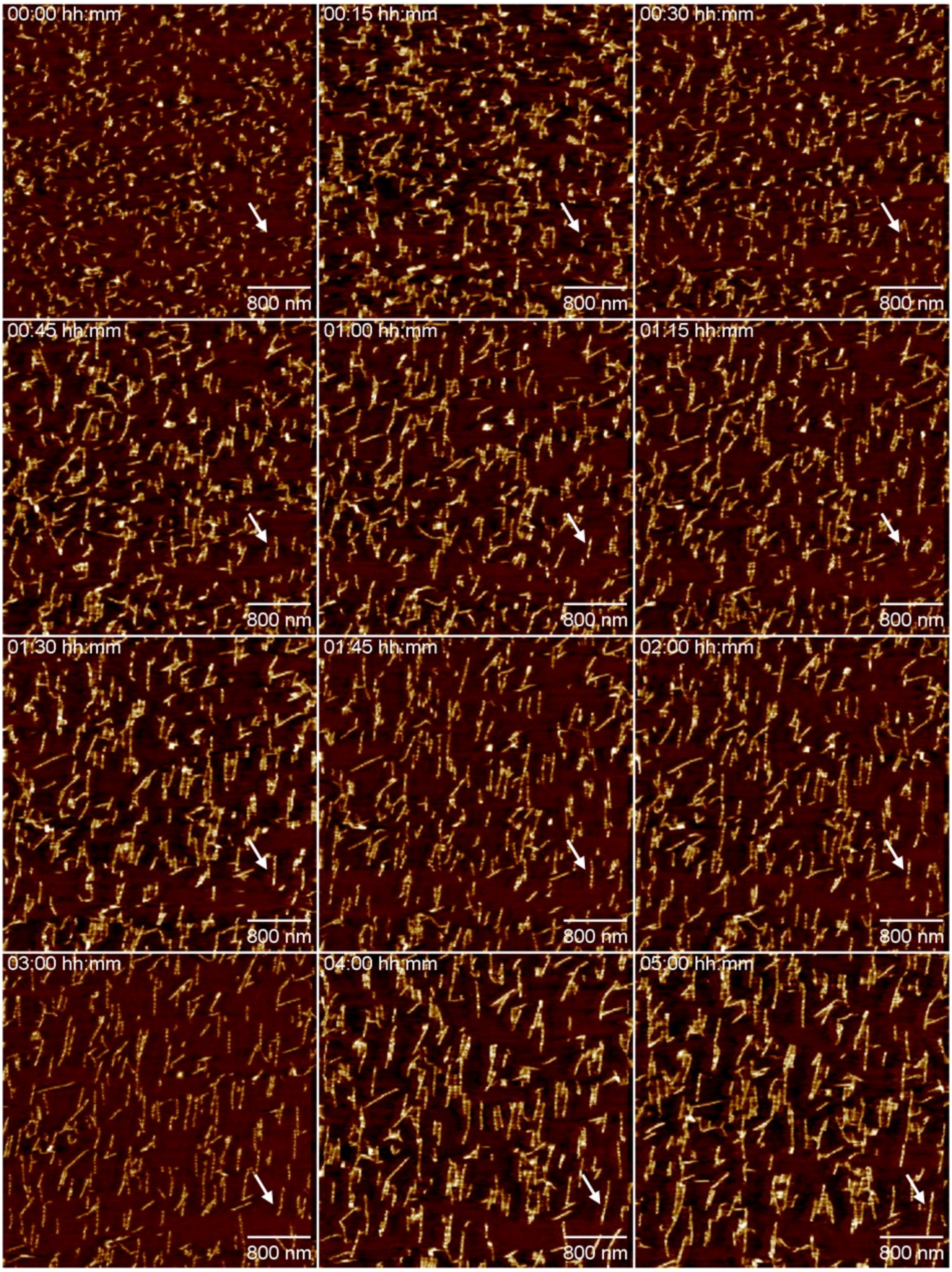

Figure 24 ***Time-lapse of random stacking polymerization over 5 h***
Mica surface-assisted random stacking polymerization of 3 nM monomer in TEMg20 + 50 mM $NaCl_2$ at room temperature captured at a rate of one frame per 32 seconds with 256 samples/line in PeakForce Fast Tapping mode with PEAKFORCE-HIRS-F-A probe at a 200 mV drive amplitude. The white arrow traces exemplary polymer formation from several short oligomers over all frames.

Thermal Properties of DNA Origami Polymers

To further characterize the two dominant polymerization mechanisms, the melting profiles of pre-assembled polymers were recorded for polymers obtained by random stacking and for polymers derived by the head-to-tail hybridization of the individual monomers (Figure 25a). For the random stacking thermal analysis, four assays were used to examine each of the individual interface associations (AB, AA, and BB) and the simultaneous association of all interfaces (Figure 10). Melting temperatures at $\theta = 0.5$ ($T_{0.5}$) and at $d^2\theta / dT^2 = 0$ (T_m) can be found in Table 9. Compared to random stacking, hybridization filament melting temperatures were 2.3 °C ($T_{0.5}$) or 2.5 °C (T_m) higher than the most stable stacking configuration with a distinct right-shift of the FRET curve (Figure 25a, grey curve). These findings illustrate a structurally more stable hybridization polymer chain at equilibrium, despite its formation pathway being kinetically disfavored.

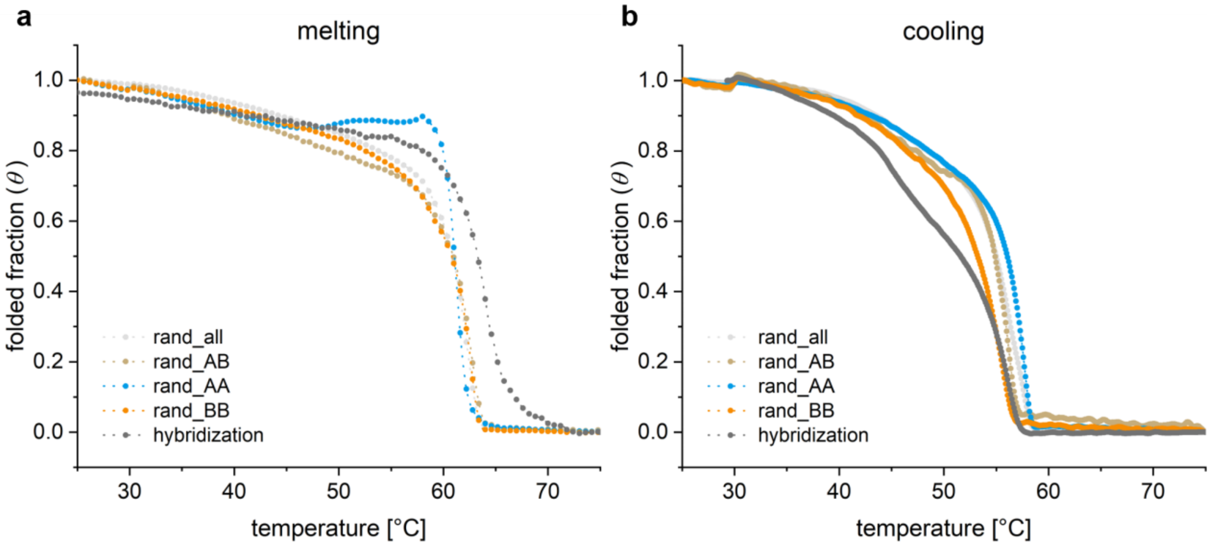

Figure 25 ***FRET profiles of DNA origami filaments***

Thermal melting and cooling profiles of global random stacking (rand_all) and individual interface combinations (rand_AB, rand_AA, rand_BB) and hybridization polymers. a) Melting with a rate of +0.1 °C/min from 25 °C to 75 °C was performed on polymers pre-assembled from 50 nM monomer and a two-fold excess of fluorophores at 40 °C for 20 h in aliquots already placed into PCR-plates. b) Cooling profiles were obtained from the same concentrations of the unassembled scaffold, core, and polymerization staples and fluorophores with -0.1 °C/min from 75 °C to 25 °C. FAM emissions were recorded, and calculated FRET efficiency normalized for better comparison.

Considering the $T_{0.5}$, no noticeable difference between the four stacking types could be found. The T_m, however, revealed the AB association (Figure 25a, beige curve) to be thermally the most stable of the stacking combinations. As AB dominates the global random stacking association (Figure 20b) due to its perfectly fitting helical patches, it is unsurprising to identify it as thermally the most stable. With 49 % of the observed stacking bonds being AB, its T_m of 62.5 °C self-evidently revealed a significant influence on global random stacking stability with a T_m of 62.3 °C. The thermal stability of the remaining AA and BB pairings did not differ noticeably, with a T_m of 61.1 °C respectively and a 0.3 °C difference favoring AA in $T_{0.5}$. In contrast to the dimer findings, BB-stacking in random filaments was not thermally more stable than the AA association. Stacking at the AA-interface (Figure 25a, blue curve) demonstrated a rather steep decrease in FRET efficiency around the melting point, indicating a rapid disassembly of the interface in the polymer compared to the more sigmoidal trajectories of other interface combinations.

Table 9 ***$T_{0.5}$ and T_m of thermal polymer profiles***

interface	**melting [°C]**		**cooling [°C]**	
	$T_{0.5}$	**T_m**	**$T_{0.5}$**	**T_m**
rand_all	60.9	62.3	55.0	57.5
rand_AB	60.9	62.5	54.9	56.2
rand_AA	61.0	61.1	56.1	57.7
rand_BB	60.7	61.1	53.2	55.7
hybridization	63.3	65.0	51.6	56.0

Additionally, cooling profiles of polymer assembly over a thermal gradient directly after filament melting were examined (Figure 25b). Due to the suboptimal temperature profile for polymerization (short temperature phase around 40 °C), fewer association events could be recorded, resulting in lower E_{FRET} values as compared to the isothermal assemblies. The hybridization cooling curve exhibited the lowest association temperature with $T_{0.5}$ = 51.6 °C. Like the dimerization thermal profiles, BB-stacking revealed the most considerable extent of hysteresis and the lowest association temperature of $T_{0.5}$ = 53.2 °C and T_m = 55.7 °C. Surprisingly, AB-stacking had the second lowest association temperature ($T_{0.5}$ = 54.9 °C, T_m = 56.2 °C). As previously postulated for the dimeric bonds, a higher number of perfectly stacking helices introduces sterical barriers for interface formation due to the multitude of helices that need to fit together. AA association in filament formation hits the sweet spot with 16 perfectly stacking helices that stabilize the association while minimizing sterical hindrances. Comparing the final association distributions of the thermal gradient to the isothermal assemblies might be interesting. Based on association temperatures, the results might differ, offering more pathways for controlling filament formation.

Kinetic Characterization of isothermal Filament Formation

To quantify the monomer and dimer association rates into different types of DNA origami filaments, the FRET strategy described in Figure 10 was applied to monitor seven different types of interface associations (Figure 11). Three assays monitored the formation of the periodic $(AB)_n$, $(ABBA)_n$, and $(BAAB)_n$ polymers in a head-to-tail, head-to-head, and tail-to-tail association. The remaining assays were applied to study the global random stacking association and its individual interface combinations AB, AA, and BB within the $(AB)_{rand}$ polymer. Isothermal experiments at 30 °C, 35 °C, and 40 °C were conducted for a range of monomer and dimer concentrations to obtain the initial reaction rate, initial association rate coefficient (k_a^{in}), and ultimately the energetic barrier (E_{act}). Detailed information on the underlying data analysis process can be found on page 36.

Table 10 ***Initial association rate coefficients (k_a^{in} in min^{-1}) for 30 °C, 35 °C, and 40 °C polymerization and activation energies (E_{act} in kcal mol^{-1}) for initial linear polymerization phase of varying interface combinations and association types***

T [°C]	$(AB)_n$ hybr	rand_all	rand_AB	rand_AA	rand_BB	$(ABBA)_n$	$(BAAB)_n$
30	0.029 ± 0.001	0.18 ± 0.01	0.17 ± 0.01	0.11 ± 0.01	0.32 ± 0.03	0.17 ± 0.01	0.37 ± 0.02
35	0.052 ± 0.004	0.26 ± 0.01	0.27 ± 0.01	0.17 ± 0.01	0.35 ± 0.04	0.27 ± 0.01	0.52 ± 0.04
40	0.067 ± 0.005	0.42 ± 0.02	0.49 ± 0.01	0.24 ± 0.02	0.44 ± 0.02	0.43 ± 0.02	0.65 ± 0.04
E_{act}	15.6 ± 3	16 ± 1	20 ± 2	15 ±1	6.1 ± 0.1	17.3 ± 0.3	11 ± 1

The $(AB)_n$ filament derived from base hybridization (Figure 27) revealed minimal k_a^{in} values that were five to 13-fold lower compared to polymers obtained from base stacking. Initial reaction rates ranged from 0.74 pM s^{-1} for 5 nM initial monomer at 30 °C to 40.72 pM s^{-1} for 35 nM monomer at 40 °C. The resulting association rate coefficients k_a^{in} are summarized in Table 10 and Figure 26a and vary from 0.03 min^{-1}

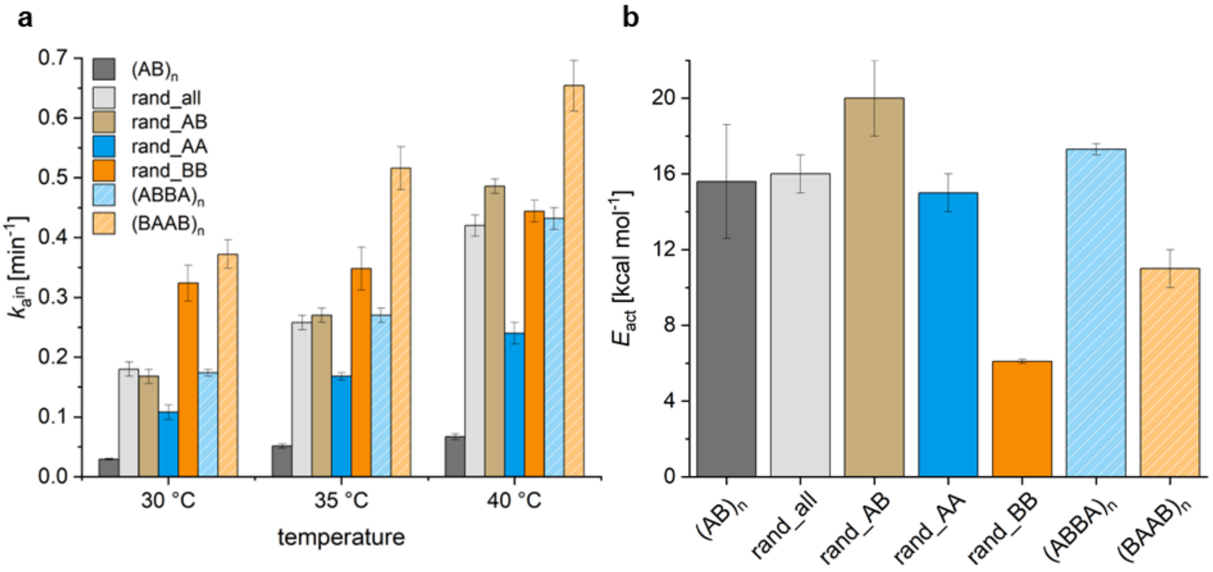

Figure 26 ***Kinetic parameters of DNA origami filament growth***
a) Initial association rate coefficients (k_a^{in}) for the initial linear phase of polymerization reactions for different interface and mechanism combinations at 30 °C, 35 °C, and 40 °C derived from Figure 27 to Figure 33. Solid colors mark monomeric polymer origin, while striped bars show filament data derived from dimers. b) Temperature-dependence of k_a^{in} was transformed into activation energies (E_{act}) by applying Arrhenius' equation.

to 0.07 min^{-1} for hybridization cumulating in an activation energy of 15.6 kcal mol^{-1} (Figure 26b). The E_{act} of all combined and weighted random stacking associations was in a similar range of 16 kcal mol^{-1} but with significantly higher initial growth rates between 9.56 pM s^{-1} for 5 nM at 30 °C and 223.43 pM s^{-1} for 35 nM at 40 °C (Figure 28). The resulting initial association rate coefficients of 0.18 min^{-1} (30 °C) to 0.42 min^{-1} (40 °C) were also five to six times greater than those observed for hybridization-based polymers.

Regarding the individual association types within the random stacking reaction, the observed FRET curves were normalized to the individual equilibrium interface distributions previously examined (Figure 20). Therefore, single initial growth rates could not be compared, but the obtained association rate coefficients are a good indicator of the temperature dependence of the initial polymerization reaction. At 30 °C, BB-stacking (Figure 31) exhibited the highest association rate coefficient of 0.32 min$^{-1,}$ which was about twice as high as for the perfectly aligning AB-stacking (Figure 29) with 0.17 min^{-1}, while initial AA-stacking (Figure 30) was the slowest with 0.11 min^{-1}.

An increase in reaction temperature to 40 °C had the most substantial impact on AB association to a k_a^{in} of 0.49 min^{-1} and a 2.88-fold increase. AA-stacking with eight gapped helices demonstrated a mediocre k_a^{in} increase of 2.12-fold to 0.24 min^{-1} while being the slowest of all examined stacking types. BB-stacking association rate coefficient only slightly increased by 37.5 % to 0.44 min^{-1} at 40 °C. The temperature dependence of the random stacking association of the monomer is correlated to the corresponding interface shape-complementarity. For the perfectly matching AB-stacking, the high number of helices required to associate present an initial energetic barrier that can be overcome at higher temperatures, ensuing in the highest observed activation energy of 20 kcal mol^{-1}. With 16 out of 24 helices perfectly matching and eight helices with a 1 bp gap, the AA association exhibited an E_{act} of 15 kcal mol^{-1}, followed by 6.1 kcal mol^{-1} for BB-stacking with only eight perfectly matching helices. The BB-interface association within the randomly stacked $(AB)_{rand}$ filament simultaneously represents the association type with the lowest observed activation energy. The global random stacking activation energy of 16 kcal mol^{-1} naturally comprises a weighted mean of all three incorporated association types.

The highest association rate coefficient at all observed temperatures could be found for the BB association of BAAB dimer tips into ordered $(BAAB)_n$ filaments (Figure 33) with k_a^{in} ranging from 0.37 to 0.65 min^{-1}. Interestingly, high initial monomer concentrations at high temperatures demonstrated a noticeable FRET decrease after the initial association toward equilibrium. This phenomenon could not be recognized for the almost two-fold slower dimer AA association into $(ABBA)_n$ filaments (Figure 32). While k_a^{in} only ranged from 0.17 to 0.43 min^{-1}, assembled filaments ultimately revealed higher long-term stability.

Dimers associated faster than corresponding monomer interfaces observed in random stacking by about 50 %. In contrast to the three simultaneously available association types present in the random stacking (AB, AA, and BB), the monovalent tip type presented at the dimer interfaces only leads to one possible stacking pathway, reducing dissociation events due to binding competition. As expected for building units having double the molecular weight of the monomer 24-helix bundle and presumably a lower mobility, the effect of increased temperatures on k_a^{in} was more distinct. Therefore, both polymer types originating from dimers had a slightly higher activation energy of 17.3 and 11 kcal mol^{-1} for $(ABBA)_n$ and $(BAAB)_n$, respectively. The overall trend already observed for the AA and BB associations was maintained.

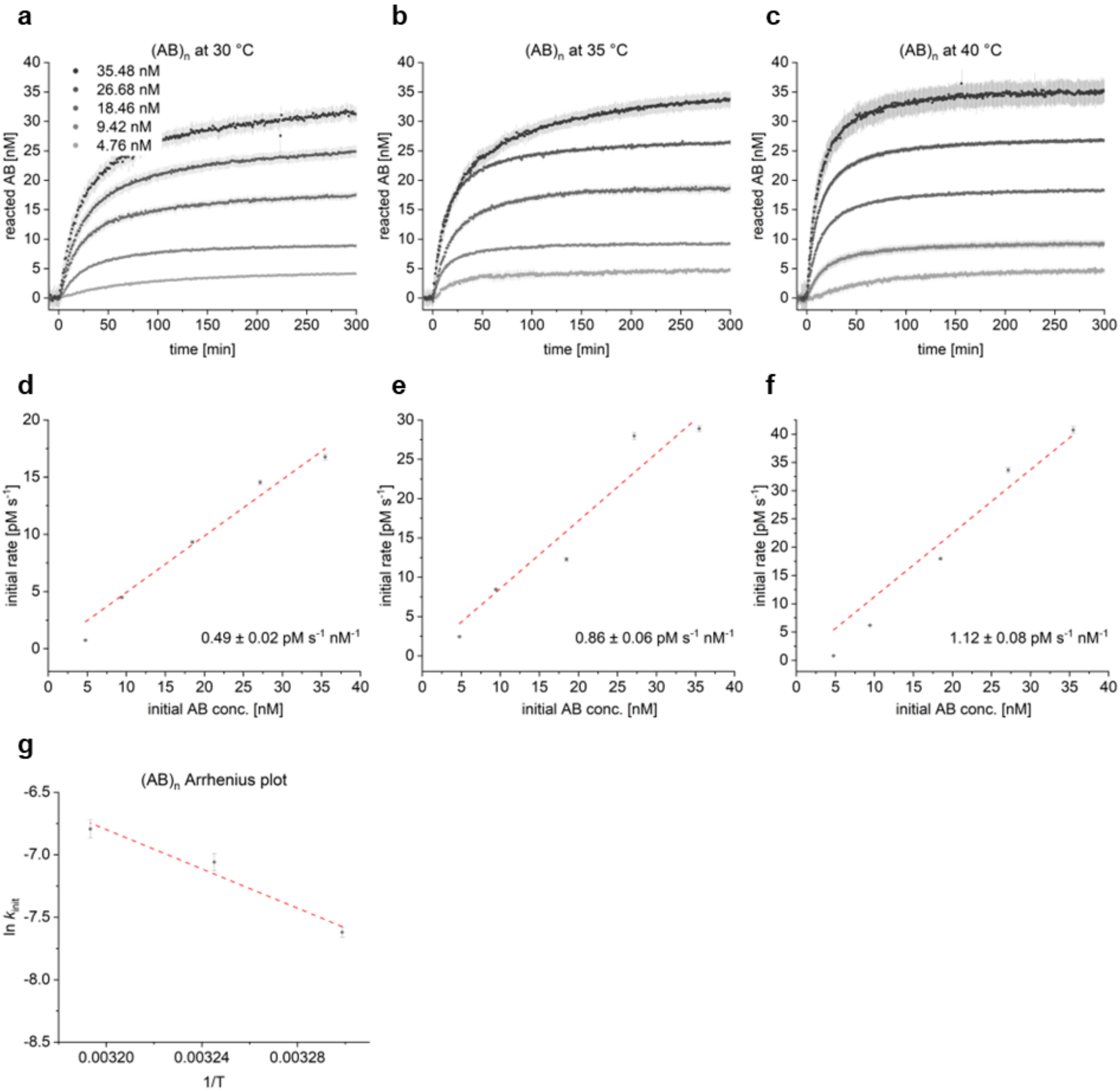

Figure 27 ***Isothermal hybridization polymerization***

Isothermal filament formation of the hybridization polymerization at 30 °C (a), 35 °C (b), and 40 °C (c) with varying initial monomer concentrations ranging from 5 to 35 nM. Reactions were initialized by adding ten-fold excess of polymerization staples to the pre-heated samples, and FAM emission of the associated FRET pair was recorded until equilibrium was reached after 8 to 16 hours. The initial linear fit of FRET curves yielded the initial reaction rates for the corresponding monomer concentrations at the given temperatures. Linear dependence on initial monomer concentration yielded the association rate coefficients (k_a^{in}) (d - f), and by applying the Arrhenius equation, the activation energy for the hybridization polymerization mechanism of 15.6 ± 3 kcal mol^{-1} could be calculated (g).

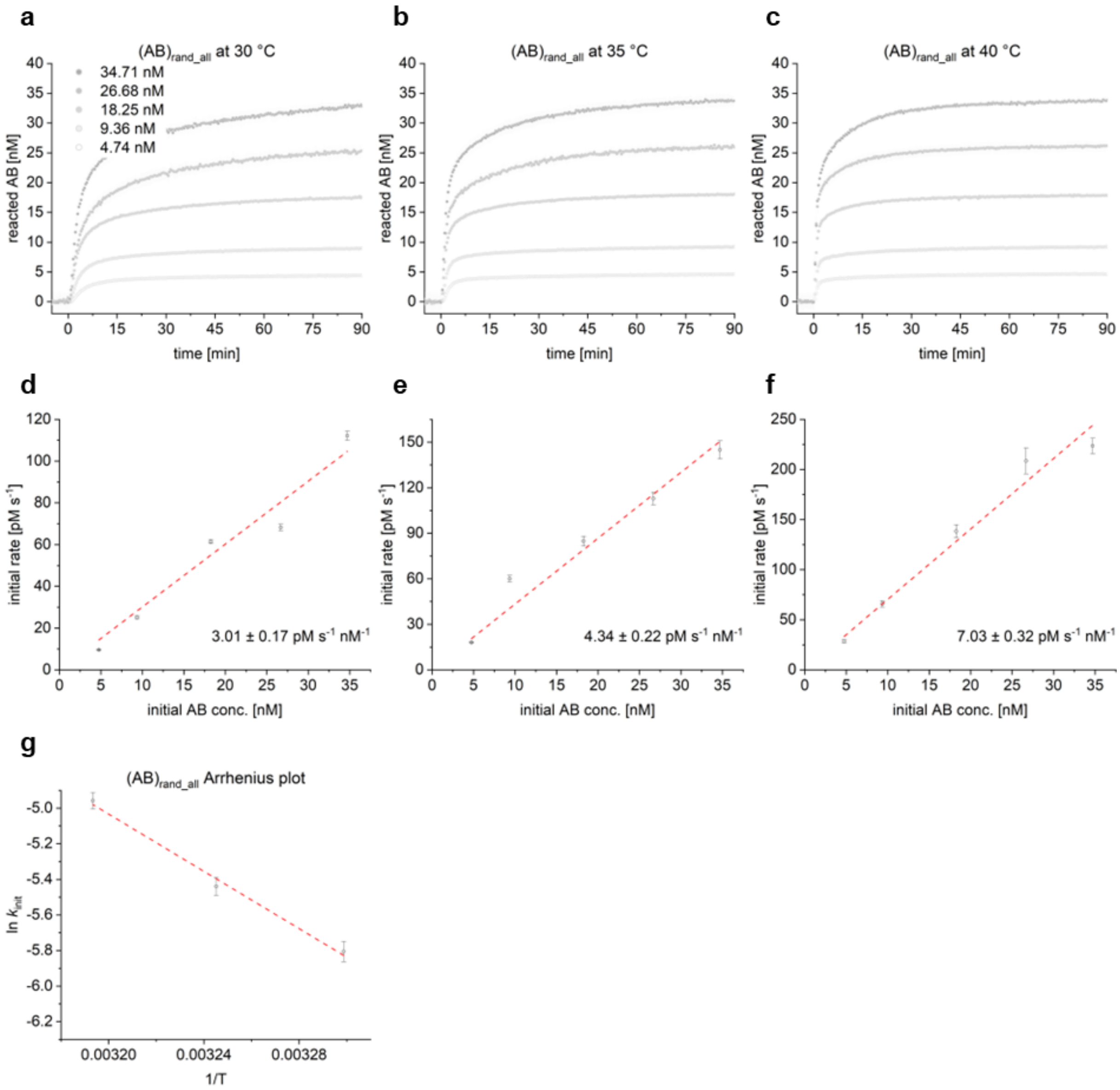

Figure 28 ***Isothermal global random stacking polymerization***

Isothermal filament formation of the global random stacking polymerization $(AB)_{rand\_all}$ at 30 °C (a), 35 °C (b), and 40 °C (c) with varying initial monomer concentrations ranging from 5 to 35 nM. Reactions were initialized by adding ten-fold excess of polymerization staples to the pre-heated samples, and FAM emission of the associated FRET pair was recorded until equilibrium was reached after 1.5 to 3 hours. The initial linear fit of FRET curves yielded the initial reaction rates for the corresponding monomer concentrations at the given temperatures. Linear dependence on initial monomer concentration yielded the association rate coefficients (k_a^{in}) (d - f), and by applying the Arrhenius equation, the activation energy for the global random stacking polymerization mechanism of 16 ± 1 kcal mol^{-1} could be calculated (g).

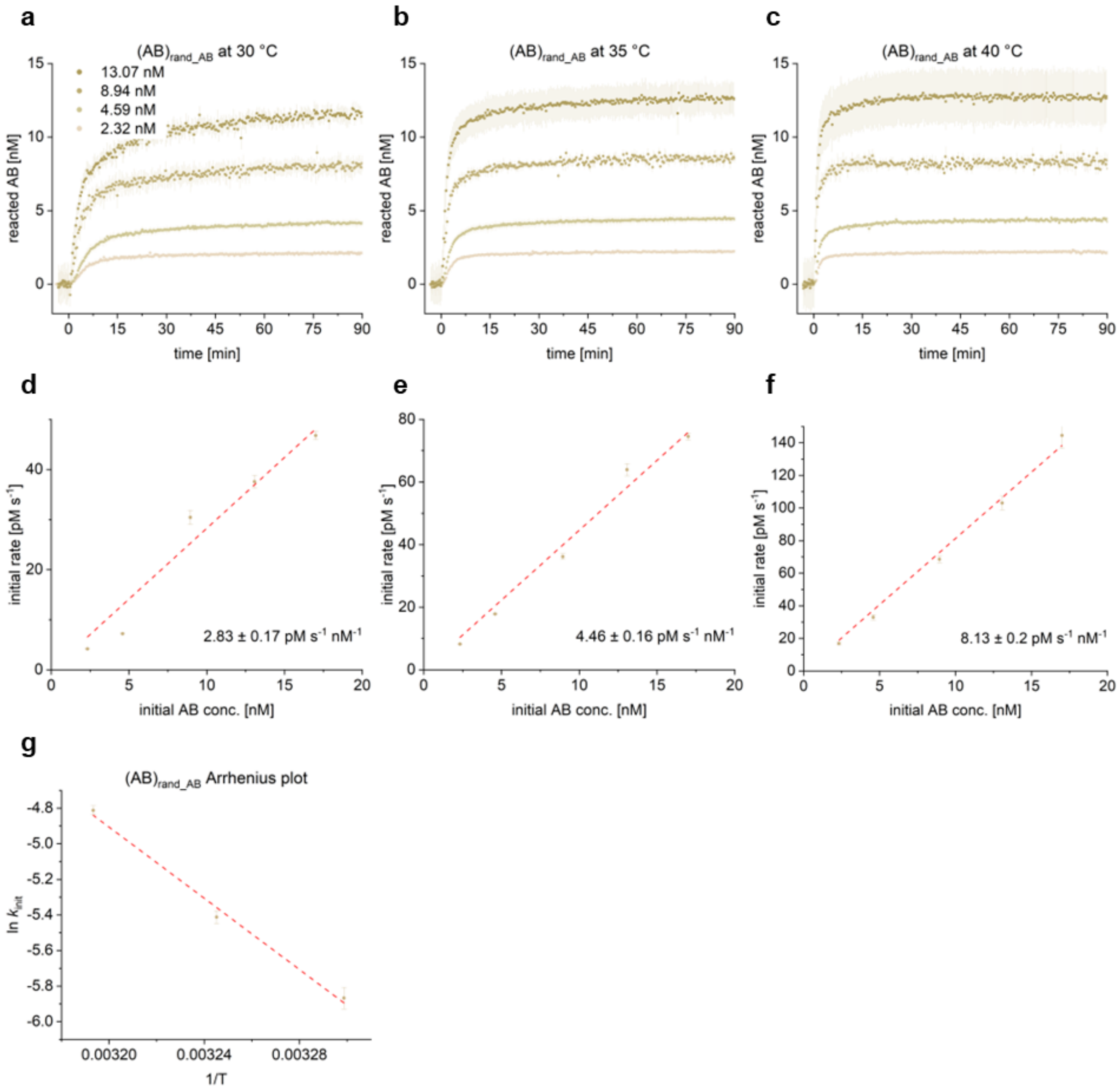

Figure 29 ***Isothermal AB association of random stacking polymerization***
Isothermal filament formation of the AB random stacking polymerization $(AB)_{rand\_AB}$ at 30 °C (a), 35 °C (b), and 40 °C (c) with varying initial monomer concentrations ranging from 5 to 35 nM with effective concentrations ranging from 2 to 13 nM based on Figure 13. Reactions were initialized by adding ten-fold excess of polymerization staples to the pre-heated samples, and FAM emission of the associated FRET pair was recorded until equilibrium was reached after 1.5 to 3 hours. The initial linear fit of FRET curves yielded the initial reaction rates for the corresponding monomer concentrations at the given temperatures. Linear dependence on initial monomer concentration yielded the association rate coefficients (k_a^{in}) (d - f), and by applying the Arrhenius equation, the activation energy for the AB random stacking polymerization mechanism of 20 ± 2 kcal mol^{-1} could be calculated (g).

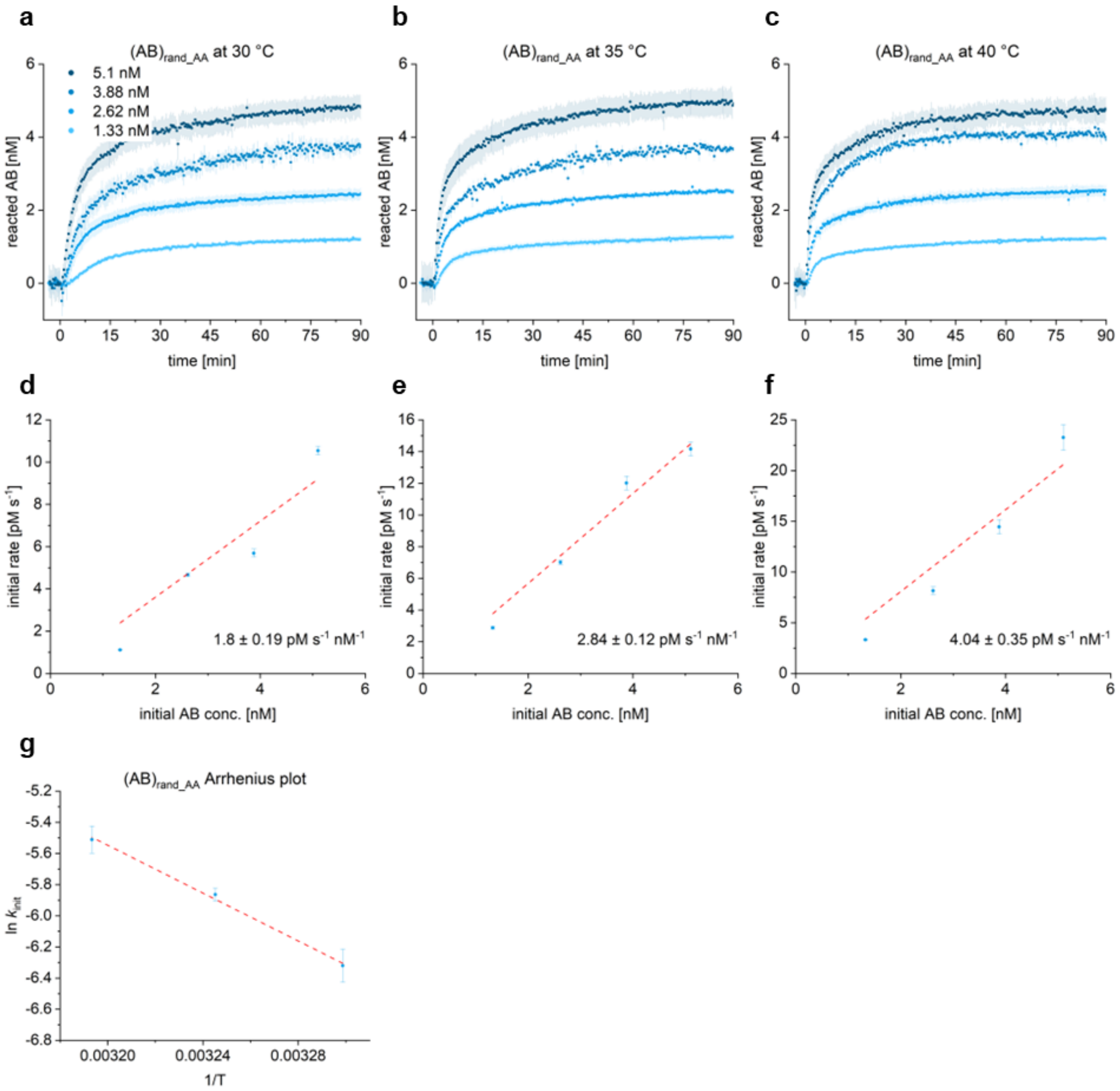

Figure 30 ***Isothermal AA association of random stacking polymerization***
Isothermal filament formation of the AA random stacking polymerization $(AB)_{rand\_AA}$ *at 30 °C (a), 35 °C (b), and 40 °C (c) with varying initial monomer concentrations ranging from 5 to 35 nM with effective concentrations ranging from 1 to 5 nM based on Figure 13. Reactions were initialized by adding ten-fold excess of polymerization staples to the pre-heated samples, and FAM emission of the associated FRET pair was recorded until equilibrium was reached after 1.5 to 3 hours. The initial linear fit of FRET curves yielded the initial reaction rates for the corresponding monomer concentrations at the given temperatures. Linear dependence on initial monomer concentration yielded the association rate coefficients* (k_a^{in}) *(d - f), and by applying the Arrhenius equation, the activation energy for the AA random stacking polymerization mechanism of 15 ± 1 kcal* mol^{-1} *could be calculated (g).*

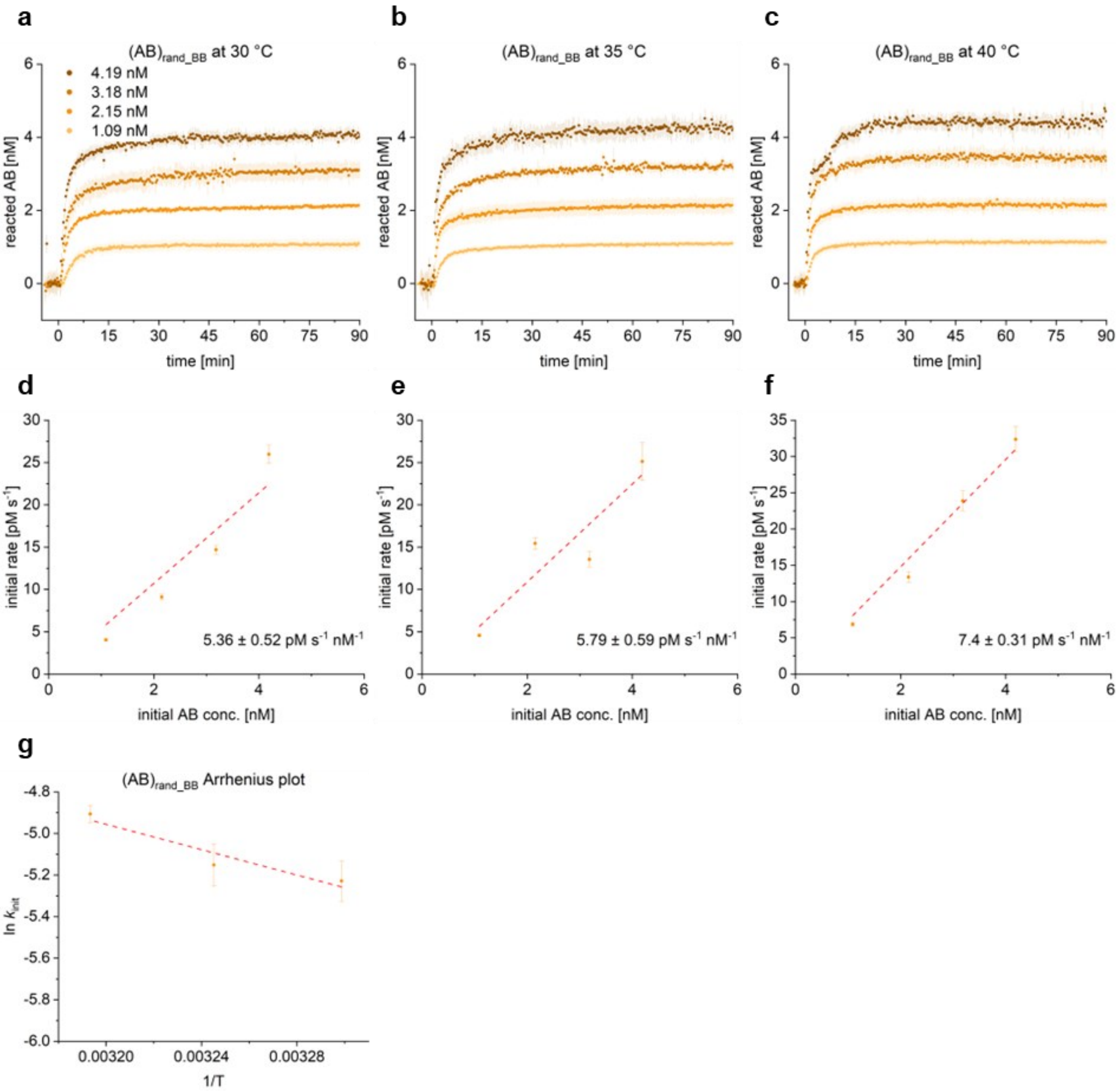

Figure 31 ***Isothermal BB association of random stacking polymerization***

Isothermal filament formation of the BB random stacking polymerization (AB)$_{rand\_BB}$ *at 30 °C (a), 35 °C (b), and 40 °C (c) with varying initial monomer concentrations ranging from 5 to 35 nM with effective concentrations ranging from 1 to 4 nM based on Figure 20. Reactions were initialized by adding ten-fold excess of polymerization staples to the pre-heated samples, and FAM emission of the associated FRET pair was recorded until equilibrium was reached after 1.5 to 3 hours. The initial linear fit of FRET curves yielded the initial reaction rates for the corresponding monomer concentrations at the given temperatures. Linear dependence on initial monomer concentration yielded the association rate coefficients (*k_a^{in}*) (d - f), and by applying the Arrhenius equation, the activation energy for the BB random stacking polymerization mechanism of 6.1 ± 0.1 kcal mol*$^{-1}$ *could be calculated (g).*

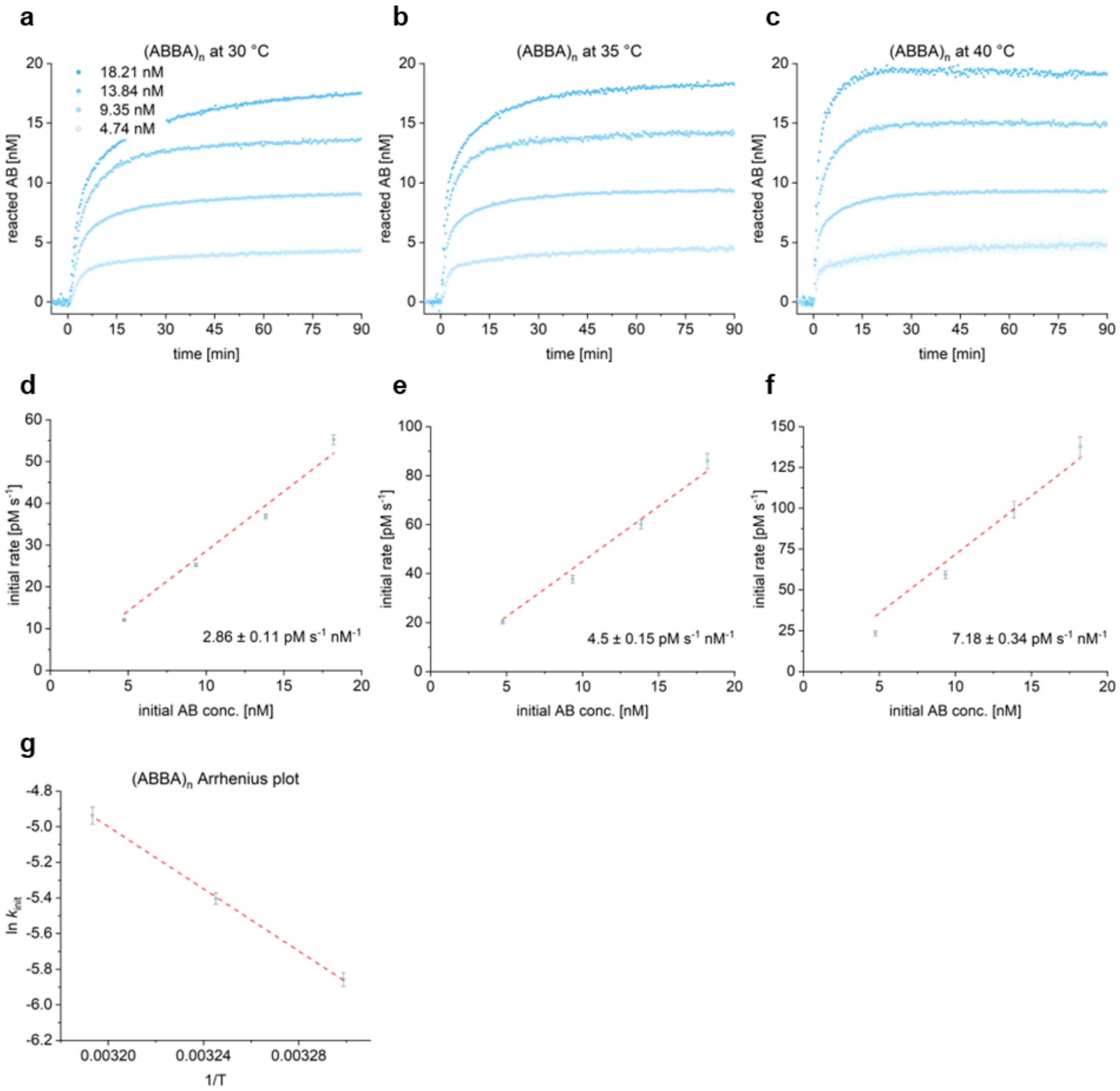

Figure 32 ***Isothermal ABBA dimer stacking polymerization***
Isothermal filament formation of the ABBA dimer into $(ABBA)_n$ *filaments at 30 °C (a), 35 °C (b), and 40 °C (c) with varying initial dimer concentrations ranging from 5 to 18 nM. Reactions were initialized by adding ten-fold excess polymerization staples to the pre-heated samples, and FAM emission of the associated FRET pair was recorded until equilibrium was reached after 1.5 to 3 hours. The initial linear fit of FRET curves yielded the initial reaction rates for the corresponding monomer concentrations at the given temperatures. Linear dependence on initial monomer concentration yielded the association rate coefficients* (k_a^{in}) *(d - f), and by applying the Arrhenius equation, the activation energy for the* $(ABBA)_n$ *polymerization mechanism of 17.3 ± 0.3 kcal* mol^{-1} *could be calculated (g).*

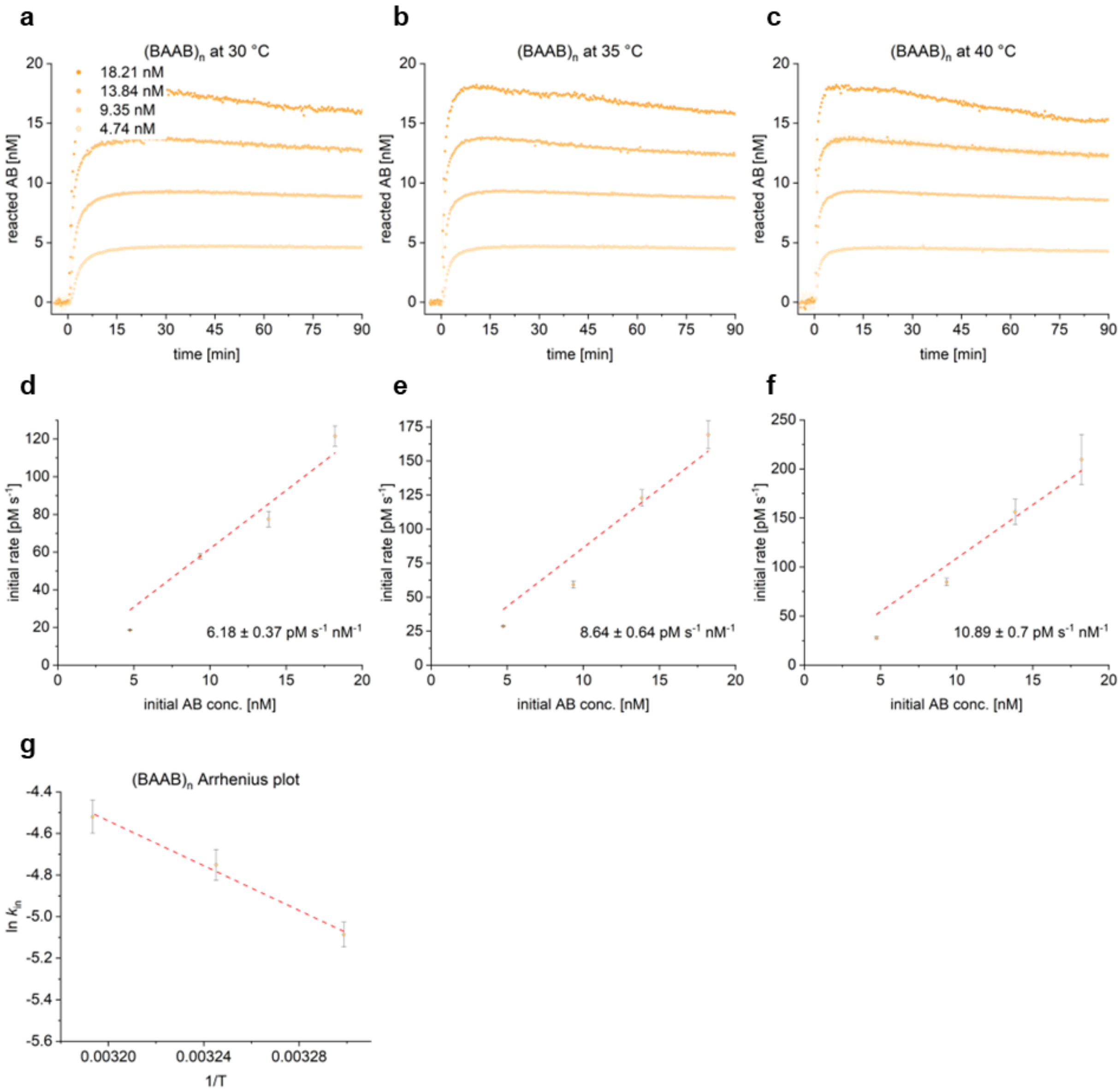

Figure 33 ***Isothermal BAAB dimer stacking polymerization***

Isothermal filament formation of the BAAB dimer into $(BAAB)_n$ filaments at 30 °C (a), 35 °C (b), and 40 °C (c) with varying initial dimer concentrations ranging from 5 to 18 nM. Reactions were initialized by adding ten-fold excess polymerization staples to the pre-heated samples, and FAM emission of the associated FRET pair was recorded until equilibrium was reached after 1.5 to 3 hours. The initial linear fit of FRET curves yielded the initial reaction rates for the corresponding monomer concentrations at the given temperatures. Linear dependence on initial monomer concentration yielded the association rate coefficients (k_a^{in}) (d - f), and by applying the Arrhenius equation, the activation energy for the $(BAAB)_n$ polymerization mechanism of 11 ± 1 kcal mol^{-1} could be calculated (g).

Varying Hybridization Sites

As described above (pp. 44), the finetuning of the thermal stability and association temperature of dimer stacking events was successfully achieved by systematically varying the number of activated helices for head-to-head or tail-to-tail binding. This time, the kinetics of the head-to-tail filament association at a given temperature were investigated by applying the established FRET strategy described in Figure 10. Accordingly, inactive monomers were assembled with a two-fold excess of fluorescent dyes (p. 33), and monomer concentrations were adjusted to 15 nM in TEMg20. Various symmetric arrangements of helices activated for hybridization base pairing (Figure 34a) were examined by adding a ten-fold excess of the corresponding polymerization staples to pre-heated monomer samples at 40 °C. FAM-emission was consequently recorded over 24 h and derived FRET efficiency normalized to initial monomer concentration. Initial reaction rates were determined from the linear slope of the FRET curves (Figure 34b) as described on page 36.

Table 11 ***Initial reaction rates for varying combinations of hybridization sites at 40 °C***

interface	k_a^{in} at 40 °C [pM s^{-1}]
outer	12.28 ± 1.03
full	10.03 ± 0.76
right	9.94 ± 1.56
left	6.81 ± 0.53
inner	4.92 ± 1.07

The obtained initial reaction rates (k_a^{in}) are summarized in Table 11 and Figure 34c. Analyzed interface layouts included **full** activation of the remaining 22 unlabeled helices, activation of the 14 **outer** helices, and, consequently, analysis of the eight **inner** helices. Additionally, 14 upper **right** helices distant from the FRET pair and 12 lower **left** helices surrounding the FRET pair were examined for kinetic impacts. With 12 pM/s, the hybridization at the outer helices occurred most rapidly, while activating all accessible helices resulted in a slightly slower initial reaction rate of 10 pM/s. Activation of the inner helices yielded a two times slower (5 pM/s) polymerization compared to the full activation.

Presumably, the number of activated helices plays a minor role compared to the accessibility of the unpaired scaffold. While fewer possible binding events would decrease the likelihood of cooperative binding at neighboring helices, sterical inaccessibility of the interior binding sites by flexible scaffold regions is the significant kinetic impact factor. Comparing the right to the left construct confirms this hypothesis. Activation of the right helices yielded a k_a^{in} of 10 pM/s, whereas the left side's initial reaction rate was significantly lower with 7 pM/s. Firstly, the right construct displays 14 hybridized helices in contrast to 12 for the left construct, with the sequence-specific binding energies also playing a considerable part. Secondly, the local structural environment near the FRET pair likely impeded the rapid polymerization of the left-side construct.

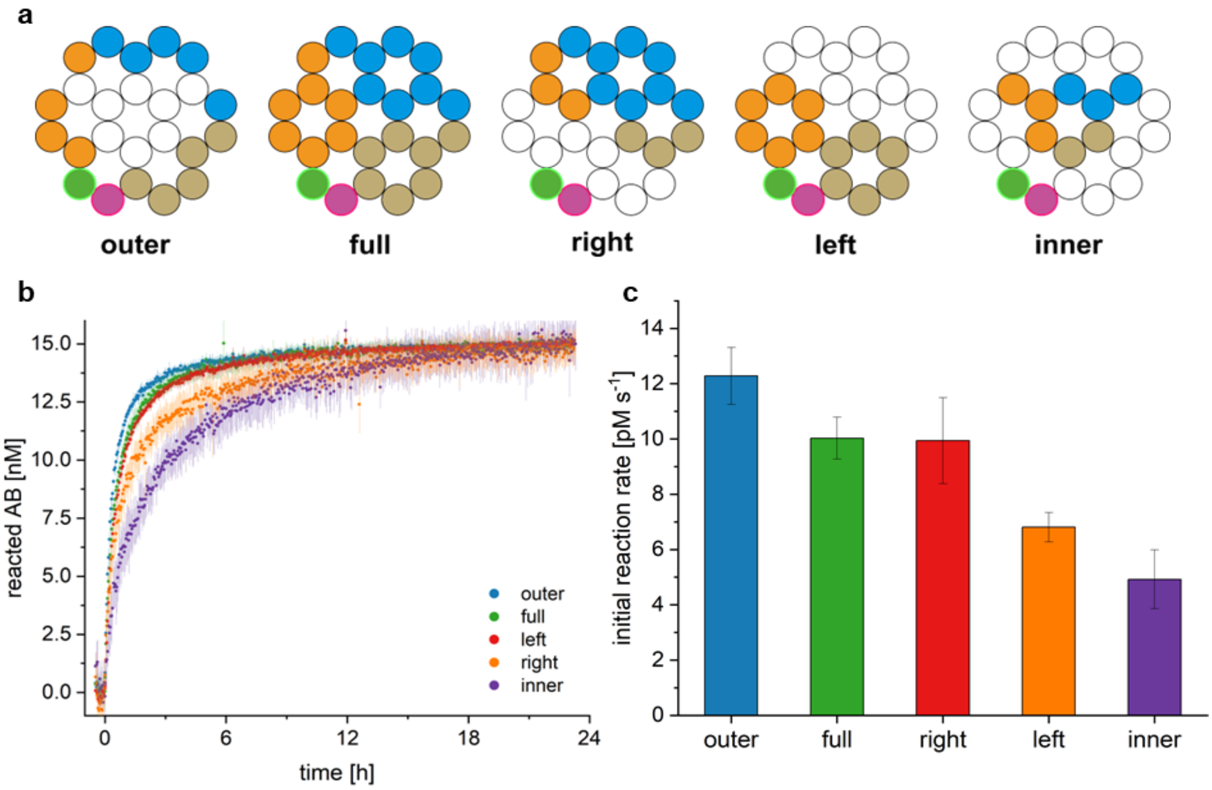

Figure 34 ***Varying number and positioning of hybridization sites for $(AB)_n$ filament formation***
a) Activation of 8 (inner) to 22 (full) out of 24 helices for hybridization polymerization in varying regions of the 24-helix bundle monomer with the remaining two helices binding a fluorescein or rhodamine dye (green and purple helices) or corresponding unlabeled sequences. Positioning of actively binding helices ranges from full activation to exclusively outer or inner helices or left or right regions. b) Isothermal FRET measurements of 50 nM pre-assembled monomers already fluorescently labeled at 40 °C in TEMg20 were recorded after the addition of a ten-fold excess of the depicted interfaces over 24 h. c) Initial linear reaction rates were extracted from the obtained FRET curves for each interface variation.

Polymer Dynamics

The dynamic behavior and overturn of polymeric structures in response to equilibrium perturbation can reveal interesting information on the mechanism of filament formation. For this purpose, fluorescently labeled equilibrium structures obtained from hybridization and random stacking were mixed with unlabeled monomers, and changes in FRET efficiency of the samples were recorded. No change in E_{FRET} would indicate either filament elongation at already formed polymer tips or a new assembly of oligomers (Figure 35c, right). In comparison, an E_{FRET} decrease would indicate the interruption of intra-filamentous bonds by either chain scission or monomer integration events (Figure 35c, left).

Monomers with the respective fluorophore labeling described in Figure 10 were assembled from 50 nM scaffold, and 47.5 nM fluorophore-labeled oligonucleotides, while the remaining core staples were used in ten-fold excess. This approach was chosen to limit the likelihood of free fluorophores binding to the newly added unlabeled monomers while retaining a theoretical FRET yield of 90.25 % for the marked monomers. A final concentration of 20 nM labeled monomers in TEMg20 was heated to 40 °C and polymerized via hybridization or random stacking by adding a ten-fold excess of polymerization staples while FAM emission was recorded. After reaching equilibrium (16 h for hybridization and 2 h for random stacking), equimolar amounts of fresh unlabeled monomers were added at the timepoints indicated by the arrows in Figure 35a and b.

At equilibrium, hybridization-driven polymers reached E_{FRET} values of 0.55 (Figure 35a). The moderate levels of FRET efficiency might be due to the sterical effects discussed above. Adding monomers to the established polymers did not noticeably alter the FRET signal, which indicates that the unlabeled monomers either elongate preexisting polymer tips or form new oligomers (mechanism in Figure 35c, right). Random stacking, however, showed a moderate decrease in FRET efficiency from 0.64 at equilibrium to 0.55 after monomer addition (Figure 35b). Therefore, a fraction of the newly introduced monomers either cause chain scission by breaking down longer filaments and binding at the so-formed tips or integrates into the filament via a scission/condensation mechanism. Since the decrease in E_{FRET} is about 14% of the initial value, the majority of introduced monomers probably still form new oligomers.

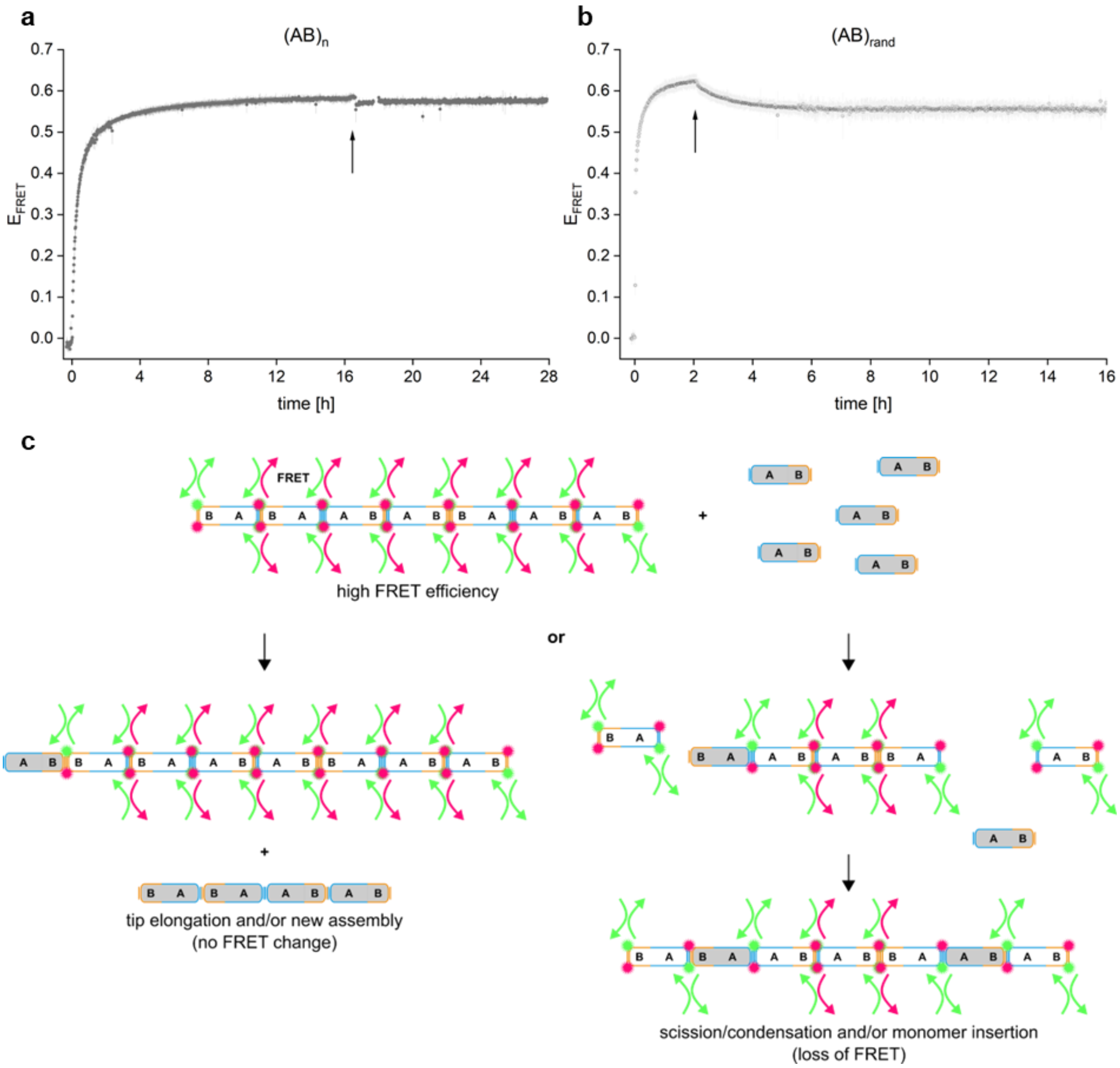

Figure 35 ***Monitoring of potential polymer turnover after monomer addition to equilibrium filaments***

FRET curves of a) hybridization and b) random stacking polymerization at 40 °C from 20 nM monomer in TEMg20 labeled with one or two FRET pairs, and a ten-fold excess of polymerization staples reacted to equilibrium. Subsequent addition of equimolar unlabeled monomers and the corresponding effect on FRET efficiency is marked with arrows after 16 h for hybridization and 2 h for random stacking. c) Two mechanisms to explain potential changes in fluorescence signal are depicted.

Conclusion

This chapter examined the versatile possibilities of associating 24-helix bundle monomers and dimers into ordered periodic DNA origami filaments or randomly associated polymers. Distinct differences between the two investigated association mechanisms, e.g., base hybridization and base stacking, could be uncovered, as well as significant differences between stacking filaments based on monomer or dimer association. In contrast to naturally occurring polymers[205,206], hybridization and random stacking polymers revealed extremely low critical monomer concentrations at equilibrium conditions between 30 °C and 40 °C. For the random stacking polymerization, the observed c_{crit} value was temperature independent and ranged from 1.6 pN to 3.2 pN. Hybridization polymerization exhibited a temperature dependence with c_{crit} decreasing by 90.7 % with a temperature increase of 10 °C from 111.5 pN at 30 °C to 10.4 pN at 40 °C.

The initial length distribution within the first hour demonstrated a clear tendency towards longer random stacking filaments compared to polymers obtained by base hybridization. Due to a general clustering tendency of the elongated filaments, the accurate determination of equilibrium length distributions poses significant difficulties. In the early phase of the polymerization, longer chains are obtained by random stacking when compared to hybridization, and this tendency is likely valid at equilibrium conditions, too, as previously described by Pfeifer et al.[136]. The longest observed $(AB)_n$ filaments reached lengths of up to 4.5 µm while $(AB)_{rand}$ got up to 6 µm long. Significantly, recorded filament lengths heavily depended on the chosen imaging method, with negatively stained TEM imaging resulting in more extended observable structures than those obtained by the same samples imaged by AFM.

Isothermal FRET studies and AFM imaging (Supplementary Figure 4) showed a brief initial lag-phase of 30 sec before the start of polymerization, during which staples presumably bind to the inactive scaffold interfaces. This phase was most notable for random stacking, as a certain threshold of activated helices is required for stacking association. Fast scan AFM imaging revealed a relatively rigid oligomerization for stacking bonds compared to a more flexible orientation and deferred association for hybridization. During stacking, monomers literally either stick together in the correct orientation or dissociate again, while hybridization events are deferred with monomer interfaces progressively readjusting their relative orientation until full binding is established. Thermal stability studies revealed a considerably higher melting stability (by over 2 °C) of the hybridization-derived (AB)$_n$ polymer over any structures associated by base stacking. This higher stability was also observed during dynamic polymer turnover experiments in which filament scission could only be recorded in randomly stacked polymers while hybridization filaments were growing via tip elongation.

The leading cause for the observed difference between the hybridization and stacking mechanism likely lies within the interface binding process. In the initial step of the process, polymerization-inducing staple strands bind to their complementary scaffold regions of the inactive monomer. For stacking, the entirety of the oligonucleotide binds to the unpaired scaffold region forming blunt ends that enable stacking interactions. While strand displacement with an identical staple is possible, this is not supposed to lead to an energetic gain. After sufficient activated helices are accumulated, interface association via ππ-bonds occurs. For hybridization, the added staples also bind to one side of the unpaired complementary scaffold, with the remaining single-stranded region being initially unbound due to the saturation of the interfaces with two identical sets of staples. One set of oligonucleotides must be displaced by its counterpart to connect the helices of two distinct monomers via base pairing. This most probably represents the energetic barrier affecting early polymerization (Figure 36). In later phases of the polymerization, this effect is likely mitigated by cooperative effects caused by the spatial proximity of the involved strands.

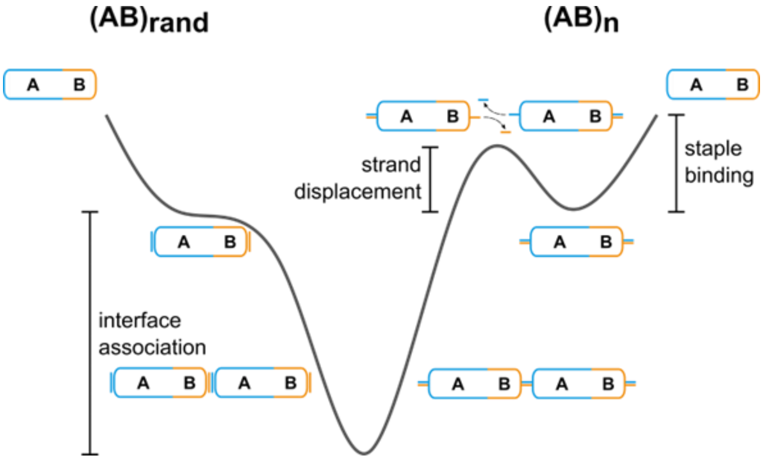

Figure 36 ***Possible mechanistic and energetic difference between random stacking and hybridization polymerization***
For stacking and hybridization-induced polymerization, an initial binding event of complementary oligonucleotides to the inactive monomer occurs. For stacking, the complementarity of the entire sequence leads to the formation of blunt ends and subsequent stacking after sufficient helices have been activated. For hybridization, the staple is complementary to two sides of the monomer and will initially bind to one interface with an unpaired overhang. This sequence then displaces its counterpart on the corresponding interface to connect two monomers in a head-to-tail fashion presenting an energetic barrier.

While thermal stability and kinetics were mainly influenced by the already discussed flexibility of the gapped stacking helices, the association distribution of the random assembly was based on the symmetry match of the interfaces, adding another layer of consideration for polymerization finetuning. Additionally, using dimers as building units will increase the polymerization velocity by solely enabling the head-to-head or tail-to-tail isologous associations.

The following results will be published shortly in the article *DNA Origami Polymerization with a DNA Reaction Network*, by Stenke, LJ., Weiß, M., and Saccà, B., currently in preparation.

DNA Origami Polymerization with a DNA Reaction Network

After a thorough investigation of the mechanisms, kinetics, and dynamics of the polymerization of the 24-hb DNA origami, introducing a more dynamic approach to polymerization was of great interest. Inspired by the enzyme-free autocatalytic DNA reaction network (DRN) designed by Srinivas et al.[181], the designed exponential strand release was successfully incorporated into the hybridization-based polymerization approach of the 24-helix bundle, albeit with a significant design change in the associating interface. The DRN elegantly omits the need for one or several catalyzing DNases previously often used for driving DNA reaction networks[166–170]. There have been successful demonstrations of coupling a chemical reaction network (CRN) to DNA structures to achieve higher-ordered structures[214–217]. However, most approaches employed single DNA strands or small DNA tiles. The here presented approach now combines a DRN with a MDa-sized DNA origami driven polymerization, exploring approaches for controlling the reversibility of the process. These studies may thus contribute to open new perspectives on the development of active materials for applications in synthetic biology (Figure 45).

Integrating a unique DNA Fuel Strand into DNA Origami Polymerization

First, the successful integration of a unique and identical fuel strand into the DNA origami polymerization had to be established. The polymerization processes investigated in the previous chapter (pp. 60) relied on the sequence complementarity of *several* staple strands to the unpaired scaffold portions available at the A- and/or B-interface. Many distinguished staple sequences are required to connect 24 unpaired scaffold domains at two interfaces directly. Integrating a DRN that releases only *one* single-stranded DNA oligonucleotide at every cycle of the auto-catalytic reaction presents a new challenge in interface design. First, direct binding to the DNA origami scaffold is not attainable. Thus, an adaptor interface was designed that enables the direct binding of the A- to the B-interface upon addition of a fuel strand originated by the DRN. The adaptor interface contains a portion that is complementary to the unpaired scaffold and single-stranded overhangs that are complementary to the DRN fuel strand (caDNAno design in Supplementary Figure 7).

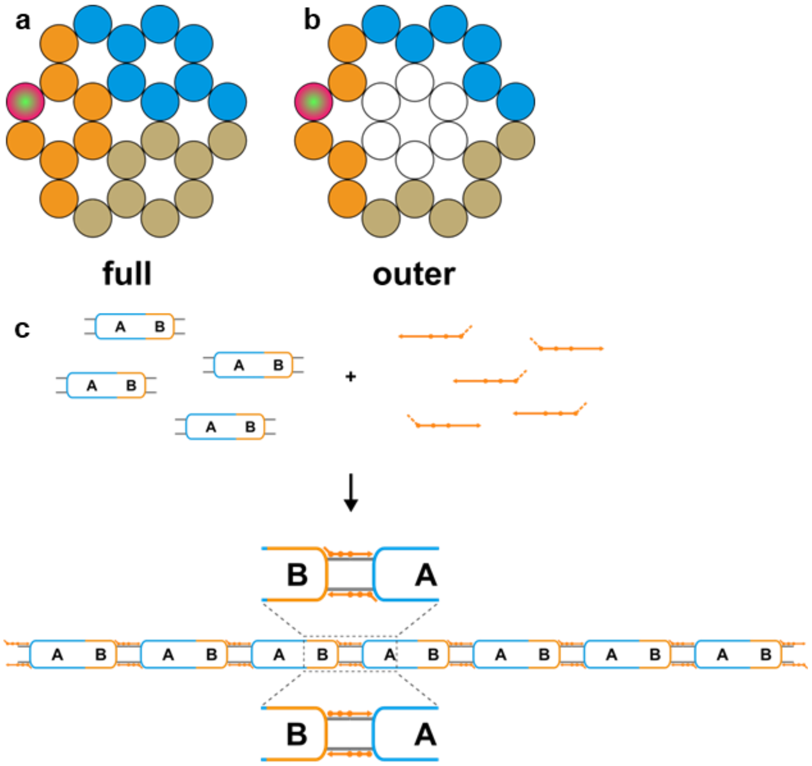

Figure 37 ***Concept of DNA origami polymerization with identical fuel staple***
Interface activation and FRET pair positioning of a) a full set of helices or b) the outer 18 helices to reduce required fuel (design details in Supplementary Figure 7). The colors of the three patches indicate the level of protrusion of helical patches at the connected AB-interface (blue: A protrudes, orange: B protrudes, beige: similar protrusion). c) Polymerization by binding multiple fuel staples to single-stranded protrusions at activated DNA origami interfaces either with (upper zoom in) or without (lower zoom in) five-base toehold domain.

To accommodate the helical twist of the B-DNA double helix, the original oligonucleotide released from the DRN was elongated by two bases to a total length of 31 bases corresponding to three helical turns in between two adjacent monomers. This resulted in two protruding single strands with either 15 or 16 bases complementary to the elongated fuel strand (Figure 37c, orange fuel strands binding to grey protruding single strands on the origami). In previous experiments regarding hybridization-based polymerization, addressing selected outer helices of the 24-helix bundle resulted in an improved initial polymerization rate (Figure 34). Additionally, integrating an identical DNA strand into up to 24 helices requires high concentrations of the respective staple, which could be lowered with a reduced number of connecting helices. Therefore, two variations of helix activation were tested with either full activation of all 24 helices (Figure 37a) or only activation of the outer 18 helices (Figure 37b). A FRET pair for monitoring the association process was placed end-to-end (3' and 5') at opposite sides of directly connected helices based on shape-complementarity.

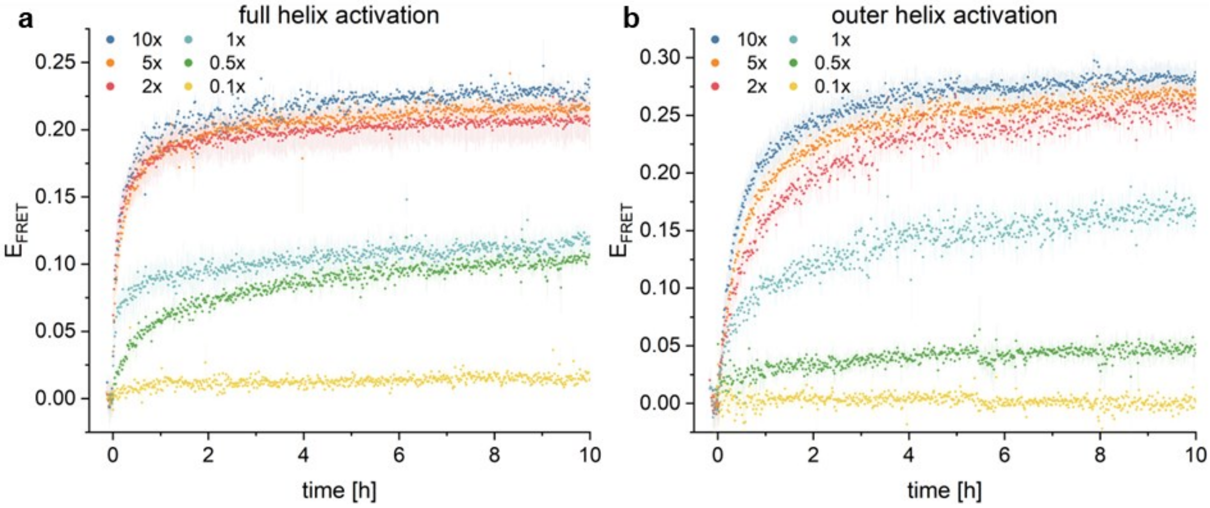

Figure 38 ***Titration of sufficient fuel excess for different interface designs in TEMg20***
15 nM of PEG purified 24-helix bundle monomer polymerized with different excess of fuel strand (0.1 – 10x) in TEMg20 at 40 °C with a) full helix activation or b) outer 18 helix activation. Fuel excess indicated per available binding site of an active interface.

Table 12 ***Initial reaction rates of fuel titration of two distinct interfaces in TEMg20***

fuel excess	**initial rate[E_{FRET}/h] -full**	**equilibrium E_{FRET}**	**initial rate [E_{FRET}/h] -outer**	**equilibrium E_{FRET}**
10x	1.93 ± 0.16	0.23 ± 0.01	0.62 ± 0.02	0.29 ± 0.01
5x	1.68 ± 0.19	0.22 ± 0.01	0.5 ± 0.02	0.27 ± 0.01
2x	2.2 ± 0.37	0.21 ± 0.01	0.33 ± 0.01	0.26 ± 0
1x	0.71 ± 0.07	0.12 ± 0.01	0.34 ± 0.02	0.17 ± 0.01
0.5x	0.12 ± 0	0.11 ± 0.01	0.03 ± 0	0.05 ± 0.01
0.1x	0.03 ± 0.01	0.02 ± 0.01	-	0 ± 0.01

Contrary to the scaffold anchored hybridization polymerization, the fully activated interface (Figure 38a) polymerized about three times as fast (Table 12) compared to the outer activated helices (Figure 38b). Looking at this from a probabilistic perspective can help understand the observed effects. Hybridization with identical connecting staples offers a broader range of possible binding events with an increase in the number of successfully connected helices, given that the concentration of connectors scales with the binding sites. Opposed to this, many distinct connecting staples can only bind to a specific complementary site; therefore, many successful events must simultaneously occur to enable full binding.

Interestingly, the maximal equilibrium FRET efficiency of the interface with outer helix activation reached a plateau of 0.27 for a ten-fold fuel excess, while the corresponding value for the full helix activation reached only a value of 0.22. As the fluorophore labeling strategy and remaining parameters were identical, differences in E_{FRET} might be an indication of the relative differences in the degree of polymerization. This means that despite a slower initial polymerization, the polymers stemming from the outer helix design with a fuel excess of one-fold or higher may potentially result in longer polymers than those achieved by the full design. To clarify this point, AFM images of the two types of polymers were collected. Supplementary Figure 8 shows the equilibrium structures of both polymer types with either the full (Supplementary Figure 8a) or outer (Supplementary Figure 8b) interface design for a ten-fold fuel excess and 1 nM initial monomer. Similar to previous observations, the surface coverage did not equal the theoretical input amount, indicating surface-dependent effects and cluster formation in fuel-induced polymerization as well. However, both interface variations successfully formed polymers of up to 2 µm. As expected, the filaments obtained from identical connecting strands generally formed longer filaments than those originating from several distinct connecting strands, supporting the idea of a higher binding probability when relying on multiple but sequence-identical hybridization events.

For both interface designs, outer and full, a two-fold excess of fuel strands per binding site led to a satisfying extent of polymerization. Although the polymerization rate of the outer design was somewhat slower, this design was ultimately chosen for further investigation and was used in combination with a fully functional DRN because of the 25 % lower fuel consumption.

A magnesium chloride titration was performed on 15 nM DNA origami monomers with activated outer helices to determine the ideal conditions for fuel-induced polymerization. As demonstrated above, a two-fold excess (540 nM) of fuel staple per available binding site yielded a suitable polymerization extent while minimizing the required material. The reaction was run at 40 °C with TEMg buffer and magnesium concentrations ranging from 12.5 to 20 mM. The initial reaction rates of the linear phase are summarized in Table 13, and obtained FRET curves are shown in Figure 39a.

Interestingly, equilibrium FRET efficiencies correlated with magnesium concentrations in an inverted manner while the initial polymerization rate directly scaled with higher magnesium concentrations with an increase of 0.95 ± 0.07 pM s^{-1} every 1 mM $MgCl_2$ (Figure 39b). A putative effect of different $MgCl_2$ concentrations on the fluorophore emission can be excluded on the bases of previous reports[218]. In TEMg12.5, the initial polymerization occurred at 3.77 pM s^{-1}, while TEMg20 had an initial reaction rate of 10.3 pM s^{-1}. Regardless of the initial reaction rate, polymerization under all tested magnesium conditions reached a plateau within the first two hours with no significant differences in the trend of the FRET curves (Figure 39a).

TEM images of 1 nM of equilibrium filaments polymerized in the respective TEMg buffer (Figure 39c - f) demonstrated that structures could easily reach lengths of 3 µm and more. With increasing magnesium concentrations, the clustering of the polymers became more severe. Unfortunately, overall clustering prevented accurate length determination, but the TEM images confirmed generally elongated structures in TEMg12.5 compared to TEMg20.

Table 13 ***Initial reaction rate of fuel-induced polymerization with different $MgCl_2$ concentrations***

$MgCl_2$ conc. [mM]	initial rate [pM s^{-1}]	equilibrium E_{FRET}
12.5	3.77 ± 0.1	0.26 ± 0
15	6.28 ± 0.31	0.24 ± 0.01
17	8.72 ± 0.52	0.23 ± 0
20	10.3 ± 0.85	0.21 ± 0.01

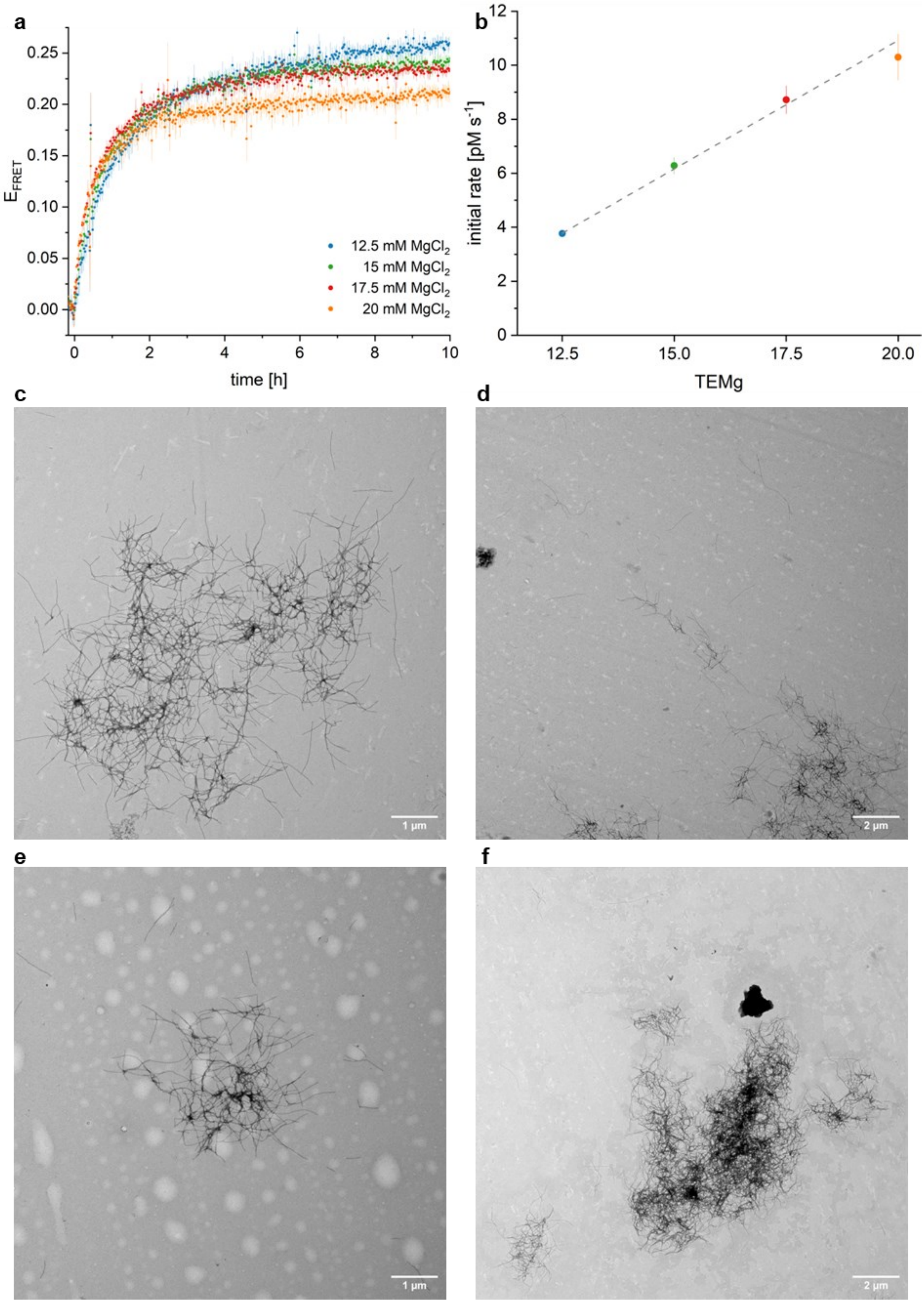

Figure 39 ***Magnesium titration of fuel-induced DNA origami polymerization***
a) 15 nM of PEG-purified DNA origami monomer with active outer helices in TEMg buffers with $MgCl_2$ concentrations ranging from 12.5 mM to 20 mM and a two-fold fuel excess. b) Initial reaction rate of polymerization plotted vs. magnesium concentration yielding a rate increase of 0.95 ± 0.07 pM s^{-1} per additional 1 mM $MgCl_2$. c - f) Resulting TEM images of obtained equilibrium polymer samples polymerized from 1 nM activated monomer in c) TEMg12.5, d) TEMg15, e) TEMg17.5 or f) TEMg20 at 40 °C for 20 h.

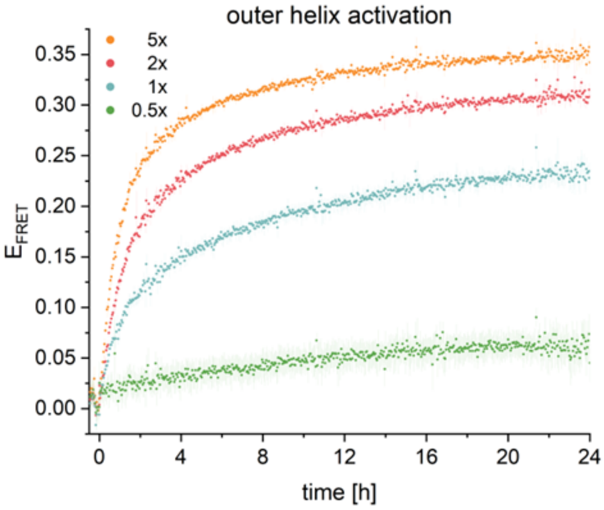

Figure 40 ***Titration of required fuel excess for outer interface design in TEMg12.5***
15 nM of PEG-purified 24-helix bundle monomer polymerized with different excess of fuel strand (0.5 – 5x) in TEMg12.5 at 40 °C with a) outer helix activation. Fuel excess is indicated per available binding site of an active interface.

To obtain a reliable reference for the DRN-driven polymerization, a set of FRET curves was recorded using different molar equivalents of fuel strands in TEMg12.5 for hybridization at the outer interface, analogous to Figure 38 (Figure 40). As expected, equilibrium E_{FRET} was slightly higher with a maximum of 0.36 for 5x fuel excess compared to 0.27 in TEMg20 (Table 12), and the reaction rates slowed. Compared to the $MgCl_2$ titration for polymerization (Figure 39), the initial rates in TEMg12.5 decreased by about 50 % (Table 14).

Table 14 ***Initial reaction rates of fuel titration of outer interface in TEMg12.5***

fuel excess	initial rate [E_{FRET}/h] -outer	equilibrium E_{FRET}
5x	0.24 ± 0.01	0.36 ± 0
2x	0.14 ± 0	0.31 ± 0.01
1x	0.11 ± 0	0.23 ± 0.01
0.5x	0.04 ± 0.01	0.07 ± 0.02

Characterizing Fuel-Release of DRN

The DRN chosen to fuel the DNA origami polymerization[181] follows an autocatalytic *U + V → 2 U + fuel* reaction pattern with the established *fuel strand* as a convenient side product, not affecting the course of the DRN reaction (Figure 41). In brief, either a *U1* or *U2 strand* (identical in the green regions) binds the *fuel complex*, displaces the single-stranded *fuel strand* in the process (Figure 41, orange strand), and reveals a toehold region where the *V strand* subsequently binds. This displaces the *connector,* which can bind to a complementary region of a pre-existing *U complex*, displaces *U1,* and frees the toehold region for the association of the *helper strand,* which finally releases *U2*, thus terminating one cycle and enabling the starting of the next (p. 15).

To successfully integrate the DRN designed by Srinivas et al.[181] into a DNA origami polymerization, buffer and temperature conditions must simultaneously be suitable for both reactions. The complexes were originally annealed in TEMg12.5 and reacted in TENa buffer containing 0.5 M NaCl, but the lower $MgCl_2$ concentrations slightly negatively affected the rate of DNA origami polymerization (Figure 39a). Consequently, a screening from 12.5 up to 20 mM $MgCl_2$ was conducted for the DRN reaction. Similarly, 30 °C and 40 °C were examined as reaction temperatures to facilitate DNA origami polymerization instead of the original reaction temperature of 25 °C (Figure 42). The *fuel complex* with its incorporated *fuel strand* was labeled with a FAM and TAMRA fluorescent dye, as shown in Figure 41, to monitor the release of the *fuel strand* throughout the DRN reaction. The reaction cycle was induced by adding the *U complex* containing a fraction of unbound *U strands* (Supplementary Figure 9). 50 nM of complexes with a five-fold excess of *V* and *helper strands* were screened.

Initially, the FRET value of the unreacted complexes was close to maximum with roughly 95 to 93 % energy transfer efficiency. All monitored reaction conditions had a satisfying signal output. After 24 h, *fuel* release at both temperatures and all magnesium concentrations from 12.5 to 20 mM finally ceased with E_{FRET} values ranging from 0.22 ± 0.02 to 0.28 ± 0.03 in TEMg12.5 and TEMg20, regardless of the reaction temperature. Generally, final FRET values were directly correlated to the used magnesium concentrations (Figure 42a and b) and were more favorable in TEMg12.5. In TEMg12.5, the DRN released about 71 % of *fuel strands*, while in TEMg20 the release was only 64 % (Table 15). Figure 42c compares the reaction rates at 30 °C and 40 °C for the margin $MgCl_2$ concentrations, revealing an overall faster reaction at 40 °C, which was also favorable for DNA origami polymerization.

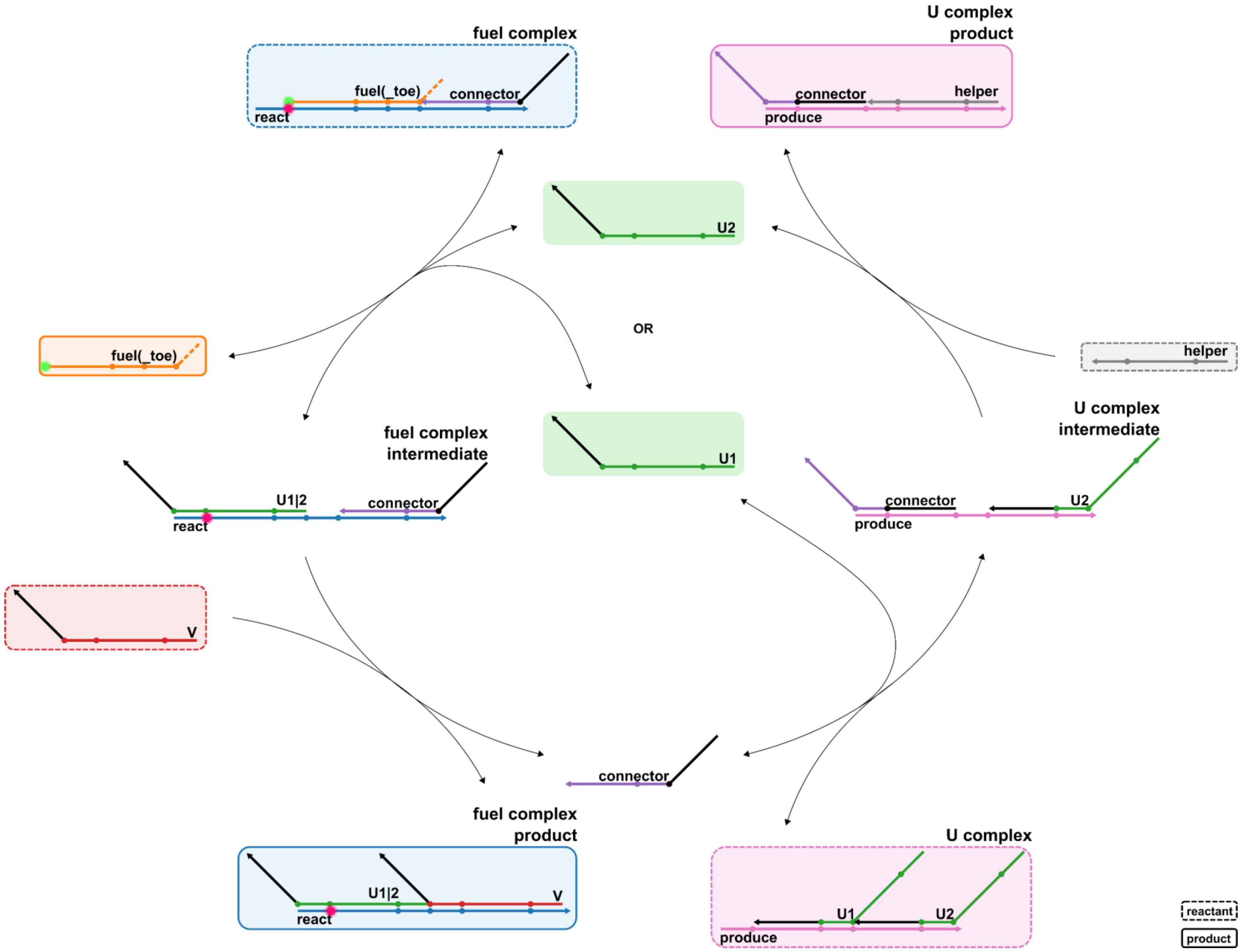

Figure 41 ***Adapted DRN with FRET labeling strategy for monitoring fuel release***
Either U1 or U2 strand (identical in green region) binds the fuel complex and displaces single-stranded fuel strand, which optionally carries a toehold region (dashed area). V strand displaces connector, which in turn binds to U complex and displaces U1 and frees toehold region for helper strand which releases U2 strand. The DRN follows the reaction equation U + V → 2 U.

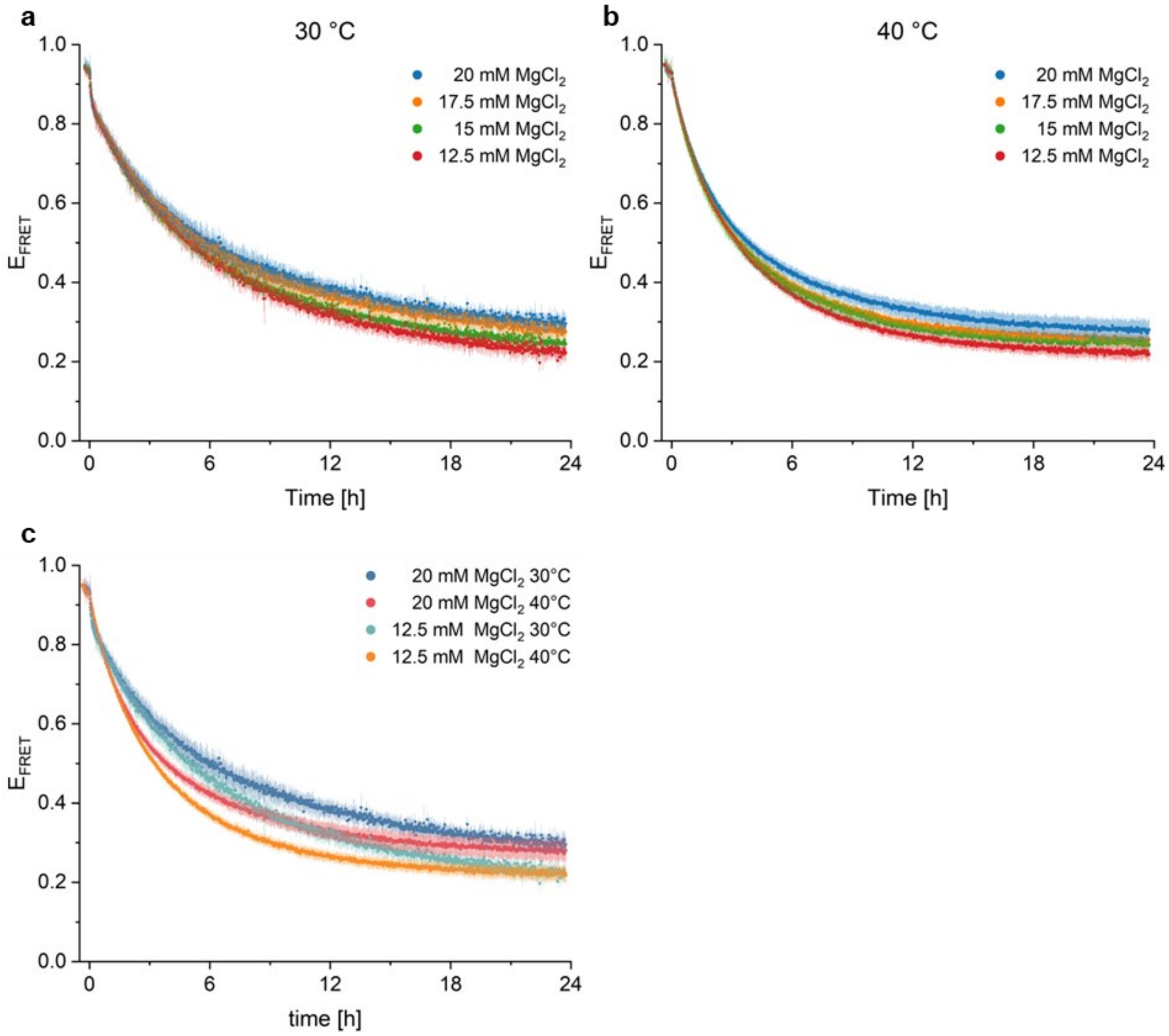

Figure 42 ***Optimizing conditions for fuel release from DRN***
Complete DRN reaction of 50 nM complexes and 250 nM V and helper strands as depicted in Figure 41 with FRET labeling for fuel release monitoring initiated by the addition of U complex. The reaction was screened for four different magnesium conditions from 12.5 mM to 20 mM in TEMg buffer and tested at two temperatures a) 30 °C and b) 40 °C. c) Both temperatures and margin $MgCl_2$ conditions are directly compared in one graph.

Table 15 ***Total fuel release after 24 h for varying $MgCl_2$ concentrations and temperatures***

$MgCl_2$ conc. [mM]	**total fuel release 30 °C**	**total fuel release 40 °C**
12.5	0.71 ± 0.04	0.71 ± 0.03
15	0.69 ± 0.03	0.69 ± 0.02
17.5	0.67 ± 0.03	0.67 ± 0.03
20	0.64 ± 0.03	0.65 ± 0.04

DNA Origami Polymerization coupled to an active DRN

Before combining the *fuel strand* released by the DNA reaction network and the DNA origami monomer, potential interactions of the isolated *fuel complex* and activated DNA origami had to be investigated. Two possible interactions were examined by applying distinct FRET labeling strategies. Each strategy is designed to allow for the monitoring of one part of the cycle in the absence of the other part. Effects on the baseline E_{FRET} would indicate the extent of the impact given by the subsequent addition of the second part of the cycle. Labeling the *fuel strand* and its complementary counter strand within the *fuel complex* was applied to monitor the possible interaction between the complex and an activated monomer (Figure 43a). The E_{FRET} before the addition of the monomer was 0.95 and remained constant after monomer introduction. Consequently, the mere presence of activated DNA origami interfaces did not dislodge the *fuel strand* from the complex structure on its own.

Nevertheless, unlabeled parts of the *fuel complex* or potentially unbound *fuel strands*, present in low quantity, if at all (Supplementary Figure 9), could theoretically bind and connect the activated interfaces. FRET labeling of protruding strands complementary to the *fuel strand* revealed no increase in E_{FRET} after *fuel complex* addition with no detectable polymerization induced by the fully assembled *fuel complex* (Figure 43b). Altogether, these data suggest that no undesirable interactions between the *fuel complex* and the DNA origami monomer take place, meaning that the *fuel complex* does not suffer from any appreciable leakage. In turn, the *fuel staple* released by the active autocatalytic DRN can be employed for DNA origami polymerization.

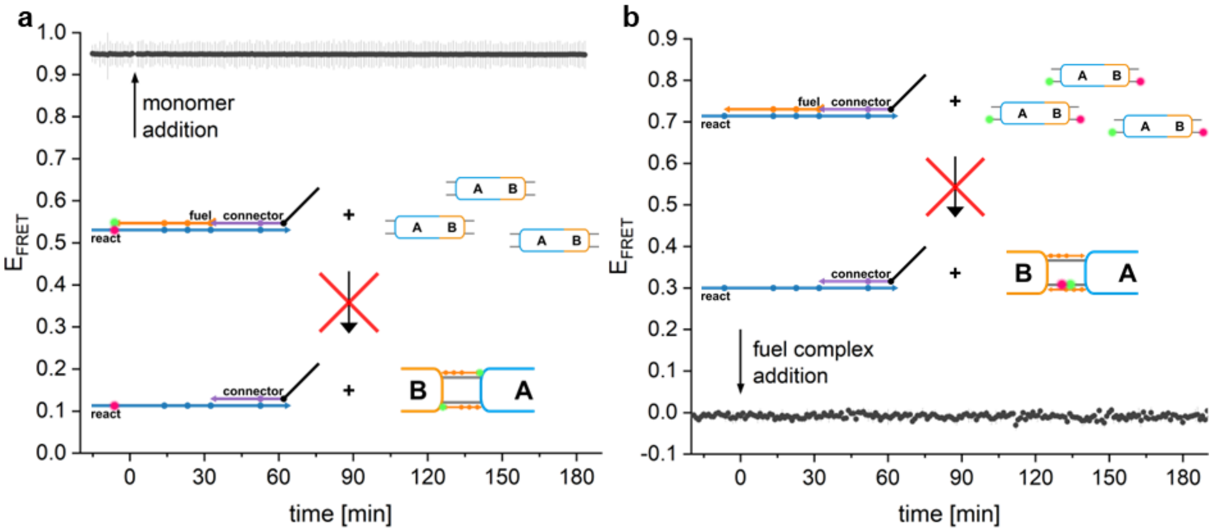

Figure 43 ***24-helix bundle DNA origami with isolated fuel complex***
15 nM of PEG purified monomer with activated outer helices and a two-fold excess of preassembled fuel complex per binding site (540 nM) in TEMg12.5 at 40 °C. Two different FRET labeling strategies were employed to a) monitor if the presence of activated monomers could dislodge the fuel strand from the fuel complex or b) show if any potentially unbound fuel strands could induce polymerization.

Finally, DNA origami polymerization was coupled to the modified DRN. As concluded from the previous experiments, only the outer 18 helices of the 24-helix bundle were activated for *fuel strand* binding to reduce the required DRN concentration, and polymerization was performed in TEMg12.5 at 40 °C. The polymerization process was monitored by FRET as described on page 90ff. The resulting FRET curves for two-fold and five-fold DRN excess per binding site are shown in Figure 44a. The *fuel* and *U complexes* had a final concentration of 0.54 mM and 1.35 mM, respectively, while the *V* and *helper strands* were used in five-fold excess respective to the complexes. DNA origami and DRN, besides the *U complex*, were mixed and preheated. The addition of the *U complex* induced the DRN reaction and subsequent polymerization.

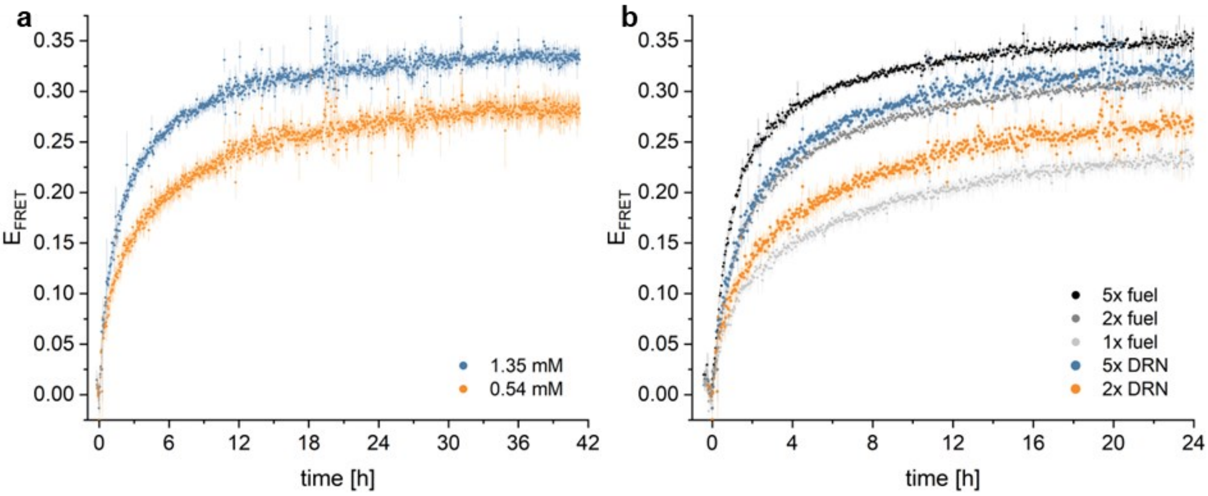

Figure 44 ***24-helix bundle with activated outer helices combined with complete DRN***
a) FRET reaction curves of 15 nM PEG purified 24-helix bundle DNA origami monomer with activated outer helices combined with two-fold (orange) or five-fold (blue) theoretical excess of the complete DNA reaction network or 0.54 mM or 1.35 mM concentration of complexes respectively. Polymerization was induced by adding the U complex at t = 0 in TEMg12.5 buffer at 40 °C for 42 h. b) Obtained E_{FRET} *curves put in perspective by comparison against DNA origami polymerization with the isolated fuel strand and one-fold to five-fold excess per binding site (data from Figure 40, grey curves).*

Figure 44b compares the FRET polymerization curves from *fuel* released by the autocatalyzing DRN reaction to reference curves obtained with the isolated *fuel strand*. There are two aspects to consider when comparing these polymerization modes. First, the DRN reaction gradually releases the *fuel strand*, although the initial rate is arguably relatively high (Figure 42). Second, the DRN reactions do not release all the *fuel strands*. Indeed, as described above, about 15 nM of fuel, or 30 %, remained complexed under the chosen conditions (Table 15). As usual, the initial reaction rate was determined by linear fitting of the initial increase of E_{FRET} over time (p. 37). The two-fold excess or 0.54 mM of DRN resulted in an initial E_{FRET} increase of 13 % per hour, while that of the five-fold excess was around 17 % (Table 16). For comparison, the fuel-only polymerizations of two-fold and five-fold excess had higher rates of 14 %/h and 24 %/h, respectively, and slightly higher equilibrium E_{FRET} values (2x: 28 % vs. 31 %, 5x: 33 % vs. 36 %). This indicates a slightly lower degree of polymerization of the DRN-driven filaments compared to the fuel-driven process (Table 14). A visual comparison of the DRN with respective reference curves yielded no apparent lag in polymerization, likely due to the already slow polymerization and its cooperativity effect. The present data indicate that the DRN complexes' conversion level only moderately limits the DNA origami polymerization fueled by the chosen DRN.

Table 16 ***Initial reaction rates and equilibrium E_{FRET} of DNA origami polymerization with full DRN***

theoretical DRN excess	**initial rate [E_{FRET}/h]**	**equilibrium E_{FRET}**
5x	0.17 ± 0.01	0.33 ± 0.01
2x	0.13 ± 0.01	0.28 ± 0.01

Competing with and reversing the dynamic Polymerization

Biologically derived polymers are controlled through an intricate interplay of molecular processes that can induce polymer growth at required sites but will also cause structural disintegration when necessary[140,205,206]. A multitude of factors can delicately finetune enzyme-free chemical reaction networks[178]. One possible way to regulate an in vitro polymerization process is by introducing an antagonist that competes with or reverses the polymerization process. Figure 45 illustrates the here-introduced concept of an antagonist DNA strand called *remover*. First, the previously characterized DRN with its polymerization-driving *fuel strand* needed to be modified by introducing a five nucleotide-long 5' toehold domain sticking out from the DNA origami binding interface. Consequently, a perfectly complementary *remover strand* will dislocate the modified *fuel_toe strand*, promoting monomer dissociation and reversing the polymerization process. Additionally, conditions can be optimized to enable the concurrent occurrence of competitive filament growth, leading to a dynamic steady state which better mimics polymerization of natural protein filaments.

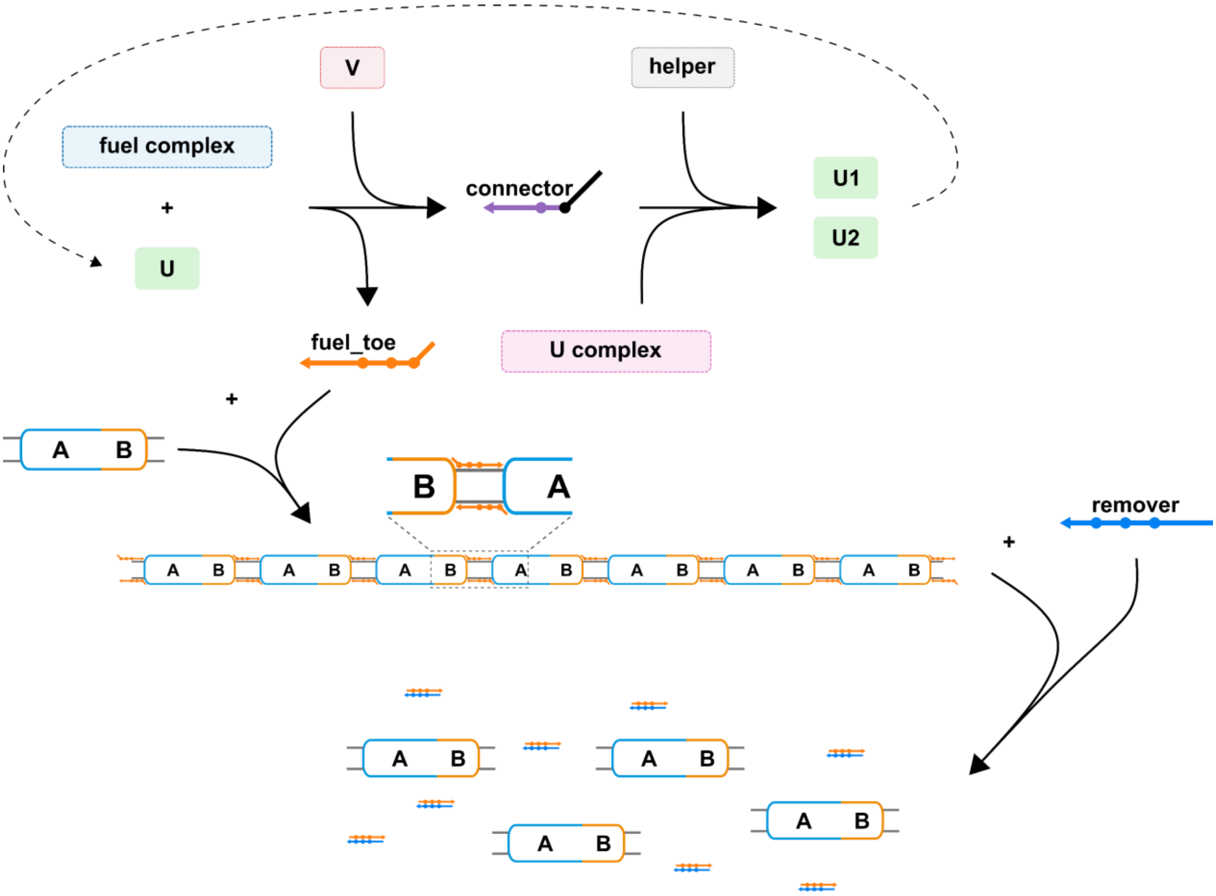

Figure 45 ***Reversibility concept of DRN-fueled polymerization***
DNA origami polymerization driven by DRN-released modified fuel strands that contain a 5' toehold domain that does not bind to the DNA origami interface. A fully complementary remover strand can subsequently release the fuel_toe strand from the DNA origami interface and reverse the polymerization.

A first pilot test was performed, wherein the 24-helix bundle with activated outer helices was polymerized with a range of different excess concentrations of the *fuel_toe strand* with a 5' five bases long toehold (Figure 46a) analogous to the experiment described in Figure 40. Initial reaction rates and equilibrium E_{FRET} indicated, respectively, the kinetics and the efficiency of the reaction (Table 17) and were significantly lower than those obtained in identical reaction conditions for the *fuel strand* lacking the toehold. Overall, the initial rates were more than ten times slower than without toehold, and a five-fold *fuel_toe* excess led to an increase in 0.015 E_{FRET}/h, while the resulting filaments exhibited in the same conditions a two-fold less effective energy transfer with an E_{FRET} of 19 %. Additionally, there was a more distinct scattering of data points in the toehold FRET curves, which could indicate a higher number of binding and unbinding events during the polymerization.

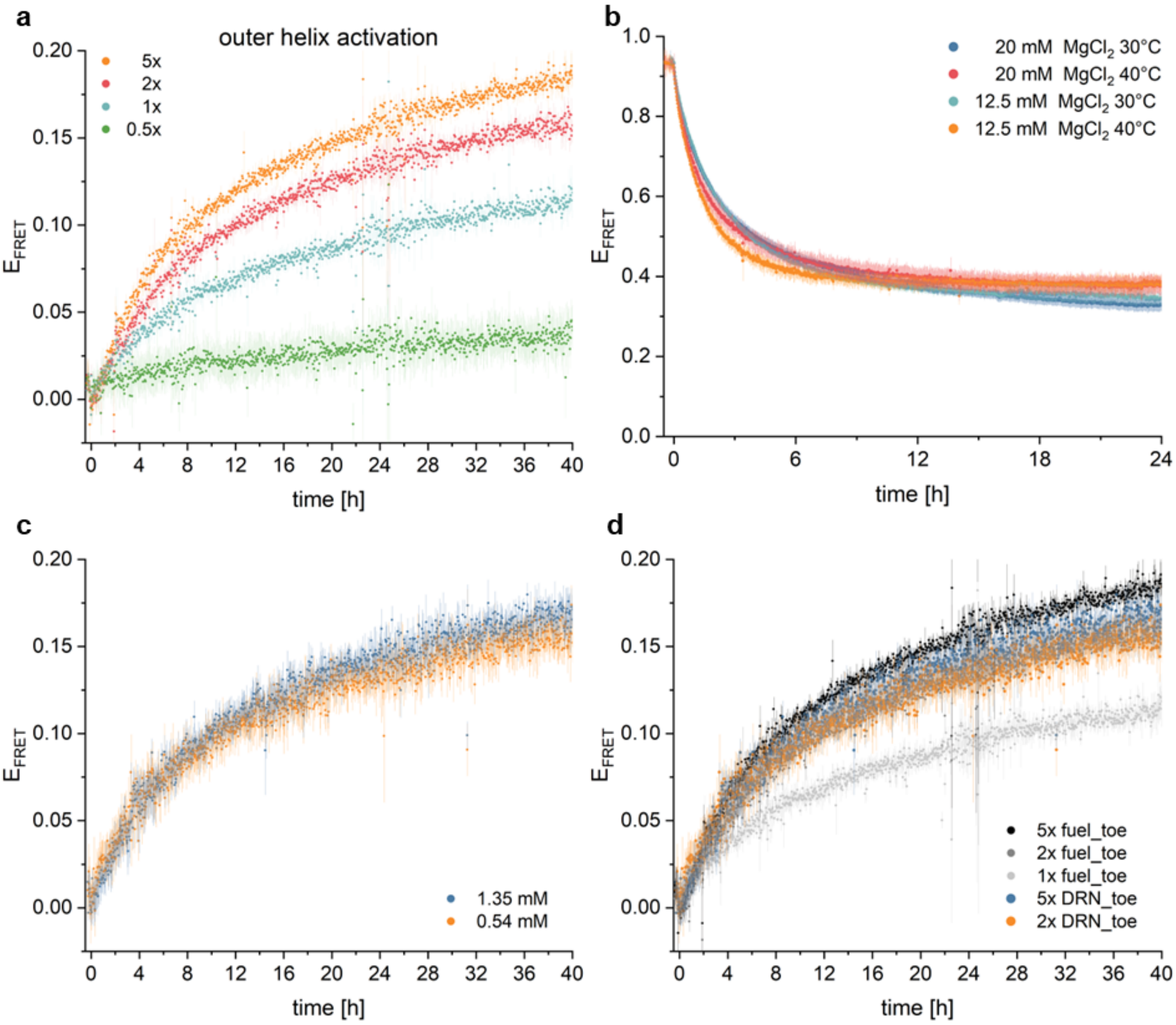

Figure 46 ***DNA origami polymerization with fuel_toe strand modified with a toehold domain***
a) 15 nM of PEG purified 24-helix bundle DNA origami with activated outer helices polymerized by addition of 0.5-fold to five-fold excess (135 nM to 1.35 mM) of fuel_toe strand with a 5' five bases long toehold domain not binding to the origami interface in TEMg12.5 at 40 °C. b) fuel_toe release from fuel complex of complete DRN in TEMg12.5 and TEMg20 at 30 °C and 40 °C respectively. c) 15 nM 24-helix bundle with activated outer helices polymerized with 0.54 mM (orange curve) or 1.35 mM (blue curve) DRN with fuel_toe in TEMg12.5 at 40 °C. d) DNA origami polymerization with DRN_toe (c) in comparison to polymerization with isolated fuel_toe strand (a).

Table 17 ***Initial reaction rates of fuel_toehold titration of the outer interface in TEMg12.5***

fuel_toe excess	initial rate [E_{FRET}/h] -outer	equilibrium E_{FRET}
5x	0.015 ± 0	0.19 ± 0
2x	0.012 ± 0	0.16 ± 0.01
1x	0.0075 ± 0	0.12 ± 0.01
0.5x	0.0026 ± 0	0.04 ± 0.01

The *fuel_toe* release from the completely assembled DRN was also characterized at different temperatures and buffer magnesium concentrations (Figure 46b). In comparison to the *fuel* release curves without the toehold domain (or with just two bases protruding from the fuel complex as opposed to seven) (Figure 42), the DRN reaction was faster but had a slightly worse yield of 54 to 60 % (Table 18).

Table 18 ***Total fuel_toe release after 24 h with varying $MgCl_2$ concentrations and temperatures***

$MgCl_2$ conc. [mM]	total fuel_toe release 30 °C	total fuel_toe release 40 °C
12.5	0.6 ± 0.02	0.54 ± 0.03
20	0.6 ± 0.04	0.54 ± 0.05

Combining the DRN with the toehold-modified fuel strand, the DNA origami polymerization reaction, and either a theoretical two-fold or five-fold excess of f*uel_toe strand* initially bound to the *fuel complex* gave the FRET curves in Figure 46c. Figure 46d directly compares the data to the *fuel_toe*-only reference curves in Figure 46a. As was observed for the reference, the DRN-fueled polymerization was significantly slower than its counterpart without a toehold domain (Table 19). For a five-fold excess of DRN or 1.35 mM of the initial complexes, the initial reaction rate was about ten-fold lower with 0.015 E_{FRET}/h than for the DRN-fueled polymerization without a toehold domain at initially 0.17 E_{FRET}/h. As the DRN reaction did not release the entirety of *fuel_toe strands*, the observed equilibrium FRET efficiency was also slightly lower than that of the reference with 17 % for a five-fold DRN_toe excess. Nevertheless, DRN_toe-fueled DNA origami polymerization curves were remarkably similar to their *fuel_toe*-only reference curves, as observed for the DRN without a toehold domain.

Table 19 ***Initial reaction rates and equilibrium E_{FRET} of DNA origami polymerization with complete DRN with fuel_toe***

DRN_toe excess	initial rate [E_{FRET}/h] -outer	equilibrium E_{FRET}
5x	0.015 ± 0	0.17 ± 0.01
2x	0.016 ± 0	0.15 ± 0.01

While varying $MgCl_2$ concentrations had a modest effect on the DNA origami polymerization with the unmodified *fuel strand*, the effect on the modified fu*el_toe strand* was significantly more potent (Figure 47a). Not only was there a difference in initial reaction velocity ten-fold larger with an E_{FRET} increase per hour of 0.12 for 20 mM $MgCl_2$ and only 0.01 for 12.5 mM $MgCl_2$. The equilibrium FRET efficiency differed from 23 % to 15 % for TEMg20 and TEMg12.5, respectively (Table 20). AFM imaging confirmed the effects on filament length for varying magnesium concentrations when polymerized with the *fuel_toe strand* (Figure 47b and c). Higher $MgCl_2$ concentrations yielded significantly longer filaments of up to 2 µm, demonstrating an extent of clustering seen by the decreased mica coverage. 12.5 mM of $MgCl_2$ had a higher quantity of shorter fragments and monomers.

Table 20 ***Initial reaction rates and equilibrium E_{FRET} of DNA origami polymerization with fuel_toe at different $MgCl_2$ concentrations***

$MgCl_2$ conc. [mM]	initial rate [E_{FRET}/h]	equilibrium E_{FRET}
12.5	0.01 ± 0	0.15 ± 0.01
20	0.12 ± 0	0.23 ± 0.01

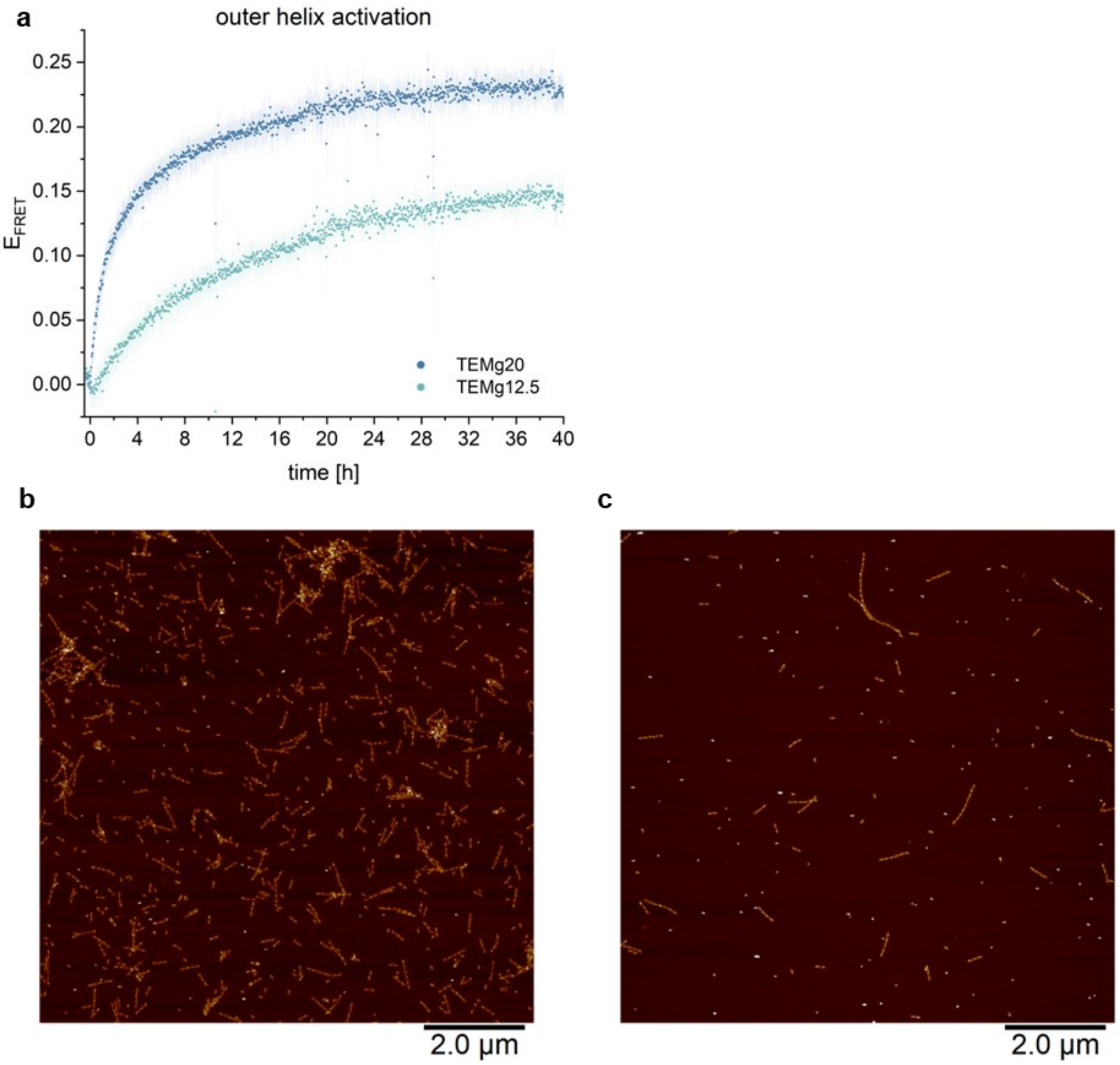

Figure 47 ***24-helix bundle polymerization via fuel_toehold at different $MgCl_2$ concentrations***
a) 15 nM PEG purified 24-helix bundle DNA origami with attached FRET pair to adjacent interface protrusions polymerized with a two-fold excess (540 nM) of fuel_toehold strand in either TEMg12.5 or TEMg20 at 40 °C for 42 h. AFM in air imaging of resulting equilibrium structures obtained from polymerization in b) TEMg12.5 or c) TEMg20 diluted to 1 nM theoretical monomer content with the respective buffer.

Usually, DNA origami filaments have been employed for the construction of long and rigid polymer structures. Here, however, the goal was to introduce the option for dynamic polymer behavior requiring an efficient structural dismantling process. Therefore, the conditions had to be optimized for two opposite reactions occurring simultaneously. A higher magnesium concentration in the TEMg20 buffer yielded nicely elongated polymers for full and outer interface activation (Supplementary Figure 10a and b) with longer filaments for the full interface and a pronounced clustering effect. However, reversing the established filaments back into monomers by remover strand addition was only mildly successful (Supplementary Figure 10c and d). Parts of the clusters were dissipated for the full interface activation, but filaments of up to 3 µm remained with very few monomers. For the outer helix interface activation, adding the remover strand resulted in more monomers compared to the full interface, but most monomers were still bound in oligomeric structures.

Subsequently, a compromise between filament elongation and dissociation was required. To facilitate filament shrinking, a lower magnesium concentration in TEMg12.5 buffer and interface activation of the outer 18 helices were chosen as a starting point. FRET curves of DNA origami monomers polymerized with a two-fold excess of *fuel_toe strands* analogous to the established conditions of Figure 46a and Figure 47a were recorded at 40 °C for 24 h. Afterward, an excess of one to ten *remover strands* per *fuel_toe strand* was introduced to the filaments while keeping the polymerization reaction conditions constant for another 40 h (Figure 48a).

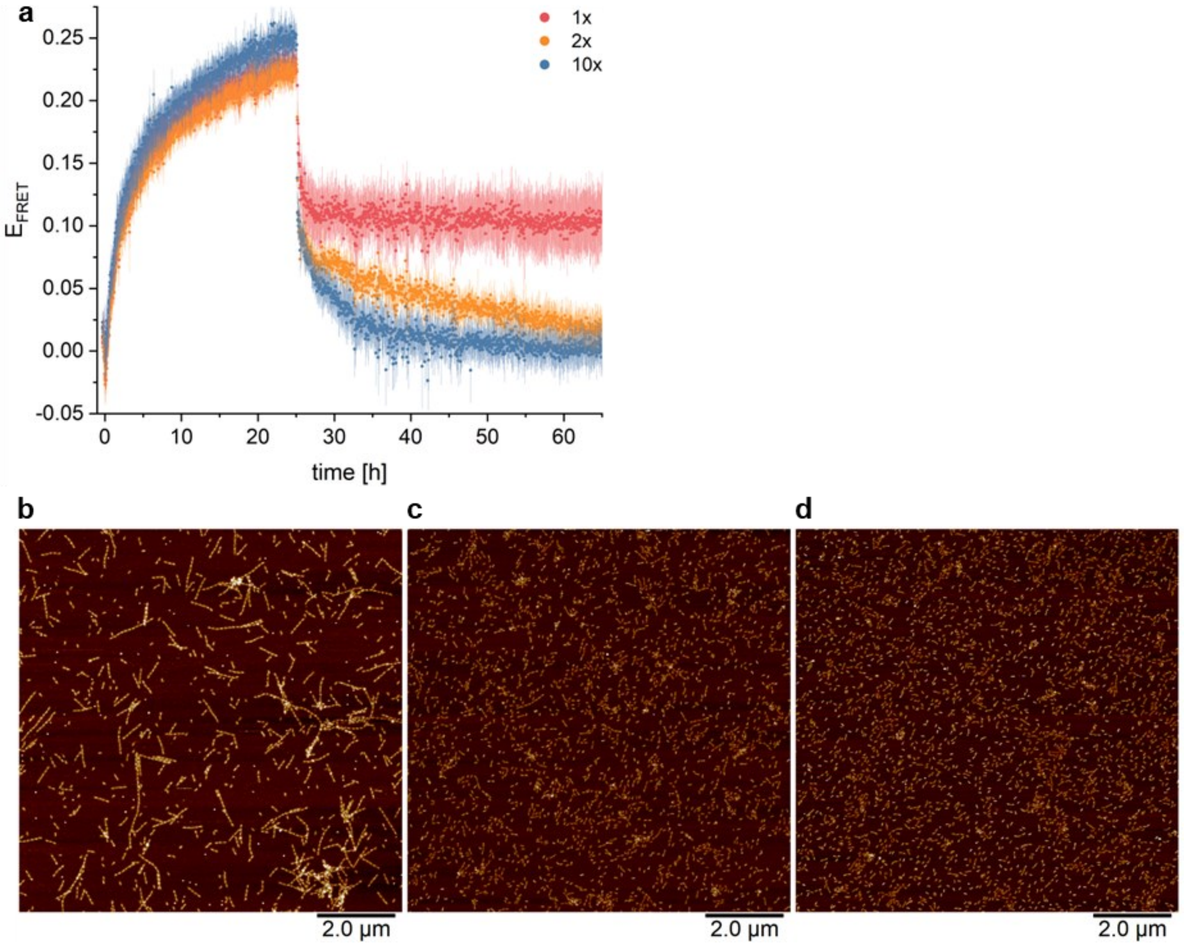

Figure 48 ***Fuel_toe-mediated polymerization with subsequent remover strand titration series***
15 nM of PEG purified 24-helix bundle DNA origami monomer with activated outer helices polymerized with a two-fold excess (540 nM) of fuel_toe strand in TEMg12.5 at 40 °C for 24 h. a) FRET curves for the polymerization reaction and subsequent addition of filament shrinkage inducing remover strand with a one-fold (540 nM), two-fold (1.08 µM), and ten-fold (5.4 µM) excess in reference to the present fuel_toe strand. AFM in air imaging of reversed polymerization after a total of 65 h with samples diluted to 1 nM DNA origami for b) one-fold, c) two-fold, and d) ten-fold of remover addition, respectively.

The filament shrinking profiles and endpoint constructs (Figure 48b - d) differed significantly depending on the added *remover strand* concentration. With an equimolar amount of *remover strands*, a sharp drop in E_{FRET} over the first few hours to a final 10 % FRET efficiency (Table 21) could be observed, resulting in many fragments between 1 µm and 2 µm and only some free monomers. For a two-fold excess, E_{FRET} slowly decreased to 2 % over 40 h, and only some minor oligomers remained visible. The ten-fold excess, however, could reverse all filament structures back into monomers over 20 h, proving the reversibility concept viable.

Table 21 ***Final E_{FRET} 40 h after remover addition to fuel_toe-mediated polymers***

remover excess	**equilibrium E_{FRET}**
1x	0.10 ± 0.03
2x	0.02 ± 0.01
10x	0.01 ± 0.01

Next, the interplay of the complete DRN with the *remover* strand at equilibrium was investigated. The initial setup was equal to that described in Figure 46c, with the outer helices of the monomer being activated and a theoretical two-fold or five-fold excess *fuel_toe complex* per interface binding site, with the *fuel* bearing a toehold for further displacement. After 42 h recorded polymerization and a two-day equilibration, a five-fold excess of *remover strand* per theoretically present *fuel_toe strand* was added to the assembled filaments (Figure 49). A complete drop in FRET efficiency was observed for both DRN and remover conditions over 30 h. Curve profiles were almost identical except for the slightly differing starting E_{FRET} values due to different *fuel_toe* excess.

As demonstrated before, the level of conversion of the DRN_toe reaction was close to 60 % (Figure 46b), with potentially slightly higher *fuel_toe* release in the presence of the DNA origami monomer and higher complex concentrations. However, in the present conditions, a good fraction of *fuel_toe strands* still remains bound within the unreacted fuel complex, limiting the boost of the DNA origami polymerization. Those *fuel_toe strands* will ultimately react with the introduced *remover strand* (Supplementary Figure 11). Therefore, coupling the DRN_toe reaction with the DNA origami polymerization will be slightly limited in the polymerization capacities, and additionally, the full extent of included *fuel_toe strands* needs to be considered for the successful reverse reaction.

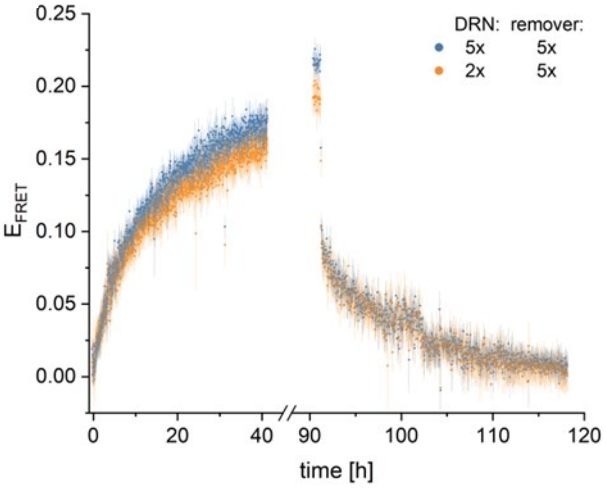

Figure 49 ***24-helix bundle polymerization with complete DRN_toe and subsequent remover strand addition***
15 nM PEG-purified 24-helix DNA origami with activated outer helices in TEMg12.5 polymerized with a theoretical excess of two-fold (540 nM, orange) and five-fold (1.35 nM, blue) DRN_toe per binding site at 40 °C for 42 h. 48 h after polymerization endpoint recording, five-fold excess of remover strand per theoretically present fuel_toe strand (2.7 µM and 6.75 µM respectively) was added to the filaments, and shrinkage was recorded for another 30 h.

So far, the effect of the *remover strand* on the endpoint polymers has been characterized. Following experiments investigated the dynamic effects on the active DNA origami polymerization process (Figure 50). For a first assessment, the less complex DNA origami polymerization driven by the individual *fuel_toe strand* was analyzed upon the addition of different remover concentrations after 6 h (Figure 50a). While an excess of 0.5-fold *remover* led to a decrease in polymerization velocity and endpoint E_{FRET}, the addition of equimolar or higher concentrations caused the subsequent shrinking of the filament structures. The extent of this effect correlated with the concentration of *remover strands*.

For the more complex system of active DRN_toe-driven DNA origami polymerization, the effect of the added *remover strand* was slightly dampened compared to the isolated *fuel_toe strand*. Adding 135 nM *remover strands* to the 24-helix bundle polymerization with 540 nM DRN complexes did not significantly decrease filament polymerization (Figure 50b, compared to Figure 47a). 270 nM to 540 nM or 0.5-fold to equimolar amounts of *remover strand* compared to the total *fuel_toe* concentration in the samples decreased the polymerization potential while not shrinking the filaments (Figure 50b and c). While equimolar amounts of *remover strands* reversed the polymerization reaction in the presence of the isolated *fuel_toe strand*, the system with an active DRN required double the amount of *removers* to reverse the polymerization.

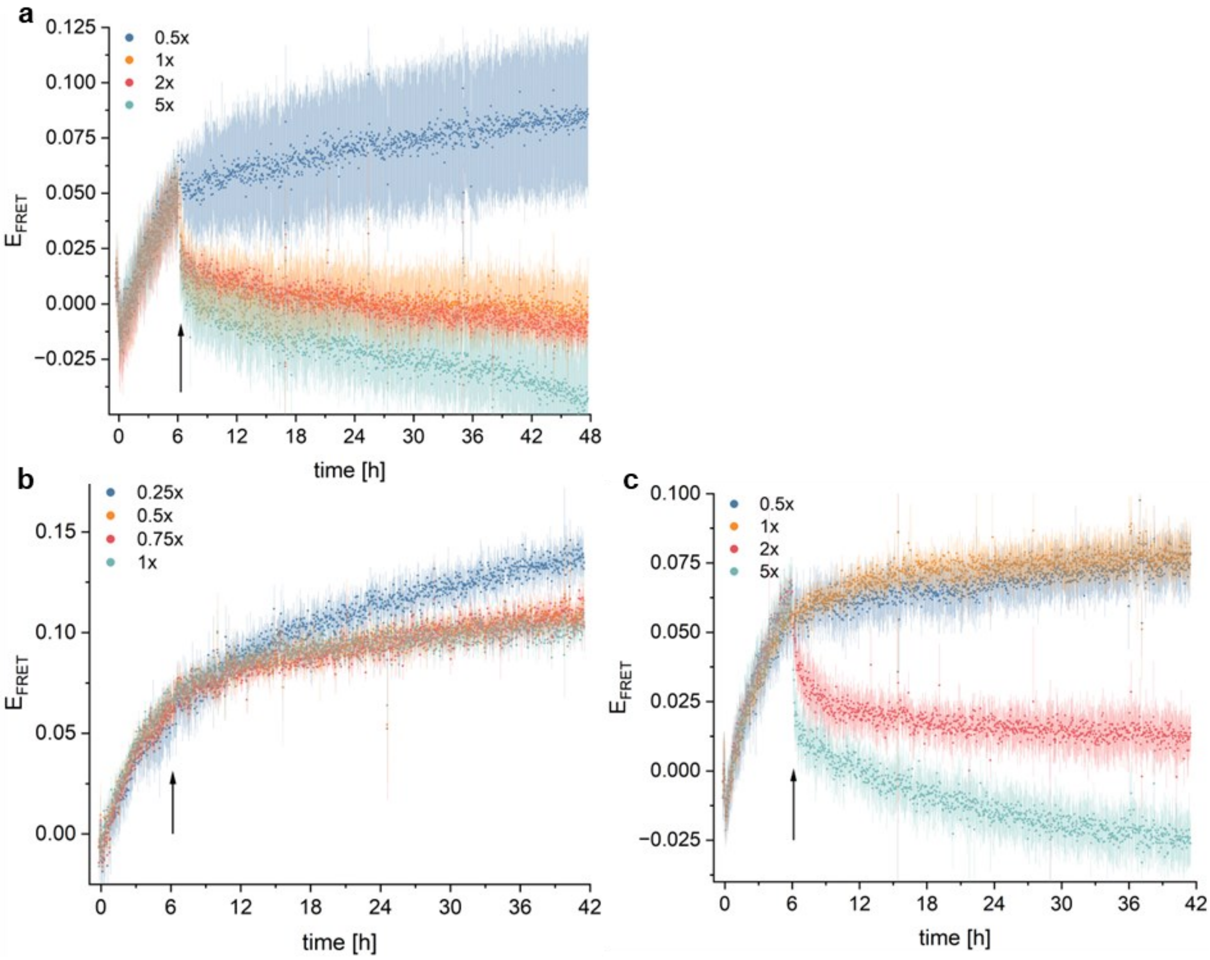

Figure 50 ***DNA origami polymerization with dynamic regulation by remover strand addition***
a) 15nM PEG-purified DNA origami with activated outer helices polymerized with a two-fold excess of fuel_toe strand (540 nM) in TEMg12.5 at 40 °C for 6 h before the addition of 270 nM to 2.7 µM (excess of 0.5x to 5x per fuel_toe strand) remover strand to the active polymerization process for 42 h. Polymerization induced instead by 540 nM of DRN_toe complexes with 2.7 µM of V and helper strands, respectively, with the addition of b) 135 nM to 540 nM (0.25x to 1x excess) or c) 270 nM to 2.7 µM (0.5x to 5x excess) remover after 6 h respectively. Arrows indicate the time point of remover strand addition.

In the case of the complex DRN system coupled to the DNA origami polymerization reaction, the *remover strand* cannot only interact with the free *fuel_toe strands* and the ones bound by the origami interface but also with the *fuel_toe* contained in the initial *fuel complex*. Therefore, a shift in equilibrium distributions is likely. Additionally, more *fuel_toe* will be released from its complex, thus driving the autocatalyzing DRN circuit (Supplementary Figure 11).

Conclusion

A chemical reaction network driven by DNA displacement reactions was used to successfully fuel a filament polymerization of DNA origami monomers. Not only this, but introducing a toehold domain and a complementary *remover strand* enabled precise control and finetuning over the polymerization process up to the complete reversing of the filament structures back into monomers. In many cases, DNA origami monomers are connected by more than 20 staple strands binding to the unpaired scaffold edges. To successfully integrate a single type of a unique connector strand, the identical complementary single-stranded regions protruded from the scaffold edges in a way similar to Groeer and Walthers's 3D DNA Origami Nanotubes[150] and were subsequently connected by the addition of the *fuel strand*. The polymerization process was monitored by the energy transfer of a pair of fluorophores bound to adjacent helices of the interfaces. Compared to the earlier studies on polymerization kinetics (see pp. 73), the recorded FRET efficiencies were lower due to the more flexible helix interactions and unideal[219] but necessary fluorophore positioning.

The velocity and degree of polymerization could be finetuned by altering the number of activated helices of the 24-helix bundle interface. Additionally, the fuel-driven polymerization was found to be dependent on the present $MgCl_2$ concentration, with a lower cation concentration slightly slowing polymerization velocity but increasing the final polymer length and decreasing clustering. The release of the modified *fuel strand* from its original complex also depended on temperature and salt conditions but was overall very satisfying. The isolated *fuel complexes* did not react with the DNA origami interface in any significant matter. When combining the DNA origami polymerization from monomer structures with the fully activated DRN, the slightly reduced *fuel strand* output had the most considerable influence on the polymerization reaction, leading to a slightly lower equilibrium FRET efficiency. Otherwise, the reaction velocity was surprisingly not affected to any noticeable extent.

The polymerization process could also be reversed by adding a five-base long toehold domain to the 5' end of the *fuel strand*, referred to as *fuel_toe*, that could be displaced from the DNA origami interface by the addition of an entirely complementary *remover strand*. The 24-helix bundle polymerization driven by the *fuel_toe strand* had a stronger dependence on the present cation concentrations and a slower polymerization rate with shorter filaments. Higher $MgCl_2$ concentrations improved these aspects while impeding the reverse process. Therefore, a balance had to be kept between ideal conditions for the forward and reverse reaction. Compared to the DRN with the original *fuel strand*, the release of the *fuel_toe strand* from the starting complex was less efficient. Otherwise, like with the *fuel strand*, the DRN had no significant effect on DNA origami polymerization. Reversing the reaction required a significant excess of *remover strands* per present *fuel_toe*. For a near 100% monomer yield, five to ten-fold excess per *fuel_toe* and about 20 h were required in optimized conditions. Adding different amounts of *remover strands* to the active polymerization could finetune the polymerization to the point of precisely reversing the reaction.

Some interesting further insights could be gained by investigating the persistence lengths of these polymers hybridized via identical protrusions when compared to those analyzed in the previous section, which were obtained by direct and mutual hybridization between the monomeric units. Additionally, further adjusting the salt and temperature conditions could finetune the polymerization process, equilibrium structures, and reversibility. Several competitive cycles of growing and shrinking with a competing and reversing reaction should also be possible. Ultimately creating an additional DRN which releases the remover strand upon internal or external inputs would lead one step closer to intelligent and dynamic reactions and networks.

Perspective

This Ph.D. thesis allowed to gain new and exciting insights into the thermodynamic and kinetic dimerization and polymerization behavior of the ditopic 24-helix DNA origami bundle. Besides, a DNA reaction network was successfully coupled to DNA origami polymerization for the first time, which could also be finetuned and reversed. Significant advances in the understanding and designing of association systems for synthetic biology applications were made.

A promising tool for DNA origami interface recognition and kinetic regulation was the one base pair gap. Previous research demonstrated the flexible capabilities of DNA stretching over individually omitted bases[39,201–203]. Now, carefully regulating the numbers of perfectly stacking, gapped, and inactive helices at an interface allows for precise control over thermal hysteresis behavior and individually addresses association and dissociation effects. This could lead to easily plannable stacking-based thermal switches, similar to the hybridization-based approaches from Tigges et al.[149] and Chen at al.[220], allowing for modular and fast adaptation to new temperature conditions using the same structure. Alternatively, such a switch could also be sensitive to ion concentrations[221,222] under isothermal conditions and give easily readable output via FRET.

In polymers, the stiffness of stacked structures connected through gapped helices could also be easily regulated by altering the number of gaps as usually done for individual bases[223]. Essentially, 1 bp gaps can be viewed as additional and easy-to-implement design parameters to manipulate kinetic and thermodynamic features of hierarchical DNA origami stacked architectures. So far, hierarchical self-assembly of DNA origami has been characterized mainly by detailed examination of the equilibrium products[136,149,152,153,224–226]. This study additionally illuminated the kinetic and energetic properties influencing the path toward equilibrium and focused in detail on the initial behavior. It is also the first time that the impact of base hybridization was compared to base stacking for identical core units. Much insight into the programmability of ditopic DNA origami polymerization has been gained. Stacking generally is superior to hybridization when it comes to reaction velocity. Reducing potential interactions by isologous self-association with gapped helices speeds up the initial reaction. However, gapped associations come with decreased long-term stability, where shape-complementarity has a significant impact. Overall, polymers assembled via hybridization take longer due to the displacement of one out of two interface binding strands but are advantageous regarding stability. These findings contribute to new input on rationally designed supramolecular polymers and advanced nano materials.

By integrating the exponential output from an enzyme-free autocatalytic DNA reaction network[181] with the supramolecular DNA origami polymerization, first insights into the manipulation of polymer dynamics could be gained. These can be used for future applications in synthetic biology and for mimicking the dynamic behavior of natural filaments. Based on dynamic approaches, DNA origami platforms have been used to assemble DNA discs into supramolecular polymers[227] or to precisely guide the chemical synthesis of inorganic polymers[228,229]. The dynamic assembly of a 1D supramolecular polymer at an air-water interface reacting to compression and expansion inputs was achieved by integrating cationic lipids into the DNA origami monomer[230]. Here, a nature-like regulator for the polymerization process was also introduced to build on the approach from Tigges et al.[149] and to add the precise control of reaction kinetics. A further improvement of this work could rely on the modification of the connecting interface whereby the fuel strand could mediate stacking or even a combination of hybridization and stacking interactions to tune the kinetics of the association/dissociation step. Additionally, competitive growing and shrinking mechanisms could be controlled through the addition of non-DNA components integrated within the fuel, which are responsive to external stimuli such as pH, light, or small molecule effectors. In this way, the two competing processes would be regulated by orthogonal inputs, enabling the optimization of individual reaction paths and minimizing unwanted cross-talks between them. Ideally, the final result would be the generation of a transient signal, whereby the onset of the DRN cycle would lead to the spontaneous growth of the polymer, followed by its autonomous shrinking until the system reaches a steady state. From a longer and even more ambitious perspective, such systems could be coupled to biochemical negative feedback loops to enable the generation of spatio-temporal oscillatory patterns.

References

(1) Stenke, L. J.; Saccà, B. Growth Rate and Thermal Properties of DNA Origami Filaments. *Nano Lett.* **2022**, *22* (22), 8818–8826. https://doi.org/10.1021/acs.nanolett.2c02255.

(2) Stenke, L. J.; Saccà, B. Design, Mechanical Properties, and Dynamics of Synthetic DNA Filaments. *Bioconjugate Chem.* **2023**, *34* (1), 37–50. https://doi.org/10.1021/acs.bioconjchem.2c00312.

(3) Winat, L. J.; Saccà, B. The Primordial Life of DNA Dynamic Networks. *Nature Catalysis* **2020**, *3* (11), 865–866. https://doi.org/10.1038/s41929-020-00536-3.

(4) Dahm, R. Discovering DNA: Friedrich Miescher and the Early Years of Nucleic Acid Research. *Hum Genet* **2008**, *122* (6), 565–581. https://doi.org/10.1007/s00439-007-0433-0.

(5) Dahm, R. Friedrich Miescher and the Discovery of DNA. *Developmental Biology* **2005**, *278* (2), 274–288. https://doi.org/10.1016/j.ydbio.2004.11.028.

(6) Altmann, R. Ueber Nucleinsäuren. *Archiv für Anatomie und Physiologie. Physiologische Abteilung Leipzig* **1889**, 524–536.

(7) Kossel, A.; Neumann, A. Über Das Thymin, Ein Spaltungsprodukt Der Nukleinsäure. *Ber. Deutsch. Chem. Ges.* **1893**, *26*, 2753–2756.

(8) Levene, P. A. THE STRUCTURE OF YEAST NUCLEIC ACID. *Journal of Biological Chemistry* **1919**, *40* (2), 415–424. https://doi.org/10.1016/S0021-9258(18)87254-4.

(9) Avery, O. T.; MacLeod, C. M.; McCarty, M. STUDIES ON THE CHEMICAL NATURE OF THE SUBSTANCE INDUCING TRANSFORMATION OF PNEUMOCOCCAL TYPES. *Journal of Experimental Medicine* **1944**, *79* (2), 137–158. https://doi.org/10.1084/jem.79.2.137.

(10) Chargaff, E. Chemical Specificity of Nucleic Acids and Mechanism of Their Enzymatic Degradation. *Experientia* **1950**, *6* (6), 201–209. https://doi.org/10.1007/BF02173653.

(11) Portin, P. The Birth and Development of the DNA Theory of Inheritance: Sixty Years since the Discovery of the Structure of DNA. *J Genet* **2014**, *93* (1), 293–302. https://doi.org/10.1007/s12041-014-0337-4.

(12) Watson, J. D.; Crick, F. H. C. Molecular Structure of Nucleic Acids: A Structure for Deoxyribose Nucleic Acid. *Nature* **1953**, *171* (4356), 737–738. https://doi.org/10.1038/171737a0.

(13) Watson, J. D.; Crick, F. H. C. Genetical Implications of the Structure of Deoxyribonucleic Acid. *Nature* **1953**, *171* (4361), 964–967. https://doi.org/10.1038/171964b0.

(14) Franklin, R. E.; Gosling, R. G. Molecular Configuration in Sodium Thymonucleate. *Nature* **1953**, *171* (4356), 740–741. https://doi.org/10.1038/171740a0.

(15) Wilkins, M. H. F.; Stokes, A. R.; Wilson, H. R. Molecular Structure of Nucleic Acids: Molecular Structure of Deoxypentose Nucleic Acids. *Nature* **1953**, *171* (4356), 738–740. https://doi.org/10.1038/171738a0.

(16) Crick, F. H. On Protein Synthesis. *Symp Soc Exp Biol* **1958**, *12*, 138–163.

(17) Crick, F. H. C.; Barnett, L.; Brenner, S.; Watts-Tobin, R. J. General Nature of the Genetic Code for Proteins. *Nature* **1961**, *192* (4809), 1227–1232. https://doi.org/10.1038/1921227a0.

(18) Crick, F. Central Dogma of Molecular Biology. *Nature* **1970**, *227* (5258), 561–563. https://doi.org/10.1038/227561a0.

(19) Oba, Y.; Takano, Y.; Furukawa, Y.; Koga, T.; Glavin, D. P.; Dworkin, J. P.; Naraoka, H. Identifying the Wide Diversity of Extraterrestrial Purine and Pyrimidine Nucleobases in Carbonaceous Meteorites. *Nat Commun* **2022**, *13* (1), 2008. https://doi.org/10.1038/s41467-022-29612-x.

(20) Neidle, S. Beyond the Double Helix: DNA Structural Diversity and the PDB. *Journal of Biological Chemistry* **2021**, *296*, 100553. https://doi.org/10.1016/j.jbc.2021.100553.

(21) Minchin, S.; Lodge, J. Understanding Biochemistry: Structure and Function of Nucleic Acids. *Essays in Biochemistry* **2019**, *63* (4), 433–456. https://doi.org/10.1042/EBC20180038.

(22) Damaschun, G.; Damaschun, H.; Misselwitz, R.; Pospelov, V. A.; Zalenskaya, I. A.; Zirwer, D.; Müller, J. J.; Vorobev, V. I. How Many Base-Pairs per Turn Does DNA Have in Solution and in Chromatin? An Answer from Wide-Angle X-Ray Scattering. *Biomed Biochim Acta* **1983**, *42* (6), 697–703.

(23) Marmur, J.; Doty, P. Determination of the Base Composition of Deoxyribonucleic Acid from Its Thermal Denaturation Temperature. *J. Mol. Biol.* **1962**, *5*, 109–118.

(24) Subirana, J. A.; Soler-López, M. Cations as Hydrogen Bond Donors: A View of Electrostatic Interactions in DNA. *Annu. Rev. Biophys. Biomol. Struct.* **2003**, *32* (1), 27–45. https://doi.org/10.1146/annurev.biophys.32.110601.141726.

(25) Wahl, M. C.; Sundaralingam, M. Crystal Structures of A-DNA Duplexes. *Biopolymers* **1997**, *44* (1), 45–63. https://doi.org/10.1002/(SICI)1097-0282(1997)44:1<45::AID-BIP4>3.0.CO;2-#.

(26) Ussery, D. W. DNA Structure: A-, B- and Z-DNA Helix Families. In *eLS*; John Wiley & Sons, Ltd, Ed.; Wiley, 2002. https://doi.org/10.1038/npg.els.0003122.

(27) Rich, A.; Nordheim, A.; Wang, A. H.-J. THE CHEMISTRY AND BIOLOGY OF LEFT-HANDED Z-DNA. *Annu. Rev. Biochem.* **1984**, *53* (1), 791–846. https://doi.org/10.1146/annurev.bi.53.070184.004043.

(28) Sponer, J.; Leszczynski, J.; Hobza, P. Electronic Properties, Hydrogen Bonding, Stacking, and Cation Binding of DNA and RNA Bases. *Biopolymers* **2001**, *61* (1), 3–31. https://doi.org/10.1002/1097-0282(2001)61:1<3::AID-BIP10048>3.0.CO;2-4.

(29) Hunter, C. A. Sequence-Dependent DNA Structure. *Bioessays* **1996**, *18* (2), 157–162. https://doi.org/10.1002/bies.950180212.

(30) Altun, A.; Garcia-Ratés, M.; Neese, F.; Bistoni, G. Unveiling the Complex Pattern of Intermolecular Interactions Responsible for the Stability of the DNA Duplex. *Chem. Sci.* **2021**, *12* (38), 12785–12793. https://doi.org/10.1039/D1SC03868K.

(31) Kruse, H.; Banáš, P.; Šponer, J. Investigations of Stacked DNA Base-Pair Steps: Highly Accurate Stacking Interaction Energies, Energy Decomposition, and Many-Body Stacking Effects. *J. Chem. Theory Comput.* **2019**, *15* (1), 95–115. https://doi.org/10.1021/acs.jctc.8b00643.

(32) Matta, C. F.; Castillo, N.; Boyd, R. J. Extended Weak Bonding Interactions in DNA: π-Stacking (Base−Base), Base−Backbone, and Backbone−Backbone Interactions. *J. Phys. Chem. B* **2006**, *110* (1), 563–578. https://doi.org/10.1021/jp054986g.

(33) DeVoe, H.; Tinoco, I. The Stability of Helical Polynucleotides: Base Contributions. *Journal of Molecular Biology* **1962**, *4* (6), 500–517. https://doi.org/10.1016/S0022-2836(62)80105-3.

(34) Crothers, D. M.; Zimm, B. H. Theory of the Melting Transition of Synthetic Polynucleotides: Evaluation of the Stacking Free Energy. *Journal of Molecular Biology* **1964**, *9* (1), 1–9. https://doi.org/10.1016/S0022-2836(64)80086-3.

(35) Huguet, J. M.; Ribezzi-Crivellari, M.; Bizarro, C. V.; Ritort, F. Derivation of Nearest-Neighbor DNA Parameters in Magnesium from Single Molecule Experiments. *Nucleic Acids Research* **2017**, *45* (22), 12921–12931. https://doi.org/10.1093/nar/gkx1161.

(36) Mak, C. H. Unraveling Base Stacking Driving Forces in DNA. *The Journal of Physical Chemistry B* **2016**, *120* (26), 6010–6020. https://doi.org/10.1021/acs.jpcb.6b01934.

(37) Vendeix, F. A. P.; Munoz, A. M.; Agris, P. F. Free Energy Calculation of Modified Base-Pair Formation in Explicit Solvent: A Predictive Model. *RNA* **2009**, *15* (12), 2278–2287. https://doi.org/10.1261/rna.1734309.

(38) Zhang, T.; Zhang, C.; Dong, Z.; Guan, Y. Determination of Base Binding Strength and Base Stacking Interaction of DNA Duplex Using Atomic Force Microscope. *Scientific Reports* **2015**, *5* (1). https://doi.org/10.1038/srep09143.

(39) Yakovchuk, P.; Protozanova, rina; Frank-Kamenetskii, D. Base-Stacking and Base-Pairing Contributions into Thermal Stability of the DNA Double Helix. *Nucleic Acids Research* **2006**, *34* (2), 564–574. https://doi.org/10.1093/nar/gkj454.

(40) Duckett, D. R.; Murchie, A. I.; Lilley, D. M. The Role of Metal Ions in the Conformation of the Four-Way DNA Junction. *EMBO J.* **1990**, *9* (2), 583–590.

(41) Owczarzy, R.; You, Y.; Moreira, B. G.; Manthey, J. A.; Huang, L.; Behlke, M. A.; Walder, J. A. Effects of Sodium Ions on DNA Duplex Oligomers: Improved Predictions of Melting Temperatures. *Biochemistry* **2004**, *43* (12), 3537–3554. https://doi.org/10.1021/bi034621r.

(42) Krautbauer, R.; Rief, M.; Gaub, H. E. Unzipping DNA Oligomers. *Nano Lett.* **2003**, *3* (4), 493–496. https://doi.org/10.1021/nl034049p.

(43) Vologodskii, A.; Frank-Kamenetskii, M. D. DNA Melting and Energetics of the Double Helix. *Physics of Life Reviews* **2018**, *25*, 1–21. https://doi.org/10.1016/j.plrev.2017.11.012.

(44) Protozanova, E.; Yakovchuk, P.; Frank-Kamenetskii, M. D. Stacked–Unstacked Equilibrium at the Nick Site of DNA. *Journal of Molecular Biology* **2004**, *342* (3), 775–785. https://doi.org/10.1016/j.jmb.2004.07.075.

(45) Barone, G.; Fonseca Guerra, C.; Bickelhaupt, F. M. B-DNA Structure and Stability as Function of Nucleic Acid Composition: Dispersion-Corrected DFT Study of Dinucleoside Monophosphate Single and Double Strands. *ChemistryOpen* **2013**, *2* (5–6), 186–193. https://doi.org/10.1002/open.201300019.

(46) Vaitiekunas, P.; Crane-Robinson, C.; Privalov, P. L. The Energetic Basis of the DNA Double Helix: A Combined Microcalorimetric Approach. *Nucleic Acids Res* **2015**, *43* (17), 8577–8589. https://doi.org/10.1093/nar/gkv812.

(47) Kilchherr, F.; Wachauf, C.; Pelz, B.; Rief, M.; Zacharias, M.; Dietz, H. Single-Molecule Dissection of Stacking Forces in DNA. *Science* **2016**, *353* (6304), aaf5508–aaf5508. https://doi.org/10.1126/science.aaf5508.

(48) Zacharias, M. *Base Pairing and Stacking Contributions to Double Stranded DNA Formation*; preprint; Biophysics, 2020. https://doi.org/10.1101/2020.08.22.262667.

(49) Szalewicz, K. Hydrogen Bond. In *Encyclopedia of Physical Science and Technology*; Elsevier, 2003; pp 505–538. https://doi.org/10.1016/B0-12-227410-5/00322-7.

(50) Mo, Y. Probing the Nature of Hydrogen Bonds in DNA Base Pairs. *J Mol Model* **2006**, *12* (5), 665–672. https://doi.org/10.1007/s00894-005-0021-y.

(51) Nieuwland, C.; Hamlin, T. A.; Fonseca Guerra, C.; Barone, G.; Bickelhaupt, F. M. B-DNA Structure and Stability: The Role of Nucleotide Composition and Order. *ChemistryOpen* **2022**, *11* (2). https://doi.org/10.1002/open.202100231.

(52) Feynman, R. P. There's Plenty of Room at the Bottom. *Engineering and Science* **1960**, *23* (5), 22–36.

(53) Taniguchi, N.; Arakawa, C.; Kobayashi, T. On the Basic Concept of Nano-Technology. *Proceedings of the International Conference on Production Engineering Tokyo. Japan* **1974**, 26–29.

(54) Drexler, K. E. *Engines of Creation: The Coming Era of Nanotechnology*, 6. [print.].; Anchor books; Doubleday: New York, 1990.

(55) Toumey, C. 35 Atoms That Changed the Nanoworld. *Nature Nanotech* **2010**, *5* (4), 239–241. https://doi.org/10.1038/nnano.2010.61.

(56) Eigler, D. M.; Schweizer, E. K. Positioning Single Atoms with a Scanning Tunnelling Microscope. *Nature* **1990**, *344* (6266), 524–526. https://doi.org/10.1038/344524a0.

(57) Bayda, S.; Adeel, M.; Tuccinardi, T.; Cordani, M.; Rizzolio, F. The History of Nanoscience and Nanotechnology: From Chemical–Physical Applications to Nanomedicine. *Molecules* **2019**, *25* (1), 112. https://doi.org/10.3390/molecules25010112.

(58) Liu, Y.; Mai, S.; Li, N.; Yiu, C. K. Y.; Mao, J.; Pashley, D. H.; Tay, F. R. Differences between Top-down and Bottom-up Approaches in Mineralizing Thick, Partially Demineralized Collagen Scaffolds. *Acta Biomaterialia* **2011**, *7* (4), 1742–1751. https://doi.org/10.1016/j.actbio.2010.11.028.

(59) McNeil, S. E. Nanotechnology for the Biologist. *Journal of Leukocyte Biology* **2005**, *78* (3), 585–594. https://doi.org/10.1189/jlb.0205074.

(60) Mehnath, S.; Das, A. K.; Verma, S. K.; Jeyaraj, M. Biosynthesized/Green-Synthesized Nanomaterials as Potential Vehicles for Delivery of Antibiotics/Drugs. In *Comprehensive Analytical Chemistry*; Elsevier, 2021; Vol. 94, pp 363–432. https://doi.org/10.1016/bs.coac.2020.12.011.

(61) Hou, X.; Zaks, T.; Langer, R.; Dong, Y. Lipid Nanoparticles for MRNA Delivery. *Nat Rev Mater* **2021**, *6* (12), 1078–1094. https://doi.org/10.1038/s41578-021-00358-0.

(62) Gür, F. N.; Schwarz, F. W.; Ye, J.; Diez, S.; Schmidt, T. L. Toward Self-Assembled Plasmonic Devices: High-Yield Arrangement of Gold Nanoparticles on DNA Origami Templates. *ACS Nano* **2016**, *10* (5), 5374–5382. https://doi.org/10.1021/acsnano.6b01537.

(63) Xia, H.; Bai, S.; Hartmann, J.; Wang, D. Synthesis of Monodisperse Quasi-Spherical Gold Nanoparticles in Water via Silver(I)-Assisted Citrate Reduction. *Langmuir* **2010**, *26* (5), 3585–3589. https://doi.org/10.1021/la902987w.

(64) Mody, V.; Siwale, R.; Singh, A.; Mody, H. Introduction to Metallic Nanoparticles. *J Pharm Bioall Sci* **2010**, *2* (4), 282. https://doi.org/10.4103/0975-7406.72127.

(65) Holmannova, D.; Borsky, P.; Svadlakova, T.; Borska, L.; Fiala, Z. Carbon Nanoparticles and Their Biomedical Applications. *Applied Sciences* **2022**, *12* (15), 7865. https://doi.org/10.3390/app12157865.

(66) Huang, J.; Gambietz, S.; Saccà, B. Self-Assembled Artificial DNA Nanocompartments and Their Bioapplications. *Small* **2022**, 2202253. https://doi.org/10.1002/smll.202202253.

(67) Chen, X.-J.; Zhang, X.-Q.; Liu, Q.; Zhang, J.; Zhou, G. Nanotechnology: A Promising Method for Oral Cancer Detection and Diagnosis. *J Nanobiotechnol* **2018**, *16* (1), 52. https://doi.org/10.1186/s12951-018-0378-6.

(68) Seo, G.; Lee, G.; Kim, M. J.; Baek, S.-H.; Choi, M.; Ku, K. B.; Lee, C.-S.; Jun, S.; Park, D.; Kim, H. G.; Kim, S.-J.; Lee, J.-O.; Kim, B. T.; Park, E. C.; Kim, S. I. Rapid Detection of COVID-19 Causative Virus (SARS-CoV-2) in Human Nasopharyngeal Swab Specimens Using Field-Effect Transistor-Based Biosensor. *ACS Nano* **2020**, *14* (4), 5135–5142. https://doi.org/10.1021/acsnano.0c02823.

(69) Pfeiffer, M.; Trofymchuk, K.; Ranallo, S.; Ricci, F.; Steiner, F.; Cole, F.; Glembockyte, V.; Tinnefeld, P. Single Antibody Detection in a DNA Origami Nanoantenna. *iScience* **2021**, *24* (9), 103072. https://doi.org/10.1016/j.isci.2021.103072.

(70) Wei, Q.; Zhang, P.; Liu, T.; Pu, H.; Sun, D.-W. A Fluorescence Biosensor Based on Single-Stranded DNA and Carbon Quantum Dots for Acrylamide Detection. *Food Chemistry* **2021**, *356*, 129668. https://doi.org/10.1016/j.foodchem.2021.129668.

(71) Kamaci, U. D.; Kamaci, M. Selective and Sensitive ZnO Quantum Dots Based Fluorescent Biosensor for Detection of Cysteine. *J Fluoresc* **2021**, *31* (2), 401–414. https://doi.org/10.1007/s10895-020-02671-3.

(72) Ramesh, M.; Janani, R.; Deepa, C.; Rajeshkumar, L. Nanotechnology-Enabled Biosensors: A Review of Fundamentals, Design Principles, Materials, and Applications. *Biosensors* **2022**, *13* (1), 40. https://doi.org/10.3390/bios13010040.

(73) Mahshid, S. S.; Camiré, S.; Ricci, F.; Vallée-Bélisle, A. A Highly Selective Electrochemical DNA-Based Sensor That Employs Steric Hindrance Effects to Detect Proteins Directly in Whole Blood. *J. Am. Chem. Soc.* **2015**, *137* (50), 15596–15599. https://doi.org/10.1021/jacs.5b04942.

(74) Peng, B.; Locascio, M.; Zapol, P.; Li, S.; Mielke, S. L.; Schatz, G. C.; Espinosa, H. D. Measurements of Near-Ultimate Strength for Multiwalled Carbon Nanotubes and Irradiation-Induced Crosslinking Improvements. *Nature Nanotech* **2008**, *3* (10), 626–631. https://doi.org/10.1038/nnano.2008.211.

(75) Tang, Z. K.; Zhang, L.; Wang, N.; Zhang, X. X.; Wen, G. H.; Li, G. D.; Wang, J. N.; Chan, C. T.; Sheng, P. Superconductivity in 4 Angstrom Single-Walled Carbon Nanotubes. *Science* **2001**, *292* (5526), 2462–2465. https://doi.org/10.1126/science.1060470.

(76) Ramsden, J. J. Bionanotechnology. In *Nanotechnology*; Elsevier, 2016; pp 263–278. https://doi.org/10.1016/B978-0-323-39311-9.00017-0.

(77) Maheshwari, R.; Joshi, G.; Mishra, D. K.; Tekade, R. K. Bionanotechnology in Pharmaceutical Research. In *Basic Fundamentals of Drug Delivery*; Elsevier, 2019; pp 449–471. https://doi.org/10.1016/B978-0-12-817909-3.00012-1.

(78) Seeman, N. C. Nucleic Acid Junctions and Lattices. *J Theor Biol* **1982**, *99* (2), 237–247.

(79) Eichman, B. F.; Ortiz-Lombardía, M.; Aymamí, J.; Coll, M.; Ho, P. S. The Inherent Properties of DNA Four-Way Junctions: Comparing the Crystal Structures of Holliday Junctions. *Journal of Molecular Biology* **2002**, *320* (5), 1037–1051. https://doi.org/10.1016/S0022-2836(02)00540-5.

(80) Song, Q.; Hu, Y.; Yin, A.; Wang, H.; Yin, Q. DNA Holliday Junction: History, Regulation and Bioactivity. *IJMS* **2022**, *23* (17), 9730. https://doi.org/10.3390/ijms23179730.

(81) Seeman, N. C.; Kallenbach, N. R. DNA Branched Junctions. *Annu Rev Biophys Biomol Struct* **1994**, *23*, 53–86.

(82) Canary, J. W.; Yan, H. Nadrian C. (Ned) Seeman (1945–2021). *Nat. Nanotechnol.* **2022**, *17* (2), 108–108. https://doi.org/10.1038/s41565-021-01065-1.

(83) Seeman, N. C. DNA Nanotechnology. *Materials Today* **2003**, *6* (1), 24–29. https://doi.org/10.1016/S1369-7021(03)00129-9.

(84) Wang, Y.; Mueller, J. E.; Kemper, B.; Seeman, N. C. Assembly and Characterization of Five-Arm and Six-Arm DNA Branched Junctions. *Biochemistry* **1991**, *30* (23), 5667–5674. https://doi.org/10.1021/bi00237a005.

(85) Fu, T. J.; Seeman, N. C. DNA Double-Crossover Molecules. *Biochemistry* **1993**, *32* (13), 3211–3220. https://doi.org/10.1021/bi00064a003.

(86) Wang, W.; Lin, T.; Zhang, S.; Bai, T.; Mi, Y.; Wei, B. Self-Assembly of Fully Addressable DNA Nanostructures from Double Crossover Tiles. *Nucleic Acids Res* **2016**, *44* (16), 7989–7996. https://doi.org/10.1093/nar/gkw670.

(87) Hill, A. C.; Hall, J. High-Order Structures from Nucleic Acids for Biomedical Applications. *Mater. Chem. Front.* **2020**, *4* (4), 1074–1088. https://doi.org/10.1039/C9QM00638A.

(88) Liu, D.; Park, S. H.; Reif, J. H.; LaBean, T. H. DNA Nanotubes Self-Assembled from Triple-Crossover Tiles as Templates for Conductive Nanowires. *Proc Natl Acad Sci U S A* **2004**, *101* (3), 717–722.

(89) Agrawal, D. K.; Jiang, R.; Reinhart, S.; Mohammed, A. M.; Jorgenson, T. D.; Schulman, R. Terminating DNA Tile Assembly with Nanostructured Caps. *ACS Nano* **2017**, *11* (10), 9770–9779. https://doi.org/10.1021/acsnano.7b02256.

(90) Seeman, N. C.; Sleiman, H. F. DNA Nanotechnology. *Nat Rev Mater* **2017**, *3* (1), 17068. https://doi.org/10.1038/natrevmats.2017.68.

(91) Goodman, R. P.; Heilemann, M.; Doose, S.; Erben, C. M.; Kapanidis, A. N.; Turberfield, A. J. Reconfigurable, Braced, Three-Dimensional DNA Nanostructures. *Nature Nanotech* **2008**, *3* (2), 93–96. https://doi.org/10.1038/nnano.2008.3.

(92) Pinheiro, A. V.; Han, D.; Shih, W. M.; Yan, H. Challenges and Opportunities for Structural DNA Nanotechnology. *Nature Nanotech* **2011**, *6* (12), 763–772. https://doi.org/10.1038/nnano.2011.187.

(93) Rothemund, P. W. K. Folding DNA to Create Nanoscale Shapes and Patterns. *Nature* **2006**, *440* (7082), 297–302. https://doi.org/10.1038/nature04586.

(94) Yan, H.; LaBean, T. H.; Feng, L.; Reif, J. H. Directed Nucleation Assembly of DNA Tile Complexes for Barcode-Patterned Lattices. *Proc. Natl. Acad. Sci. U.S.A.* **2003**, *100* (14), 8103–8108. https://doi.org/10.1073/pnas.1032954100.

(95) Shih, W. M.; Quispe, J. D.; Joyce, G. F. A 1.7-Kilobase Single-Stranded DNA That Folds into a Nanoscale Octahedron. *Nature* **2004**, *427* (6975), 618–621. https://doi.org/10.1038/nature02307.

(96) Dey, S.; Fan, C.; Gothelf, K. V.; Li, J.; Lin, C.; Liu, L.; Liu, N.; Nijenhuis, M. A. D.; Saccà, B.; Simmel, F. C.; Yan, H.; Zhan, P. DNA Origami. *Nat Rev Methods Primers* **2021**, *1* (1), 13. https://doi.org/10.1038/s43586-020-00009-8.

(97) Douglas, S. M.; Marblestone, A. H.; Teerapittayanon, S.; Vazquez, A.; Church, G. M.; Shih, W. M. Rapid Prototyping of 3D DNA-Origami Shapes with CaDNAno. *Nucleic Acids Research* **2009**, *37* (15), 5001–5006. https://doi.org/10.1093/nar/gkp436.

(98) Douglas, S. M.; Chou, J. J.; Shih, W. M. DNA-Nanotube-Induced Alignment of Membrane Proteins for NMR Structure Determination. *Proceedings of the National Academy of Sciences* **2007**, *104* (16), 6644–6648. https://doi.org/10.1073/pnas.0700930104.

(99) de Llano, E.; Miao, H.; Ahmadi, Y.; Wilson, A. J.; Beeby, M.; Viola, I.; Barisic, I. Adenita: Interactive 3D Modelling and Visualization of DNA Nanostructures. *Nucleic Acids Research* **2020**, *48* (15), 8269–8275. https://doi.org/10.1093/nar/gkaa593.

(100) Kopielski, A.; Schneider, A.; Csáki, A.; Fritzsche, W. Isothermal DNA Origami Folding: Avoiding Denaturing Conditions for One-Pot, Hybrid-Component

Annealing. *Nanoscale* **2015**, *7* (5), 2102–2106. https://doi.org/10.1039/C4NR04176C.

(101) Sobczak, J.-P. J.; Martin, T. G.; Gerling, T.; Dietz, H. Rapid Folding of DNA into Nanoscale Shapes at Constant Temperature. *Science* **2012**, *338* (6113), 1458–1461. https://doi.org/10.1126/science.1229919.

(102) Dunn, K. E.; Dannenberg, F.; Ouldridge, T. E.; Kwiatkowska, M.; Turberfield, A. J.; Bath, J. Guiding the Folding Pathway of DNA Origami. *Nature* **2015**, *525* (7567), 82–86. https://doi.org/10.1038/nature14860.

(103) Schneider, F.; Möritz, N.; Dietz, H. The Sequence of Events during Folding of a DNA Origami. *Sci. Adv.* **2019**, *5* (5), eaaw1412. https://doi.org/10.1126/sciadv.aaw1412.

(104) Wagenbauer, K. F.; Engelhardt, F. A. S.; Stahl, E.; Hechtl, V. K.; Stömmer, P.; Seebacher, F.; Meregalli, L.; Ketterer, P.; Gerling, T.; Dietz, H. How We Make DNA Origami. *Chembiochem* **2017**, *18* (19), 1873–1885. https://doi.org/10.1002/cbic.201700377.

(105) Majikes, J. M.; Patrone, P. N.; Kearsley, A. J.; Zwolak, M.; Liddle, J. A. Failure Mechanisms in DNA Self-Assembly: Barriers to Single-Fold Yield. *ACS Nano* **2021**, *15* (2), 3284–3294. https://doi.org/10.1021/acsnano.0c10114.

(106) Andersen, E. S.; Dong, M.; Nielsen, M. M.; Jahn, K.; Lind-Thomsen, A.; Mamdouh, W.; Gothelf, K. V.; Besenbacher, F.; Kjems, J. DNA Origami Design of Dolphin-Shaped Structures with Flexible Tails. *ACS Nano* **2008**, *2* (6), 1213–1218. https://doi.org/10.1021/nn800215j.

(107) Dietz, H.; Douglas, S. M.; Shih, W. M. Folding DNA into Twisted and Curved Nanoscale Shapes. *Science* **2009**, *325* (5941), 725–730.

(108) Wagenbauer, K. F.; Sigl, C.; Dietz, H. Gigadalton-Scale Shape-Programmable DNA Assemblies. *Nature* **2017**, *552* (7683), 78–83. https://doi.org/10.1038/nature24651.

(109) Yao, G.; Zhang, F.; Wang, F.; Peng, T.; Liu, H.; Poppleton, E.; Šulc, P.; Jiang, S.; Liu, L.; Gong, C.; Jing, X.; Liu, X.; Wang, L.; Liu, Y.; Fan, C.; Yan, H. Meta-DNA Structures. *Nat. Chem.* **2020**, *12* (11), 1067–1075. https://doi.org/10.1038/s41557-020-0539-8.

(110) Erkelenz, M.; Kosinski, R.; Giesler, H.; Sritharan, O.; Jose, J.; Saccà, B.; Schlücker, S. A Switchable DNA Origami/Plasmonic Hybrid Device with a Precisely Tuneable DNA-Free Interparticle Gap. *Chem. Commun.* **2022**, *58* (97), 13479–13482. https://doi.org/10.1039/D2CC05324A.

(111) Zhang, D. Y.; Seelig, G. Dynamic DNA Nanotechnology Using Strand-Displacement Reactions. *Nat Chem* **2011**, *3* (2), 103–113.

(112) Yurke, B.; Turberfield, A. J.; Mills, A. P.; Simmel, F. C.; Neumann, J. L. A DNA-Fuelled Molecular Machine Made of DNA. *Nature* **2000**, *406* (6796), 605–608. https://doi.org/10.1038/35020524.

(113) Gerling, T.; Wagenbauer, K. F.; Neuner, A. M.; Dietz, H. Dynamic DNA Devices and Assemblies Formed by Shape-Complementary, Non-Base Pairing 3D Components. *Science* **2015**, *347* (6229), 1446–1452. https://doi.org/10.1126/science.aaa5372.

(114) Wang, J.; Li, Z.; Willner, I. Dynamic Reconfigurable DNA Nanostructures, Networks and Materials. *Angew Chem Int Ed* **2023**. https://doi.org/10.1002/anie.202215332.

(115) Ge, Z.; Gu, H.; Li, Q.; Fan, C. Concept and Development of Framework Nucleic Acids. *J. Am. Chem. Soc.* **2018**, *140* (51), 17808–17819. https://doi.org/10.1021/jacs.8b10529.

(116) Hong, F.; Zhang, F.; Liu, Y.; Yan, H. DNA Origami: Scaffolds for Creating Higher Order Structures. *Chem Rev* **2017**, *117* (20), 12584–12640.

(117) Shani, L.; Tinnefeld, P.; Fleger, Y.; Sharoni, A.; Shapiro, B. Ya.; Shaulov, A.; Gang, O.; Yeshurun, Y. DNA Origami Based Superconducting Nanowires. *AIP Advances* **2021**, *11* (1), 015130. https://doi.org/10.1063/5.0029781.

(118) Yan, H.; Park, S. H.; Finkelstein, G.; Reif, J. H.; LaBean, T. H. DNA-Templated Self-Assembly of Protein Arrays and Highly Conductive Nanowires. *Science* **2003**, *301* (5641), 1882–1884.

(119) Kuzyk, A.; Schreiber, R.; Fan, Z.; Pardatscher, G.; Roller, E.-M.; Högele, A.; Simmel, F. C.; Govorov, A. O.; Liedl, T. DNA-Based Self-Assembly of Chiral Plasmonic Nanostructures with Tailored Optical Response. *Nature* **2012**, *483* (7389), 311–314. https://doi.org/10.1038/nature10889.

(120) Zhang, Y.; Mao, X.; Li, F.; Li, M.; Jing, X.; Ge, Z.; Wang, L.; Liu, K.; Zhang, H.; Fan, C.; Zuo, X. Nanoparticle-Assisted Alignment of Carbon Nanotubes on DNA Origami. *Angew. Chem. Int. Ed.* **2020**, *59* (12), 4892–4896. https://doi.org/10.1002/anie.201916043.

(121) Steinhauer, C.; Jungmann, R.; Sobey, T.; Simmel, F.; Tinnefeld, P. DNA Origami as a Nanoscopic Ruler for Super-Resolution Microscopy. *Angew. Chem. Int. Ed.* **2009**, *48* (47), 8870–8873. https://doi.org/10.1002/anie.200903308.

(122) Kosinski, R.; Perez, J. M.; Schöneweiß, E.-C.; Ruiz-Blanco, Y. B.; Ponzo, I.; Bravo-Rodriguez, K.; Erkelenz, M.; Schlücker, S.; Uhlenbrock, G.; Sanchez-Garcia, E.; Saccà, B. The Role of DNA Nanostructures in the Catalytic Properties of an Allosterically Regulated Protease. *Sci. Adv.* **2022**, *8* (1), eabk0425. https://doi.org/10.1126/sciadv.abk0425.

(123) Fu, J.; Liu, M.; Liu, Y.; Woodbury, N. W.; Yan, H. Interenzyme Substrate Diffusion for an Enzyme Cascade Organized on Spatially Addressable DNA Nanostructures. *J. Am. Chem. Soc.* **2012**, *134* (12), 5516–5519. https://doi.org/10.1021/ja300897h.

(124) Douglas, S. M.; Bachelet, I.; Church, G. M. A Logic-Gated Nanorobot for Targeted Transport of Molecular Payloads. *Science* **2012**, *335* (6070), 831–834. https://doi.org/10.1126/science.1214081.

(125) Kopperger, E.; List, J.; Madhira, S.; Rothfischer, F.; Lamb, D. C.; Simmel, F. C. A Self-Assembled Nanoscale Robotic Arm Controlled by Electric Fields. *Science* **2018**, *359* (6373), 296–301. https://doi.org/10.1126/science.aao4284.

(126) Katiyar, N. K.; Goel, G.; Hawi, S.; Goel, S. Nature-Inspired Materials: Emerging Trends and Prospects. *NPG Asia Mater* **2021**, *13* (1), 56. https://doi.org/10.1038/s41427-021-00322-y.

(127) Hirschi, S.; Ward, T. R.; Meier, W. P.; Müller, D. J.; Fotiadis, D. Synthetic Biology: Bottom-Up Assembly of Molecular Systems. *Chem. Rev.* **2022**, *122* (21), 16294–16328. https://doi.org/10.1021/acs.chemrev.2c00339.

(128) Benner, S. A.; Sismour, A. M. Synthetic Biology. *Nat Rev Genet* **2005**, *6* (7), 533–543. https://doi.org/10.1038/nrg1637.

(129) Alberts, B.; Johnson, A.; Lewis, J.; Raff, M.; Roberts, K.; Walter, P. *Molecular Biology of the Cell*, 5th ed.; Garland Science, 2008.

(130) Guo, K.; Shillcock, J.; Lipowsky, R. Self-Assembly of Actin Monomers into Long Filaments: Brownian Dynamics Simulations. *The Journal of Chemical Physics* **2009**, *131* (1), 015102. https://doi.org/10.1063/1.3159003.

(131) Gurung, R.; Yadav, R.; Brungardt, J. G.; Orlova, A.; Egelman, E. H.; Beck, M. R. Actin Polymerization Is Stimulated by Actin Cross-Linking Protein Palladin. *Biochemical Journal* **2016**, *473* (4), 383–396. https://doi.org/10.1042/BJ20151050.

(132) Borisy, G.; Heald, R.; Howard, J.; Janke, C.; Musacchio, A.; Nogales, E. Microtubules: 50 Years on from the Discovery of Tubulin. *Nat Rev Mol Cell Biol* **2016**, *17* (5), 322–328. https://doi.org/10.1038/nrm.2016.45.

(133) Apel, D.; Surette, M. G. Bringing Order to a Complex Molecular Machine: The Assembly of the Bacterial Flagella. *Biochimica et Biophysica Acta (BBA) - Biomembranes* **2008**, *1778* (9), 1851–1858. https://doi.org/10.1016/j.bbamem.2007.07.005.

(134) Yonekura, K. Growth Mechanism of the Bacterial Flagellar Filament. *Research in Microbiology* **2002**, *153* (4), 191–197. https://doi.org/10.1016/S0923-2508(02)01308-6.

(135) Rest, C.; Kandanelli, R.; Fernández, G. Strategies to Create Hierarchical Self-Assembled Structures via Cooperative Non-Covalent Interactions. *Chemical Society Reviews* **2015**, *44* (8), 2543–2572. https://doi.org/10.1039/C4CS00497C.

(136) Pfeifer, W.; Lill, P.; Gatsogiannis, C.; Saccà, B. Hierarchical Assembly of DNA Filaments with Designer Elastic Properties. *ACS Nano* **2017**, *12* (1), 44–55. https://doi.org/10.1021/acsnano.7b06012.

(137) Dominguez, R.; Holmes, K. C. Actin Structure and Function. *Annu. Rev. Biophys.* **2011**, *40* (1), 169–186. https://doi.org/10.1146/annurev-biophys-042910-155359.

(138) Perrin, B. J.; Ervasti, J. M. The Actin Gene Family: Function Follows Isoform. *Cytoskeleton* **2010**, *67* (10), 630–634. https://doi.org/10.1002/cm.20475.

(139) Wong, I. Y.; Footer, M. J.; Melosh, N. A. Electronically Activated Actin Protein Polymerization and Alignment. *J. Am. Chem. Soc.* **2008**, *130* (25), 7908–7915. https://doi.org/10.1021/ja7103284.

(140) Pollard, T. D. Mechanism of Actin Filament Self-Assembly and Regulation of the Process by Actin-Binding Proteins. *Biophys. J.* **1986**, *49* (1), 149–151. https://doi.org/10.1016/S0006-3495(86)83630-X.

(141) Pollard, T. D.; Mooseker, M. S. Direct Measurement of Actin Polymerization Rate Constants by Electron Microscopy of Actin Filaments Nucleated by Isolated Microvillus Cores. *Journal of Cell Biology* **1981**, *88* (3), 654–659. https://doi.org/10.1083/jcb.88.3.654.

(142) Bonder, E. M.; Fishkind, D. J.; Mooseker, M. S. Direct Measurement of Critical Concentrations and Assembly Rate Constants at the Two Ends of an Actin Filament. *Cell* **1983**, *34* (2), 491–501. https://doi.org/10.1016/0092-8674(83)90382-3.

(143) Anson, M. Temperature Dependence and Arrhenius Activation Energy of F-Actin Velocity Generated in Vitro by Skeletal Myosin. *Journal of Molecular Biology* **1992**, *224* (4), 1029–1038. https://doi.org/10.1016/0022-2836(92)90467-X.

(144) Pfeifer, W.; Saccà, B. From Nano to Macro through Hierarchical Self-Assembly: The DNA Paradigm. *ChemBioChem* **2016**, *17* (12), 1063–1080. https://doi.org/10.1002/cbic.201600034.

(145) Pfeifer, W.; Saccà, B. Synthetic DNA Filaments: From Design to Applications. *Biological Chemistry* **2018**, *399* (7), 773–785. https://doi.org/10.1515/hsz-2018-0110.

(146) Jungmann, R.; Scheible, M.; Kuzyk, A.; Pardatscher, G.; Castro, C. E.; Simmel, F. C. DNA Origami-Based Nanoribbons: Assembly, Length Distribution, and Twist. *Nanotechnology* **2011**, *22* (27), 275301. https://doi.org/10.1088/0957-4484/22/27/275301.

(147) de Greef, T. F. A.; Meijer, E. W. Supramolecular Polymers. *Nature* **2008**, *453* (7192), 171–173. https://doi.org/10.1038/453171a.

(148) Rajendran, A.; Endo, M.; Katsuda, Y.; Hidaka, K.; Sugiyama, H. Programmed Two-Dimensional Self-Assembly of Multiple DNA Origami Jigsaw Pieces. *ACS Nano* **2011**, *5* (1), 665–671. https://doi.org/10.1021/nn1031627.

(149) Tigges, T.; Heuser, T.; Tiwari, R.; Walther, A. 3D DNA Origami Cuboids as Monodisperse Patchy Nanoparticles for Switchable Hierarchical Self-Assembly. *Nano Lett.* **2016**, *16* (12), 7870–7874. https://doi.org/10.1021/acs.nanolett.6b04146.

(150) Groeer, S.; Walther, A. Switchable Supracolloidal 3D DNA Origami Nanotubes Mediated through Fuel/Antifuel Reactions. *Nanoscale* **2020**, *12* (32), 16995–17004. https://doi.org/10.1039/D0NR04209A.

(151) Zhang, T. DNA Origami-Based Microtubule Analogue. *Nanotechnology* **2020**, *31* (50), 50LT01. https://doi.org/10.1088/1361-6528/abb395.

(152) Li, Z.; Liu, M.; Wang, L.; Nangreave, J.; Yan, H.; Liu, Y. Molecular Behavior of DNA Origami in Higher-Order Self-Assembly. *J. Am. Chem. Soc.* **2010**, *132* (38), 13545–13552. https://doi.org/10.1021/ja106292x.

(153) Woo, S.; Rothemund, P. W. K. Programmable Molecular Recognition Based on the Geometry of DNA Nanostructures. *Nature Chemistry* **2011**, *3* (8), 620–627. https://doi.org/10.1038/nchem.1070.

(154) Schulman, R.; Winfree, E. Synthesis of Crystals with a Programmable Kinetic Barrier to Nucleation. *Proc. Natl. Acad. Sci. U.S.A.* **2007**, *104* (39), 15236–15241. https://doi.org/10.1073/pnas.0701467104.

(155) Zhan, P.; Jahnke, K.; Liu, N.; Göpfrich, K. Functional DNA-Based Cytoskeletons for Synthetic Cells. Nat Chem 2022.

(156) Yin, P.; Hariadi, R. F.; Sahu, S.; Choi, H. M. T.; Park, S. H.; LaBean, T. H.; Reif, J. H. Programming DNA Tube Circumferences. *Science* **2008**, *321* (5890), 824–826. https://doi.org/10.1126/science.1157312.

(157) Farag, N.; Ercolani, G.; Del Grosso, E.; Ricci, F. DNA Tile Self-Assembly Guided by Base Excision Repair Enzymes. *Angew Chem Int Ed* **2022**, *61* (34). https://doi.org/10.1002/anie.202208367.

(158) Gajewski, E.; Steckler, D. K.; Goldberg, R. N. Thermodynamics of the Hydrolysis of Adenosine 5'-Triphosphate to Adenosine 5'-Diphosphate. *Journal of Biological Chemistry* **1986**, *261* (27), 12733–12737. https://doi.org/10.1016/S0021-9258(18)67153-4.

(159) Giuseppone, N.; Walther, A. Out-of-Equilibrium (Supra)Molecular Systems and Materials: An Introduction. In *Out-of-Equilibrium (Supra)molecular Systems and Materials*; Giuseppone, N., Walther, A., Eds.; Wiley, 2021; pp 1–19. https://doi.org/10.1002/9783527821990.ch1.

(160) van Roekel, H. W. H.; Rosier, B. J. H. M.; Meijer, L. H. H.; Hilbers, P. A. J.; Markvoort, A. J.; Huck, W. T. S.; de Greef, T. F. A. Programmable Chemical Reaction Networks: Emulating Regulatory Functions in Living Cells Using a Bottom-up Approach. *Chem. Soc. Rev.* **2015**, *44* (21), 7465–7483. https://doi.org/10.1039/C5CS00361J.

(161) Hudson, J. L.; Mankin, J. C. Chaos in the Belousov–Zhabotinskii Reaction. *The Journal of Chemical Physics* **1981**, *74* (11), 6171–6177. https://doi.org/10.1063/1.441007.

(162) Semenov, S. N.; Wong, A. S. Y.; van der Made, R. M.; Postma, S. G. J.; Groen, J.; van Roekel, H. W. H.; de Greef, T. F. A.; Huck, W. T. S. Rational Design of Functional and Tunable Oscillating Enzymatic Networks. *Nature Chem* **2015**, *7* (2), 160–165. https://doi.org/10.1038/nchem.2142.

(163) Kim, J.; White, K. S.; Winfree, E. Construction of an in Vitro Bistable Circuit from Synthetic Transcriptional Switches. *Mol Syst Biol* **2006**, *2*, 68–68.

(164) Kim, J.; Khetarpal, I.; Sen, S.; Murray, R. M. Synthetic Circuit for Exact Adaptation and Fold-Change Detection. *Nucleic Acids Research* **2014**, *42* (9), 6078–6089. https://doi.org/10.1093/nar/gku233.

(165) Schaffter, S. W.; Schulman, R. Building in Vitro Transcriptional Regulatory Networks by Successively Integrating Multiple Functional Circuit Modules. *Nat. Chem.* **2019**, *11* (9), 829–838. https://doi.org/10.1038/s41557-019-0292-z.

(166) Padirac, A.; Fujii, T.; Rondelez, Y. Bottom-up Construction of in Vitro Switchable Memories. *Proc. Natl. Acad. Sci. U.S.A.* **2012**, *109* (47). https://doi.org/10.1073/pnas.1212069109.

(167) Kim, J.; Winfree, E. Synthetic *in Vitro* Transcriptional Oscillators. *Mol Syst Biol* **2011**, *7* (1), 465. https://doi.org/10.1038/msb.2010.119.

(168) Franco, E.; Friedrichs, E.; Kim, J.; Jungmann, R.; Murray, R.; Winfree, E.; Simmel, F. C. Timing Molecular Motion and Production with a Synthetic Transcriptional Clock. *Proc. Natl. Acad. Sci. U.S.A.* **2011**, *108* (40). https://doi.org/10.1073/pnas.1100060108.

(169) Weitz, M.; Kim, J.; Kapsner, K.; Winfree, E.; Franco, E.; Simmel, F. C. Diversity in the Dynamical Behaviour of a Compartmentalized Programmable Biochemical Oscillator. *Nature Chem* **2014**, *6* (4), 295–302. https://doi.org/10.1038/nchem.1869.

(170) Montagne, K.; Plasson, R.; Sakai, Y.; Fujii, T.; Rondelez, Y. Programming an *in Vitro* DNA Oscillator Using a Molecular Networking Strategy. *Mol Syst Biol* **2011**, *7* (1), 466. https://doi.org/10.1038/msb.2010.120.

(171) Heinen, L.; Walther, A. Programmable dynamic steady states in ATP-driven nonequilibrium DNA systems. *Sci Adv* **2019**, *5* (7), 0590.

(172) Ranallo, S.; Prévost-Tremblay, C.; Idili, A.; Vallée-Bélisle, A.; Ricci, F. Antibody-Powered Nucleic Acid Release Using a DNA-Based Nanomachine. *Nat Commun* **2017**, *8* (1), 15150. https://doi.org/10.1038/ncomms15150.

(173) Amodio, A.; Zhao, B.; Porchetta, A.; Idili, A.; Castronovo, M.; Fan, C.; Ricci, F. Rational Design of PH-Controlled DNA Strand Displacement. *J. Am. Chem. Soc.* **2014**, *136* (47), 16469–16472. https://doi.org/10.1021/ja508213d.

(174) Idili, A.; Vallée-Bélisle, A.; Ricci, F. Programmable PH-Triggered DNA Nanoswitches. *J. Am. Chem. Soc.* **2014**, *136* (16), 5836–5839. https://doi.org/10.1021/ja500619w.

(175) Simmel, F. C.; Yurke, B.; Singh, H. R. Principles and Applications of Nucleic Acid Strand Displacement Reactions. *Chem. Rev.* **2019**, *119* (10), 6326–6369. https://doi.org/10.1021/acs.chemrev.8b00580.

(176) Zhang, D. Y.; Winfree, E. Control of DNA Strand Displacement Kinetics Using Toehold Exchange. *J. Am. Chem. Soc.* **2009**, *131* (47), 17303–17314. https://doi.org/10.1021/ja906987s.

(177) Zhang, D. Y.; Turberfield, A. J.; Yurke, B.; Winfree, E. Engineering Entropy-Driven Reactions and Networks Catalyzed by DNA. *Science* **2007**, *318* (5853), 1121–1125. https://doi.org/10.1126/science.1148532.

(178) Seelig, G.; Soloveichik, D.; Zhang, D. Y.; Winfree, E. Enzyme-Free Nucleic Acid Logic Circuits. *Science* **2006**, *314* (5805), 1585–1588. https://doi.org/10.1126/science.1132493.

(179) Chen, Y.-J.; Dalchau, N.; Srinivas, N.; Phillips, A.; Cardelli, L.; Soloveichik, D.; Seelig, G. Programmable Chemical Controllers Made from DNA. *Nature Nanotech* **2013**, *8* (10), 755–762. https://doi.org/10.1038/nnano.2013.189.

(180) Woods, D.; Doty, D.; Myhrvold, C.; Hui, J.; Zhou, F.; Yin, P.; Winfree, E. Diverse and Robust Molecular Algorithms Using Reprogrammable DNA Self-Assembly. *Nature* **2019**, *567* (7748), 366–372. https://doi.org/10.1038/s41586-019-1014-9.

(181) Srinivas, N.; Parkin, J.; Seelig, G.; Winfree, E.; Soloveichik, D. Enzyme-Free Nucleic Acid Dynamical Systems. *Science* **2017**, *358* (6369), eaal2052. https://doi.org/10.1126/science.aal2052.

(182) Arbona, J.-M.; Aimé, J.-P.; Elezgaray, J. Folding of DNA Origamis. *Frontiers in Life Science* **2012**, *6* (1–2), 11–18. https://doi.org/10.1080/21553769.2013.768556.

(183) Arbona, J.-M.; Aimé, J.-P.; Elezgaray, J. Cooperativity in the Annealing of DNA Origamis. *The Journal of Chemical Physics* **2013**, *138* (1), 015105. https://doi.org/10.1063/1.4773405.

(184) Arbona, J. M.; Elezgaray, J.; Aimé, J. P. Modelling the Folding of DNA Origami. *EPL* **2012**, *100* (2), 28006. https://doi.org/10.1209/0295-5075/100/28006.

(185) Snodin, B. E. K.; Romano, F.; Rovigatti, L.; Ouldridge, T. E.; Louis, A. A.; Doye, J. P. K. Direct Simulation of the Self-Assembly of a Small DNA Origami. *ACS Nano* **2016**, *10* (2), 1724–1737. https://doi.org/10.1021/acsnano.5b05865.

(186) Dannenberg, F.; Dunn, K. E.; Bath, J.; Kwiatkowska, M.; Turberfield, A. J.; Ouldridge, T. E. Modelling DNA Origami Self-Assembly at the Domain Level. *The Journal of Chemical Physics* **2015**, *143* (16), 165102. https://doi.org/10.1063/1.4933426.

(187) Schindelin, J.; Arganda-Carreras, I.; Frise, E.; Kaynig, V.; Longair, M.; Pietzsch, T.; Preibisch, S.; Rueden, C.; Saalfeld, S.; Schmid, B.; Tinevez, J.-Y.; White, D. J.; Hartenstein, V.; Eliceiri, K.; Tomancak, P.; Cardona, A. Fiji: An Open-Source Platform for Biological-Image Analysis. *Nat Methods* **2012**, *9* (7), 676–682. https://doi.org/10.1038/nmeth.2019.

(188) Arganda-Carreras, I.; Fernández-González, R.; Muñoz-Barrutia, A.; Ortiz-De-Solorzano, C. 3D Reconstruction of Histological Sections: Application to Mammary Gland Tissue. *Microsc. Res. Tech.* **2010**, *73* (11), 1019–1029. https://doi.org/10.1002/jemt.20829.

(189) Aghebat Rafat, A.; Pirzer, T.; Scheible, M. B.; Kostina, A.; Simmel, F. C. Surface-Assisted Large-Scale Ordering of DNA Origami Tiles. *Angew. Chem. Int. Ed.* **2014**, *53* (29), 7665–7668. https://doi.org/10.1002/anie.201403965.

(190) Kielar, C.; Ramakrishnan, S.; Fricke, S.; Grundmeier, G.; Keller, A. Dynamics of DNA Origami Lattice Formation at Solid–Liquid Interfaces. *ACS Appl. Mater. Interfaces* **2018**, *10* (51), 44844–44853. https://doi.org/10.1021/acsami.8b16047.

(191) Woo, S.; Rothemund, P. W. K. Self-Assembly of Two-Dimensional DNA Origami Lattices Using Cation-Controlled Surface Diffusion. *Nat Commun* **2014**, *5* (1), 4889. https://doi.org/10.1038/ncomms5889.

(192) Cao, H. H.; Abel, G. R.; Gu, Q.; Gueorguieva, G.-A. V.; Zhang, Y.; Nanney, W. A.; Provencio, E. T.; Ye, T. Seeding the Self-Assembly of DNA Origamis at Surfaces. *ACS Nano* **2020**, *14* (5), 5203–5212. https://doi.org/10.1021/acsnano.9b09348.

(193) Sprengel, A.; Lill, P.; Stegemann, P.; Bravo-Rodriguez, K.; Schöneweiß, E.-C.; Merdanovic, M.; Gudnason, D.; Aznauryan, M.; Gamrad, L.; Barcikowski, S.; Sanchez-Garcia, E.; Birkedal, V.; Gatsogiannis, C.; Ehrmann, M.; Saccà, B. Tailored Protein Encapsulation into a DNA Host Using Geometrically Organized Supramolecular Interactions. *Nature Communications* **2017**, *8*, 14472. https://doi.org/10.1038/ncomms14472.

(194) Wu, L.; Huang, C.; Emery, B. P.; Sedgwick, A. C.; Bull, S. D.; He, X.-P.; Tian, H.; Yoon, J.; Sessler, J. L.; James, T. D. Förster Resonance Energy Transfer (FRET)-Based Small-Molecule Sensors and Imaging Agents. *Chem. Soc. Rev.* **2020**, *49* (15), 5110–5139. https://doi.org/10.1039/C9CS00318E.

(195) Neuman, K. C.; Block, S. M. Optical Trapping. *Review of Scientific Instruments* **2004**, *75* (9), 2787–2809. https://doi.org/10.1063/1.1785844.

(196) Kaminska, I.; Bohlen, J.; Mackowski, S.; Tinnefeld, P.; Acuna, G. P. Strong Plasmonic Enhancement of a Single Peridinin–Chlorophyll *a* –Protein Complex on DNA Origami-Based Optical Antennas. *ACS Nano* **2018**, *12* (2), 1650–1655. https://doi.org/10.1021/acsnano.7b08233.

(197) Puchkova, A.; Vietz, C.; Pibiri, E.; Wünsch, B.; Sanz Paz, M.; Acuna, G. P.; Tinnefeld, P. DNA Origami Nanoantennas with over 5000-Fold Fluorescence Enhancement and Single-Molecule Detection at 25 MM. *Nano Lett.* **2015**, *15* (12), 8354–8359. https://doi.org/10.1021/acs.nanolett.5b04045.

(198) Segel, L. A.; Edelstein-Keshet, L. *A Primer on Mathematical Models in Biology*; Society for Industrial and Applied Mathematics: Philadelphia, 2013.

(199) Wei, X.; Nangreave, J.; Jiang, S.; Yan, H.; Liu, Y. Mapping the Thermal Behavior of DNA Origami Nanostructures. *J. Am. Chem. Soc.* **2013**, *135* (16), 6165–6176. https://doi.org/10.1021/ja4000728.

(200) Broekmans, O. D.; King, G. A.; Stephens, G. J.; Wuite, G. J. L. DNA Twist Stability Changes with Magnesium(2 +) Concentration. *Phys. Rev. Lett.* **2016**, *116* (25), 258102. https://doi.org/10.1103/PhysRevLett.116.258102.

(201) Guo, H.; Tullius, T. D. Gapped DNA Is Anisotropically Bent. *Proc. Natl. Acad. Sci. U.S.A.* **2003**, *100* (7), 3743–3747. https://doi.org/10.1073/pnas.0737062100.

(202) Du, Q.; Vologodskaia, M.; Kuhn, H.; Frank-Kamenetskii, M.; Vologodskii, A. Gapped DNA and Cyclization of Short DNA Fragments. *Biophysical Journal* **2005**, *88* (6), 4137–4145. https://doi.org/10.1529/biophysj.104.055657.

(203) Mills, J. B.; Cooper, J. P.; Hagerman, P. J. Electrophoretic Evidence That Single-Stranded Regions of 1 or More Nucleotides Dramatically Increase the Flexibility of DNA. *Biochemistry* **1994**, *33* (7), 1797–1803. https://doi.org/10.1021/bi00173a024.

(204) Carlier, M.-F.; Pantaloni, D. Control of Actin Dynamics in Cell Motility. *Journal of Molecular Biology* **1997**, *269* (4), 459–467. https://doi.org/10.1006/jmbi.1997.1062.

(205) Pollard, T. D.; Blanchoin, L.; Mullins, R. D. Molecular Mechanisms Controlling Actin Filament Dynamics in Nonmuscle Cells. *Annu. Rev. Biophys. Biomol. Struct.* **2000**, *29* (1), 545–576. https://doi.org/10.1146/annurev.biophys.29.1.545.

(206) Jonasson, E. M.; Mauro, A. J.; Li, C.; Labuz, E. C.; Mahserejian, S. M.; Scripture, J. P.; Gregoretti, I. V.; Alber, M.; Goodson, H. V. Behaviors of Individual Microtubules and Microtubule Populations Relative to Critical Concentrations: Dynamic Instability Occurs When Critical Concentrations Are Driven Apart by Nucleotide Hydrolysis. *MBoC* **2020**, *31* (7), 589–618. https://doi.org/10.1091/mbc.E19-02-0101.

(207) Zimmerle, C. T.; Frieden, C. Effect of Temperature on the Mechanism of Actin Polymerization. *Biochemistry* **1986**, *25* (21), 6432–6438. https://doi.org/10.1021/bi00369a014.

(208) Flory, P. J. Fundamental Principles of Condensation Polymerization. *Chem. Rev.* **1946**, *39* (1), 137–197. https://doi.org/10.1021/cr60122a003.

(209) Flory, P. J. Molecular Size Distribution in Linear Condensation Polymers [1]. *J. Am. Chem. Soc.* **1936**, *58* (10), 1877–1885. https://doi.org/10.1021/ja01301a016.

(210) Zhao, D.; Moore, J. S. Nucleation–Elongation: A Mechanism for Cooperative Supramolecular Polymerization. *Org. Biomol. Chem.* **2003**, *1* (20), 3471–3491. https://doi.org/10.1039/B308788C.

(211) Yokozawa, T.; Ohta, Y. Transformation of Step-Growth Polymerization into Living Chain-Growth Polymerization. *Chem. Rev.* **2016**, *116* (4), 1950–1968. https://doi.org/10.1021/acs.chemrev.5b00393.

(212) Ebdon, J. R. Introduction to Polymers (Second Edition) R. J. Young and P. A. Lovell Chapman and Hall, London, 1991. Pp. 443, Price £16.95. ISBN 0-412-30640-9 (PB); ISBN 0–412–30630–1 (HB). *Polym. Int.* **1992**, *27* (2), 207–208. https://doi.org/10.1002/pi.4990270217.

(213) Li, W.; Yang, Y.; Jiang, S.; Yan, H.; Liu, Y. Controlled Nucleation and Growth of DNA Tile Arrays within Prescribed DNA Origami Frames and Their Dynamics. *J. Am. Chem. Soc.* **2014**, *136* (10), 3724–3727. https://doi.org/10.1021/ja411446q.

(214) Del Grosso, E.; Prins, L. J.; Ricci, F. Transient DNA-Based Nanostructures Controlled by Redox Inputs. *Angew. Chem. Int. Ed.* **2020**, *59* (32), 13238–13245. https://doi.org/10.1002/anie.202002180.

(215) Green, L. N.; Subramanian, H. K. K.; Mardanlou, V.; Kim, J.; Hariadi, R. F.; Franco, E. Autonomous Dynamic Control of DNA Nanostructure Self-Assembly. *Nat. Chem.* **2019**, *11* (6), 510–520. https://doi.org/10.1038/s41557-019-0251-8.

(216) Venkataraman, S.; Dirks, R. M.; Rothemund, P. W. K.; Winfree, E.; Pierce, N. A. An Autonomous Polymerization Motor Powered by DNA Hybridization. *Nature Nanotech* **2007**, *2* (8), 490–494. https://doi.org/10.1038/nnano.2007.225.

(217) Dong, J.; Zhou, C.; Wang, Q. Towards Active Self-Assembly Through DNA Nanotechnology. *Top Curr Chem (Z)* **2020**, *378* (2), 33. https://doi.org/10.1007/s41061-020-0297-5.

(218) Liu, W.-T.; Wu, J.-H.; Li, E. S.-Y.; Selamat, E. S. Emission Characteristics of Fluorescent Labels with Respect to Temperature Changes and Subsequent Effects on DNA Microchip Studies. *Appl Environ Microbiol* **2005**, *71* (10), 6453–6457. https://doi.org/10.1128/AEM.71.10.6453-6457.2005.

(219) Didenko, V. V. DNA Probes Using Fluorescence Resonance Energy Transfer (FRET): Designs and Applications. *BioTechniques* **2001**, *31* (5), 1106–1121. https://doi.org/10.2144/01315rv02.

(220) Chen, Z.; Chen, K.; Xie, C.; Liao, K.; Xu, F.; Pan, L. Cyclic Transitions of DNA Origami Dimers Driven by Thermal Cycling. *Nanotechnology* **2023**, *34* (6), 065601. https://doi.org/10.1088/1361-6528/aca02f.

(221) Liber, M.; Tomov, T. E.; Tsukanov, R.; Berger, Y.; Popov, M.; Khara, D. C.; Nir, E. Study of DNA Origami Dimerization and Dimer Dissociation Dynamics and of the Factors That Limit Dimerization. *Small* **2018**, *14* (23), 1800218. https://doi.org/10.1002/smll.201800218.

(222) Yang, S.; Liu, W.; Nixon, R.; Wang, R. Metal-Ion Responsive Reversible Assembly of DNA Origami Dimers: G-Quadruplex Induced Intermolecular Interaction. *Nanoscale* **2018**, *10* (8), 3626–3630. https://doi.org/10.1039/C7NR09458B.

(223) Lee, C.; Kim, K. S.; Kim, Y.-J.; Lee, J. Y.; Kim, D.-N. Tailoring the Mechanical Stiffness of DNA Nanostructures Using Engineered Defects. *ACS Nano* **2019**, *13* (7), 8329–8336. https://doi.org/10.1021/acsnano.9b03770.

(224) Buchberger, A.; Simmons, C. R.; Fahmi, N. E.; Freeman, R.; Stephanopoulos, N. Hierarchical Assembly of Nucleic Acid/Coiled-Coil Peptide Nanostructures. *J. Am. Chem. Soc.* **2020**, *142* (3), 1406–1416. https://doi.org/10.1021/jacs.9b11158.

(225) Berengut, J. F.; Wong, C. K.; Berengut, J. C.; Doye, J. P. K.; Ouldridge, T. E.; Lee, L. K. Self-Limiting Polymerization of DNA Origami Subunits with Strain Accumulation. *ACS Nano* **2020**, *14* (12), 17428–17441. https://doi.org/10.1021/acsnano.0c07696.

(226) Franquelim, H. G.; Dietz, H.; Schwille, P. Reversible Membrane Deformations by Straight DNA Origami Filaments. *Soft Matter* **2021**, *17* (2), 276–287. https://doi.org/10.1039/D0SM00150C.
(227) Schill, J.; Rosier, B. J. H. M.; Gumí Audenis, B.; Magdalena Estirado, E.; Greef, T. F. A.; Brunsveld, L. Assembly of Dynamic Supramolecular Polymers on a DNA Origami Platform. *Angew. Chem. Int. Ed.* **2021**, *60* (14), 7612–7616. https://doi.org/10.1002/anie.202016244.
(228) Xu, X.; Winterwerber, P.; Ng, D.; Wu, Y. DNA-Programmed Chemical Synthesis of Polymers and Inorganic Nanomaterials. *Top Curr Chem (Z)* **2020**, *378* (2), 31. https://doi.org/10.1007/s41061-020-0292-x.
(229) Hannewald, N.; Winterwerber, P.; Zechel, S.; Ng, D. Y. W.; Hager, M. D.; Weil, T.; Schubert, U. S. DNA Origami Meets Polymers: A Powerful Tool for the Design of Defined Nanostructures. *Angew. Chem. Int. Ed.* **2021**, *60* (12), 6218–6229. https://doi.org/10.1002/anie.202005907.
(230) Yonamine, Y.; Cervantes-Salguero, K.; Minami, K.; Kawamata, I.; Nakanishi, W.; Hill, J. P.; Murata, S.; Ariga, K. Supramolecular 1-D Polymerization of DNA Origami through a Dynamic Process at the 2-Dimensionally Confined Air–Water Interface. *Phys. Chem. Chem. Phys.* **2016**, *18* (18), 12576–12581. https://doi.org/10.1039/C6CP01586G.

Appendix

List of Abbreviations

Abbreviation	Description
µ	micro
2D	three dimensional
3D	two dimensional
A	adenine
Å	Angstrom
ADP	adenosine diphosphate
AFM	atomic force microscope
AGE	agarose gel electrophoresis
AMP	adenosine monophosphate
APS	ammonium persulfate
ATP	adenosine triphosphate
AuNP	gold nanoparticle
bp	base pair
C	cytosine
c_{crit}	critical concentration
CRN	chemical reaction network
Da	Dalton
DNA	deoxyribonucleic acid
DRN	DNA reaction network
dsDNA	double-stranded DNA
DX	double crossover
E_{act}	activation energy
EDTA	ethylenediamine tetra acetic acid
E_{FRET}	FRET efficiency
EtBr	ethidium bromide
FAM	6-carboxyfluorescein
FD	Force-Distance
FRET	Förster resonance energy transfer
G	guanine
g	gram
GPL	General Public License
h	hour

HJ	Holliday junction
IBM	International Business Machines
IMCES	Imaging Center Essen
IR	infra-red
k	kilo
k_a^{in}	initial association rate coefficient
L/l	liter
LPG	long pass green
M	mega
m	milli
$MgCl_2$	magnesium chloride
min	minute
n	nano
NaCl	sodium chloride
PAGE	polyacrylamide gel electrophoresis
PCR	polymerase chain reaction
PEG	polyethylene glycol
PEN	Polymerase, Exonuclease, and Nickase
rcf	relative centrifugal force
RNA	ribonucleic acid
rpm	revolutions per minute
ssDNA	single-stranded DNA
STM	scanning tunnel microscope
T	thymine
$T_{0.5}$	temperature at $\theta = 0.5$
TAE	Tris Acetate EDTA
TAMRA	carboxytetramethylrhodamine
TBE	Tris Borate EDTA
TCEP	tris(2-carboxyethyl)phosphine
TEM	transmission electron microscope
TEMED	tetramethylethylenediamine
TEMg	Tris EDTA Magnesium
TENa	Tris EDTA Sodium
T_m	melting temperature at $d^2\theta / dT^2 = 0$
v	volume
V	volt
w	weight

List of Figures

List of Tables

Supplementary Figures

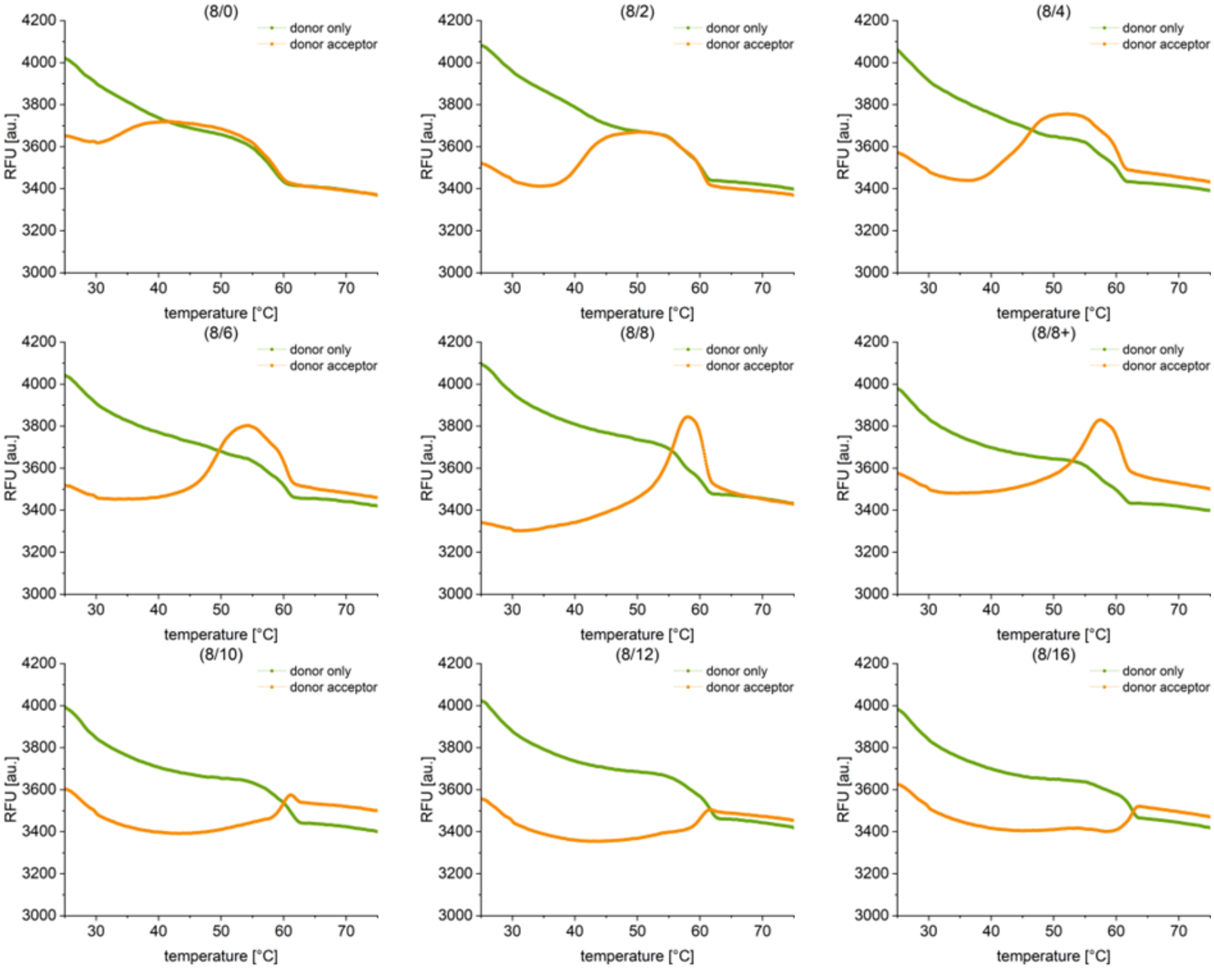

Supplementary Figure 1 ***Individual FAM intensity curves of B-stacking melting***
Donor-only vs. donor-acceptor FAM intensity curves of averaged quadruplicates for 1 bp gap variants from B(8/0) to B(8/16). 50 nM samples à 20 µl melted over a thermal gradient from 75 °C to 25 °C with a rate of +0.1 °C/min.

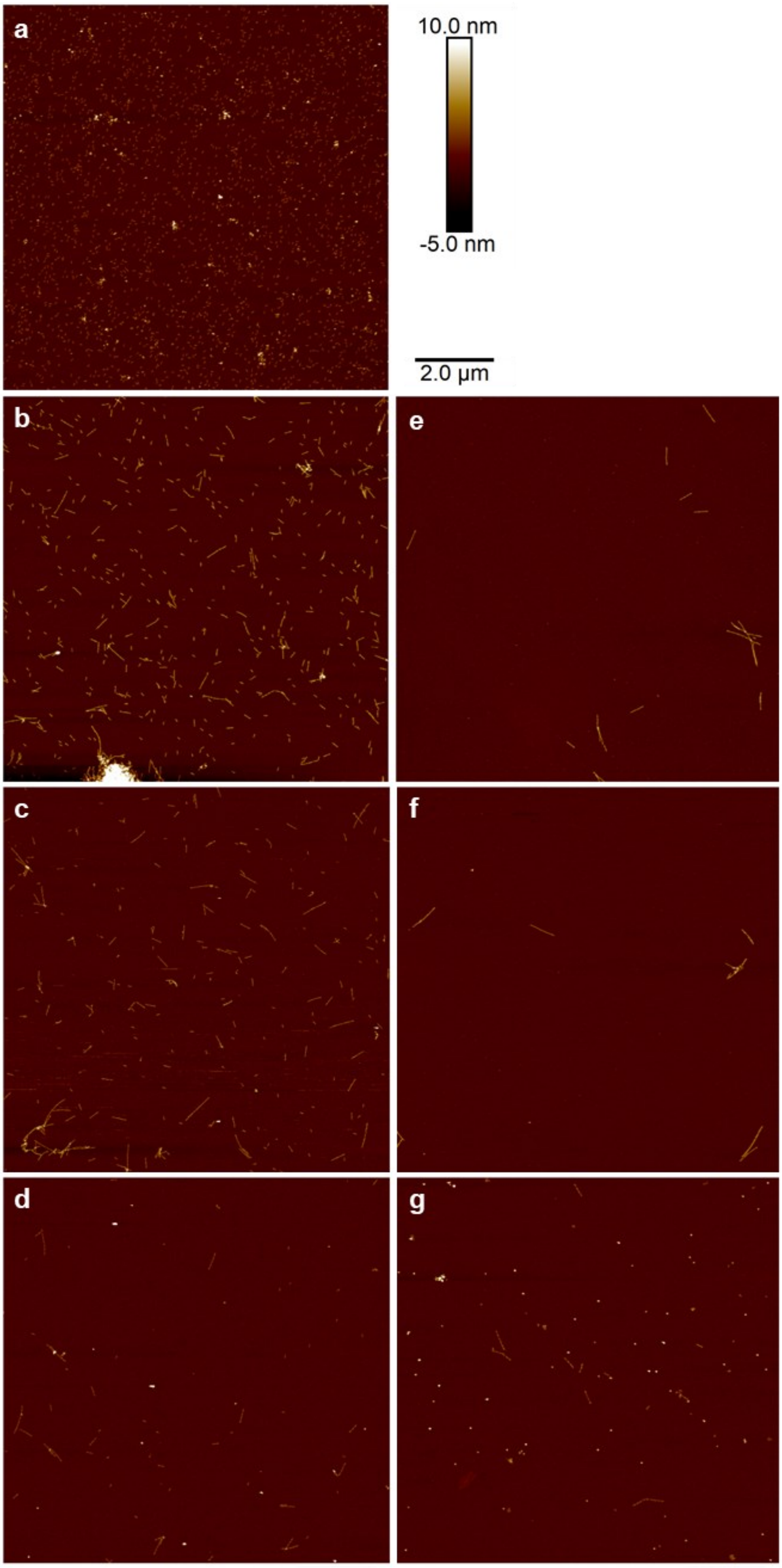

Supplementary Figure 2 ***Critical concentration of hybridization and random stacking***
Evaluation of equilibrium structures of 1 nM 24-helix bundle monomer polymerized in TEMg20 by addition of b-d) hybridization or e-g) random stacking staples at 30 °C, 35 °C, or 40 °C respectively. 100 µm^2 mica covered with 10 µl of monomer sample were used as reference (a) and free monomer numbers compared to equilibrium samples.

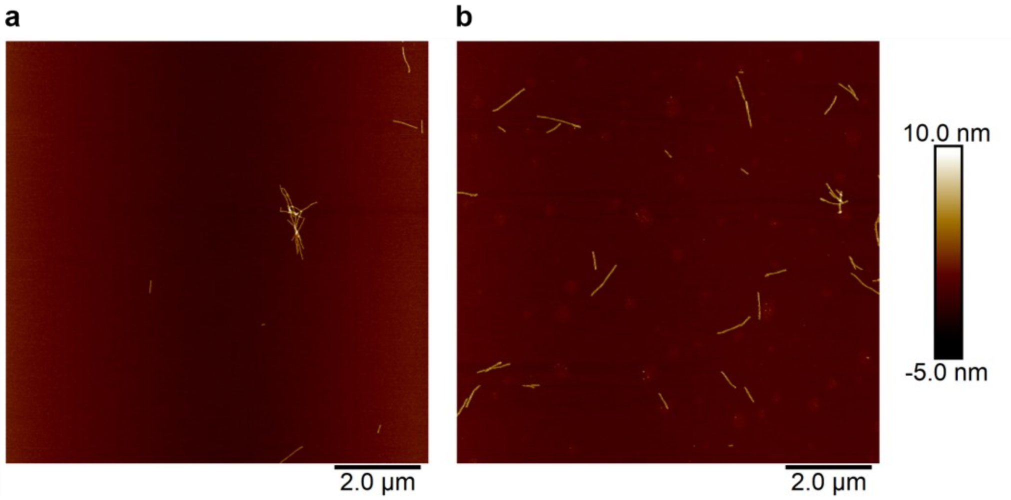

Supplementary Figure 3 ***Polymers at equilibrium after 20 h reaction***
1 nM monomer sample in TEMg20 at 40 °C with a ten-fold excess of polymerization staples, either for a) hybridization or b) random stacking, reacted for 20 h until equilibrium. Surface coverage, especially for hybridized polymers, is significantly decreased compared to the identical concentration of unpolymerized monomers.

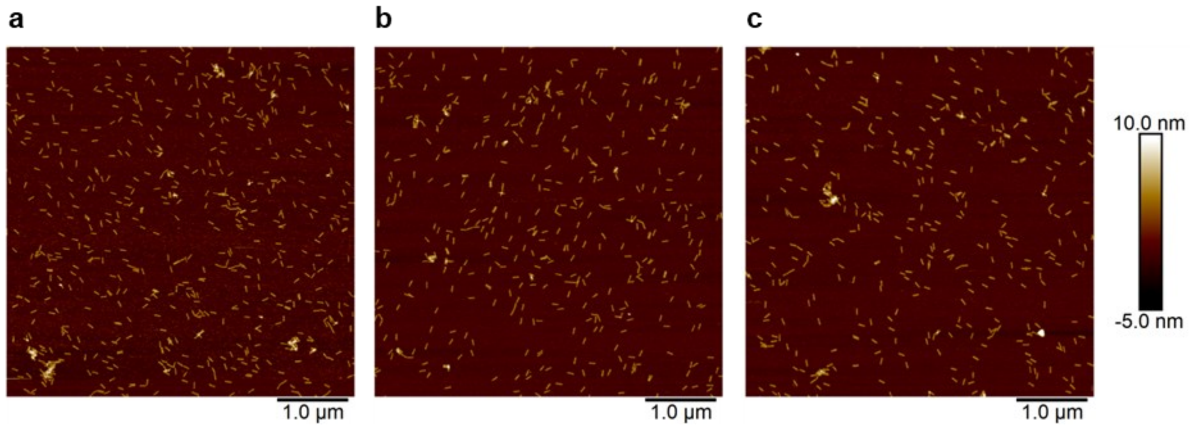

Supplementary Figure 4 ***Initial polymerization induction after 15 s***
1 nM monomers mixed with a ten-fold excess of b) hybridization or c) random stacking staples at 40 °C and incubated for 15 seconds before inhibiting further reaction by insertion into liquid nitrogen and careful thawing on ice before AFM in air imaging. a) Inactive monomers as reference to better illustrate apparent lag-phase for staple binding.

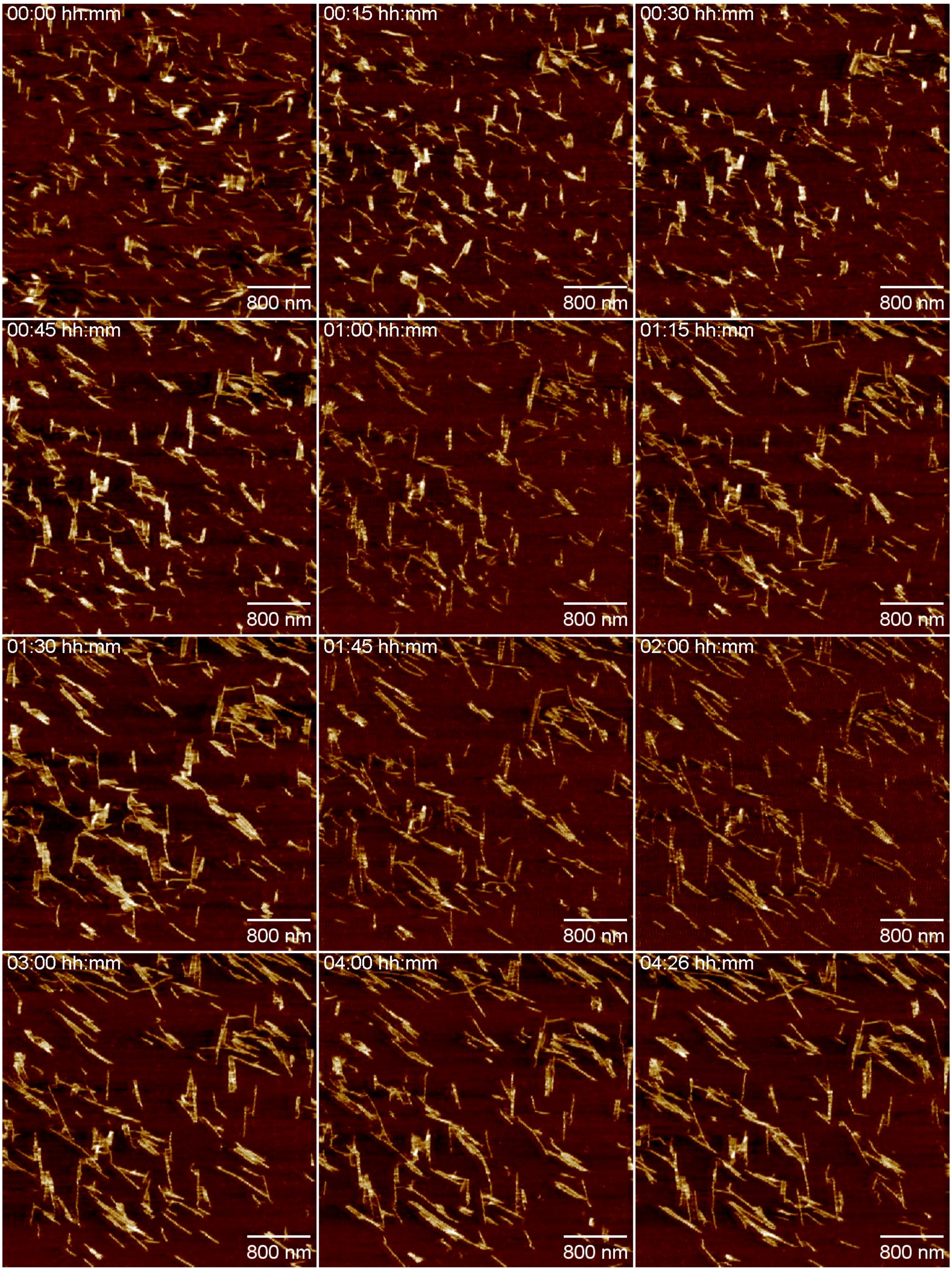

Supplementary Figure 5 ***Time-lapse of ABBA stacking***
Mica surface assisted ABBA dimer polymerization of 2 nM dimer in TEMg20 + 50 mM $NaCl_2$ at room temperature captured at a rate of one frame per 32 seconds with 256 samples/line in PeakForce Fast Tapping mode with PEAKFORCE-HIRS-F-A probe at a 200 mV drive amplitude.

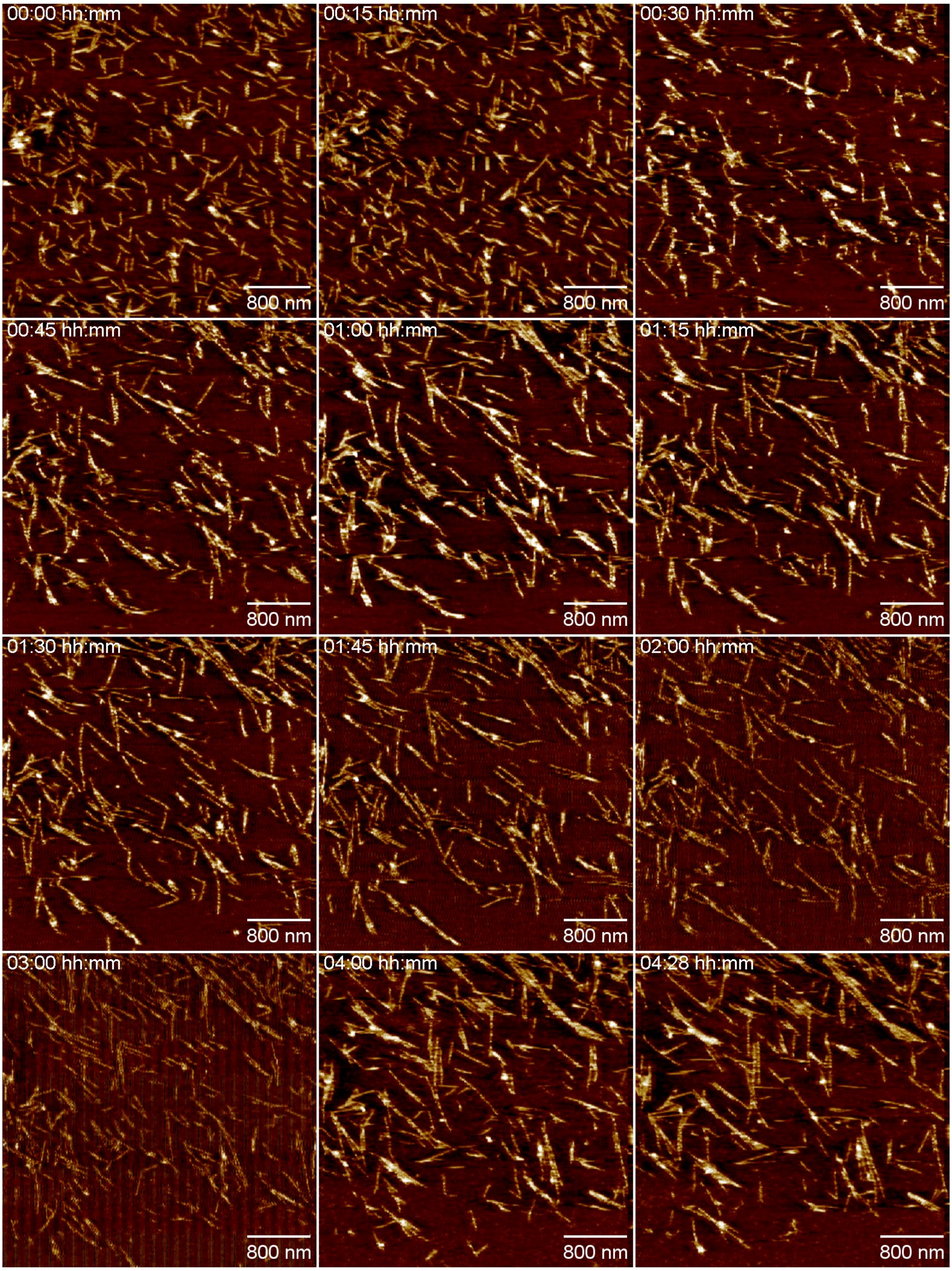

Supplementary Figure 6 ***Time-lapse of BAAB stacking***
Mica surface assisted BAAB dimer polymerization of 2 nM dimer in TEMg20 + 50 mM NaCl$_2$ at room temperature captured at a rate of one frame per 32 seconds with 256 samples/line in PeakForce Fast Tapping mode with PEAKFORCE-HIRS-F-A probe at a 200 mV drive amplitude.

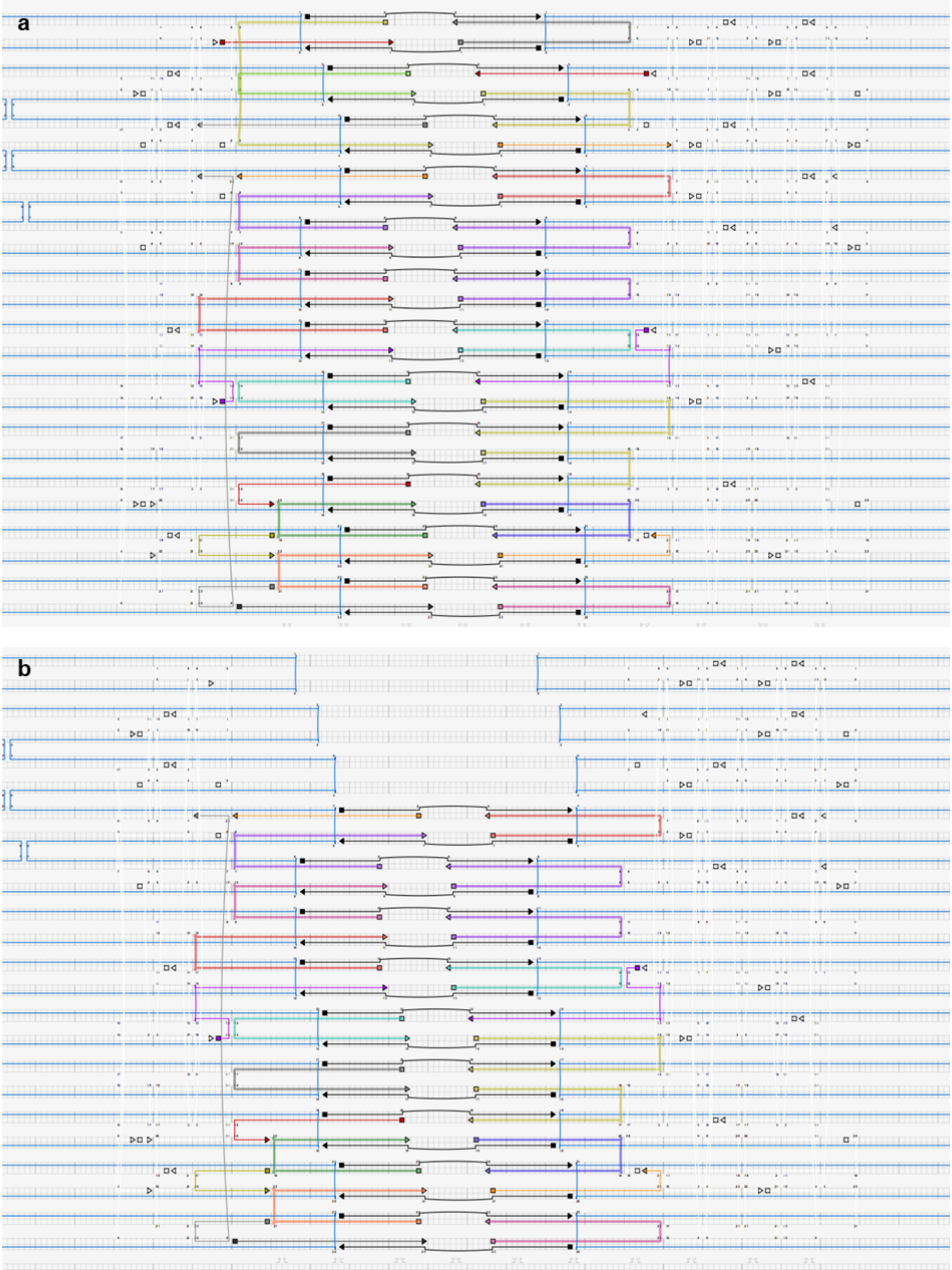

Supplementary Figure 7 ***24-helix bundle DRN connector interface caDNAno design***
B (right) and A (left) interface of the 24-helix bundle DNA origami (scaffold in blue, exemplary staples in white) with interface connector staples (colored) attached to the unpaired scaffold interface, forming single-stranded protrusions with half the complementary sequence of the connecting fuel strand (black) on each side. a) depicts all fully activated helices and b) the outer helices of the bundle structure, omitting the six inner helices.

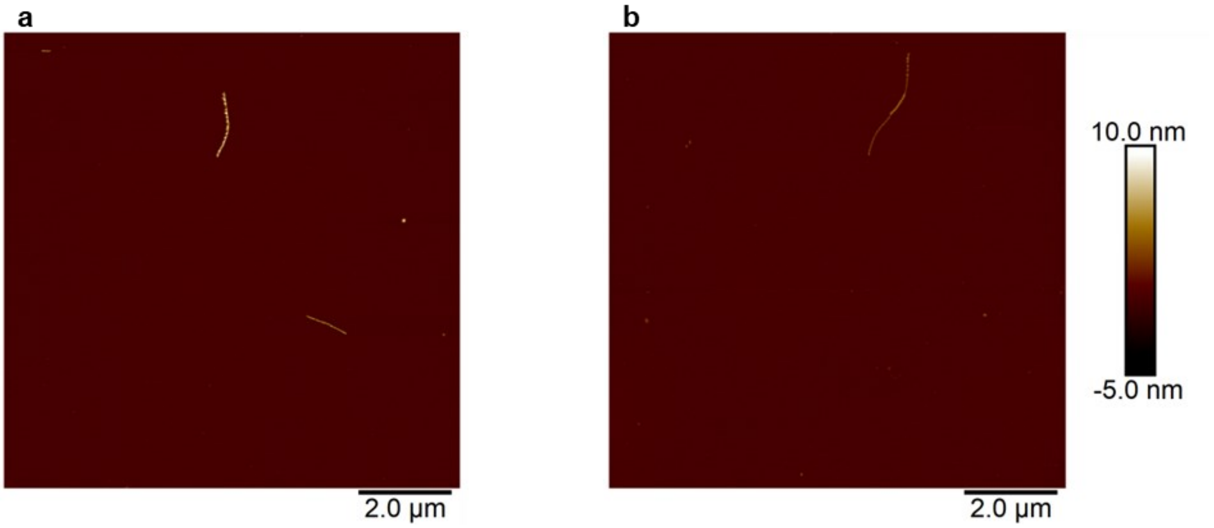

Supplementary Figure 8 ***DNA origami polymers connect by a DNA fuel strand***
AFM images of 1 nM PEG purified DNA origami monomer with either a) full interface activation or b) activation of 18 outer helices to bind identical fuel staples with a ten-fold excess per binding site. Polymerization was performed in TEMg20 at 40 °C for 20 h, and AFM images were recorded in ScanAsyst in air. Coverage of mica is severely decreased as compared to monomer reference due to previously described clustering, but observed filaments reached µm-long lengths.

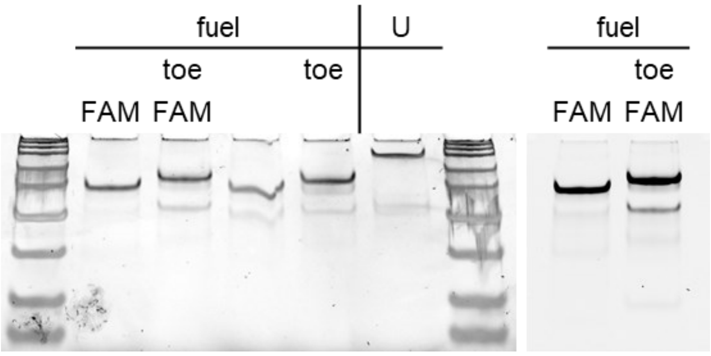

Supplementary Figure 9 ***DRN individual complexes after assembly***
1 µM complexes assembled in TEMg12.5 and run at 60 V for 3.5 h on a 15 % PAGE with TBE as running buffer. After recording FAM fluorescence, the gel was stained for 3 min with GelStar fluorescent dye in TBE, and DNA bands were scanned (ex.532 nm). Four variations of the fuel complex with either fluorescent labeling or fuel_toehold (toe) are checked for successful complex assembly, as well as the unlabeled U complex.

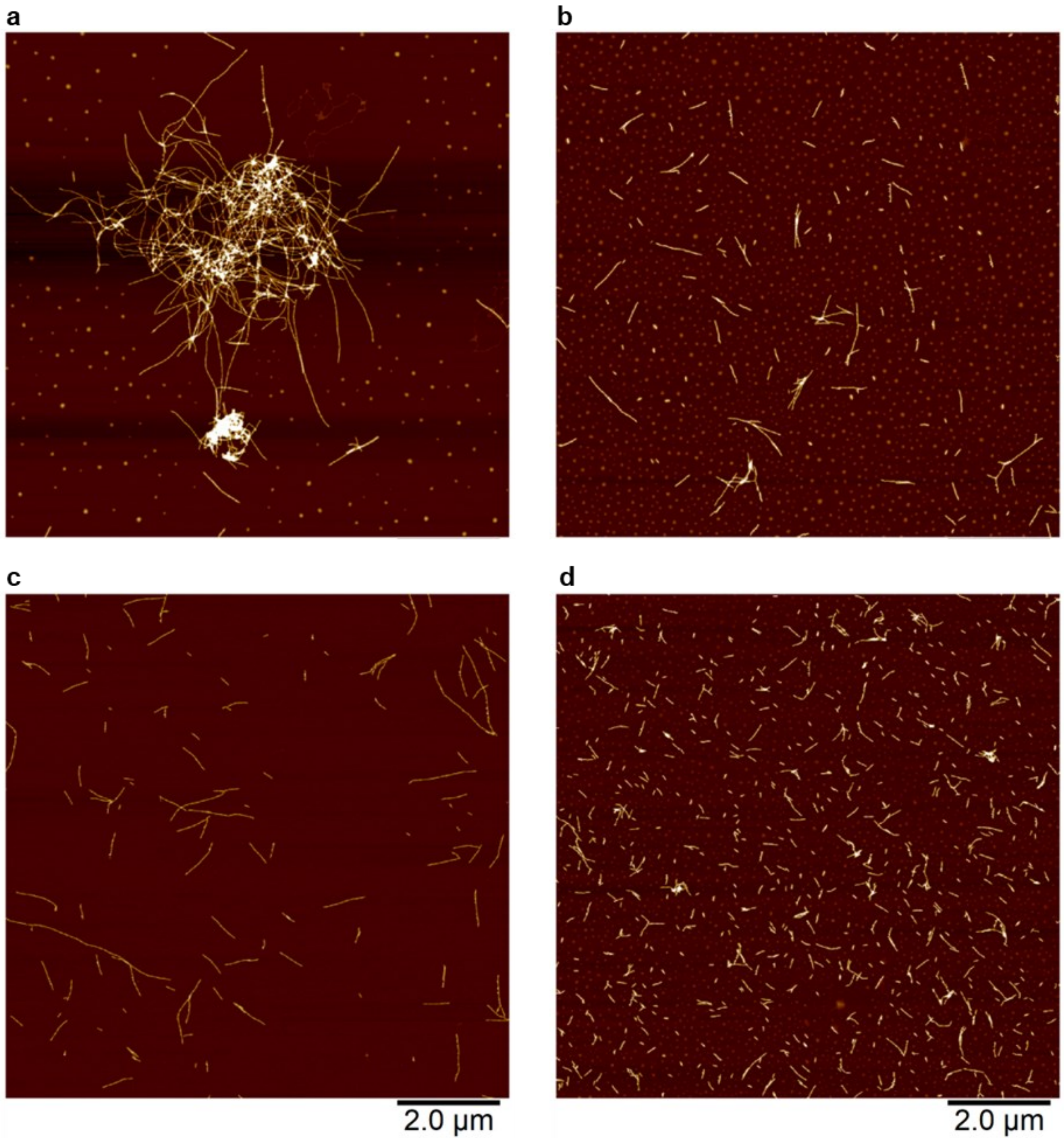

Supplementary Figure 10 ***Fuel_toe-mediated polymerization in TEMg20 with subsequent remover addition***

1nM of PEG-purified 24-helix bundle monomer with either a) full helix activation or b) outer helix activation in TEMg20 with a ten-fold excess of fuel_toe strand per binding site polymerized at 40 °C for 20 h. Subsequent addition of a two-fold excess of remover strand per added fuel_toe to polymers obtained from c) the full interface activation or d) the outer interface activation.

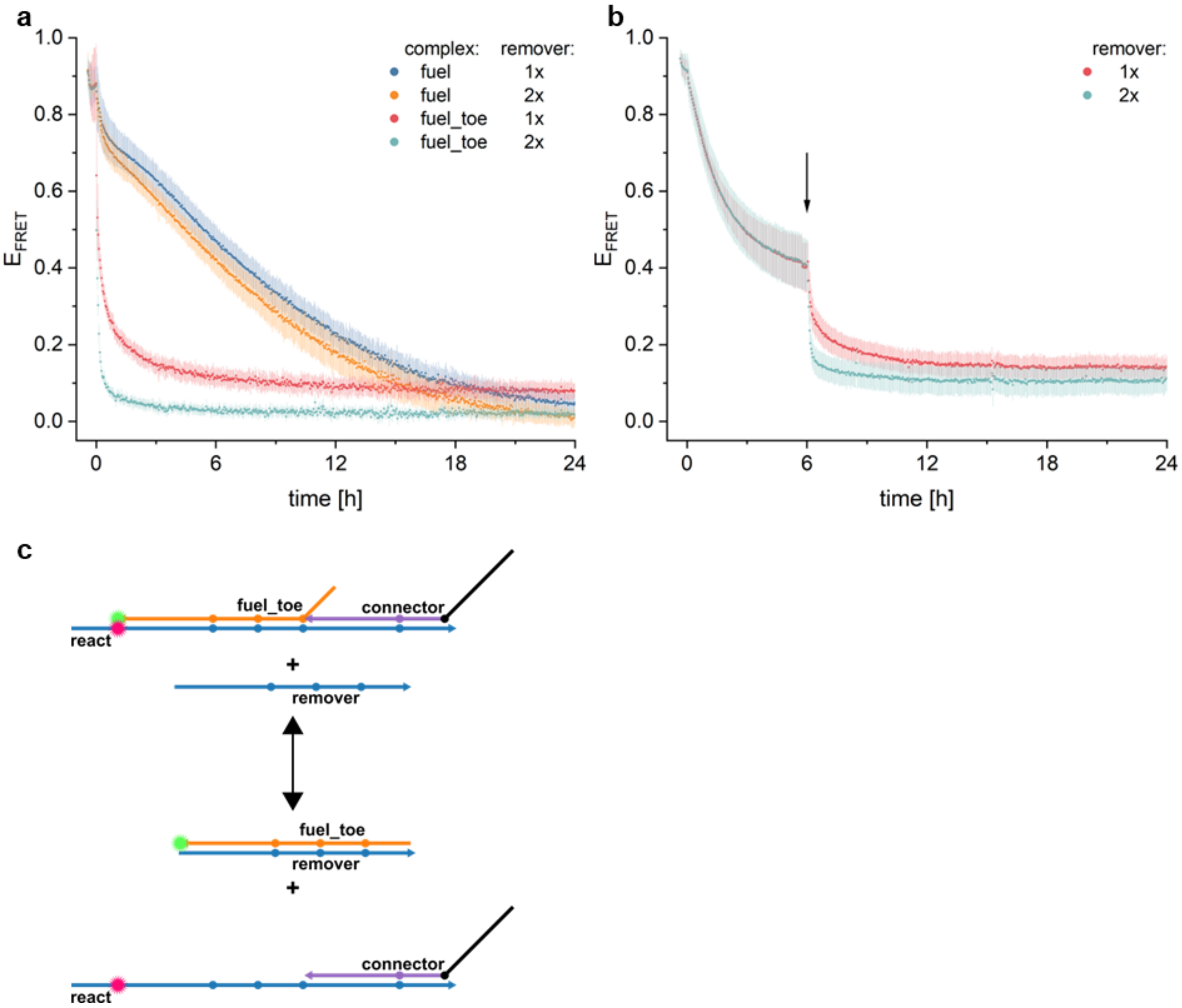

Supplementary Figure 11 ***Fuel complexes with remover strand***
a) 50 nM 1:1:1 assembled fuel or fuel_toe complexes in TEMg12.5 at 40 °C mixed with unimolar or two-fold amounts of remover strand at t = 0. b) 50 nM DRN with fuel_toe complex and 250 nM V and helper strands reacted in TEMg12.5 at 40 °C for 6 h before 50 nM (1x) or 100 nM (2x) remover strand addition. c) Exemplary complex reaction after remover addition for fuel_toe strand.

Sequences

24-helix bundle monomer core:

GCGTTTAATTAAACAGTTCAGAAAGATAGCGCAACACTTTAG
GCTAAAAAGAGTCTTTACCCTGACAGAAGTTCAAAATAGGAA
ACAGCACCATAAACCATCGATAGCCAAAATCGAACCGCAAAT
ATTACTTGAGAGTTTGCCTTTAGCCGGTCATGAACCACTGAG
ATTAAGACGGCATTACCTACCATACGGGAGAGATTCGCGAGC
TAAGCTCCTTTTGATAAGAAGCCCGTAGCAACATCGCCTCAT
CTGTTAATTCATATGGTAGCAAGGTTTGCTAAAACAGCAAGA
ACCATTCAACCGATTGAGGAATTAAAAGGAAAATTGTAGTTT
CCCAATAATAAGAGCAAAACTGAAAGTAATAAAGCCAACGCA
CATGAATTATCATCATATTATACTTGTGATACTGTTTACTTG
CGGTAACAACCCGTCGGCCTGTAGCCCCAGCAAAACGAAGCA
GGGACCGTAATGGGATAAACCAATTTTGTATAAACGGGAGAG
GCCTAACCGTGCATCTGTTAAAATTCAGGGAAGTAAATTTCA
ACTGCCTCAGGAAGATCATTGTATTGAGTTTGTTAGCGAGGA
GCTGCTCAATCGTCTGACAATATTAAAAATAATGTACCATAA
AACCAGTCACACGACCAAGAACCCTGATGCACTTTTTCCGTT
GCGTCGCGTCCAACCGTTCTAGCTAATGCCTATACATTCAAC
AAATCAGCTCTTTTTGAGAGATCTGCAAGGACATTTGGATTG
ATAACGTTAAGTCTGGAGCAAACAATGACCCTAGTAGTAGAC
AACAATGCGCATACCGAACGAACCCAGTTGAAGATTAGGAAG
GGTATACGTGCGGTCAGTATTAACATATCAAGTATTAGTTAT
CAATTGCCCTGATGGTGGTTCCGACAGTGAGAATTCGTAGTT
GGCATTAAATGAATAGCCCGAGATGGCGGTTTATCCGCTTAC
TGCCCCCTGCAAGAGTCCACTATTTCGTGCCAAGTGTACGCA
CTCCGTAGGAGCGAACGTGGCGAGGTATAACGCCAGAACCTT
AAATTGCTTCGGCGCTAGGGCGCTGCGCCGCGAGTAAATAAT
GAAGAATTACCTTATGCAACACCAAGGCTGGATCATAACCAA
CAATCAGGACGTTGGGAACAAAGCGATATTCCCTGCTCTGAT
CCTAATTTACCGTTCCAGGAACCTTTAGGATCCGCCACCCCA
GCAACAGGAGTGTACTGTAACAGTCCGTCGAGTATCACAGTA
CACATCCGGTATTCTAACCGCGCCATTAAACCCAATCATATC
GGGGACTTAAACAAAATCGTCGCTTTTCCCTTTTAACCGTTG
CGGGAAGGCACCATTAGGAGTAATGTGTAGGTGATATTTGGC
AGAAGGAAGTATATTTTTAAAAATTTTTAGAGTAGCTAATTT
GTGTCTTTCCCTACTAATGTAATACTTTTGCCCTGAGATATT
TTTAGACAGCCAAGGCAGAGCATAAAGCTAACGTAAAACAGG
TTTGTCCAGAAACTAATAAGGAATTGAGGAAATTAAAAGAAC
ATAATCTTCTTTTAGAAACCCTCAATCAATAGGTGAGGGCAC
GAGGAGGTCAATGTTTTAAATATGTCGCAAACGTAATGAAGT
ATTTTACCAGACAATCAATAGAAAGGCGCGACTGTATGGACC
TTGGGGAGGGTAAAAGAAACGCAAAGCATTACTAAAGTATGT
ATTGAAACAAATAGCTATCTTACCAGCCGTCGGTAAAGAAGT
GGATTCCTGAAAGTTTGAGTAACAACTTTACTTTTAGTCTAT
CTTATTCTCCCACGACGTTGTAAAGGTCGACGAACTGACAGA
TTTGGTCACGCTGCAAGGCGATTAAATCATGCTTAGCCCTTG
TTGCCAGTTTGGGCCTCTTCGCTATCACAATACCGCCACCTC

AAGGCACTCCCGCCATTCAGGCTGAAGCCTGAGGAGGTCAGG
AGAAATGGATACTCAAACTATCGGTCCTGAGCCCATCCACAA
ACAGGCGCAGGAGCTCGACGGGCAACAGCTGCCTGTTTGACG
ACCAGCCAAAAAATTGTTGCGTATTGGGCGCATCAAAACAAC
ACCCGCCACCAAGCATAAGCTGCATTAATGATTGGAACCTAT
CCTCGAGCATACGGTACGTGCTTTCCTCGTTAAAGCCGATCA
ATGTGAGAGAGGCCACCTACAGGGCGCGTACAGGAGCGTGTA
CCAGTCGCTGGTAAGAGTCCAATACTGCGGAATGCTTTCGAG
ACAACAATGATAAAAACTTGCCAGAGGGGGTAAATCAGTTAA
AAGGAGGTGAACCCTCAACCGGAACCAGAGCACCAATGTACC
CGGCAAAAGGGCCACCAAGCCCCCTTATTAGAGAATCACCAT
GCATTCTTACAATAACGAACAATAAACAGCCGGAAGCGGAGA
GCTTTACTAGATCGCGCGTCAGATGAATATAACAGAAAGTTT
AGAGATTTTATCATCAGTTGAGATATCATAAAACCGATGCAT
GTAAGAAAAATAAAACGAACTAACGCGAGAGCGATAGTCTAA
TTCGTAAGCGATTCACAAACAAATCACCCTCATCAGCTCGGA
TTAGAACGCGAGATTAGTTGCTATTTTCCAGCAGTAGGGGCA
AATTAATTACGAAACAAACATCAACTGATTGATGCGTTTGAA
CATCCCTCGTAAATGTTTAGACTGACGAGAATTCAAATTTTA
TACGCCGCCTGGAACTTTTGCAAATATTATAAAGCGGATTAG
TTTAGAGCCACATCTTTTCATAATAGCACCGCAAAATCGGGC
CAAAGCCTAATTATCCCAATCCAAGAGAGAAAACAAAGTAAG
CATCTTTGAAAGTACCTTTTACATTCAAAATAATGGAAAGGA
ATTAGTACGGTGTCTGGAGTTTGACCAACCTGATTATAGGGA
AGCAATATAATGCTGTATTTAGCTTTCCATTCATCGCCCATG
GACACGGAATAAGTTTAATCAATTAGACGTTTAGCAAGCCTC
AATATACATAAAGGTGGATACAGGCCTCATACGTCACCCGTA
CCCTTTTTAAGAAAAGTCACTAACCGACGACGCCTGTTATAA
GCGTTTGCGGAACAAAGTTGAGGAGACCTAAATCTTAGTCCG
TTGTAACGCCAGGGTTTGGGTACCACGGTCACTGACCTCACG
TCGAGCTGGCGAAAGGGCTGTGTGTCCGCGAATTACCCTTGA
TCGGTTGGGAAGGGCGAGAGCCGGCTCAGAATAGCGGGTCGG
GACGGTAATATCCAGAAGACAGGAGTAGAAACAAGTACCGCT
CACATCACTTGCCTGAGTCAGTGACTACCTTTAGAATCGTAT
ATATGGTCAATATATTTTAAATGCGATAAATCCATCAACGGA
TTTGCTGAAAGCCTTTATTTCAACACAAAGGAAATTTTCGCA
GATACATCCAGTACCAAAAACATTAGAGAATTATTTAAAGTA
AAAAATAGATAGTTGGCAAATCAAACCAGCAGGCTATTTTTT
ATAAAACAATTTGCTGAACCTCAAACCGCCTCTGAAAGGATT
ACCTCTAGAGTTCACCGCCTGGCCTTTGCCCTAGTAAATCAT
TTAGTCATAGGTTTTTCTTTTCACAATCGGCTCAGTGAATAC
AGATCCACACAACGCGCGGGGAGAAGGGTTGTGAAACAGTCT
CTCGGGTGCCAGTCGGGAAACCTGAAAGAACTAAACAGTGAT
GATAAGTGTTGCTTTGACGAGCACAAAGGAAGTTTTTAACCT
TGTTACCACATTCAACTAGGCATAAGGCTTGCACCCTCAAGA
CAGCATTATTACAGGTAACGACGACAACAACCGGCTACTAAA
CTGCATTAAAGCCAGAAAGCCGCCATTTCTTAACAACTGAAT
GATGGTCAGACGATTGGCAGAGCCAGCCTTTCAACTAATAAC
CCCAGGTTTTGAAGCCTGTTACAACAGTATAAGAGAATGACA

AATACCTGAGCAAAAGATTACAAAAAAAAGCAATAAGGAAAT
TCGGGCGCATGAACGAGCAGCAGGCGAAAATATTGCCCGATC
CCGAGAACCGTGCTCATAAAATCCCTTATAACAGGGTGCTGT
TTCAGAAGGAATTATTCAGTGTTGTTCCAGTATCGGCCAACA
CTCATAAGTGGCCCGTAGTGGACTCCAACGTGCTTTCCTAAT
AATAACGGGTCAATAGCAGAGCTTGACGGGGAGAATCAGATT
AAAAGTTAATATTAACCGGGAAGAAAGCGAATATGGTTTTTA
TTTAAGTTTCGATTAGAGAGTACCATCGCGTAAAGACAATAT
CTGGCTCAACTTTTTGCGGATGGCTTGCATCTTGAGGATGCG
GGCTTTTGTCCGCCAAAGACAAAAACCAGTAGTTTCAGTGCT
ATCCAACATAAAGGTAAATATTGAGTCACCGGCGAATAAAGG
CATAATAGCATGAAAACCACCAGAGGGTTAGAATGGTTATAC
TACAACGAGGGAAAGACTGACCATAAATCAAAATAGTATTAC
ATGCTTTTATCCAAGCAGTCAGGGAAACGTCCACCACCCCCT
TCGAGAATAGGAGCCAGTAATCAGTAGCGACCGTTTGCCCAC
TCTTCGAGCCCACCCTGTAACATAAAAACAGATATTATTTTG
TTCCCGACCGTCTGAATTATTTGCACGTAAACAGTAACTACC
CCCTCCCAGTGTGGGAACAAACGGAAATAATCGAAACACCAC
TTCGGATGTGTTGGTGTAGATGGGTGTTAAATTGTGTCGGTC
TACTCGGTGCGAGGGGACGACGACATTGTAAGGAACCCTTTG
TTACAATATTTGGAAATACCTACAAGTCTTTAATAGATTAAT
TAATAGAAGATATTTACATTGGCACGTAAGATATATAATAAT
CTTCTTTGACCCAGCTTAATCACCATCAATATAAAGATTAGA
CGAACGGAGAAGGAACGTAATGCCGGAGAGGACCCTCATAAC
CAGCTCATTTTCGCATTCTATCAGGTCATTGGGGAGAAAGGT
TACGTAACACAAGCAAACGATGAACGGTAATATCGGTTATAA
TTAGAACAAGTTTGAATGAAGATAAAACAGATCTGGTCAATA
GTCTAAATGCTTCTGACGCAACAGTGCCACGCATCACCTCGA
CAGGAAAGATAGAACTGGCTCATTATAAGGCGAGTAATGGAA
CAGTGGTTAATCTACGAAAGCGCATGAAAGTTGAGACTCCCT
CCTCCTTGATTCATACATGGCTTTTTAATGCTCAGTACTTAG
CCATAAATCAAGGCGTTTTAGCGATTTTCATATCGAGATAAT
AAGAGATGATATTTAACAATTTCAAATAACCACATAGCATAG
GATATAAGTTATCATTCCAAGTGAGAAT
CGCCATATTTAAGAAAATCTCCAAAAAAATAA
ACTCACATTAATGGAGGCCGATTAAAGGGAGCGGG
AGCTAAACATGCGTTGCGCTCACTGCCCCAAAGGG
CAATTTTATCCTAGCATTGACAGGAGGTCACCAGA
GCCGCCGCCGAATCTTACCAACGCTAACACGATTT
CAAACTACAACGCCTAGCTAATGCAGAACGCAATAAAC
TCGGCTGTCTTTCCTATAGCCCGGAATAGGTGAGGGTT
GTAATTGTAGCAGCCTTTACAATAAGAAGAGCGTCTTTG
TGTAGCGCGCAAAAATGAAAAAGCGCTAATATCAAGGTGAAT
AGCCTCAAAGAATTAGCAAAATTTATCTTTAGGAGAAGCAGA
CGAAAAACCGTCCCCCGATTTAAGCAAATCAGAGGGTCAGTG
CCTTGAGGTAATAAGTTTTAACGTATAGAAGGCTTCCAGCTA
TGATAGCCCTAAGTTGATAATCAGCACCGCTTCTGGACAGGAAAA
GAGCGCCATTAGCCAGCTTTCCGGAAAAGCCCCAAAAACTAGCAT
TTTGTTTAACGTTTTTCATCGGCATTTTGTCAGACTATCACCCGGA

TAGCCGAACAAAAGAAAATACTATTCATTAAGAGAGATAACCCACAAGA
GTCAATCATATGTACCCCGAACATCGCCGGTTATCTAAAAAAGCAATAA
ACGCTCAACCGCCAGCCATTGCATGCCGGAAACCAGGCAAAGTGAGCTA
AACATGTTCGTAGCATTCCACTTTCACGTTCAACGCCAACATGTAATTT

Hybridization staples:
TTAACAGCTTGCATGCCTGCAACGA
CATTATCTGGCCAACAGAGATGTAATAA
ATACATAACTTCATTTCAATTTACCTTT
AGTTGCAGCTAACCACCACACACGCAAA
CCCTCAAATCGTCATAAATATTCTTCAGG
ACTTCTTTGATTAGAGAGTCTCAAAATCGATA
AAAAGAATACACAAAGAACGCGAGAAAAAATCCAA
GTTATTACTCGTATTAAATCCTTTCCCAATTCTGC
CTTAGGTCAGATTCCATATAACAGTTGATTGCCCGAAC
AAACCTGATTTAAAGAAATTGCGTAGATTATTGAATCC
GGCGAACGAGTCAAAAGGGTGAGAAAGGCAATGAAAAA
TTTAACAGAGGCGAATTAGCCAAAAGGAATTACGAATGCAG
GAGAAACAGATGAATGAGATGGTAGTACATAAATCAATATAT
TCGCAAGACTAAAACACTCATTGAAAGAGGGAGTCAATAGTG
AAGGGACATAATGTGAGCGAGCCAGTGCCACGTTGTAGCAAT
TCTAAAGCTGAGAGCCAGCAGCACGGAGACAGTCATCATCAA
GTAGCGGTCACGCTGCGCGAAGCGGTCCACGCTGGCTGAGAG
CAAATTTTAATTATCAGATGATGGCAATTGGAAGCAAACTCCAAC
AATTTATGTCCATCCCGCCGCGCTTAATGGCAAGTGTGAGTGTTTG
TTTAATGGAAACTTAATTTCAACTTTAATTGGGCTCGGTGTACCAA
CAAAGCGAACCAGACCCATCAATATAATTAAGAATAAACAGCTTTTGCG
GGATCGTCAGGGAGTTAAAGGCCCCGGAATCATAATAGATTAAGACGCT

A-stacking staples:
GCTTTTGCGAACCAGACC
AGCTTGCATAGTTGCAGC
ACAGATGAATGAGATGGT
GCCAAAAGGTAAATATTC
ACGAATGCAGATACATAAC
TAAAACACTCATTGAAAGAGG
AATGTGAGCGAGCCAGTGCCA
TCCCAATTCTGCAAAAGAATACAC
CGGAGACAGTCATCATCAACATTA
ATTGAATCCCCCTCAAATCGTCAAATT
GGCGAACGAGTCAAAAGGGTGAGAAAGGC
CTTAGGTCAGATTCCATATAACAGTTGAT
TTAATTTCAACTTTAATTGGGCTCGGTGTACCAA
AAGCGGTCCACGCTGGCTGAGAGGCCTGCAACGA
GGAAGCAAACTCCAACCAAAGCGGGATCGTCAGGGAGTTAAAGGCC

B-stacking staples:
TCTGGCCAACCAGCAGCA
AAAGAACGCTAAATCCTT
GAGTCAATAGTGTCGCAAGAC
CGTTGTAGCAATAAGGGACAT
TAACCACCACACACGCAAATTAAC
TTCAGGTTTAACAGAGGCGAATTA
AGTACATAAATCAGACGCTGAGAA
CATCAATATAATTAAGAATAAACA
AATGAAAAATCTAAAGCTGAGAGCAGA
AAACCTGATTTAAAGAAATTGCGTAGATT
CAAATTTTAATTATCAGATGATGGCAATT
TTCATTTCAATTTACCTTTTTTAATGGAAAC
TGCCCGAACGTTATTACTCGTATGAGAAAAAATCCAAAATT
GATGTAATAAACTTCTTTGATTAGAGAGTCTCAAAATCGATA
TATGTCCATCCCGCCGCGCTTAATGGCAAGTGTGAGTGTTTG
CCGGAATCATAATAGATTAAATATATGTAGCGGTCACGCTGCGCG

Primers for C-Trap handle synthesis:
GCTTTTGCGGGATCGTCAGGGAGTTAAAGGCC/iSp9/gagatctcgatcctctacgccggacg
TAAGAATATCATAATAGATTAAGACGCTGAGAA/iSp9/gagatctcgatcctctacgccggacg
biotin-aaaggcggacaggtatccggtaagc
Dig-aaaggcggacaggtatccggtaagc

Protruding arms for AuNP hybridization:
CAATTGCCCTGATGGTGGTTCCGACAGTGAGAATTCGTAGTTGGGACCGTAAATTATTATTATTATTA
GAATGAGATGGCGGTCCACGCTGGCTGAGAGGCCTGCAACGACGGTAACAACATTATTATTATTATTA
CCGTGCTCATAAAATCCCTTATAACAGGGTGCTGTTTCGGATGTGTTGGTGTATTATTATTATTATTA
GGAATTATTCAGTGTTGTTCCAGTATCGGCCAACATACTCGGTGCGAGGGGAATTATTATTATTATTA
GTGGCCCGTAGTGGACTCCAACGTGCTTTCCTAATGAGCGCCATTAGCCAGCATTATTATTATTATTA
TGCCCCCTGCAAGAGTCCACTATTTCGTGCCAAGTGTACGCAACTGCCTCAGATTATTATTATTATTA
CATGAACGAGCAGCAGGCGAAAATATTGCCCGATCCCCTCCCAGTGTGGGAAATTATTATTATTATTA
GGCATTAAATGAATAGCCCGAGATGGCGGTTTATCCGCTTACGCCTAACCGTATTATTATTATTATTA

Fluorescently labeled staples to monitor polymerization:
[6FAM]AATGTGAGCGAGCCAGTGCCA
[TAMRA]CGTTGTAGCAATAAGGGACAT
[6FAM]TGCCCGAACGTTATTACTCGTATGAGAAAAAATCCAAAATT
CGTTGTAGCAATAAGGGACAT[TAMRA]
[TAMRA]GGAAGCAAACTCCAACCAAAGCGGGATCGTCAGGGAGTTAAAGGCC
AATGTGAGCGAGCCAGTGCCA[6FAM]

Connector interface for fuel staple integration:
TAAAGAGGTATAGCGTTCAGGTTTAACAGAGGCGAATTATGGAGAGTTGAAGGAG
TAAAGAGGTATAGCGATTGAATCCCCCTCAAATCGTCATAAATATTCTGGAGAGTTGAAGGAG
TAAAGAGGTATAGCGCATCAATATAATCCTGATTTAAAGAAATTGCGTAGATTTGGAGAGTTGAAGGAG
CTTAGGTCAGATTCCATATAACAGTTGATTGGAGAGTTGAAGGAG
TAAAGAGGTATAGCGGGAAGCAAACTCCAACCAAAGCGAACCAGACCTGGAGAGTTGAAGGAG
TAAAGAGGTATAGCGTGCCCGAACGTTATTACTCGTATTAAATCCTTTGGAGAGTTGAAGGAG
CAAATTTTAATTATCAGATGATGGCAATTTGGAGAGTTGAAGGAG
TAAAGAGGTATAGCGTCCCAATTCTGCGAACGAGTCAAAAGGGTGAGAAAGGCTGGAGAGTTGAAGGAG

TAAAGAGGTATAGCGAATGAAAAATCTAAAGCTGAGAGCCAGCAGCATGGAGAGTTGAAGGAG
TAAAGAGGTATAGCGCGGAGACAGTCATCATCAACATTATGGAGAGTTGAAGGAG
TAAAGAGGTATAGCGTCTGGCCAACAGAGATGTAATAA
TAAAGAGGTATAGCGAATGTGAGCGAGCCAGTGCCATGGAGAGTTGAAGGAG
ACTTCTTTGATTAGAGAGTCTGTCCATC
TAAAGAGGTATAGCGCGTTGTAGCAATAAGGGACATTGGAGAGTTGAAGGAG
TAAAGAGGTATAGCGAGCTTGCATGCCTGCAACGA
CCGCCGCGCTTAATGGCAAGTGTGAGTG
TAAAGAGGTATAGCGTAACCACCACACACGCAAATTAACTGGAGAGTTGAAGGAG
GTAGCGGTCACGCTGCGCGTGGAGAGTTGAAGGAG
TAAAGAGGTATAGCGAAGCGGTCCACGCTGGCTGAGAGAGTTGCAGCTGGAGAGTTGAAGGAG
TAAAGAGGTATAGCGAGTACATAAATCAATATAT
TAAAGAGGTATAGCGTTAATTTCAACTTTAATTGGGCTTGAGATGGTTGGAGAGTTGAAGGAG
TAAAGAGGTATAGCGTTCATTTCAATTTACCTTTTTTAATGGAAACTGGAGAGTTGAAGGAG
TAAAGAGGTATAGCGGCCAAAAGGAATTACGAATGCAGATACATAACTGGAGAGTTGAAGGAG
TAAAGAGGTATAGCGAAAGAACGCGAGAAAAAATCCAATCGCAAGACTGGAGAGTTGAAGGAG
GGCAAAAGAATACACTGGAGAGTTGAAGGAG
TAAAGAGGTATAGCGCCGGAATCATAATAGATTAAGACGCTGAGAATGGAGAGTTGAAGGAG
AAATAAGAATAAACATGGAGAGTTGAAGGAG
TAAAGAGGTATAGCGGCTTTTGCGGGATCGTCAGGGAGTTAAAGGCCTGGAGAGTTGAAGGAG
TAAAGAGGTATAGCGTAAAACACTCATTGAAAGAGGTGGAGAGTTGAAGGAG
TAAAGAGGTATAGCGGAGTCAATAGTGAATTTATCAAAATC
TAAAGAGGTATAGCGACAGATGAACGGTGTA
[6FAM]TAAAGAGGTATAGCGAAGCGGTCCACGCTGGCTGAGAGAGTTGCAGCTGGAGAGTTGAAGGAG
GTAGCGGTCACGCTGCGCGTGGAGAGTTGAAGGAG[TAMRA]

DRN oligonucleotides:
TCTTTACTCCTTCAACTCTCCAAACAACAATCTTCCCTCCACCG
TCTTTACTCCTTCAACTCTCCAAACAACATCCTCACACAAACGC
CCCATTTCTCTAACTAACCACCCTATACCAAACTTACATTACCG
TGTTGTTTGGAGAGTTGAAGGAGTAAAGAGGTATAGGGTGGTTAGTTAGAGAAATGGGCG
ATCTTCCCTCCACCGCCCATTTCTCTAACTAACCACC
AAATGGGCGGTGGAGGGAAGATTGTTGTTGCGTTTGTGTGAGGATGTTGTTTG
AACAACATCCTCACACAAACGCAACAACA
CGCTATACCTCTTTACTCCTTCAACTCTCCA
CATCACGCTATACCTCTTTACTCCTTCAACTCTCCA
TGGAGAGTTGAAGGAGTAAAGAGGTATAGCGTGATG
TGTTGTT-T[AMRA]-GGAGAGTTGAAGGAGTAAAGAGGTATAGGGTGGTTAGTTAGAGAAATGGGCG
CGCTATACCTCTTTACTCCTTCAACTCTCCA-[6FAM]
CATCACGCTATACCTCTTTACTCCTTCAACTCTCCA-[6FAM]

M13mp18 scaffold:
TGATAGACGGTTTTTCGCCCTTTGACGTTGGAGTCCACGTTCTTTAATAGTGGACTCTTGTTCCAAACTGGAA
CAACACTCAACCCTATCTCGGGCTATTCTTTTGATTTATAAGGGATTTTGCCGATTTCGGAACCACCATCAAAC
AGGATTTTCGCCTGCTGGGGCAAACCAGCGTGGACCGCTTGCTGCAACTCTCTCAGGGCCAGGCGGTGAAG
GGCAATCAGCTGTTGCCCGTCTCACTGGTGAAAAGAAAAACCACCCTGGCGCCCAATACGCAAACCGCCTCT
CCCCGCGCGTTGGCCGATTCATTAATGCAGCTGGCACGACAGGTTTCCCGACTGGAAAGCGGGCAGTGAGC
GCAACGCAATTAATGTGAGTTAGCTCACTCATTAGGCACCCCAGGCTTTACACTTTATGCTTCCGGCTCGTAT
GTTGTGTGGAATTGTGAGCGGATAACAATTTCACACAGGAAACAGCTATGACCATGATTACGAATTCGAGCT
CGGTACCCGGGGATCCTCTAGAGTCGACCTGCAGGCATGCAAGCTTGGCACTGGCCGTCGTTTTACAACGTC
GTGACTGGGAAAACCCTGGCGTTACCCAACTTAATCGCCTTGCAGCACATCCCCCTTTCGCCAGCTGGCGTAA
TAGCGAAGAGGCCCGCACCGATCGCCCTTCCCAACAGTTGCGCAGCCTGAATGGCGAATGGCGCTTTGCCTG
GTTTCCGGCACCAGAAGCGGTGCCGGAAAGCTGGCTGGAGTGCGATCTTCCTGAGGCCGATACTGTCGTCG
TCCCCTCAAACTGGCAGATGCACGGTTACGATGCGCCCATCTACACCAACGTGACCTATCCCATTACGGTCAA
TCCGCCGTTTGTTCCCACGGAGAATCCGACGGGTTGTTACTCGCTCACATTTAATGTTGATGAAAGCTGGCTA
CAGGAAGGCCAGACGCGAATTATTTTTGATGGCGTTCCTATTGGTTAAAAAATGAGCTGATTTAACAAAAAT
TTAATGCGAATTTTAACAAAATATTAACGTTTACAATTTAAATATTTGCTTATACAATCTTCCTGTTTTTGGGG
CTTTTCTGATTATCAACCGGGGTACATATGATTGACATGCTAGTTTTACGATTACCGTTCATCGATTCTCTTGT
TTGCTCCAGACTCTCAGGCAATGACCTGATAGCCTTTGTAGATCTCTCAAAAATAGCTACCCTCTCCGGCATT
AATTTATCAGCTAGAACGGTTGAATATCATATTGATGGTGATTTGACTGTCTCCGGCCTTTCTCACCCTTTTGA
ATCTTTACCTACACATTACTCAGGCATTGCATTTAAAATATATGAGGGTTCTAAAAATTTTTATCCTTGCGTTG
AAATAAAGGCTTCTCCCGCAAAAGTATTACAGGGTCATAATGTTTTTGGTACAACCGATTTAGCTTTATGCTC
TGAGGCTTTATTGCTTAATTTTGCTAATTCTTTGCCTTGCCTGTATGATTTATTGGATGTTAATGCTACTACTAT
TAGTAGAATTGATGCCACCTTTTCAGCTCGCGCCCCAAATGAAAATATAGCTAAACAGGTTATTGACCATTTG
CGAAATGTATCTAATGGTCAAACTAAATCTACTCGTTCGCAGAATTGGGAATCAACTGTTATATGGAATGAA
ACTTCCAGACACCGTACTTTAGTTGCATATTTAAAACATGTTGAGCTACAGCATTATATTCAGCAATTAAGCTC
TAAGCCATCCGCAAAAATGACCTCTTATCAAAAGGAGCAATTAAAGGTACTCTCTAATCCTGACCTGTTGGA
GTTTGCTTCCGGTCTGGTTCGCTTTGAAGCTCGAATTAAAACGCGATATTTGAAGTCTTTCGGGCTTCCTCTTA
ATCTTTTTGATGCAATCCGCTTTGCTTCTGACTATAATAGTCAGGGTAAAGACCTGATTTTTGATTTATGGTCA
TTCTCGTTTTCTGAACTGTTTAAAGCATTTGAGGGGGATTCAATGAATATTTATGACGATTCCGCAGTATTGG
ACGCTATCCAGTCTAAACATTTTACTATTACCCCCTCTGGCAAAACTTCTTTTGCAAAAGCCTCTCGCTATTTTG
GTTTTTATCGTCGTCTGGTAAACGAGGGTTATGATAGTGTTGCTCTTACTATGCCTCGTAATTCCTTTTGGCGT
TATGTATCTGCATTAGTTGAATGTGGTATTCCTAAATCTCAACTGATGAATCTTTCTACCTGTAATAATGTTGT
TCCGTTAGTTCGTTTTATTAACGTAGATTTTTCTTCCCAACGTCCTGACTGGTATAATGAGCCAGTTCTTAAAA
TCGCATAAGGTAATTCACAATGATTAAAGTTGAAATTAAACCATCTCAAGCCCAATTTACTACTCGTTCTGGT
GTTTCTCGTCAGGGCAAGCCTTATTCACTGAATGAGCAGCTTTGTTACGTTGATTTGGGTAATGAATATCCGG
TTCTTGTCAAGATTACTCTTGATGAAGGTCAGCCAGCCTATGCGCCTGGTCTGTACACCGTTCATCTGTCCTCT
TTCAAAGTTGGTCAGTTCGGTTCCCTTATGATTGACCGTCTGCGCCTCGTTCCGGCTAAGTAACATGGAGCAG
GTCGCGGATTTCGACACAATTTATCAGGCGATGATACAAATCTCCGTTGTACTTTGTTTCGCGCTTGGTATAA
TCGCTGGGGGTCAAAGATGAGTGTTTTAGTGTATTCTTTTGCCTCTTTCGTTTTAGGTTGGTGCCTTCGTAGT
GGCATTACGTATTTTACCCGTTTAATGGAAACTTCCTCATGAAAAAGTCTTTAGTCCTCAAAGCCTCTGTAGCC
GTTGCTACCCTCGTTCCGATGCTGTCTTTCGCTGCTGAGGGTGACGATCCCGCAAAAGCGGCCTTTAACTCCC
TGCAAGCCTCAGCGACCGAATATATCGGTTATGCGTGGGCGATGGTTGTTGTCATTGTCGGCGCAACTATCG
GTATCAAGCTGTTTAAGAAATTCACCTCGAAAGCAAGCTGATAAACCGATACAATTAAAGGCTCCTTTTGGA
GCCTTTTTTTTGGAGATTTTCAACGTGAAAAAATTATTATTCGCAATTCCTTTAGTTGTTCCTTTCTATTCTCAC
TCCGCTGAAACTGTTGAAAGTTGTTTAGCAAAATCCCATACAGAAAATTCATTTACTAACGTCTGGAAAGAC
GACAAAACTTTAGATCGTTACGCTAACTATGAGGGCTGTCTGTGGAATGCTACAGGCGTTGTAGTTTGTACT
GGTGACGAAACTCAGTGTTACGGTACATGGGTTCCTATTGGGCTTGCTATCCCTGAAAATGAGGGTGGTGG
CTCTGAGGGTGGCGGTTCTGAGGGTGGCGGTTCTGAGGGTGGCGGTACTAAACCTCCTGAGTACGGTGATA
CACCTATTCCGGGCTATACTTATATCAACCCTCTCGACGGCACTTATCCGCCTGGTACTGAGCAAAACCCCGC
TAATCCTAATCCTTCTCTTGAGGAGTCTCAGCCTCTTAATACTTTCATGTTTCAGAATAATAGGTTCCGAAATA
GGCAGGGGGCATTAACTGTTTATACGGGCACTGTTACTCAAGGCACTGACCCCGTTAAAACTTATTACCAGT
ACACTCCTGTATCATCAAAAGCCATGTATGACGCTTACTGGAACGGTAAATTCAGAGACTGCGCTTTCCATTC
TGGCTTTAATGAGGATTTATTTGTTTGTGAATATCAAGGCCAATCGTCTGACCTGCCTCAACCTCCTGTCAAT

GCTGGCGGCGGCTCTGGTGGTGGTTCTGGTGGCGGCTCTGAGGGTGGTGGCTCTGAGGGTGGCGGTTCTG
AGGGTGGCGGCTCTGAGGGAGGCGGTTCCGGTGGTGGCTCTGGTTCCGGTGATTTTGATTATGAAAAGAT
GGCAAACGCTAATAAGGGGGCTATGACCGAAAATGCCGATGAAAACGCGCTACAGTCTGACGCTAAAGGC
AAACTTGATTCTGTCGCTACTGATTACGGTGCTGCTATCGATGGTTTCATTGGTGACGTTTCCGGCCTTGCTA
ATGGTAATGGTGCTACTGGTGATTTTGCTGGCTCTAATTCCCAAATGGCTCAAGTCGGTGACGGTGATAATT
CACCTTTAATGAATAATTTCCGTCAATATTTACCTTCCCTCCCTCAATCGGTTGAATGTCGCCCTTTTGTCTTTG
GCGCTGGTAAACCATATGAATTTTCTATTGATTGTGACAAAATAAACTTATTCCGTGGTGTCTTTGCGTTTCTT
TTATATGTTGCCACCTTTATGTATGTATTTTCTACGTTTGCTAACATACTGCGTAATAAGGAGTCTTAATCATG
CCAGTTCTTTTGGGTATTCCGTTATTATTGCGTTTCCTCGGTTTCCTTCTGGTAACTTTGTTCGGCTATCTGCTT
ACTTTTCTTAAAAAGGGCTTCGGTAAGATAGCTATTGCTATTTCATTGTTTCTTGCTCTTATTATTGGGCTTAA
CTCAATTCTTGTGGGTTATCTCTCTGATATTAGCGCTCAATTACCCTCTGACTTTGTTCAGGGTGTTCAGTTAA
TTCTCCCGTCTAATGCGCTTCCCTGTTTTTATGTTATTCTCTCTGTAAAGGCTGCTATTTTCATTTTTGACGTTA
AACAAAAAATCGTTTCTTATTTGGATTGGGATAAATAATATGGCTGTTTATTTTGTAACTGGCAAATTAGGCT
CTGGAAAGACGCTCGTTAGCGTTGGTAAGATTCAGGATAAAATTGTAGCTGGGTGCAAAATAGCAACTAAT
CTTGATTTAAGGCTTCAAAACCTCCCGCAAGTCGGGAGGTTCGCTAAAACGCCTCGCGTTCTTAGAATACCG
GATAAGCCTTCTATATCTGATTTGCTTGCTATTGGGCGCGGTAATGATTCCTACGATGAAAATAAAAACGGCT
TGCTTGTTCTCGATGAGTGCGGTACTTGGTTTAATACCCGTTCTTGGAATGATAAGGAAAGACAGCCGATTA
TTGATTGGTTTCTACATGCTCGTAAATTAGGATGGGATATTATTTTTCTTGTTCAGGACTTATCTATTGTTGAT
AAACAGGCGCGTTCTGCATTAGCTGAACATGTTGTTTATTGTCGTCGTCTGGACAGAATTACTTTACCTTTTG
TCGGTACTTTATATTCTCTTATTACTGGCTCGAAAATGCCTCTGCCTAAATTACATGTTGGCGTTGTTAAATAT
GGCGATTCTCAATTAAGCCCTACTGTTGAGCGTTGGCTTTATACTGGTAAGAATTTGTATAACGCATATGATA
CTAAACAGGCTTTTTCTAGTAATTATGATTCCGGTGTTTATTCTTATTTAACGCCTTATTTATCACACGGTCGG
TATTTCAAACCATTAAATTTAGGTCAGAAGATGAAATTAACTAAAATATATTTGAAAAAGTTTTCTCGCGTTC
TTTGTCTTGCGATTGGATTTGCATCAGCATTTACATATAGTTATATAACCCAACCTAAGCCGGAGGTTAAAAA
GGTAGTCTCTCAGACCTATGATTTTGATAAATTCACTATTGACTCTTCTCAGCGTCTTAATCTAAGCTATCGCT
ATGTTTTCAAGGATTCTAAGGGAAAATTAATTAATAGCGACGATTTACAGAAGCAAGGTTATTCACTCACAT
ATATTGATTTATGTACTGTTTCCATTAAAAAAGGTAATTCAAATGAAATTGTTAAATGTAATTAATTTTGTTTT
CTTGATGTTTGTTTCATCATCTTCTTTTGCTCAGGTAATTGAAATGAATAATTCGCCTCTGCGCGATTTTGTAA
CTTGGTATTCAAAGCAATCAGGCGAATCCGTTATTGTTTCTCCCGATGTAAAAGGTACTGTTACTGTATATTC
ATCTGACGTTAAACCTGAAAATCTACGCAATTTCTTTATTTCTGTTTTACGTGCAAATAATTTTGATATGGTAG
GTTCTAACCCTTCCATTATTCAGAAGTATAATCCAAACAATCAGGATTATATTGATGAATTGCCATCATCTGAT
AATCAGGAATATGATGATAATTCCGCTCCTTCTGGTGGTTTCTTTGTTCCGCAAAATGATAATGTTACTCAAA
CTTTTAAAATTAATAACGTTCGGGCAAAGGATTTAATACGAGTTGTCGAATTGTTTGTAAAGTCTAATACTTC
TAAATCCTCAAATGTATTATCTATTGACGGCTCTAATCTATTAGTTGTTAGTGCTCCTAAAGATATTTTAGATA
ACCTTCCTCAATTCCTTTCAACTGTTGATTTGCCAACTGACCAGATATTGATTGAGGGTTTGATATTTGAGGTT
CAGCAAGGTGATGCTTTAGATTTTTCATTTGCTGCTGGCTCTCAGCGTGGCACTGTTGCAGGCGGTGTTAAT
ACTGACCGCCTCACCTCTGTTTTATCTTCTGCTGGTGGTTCGTTCGGTATTTTTAATGGCGATGTTTTAGGGCT
ATCAGTTCGCGCATTAAAGACTAATAGCCATTCAAAAATATTGTCTGTGCCACGTATTCTTACGCTTTCAGGT
CAGAAGGGTTCTATCTCTGTTGGCCAGAATGTCCCTTTTATTACTGGTCGTGTGACTGGTGAATCTGCCAATG
TAAATAATCCATTTCAGACGATTGAGCGTCAAAATGTAGGTATTTCCATGAGCGTTTTTCCTGTTGCAATGGC
TGGCGGTAATATTGTTCTGGATATTACCAGCAAGGCCGATAGTTTGAGTTCTTCTACTCAGGCAAGTGATGT
TATTACTAATCAAAGAAGTATTGCTACAACGGTTAATTTGCGTGATGGACAGACTCTTTTACTCGGTGGCCTC
ACTGATTATAAAAACACTTCTCAGGATTCTGGCGTACCGTTCCTGTCTAAAATCCCTTTAATCGGCCTCCTGTT
TAGCTCCCGCTCTGATTCTAACGAGGAAAGCACGTTATACGTGCTCGTCAAAGCAACCATAGTACGCGCCCT
GTAGCGGCGCATTAAGCGCGGCGGGTGTGGTGGTTACGCGCAGCGTGACCGCTACACTTGCCAGCGCCCTA
GCGCCCGCTCCTTTCGCTTTCTTCCCTTCCTTTCTCGCCACGTTCGCCGGCTTTCCCCGTCAAGCTCTAAATCGG
GGGCTCCCTTTAGGGTTCCGATTTAGTGCTTTACGGCACCTCGACCCCAAAAAACTTGATTTGGGTGATGGTT
CACGTAGTGGGCCATCGCCC

Publications

The primordial life of DNA dynamic networks, Winat, LJ. and Saccà, B., Nature Catalysis 3, (2020)[3]

Growth Rate and Thermal Properties of DNA Origami Filaments, Stenke, LJ. and Saccà, B., Nano Letters 22, (2022)[1]

Design, Mechanical Properties, and Dynamics of Synthetic DNA Filaments, Stenke, LJ. and Saccà, B., Bioconjugate Chemistry 34, (2023)[2]

The following article was accepted for publication:

Sequence-dependent folding of monolayered DNA origami domains, Gambietz, S., Stenke, LJ. and Saccà, B.

The following article is in preparation for publication:

DNA Origami Polymerization with a DNA Reaction Network, Stenke, LJ., Weiß, M., Saccà, B.

Posters:

Hierarchical assembly of biomimetic complexes, Pfeifer, W., Winat, LJ., Lill, P., Gatsogiannis, C. and Saccà, B., *NanTech* 2019, Aalto, Finland

Kinetics of DNA origami dimers and filaments formation, Winat, LJ., Pfeifer, W. and Saccà, B., 3rd International Symposium "Supramolecular Principles in Biological Systems", 2019, Essen, Germany awarded with a Poster Prize

Dynamics of DNA Origami Filaments Growth from a ditopic Monomer, Stenke, LJ. and Saccà, B., Functional DNA Nanotechnology (FDN) workshop, 2022, Rome, Italy

Acknowledgments

Over the last four years, I have experienced a beautiful, chaotic, stressful, and remarkable time that has ultimately resulted in personal and professional growth that I could not have imagined. I am immensely grateful to the many people who have supported, encouraged, and guided me along the way.

First and foremost, I want to express my gratitude to my awesome and inspiring PI, Prof. Dr. Barbara Saccà, for the engaging discussions and for always having the right resources for all my questions at hand. Her trust in my abilities and the freedom to explore my ideas were highly appreciated, and she was the reason for me to keep going when experiments were frustrating beyond belief so many times. Prof. Dr. Stefan Westermann and Prof. Dr. Francesco Ricci deserve special thanks for evaluating this Ph.D. thesis.

Dr. Nadine Ruchter deserves thanks for encouraging me to spend a fantastic semester abroad, which ultimately turned into two, and Prof. Dr. Michael Ehrmann for being a great early-stage mentor during my studies and inspiring me to apply to the Amgen Scholars Program. I am very grateful for the opportunity to have gained research experience and invaluable skills at the Institute Pasteur.

I feel fortunate to have been a part of the amazing Saccà lab in the past years, which is undoubtedly the best group ever to do a Ph.D. project. I am grateful for the fun times in the lab, at lunch, and at social events with Dr. Andreas Jaekel and Sayantan De. My gratitude also goes to Dr. Wolfgang Pfeifer for developing the original 24-helix bundle structure and for teaching me the foundations of DNA origami. I want to thank Pierre Stegemann for being an awesome office buddy and for the great and meaningful, and sometimes absurd discussions about more-or-less anything. My sincere thanks go out to Dr. Richard Kosinski for patiently answering the same question ten times and for his fun attitude, and to Melanie Weiß, who has been a great and attentive support during the last part of this project. I am thankful to Sabrina Gambietz for the engaging conversations, social activities, and for giving me the feeling to make a difference with my teaching and support.

I want to thank Prof. Dr. Markus Kaiser for giving me my first job at the university, thereby introducing me to the Saccà group, and for his support throughout the last years. My gratitude goes to Dr. Sabrina Ninck and Leonard Sewald for the fun lunch breaks and social events. Svenja Heimann and Jenny Bormann deserve thanks for keeping our entire labs functional and taking great care of all lab members. Likewise, I want to appreciate Svenja Kernchen for helping all of us survive the jungle of university administrative requirements.

Dr. Michael Erkelenz's support with TEM and AuNPs was invaluable, as were the evenings spent with him, Viki Erkelenz, and many more at Casa Erkelenz. Michelle Hechler, I want to thank for the deep conversations that usually went straight from saying Hi in the lab to just chattering away for way too long way too often. My dear friend Lea Chilla I want to appreciate for always having an open ear and for her support and inspiration throughout the years.

I immensely appreciate my parents, Frauke and Norbert Winat, for their unwavering support and for showing what real strength and determination mean, especially in the past year. Finally, I will be forever grateful for my husband, Sven Stenke, and his endless love, care, and support. Listening to the hundreds of times of me rambling about my research problems while trying to figure things out and making sure that I take some breaks was invaluable.

To anyone I might have forgotten to mention here, I want to apologize in advance. To best sum this up:

To whom it may concern:
Thank you!

Curriculum vitae

Der Lebenslauf ist in der Online-Version aus Gründen des Datenschutzes nicht enthalten.

Statutory declarations

Erklärung:

Hiermit erkläre ich, gem. § 7 Abs. (2) d) + f) der Promotionsordnung der Fakultät für Biologie zur Erlangung des Dr. rer. nat., dass ich die vorliegende Dissertation selbständig verfasst und mich keiner anderen als der angegebenen Hilfsmittel bedient, bei der Abfassung der Dissertation nur die angegeben Hilfsmittel benutzt und alle wörtlich oder inhaltlich übernommenen Stellen als solche gekennzeichnet habe.

Essen, den ________________ ______________________________________

Unterschrift des Doktoranden

Erklärung:

Hiermit erkläre ich, gem. § 7 Abs. (2) e) + g) der Promotionsordnung der Fakultät für Biologie zur Erlangung des Dr. rer. nat., dass ich keine anderen Promotionen bzw. Promotionsversuche in der Vergangenheit durchgeführt habe und dass diese Arbeit von keiner anderen Fakultät/Fachbereich abgelehnt worden ist.

Essen, den ________________ ______________________________________

Unterschrift des Doktoranden

Erklärung:

Hiermit erkläre ich, gem. § 6 Abs. (2) g) der Promotionsordnung der Fakultät für Biologie zur Erlangung der Dr. rer. nat., dass ich das Arbeitsgebiet, dem das Thema „Characterizing DNA Origami Linear Assemblies“ zuzuordnen ist, in Forschung und Lehre vertrete und den Antrag von Lena Stenke befürworte und die Betreuung auch im Falle eines Weggangs, wenn nicht wichtige Gründe dem entgegenstehen, weiterführen werde.

____

Name des Mitglieds der Universität Duisburg-Essen in Druckbuchstaben

Essen, den ________________ ______________________________________

Unterschrift eines Mitglieds der Universität Duisburg-Essen